MODELLING ULTRAFAST EXCITON TRANSFER IN FLUORENE-BASED ORGANIC SEMICONDUCTORS

Jean-Christophe H Denis

Submitted for the Degree of Doctor of Philosophy

Heriot-Watt University
School of Engineering and Physical Sciences
Edinburgh, December 2013.

Abstract

We present a theoretical study of exciton dynamics in solutions and films of fluorene-based molecules, complemented by experimental work carried out by our colleagues at the University of St Andrews. We start by introducing the importance and relevance of such a study, and the methods we use to model ultra-fast (pico- and sub-picosecond) exciton photo-physics in these systems. We then demonstrate that exciton transfer in solution of some branched star-shaped oligofluorene-based molecules arises from molecular geometry relaxation, and, at a slower time-scale, from Förster hopping between the arms. Straight oligofluorenes do not exhibit ultra-fast exciton transfer in solution. Finally, we introduce improvements to the standard line-dipole theory which we use to build a microscopic model for ultra-fast exciton dynamics in polyfluorene films. Our results show very good agreement with experiments and enable us to gain fundamental insight into the exciton transfer processes in these materials.

Acknowledgements

I must say I would never have been able to achieve the work presented here without the help, support and company of quite a few people around me.

First of all, I would like to express my gratitude and sincerest thanks to my supervisor, Prof. Ian Galbraith. His continuous support, ideas, comments, patience and help during these four years have resulted in an efficient and successful supervision, which led to the work I present here.

Dr. Stefan Schumacher has played a major role as well in the work presented in this thesis, thanks to his patience, support and numerous inspirational discussions and ideas. The three visits I made to Paderborn, in addition to being very useful and productive, were also very enjoyable thanks to him, his colleagues and his family. Thank you all very much!

I also address my gratitude to the experimental team in St Andrews for all the time we spent together trying to understand the work we were respectively doing, and how to successfully combine theory and experiments to make stronger science. Thanks to you, Dr. Neil Montgomery, Dr. Gordon Hedley, Dr. Arvydas Ruseckas, Alex Ward, Dr. Graham Turnbull and Prof. Ifor Samuel, our collaboration was very fruitful and resulted into more relevant and deeper research.

I must thank Dr Martin Paterson too for his helpful discussions regarding quantum chemistry and theoretical chemistry.

Additional warm thanks go to my colleagues Peter, Natalia, Matthew and Sebastian, for the enjoyable lunches and breaks we had together, which made daily PhD-life much more pleasant. Thanks for the good times, guys!

I must also thank my Best Friend, Bryony, for having proofread my thesis and for her help with my sometimes incorrect English. Thank you for your great friendship and your prompt useful work, at sometimes short notice - I will be there for you when needed.

Finally, a number of friends and relatives have helped me making this long and difficult journey easier. In particular, I would like to address special thanks to my parents, grand parents, brother and my local Edinburgh "family" who all made my daily life better and gave me the strength and motivation I needed: Abdelhamid, Bryony and Jenny. I am very lucky to have you; without you, I could not have done this.

List of publications

Part of the work presented in this thesis has been published in the form of journal articles.

- N. A. Montgomery, J.C. Denis, S. Schumacher, A. Ruseckas, P. J. Skabara, A. Kanibolotsky, M. J. Paterson, I. Galbraith, G. A. Turnbull, and I. D. W. Samuel. Optical Excitations in Star-Shaped Fluorene Molecules. *The Journal of Physical Chemistry A* **115** (14), 29132919 (2011)

  This article corresponds to the work presented in Chapter 3.

- N. A. Montgomery, G. Hedley, A. Ruseckas, J.C. Denis, S. Schumacher, A. L. Kanibolotsky, P. J. Skabara, I. Galbraith, G. A. Turnbull, and I. D. W. Samuel. Dynamics of fluorescence depolarization in branched oligofluorene-truxene molecules. *Physical Chemistry Chemical Physics* **14**, 9176 (2012)

  Some of the results described in Chapter 4 have been presented in this article.

- J.C. Denis, S. Schumacher, and I. Galbraith. Quantitative description of inter-actions between linear organic chromophores. *The Journal of Chemical Physics* **137**(22), 224102 (2012)

  The results presented in this article constitute Chapter 5.

Contents

Chapter 1

Introduction

This thesis is focused on ultra-fast (pico- and sub-picosecond) exciton transfer in polyfluorene-based organic semiconductors. In this introduction we will define what organic semiconductors are and highlight some of their key properties, before focusing on the ultra-fast photo-physics of these materials. We will then motivate the importance of understanding the fundamental physics of these materials through a study of their applications in devices, and highlight the current research challenges that these material are facing.

1.1 Organic semiconductors: Background

"Organic semiconductors", or "molecular semiconductors", are materials which, like any semiconductor, do not conduct charges as much as a metals do, but do conduct better than isolators. They are molecular materials made of organic compounds, whereas "inorganic semiconductors" are crystals made of elements from the columns II to VI in the periodic table of elements [1]. A more rigorous definition, as well as detailed basic physics principles, will be provided in Section 1.1.2.

1.1.1 A short history

Organic semiconductors emerged much later than their inorganic counterparts. Indeed, the first report of highly conductive polymers was made in 1963 [2], whereas the first inorganic semiconductor diode laser (made of gallium-arsenide) had already been created three years earlier [3]. Organic semiconductor devices therefore appeared long after their inorganic equivalents: whereas an inorganic light emitting diode (LED) was realised for the first time in 1962 [4], the first demonstration of an organic LED (OLED) dates from 1987 [5]. Similarly, organic transistors were first developed in 1986 [6], much later than the realisation of the first inorganic transistor created in 1947 [7]. This is true for photovoltaic cells as well: the first silicon solar cell was produced in 1954, with an efficiency of 6% [8]; in contrast, the first organic cell, with an efficiency of around 1%, was created in 1986 [9]. However organic lasers appeared quite early, in 1967, in the form of dye lasers, usually consisting of crystals of dye-doped polymer [10, 11], and even made a significant contribution to the development of both organic and inorganic lasers [12]. Non-dye based, organic semiconductor lasers appeared in 1992 [13].

The much more recent discovery and investigation of organic semiconductors, compared to the longer history of inorganic semiconductors, is one of the main reasons why organic semiconducting devices are not widely commercially available. However, they are the subject of important research efforts due to their advantages over inorganic semiconductors, and therefore their potential to replace them in the near future, as we shall see in the rest of this introduction.

1.1.2 Basic photo-physics of organic semiconductors

Organic semiconducting materials can be either short molecules or extremely long molecules called polymers, consisting of the repetition of a monomer unit [14]. Examples of such semiconducting molecules are presented in figure 1.1. Organic semiconducting molecules, both short and long, have a backbone of carbon atoms formed by the σ-bonds between adjacent carbon atoms, created by the individual sp^2 wavefunctions (or orbitals) [15]. They also possess a conjugated electronic system formed by the π-molecular orbitals, which are orthogonal to the σ-orbitals, and, in general, arise from the p_z atomic orbitals of the sp^2-hybridized carbon atoms [16]. These bonds are illustrated in figure 1.2, where the ethylene molecular structure is defined by the σ-bonds. The π-bonds, sketched in figure 1.2, are orthogonal to the structure of the molecule and are conjugated. This is why organic semiconducting materials are often also called "conjugated molecules". These π-bonds are much weaker than the σ-bonds, which hold the structure together, and therefore they are responsible for most of the electronic and optical properties that characterise a conjugated molecule [14].

It is common to use the acronyms HOMO and LUMO to respectively designate the highest occupied molecular orbital and the lowest unoccupied molecular orbital [14]. In most organic semiconductors, the energy of the HOMO corresponds to the top of the highest energy π-band, all the lower energy bands being filled as well, and the LUMO corresponds to the bottom of the lowest energy π^*-band (* denotes an excited orbital), all the higher energy bands being empty [14]. The organic semiconductor "bandgap" can therefore be defined by the energy difference between LUMO and HOMO (at first approximation, neglecting the exciton binding energy, for instance [18]). The π to π^* transitions are typically between 1 and 3 eV [19], leading to light absorption and emission in the visible range. The π- and π^*-bands are not necessarily extended over the whole molecule, and π- or π^*-bands of very close energies can be localised in different parts of a single molecule. The localisation on the molecule of the π- and π^*- bands involved in an electronic transition defines a chromophore [14]. Excitons in polymers are usually well represented as one dimensional excitons, extended (a few nanometres) along the chain [20]; their length is related to what is called the "conjugation length" [21], the typical length

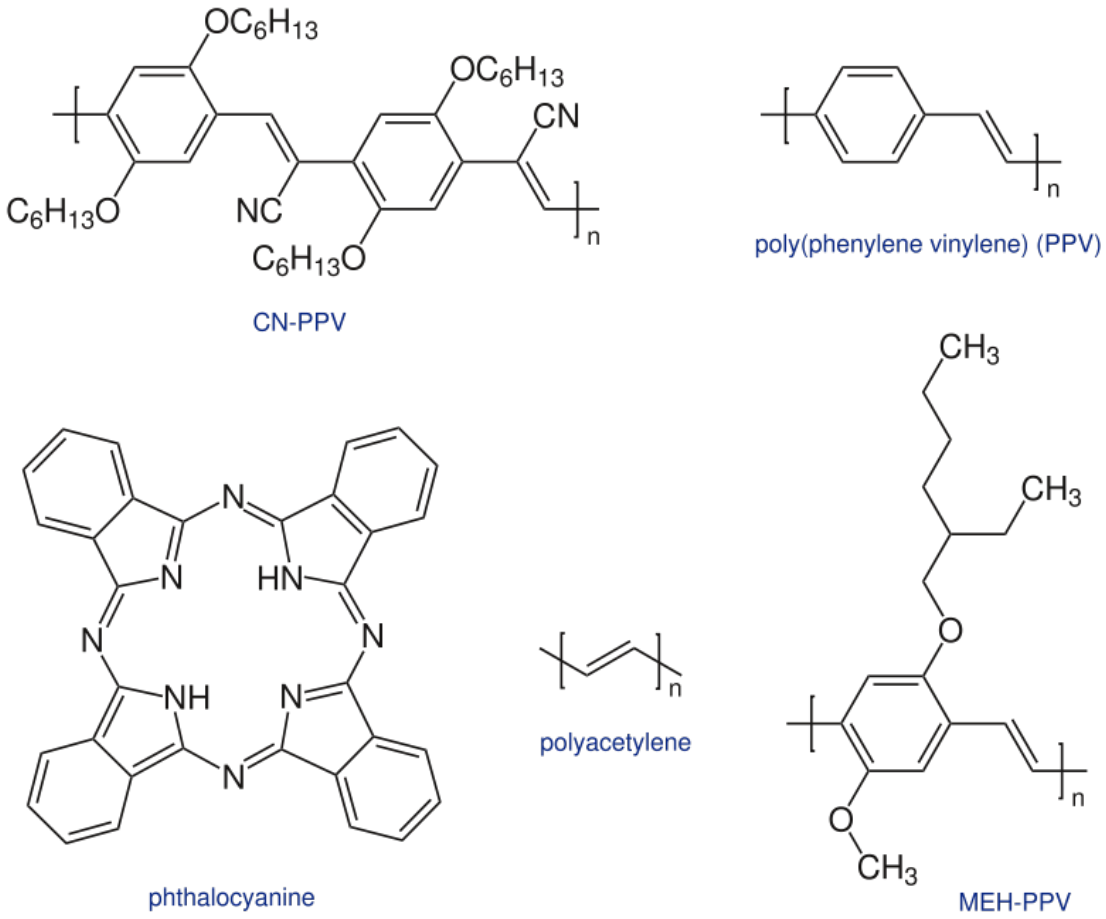

Figure 1.1: Example of a semiconducting small molecule (phthalocyanine) and semiconducting polymeric molecules, which can be used in photovoltaic cells (from reference [17]).

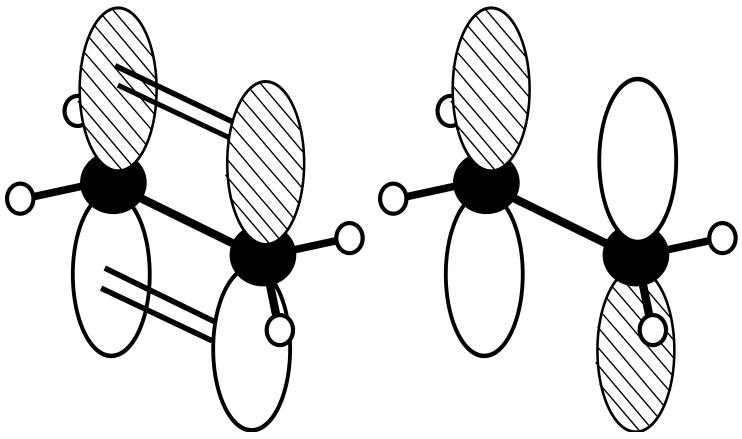

Figure 1.2: Sketch of the ethylene molecule, with representation of the HOMO, or π-bands (left) and LUMO, or π^*-bands (right) (from reference [17]).

of the polymer chain which is not significantly distorted so that the electronic properties are the ones of the straight chain. Usually, the definition of a chromophore is restrained to the transitions in the visible spectra, but we extend it to any transition in this thesis - by chromophore length we mean the spatial extent of the polymer where the transition of interest, whatever its energy, takes place. Therefore, whereas in inorganic semiconductors the bandgap arises from the extended, ordered lattice [22], in organic semiconductors the bandgap is created and present in any individual molecule.

Under photo-excitation we can observe photo-conductivity: an electron is promoted from the valence band (π-band) to the conduction band (π^*-band) by photon absorption [23]. As a result, mobile electrons and holes are created and can move as a response to an electric field. This property makes organic semiconductors suitable for the fabrication of many electronic devices such as light emitters, displays, transistors, photovoltaic cells and lasers. A detailed study of the photo-physics of organic semiconductors will be conducted in the next Section, 1.2. We will review the physics of such devices in Section 1.3.

Semiconducting polymers are stable in a variety of phases, such as gases, solutions or solids (in crystalline, semi-crystalline or amorphous forms), depending on the molecule and the processing techniques. The main difference between small molecules and polymers lies in the way they are processed to produce thin-films. Conjugated polymers need to be spin-coated or deposited by a printing-like technique, whereas small molecules are deposited onto the film from sublimation or evaporation, or can also be grown as a single-crystal much more easily than polymers [14].

We will highlight the advantages and drawbacks of organic semiconductors more specifically in the context of their use in devices in Section 1.3, but one major limitation of most organic semiconducting samples is their poor photo-chemical stability, particularly when exposed to water, oxygen and modest temperatures [23]. Techniques exist to overcome this limit, such as encapsulation, but could still be improved [24]. One of the main advantages of organic semiconductors is the ease with which they can be processed, with the possibility of utilising simple "printing techniques" [12]. In contrast, inorganic semiconductors require more complex processing techniques, such as chemical vapour deposition or molecular beam epitaxy [1].

1.2 Ultrafast photo-physics in organic semiconductors

1.2.1 Photo-excitation of a single molecule: simple picture

Following the absorption of a photon by the semiconducting molecule, an electron is promoted from the π-band to the π^*-band. A hole is created by the lack of

one electron in the HOMO, and this hole is bound to the electron due the attractive Coulombic force between them. This electron and hole bound state is described by a quasi-particle, called an "exciton" [25]. Two models exist for the exciton: the Wannier exciton and the Frenkel exciton [18]. Wannier excitons do not possess a strongly bound electron and hole (the binding energy is typically less than 0.01 eV [26]), and are therefore delocalised over many atoms, whereas electrons and holes in the Frenkel model have much stronger binding energies (with values typically reported from 0.4 to 1eV [27–29]). Wannier excitons usually describe excitons in inorganic semiconductors [23], where the dielectric constant is much higher than in organic semiconductors. Frenkel excitons usually occur in molecular semiconducting systems [23]. Therefore, in the rest of this thesis, we will refer to Frenkel excitons as simply "excitons".

A chromophore can be, to a certain extent, compared to a harmonic quantum oscillator; the outcome of this comparison is that the potential energy surface of the molecule is typically parabolic, as a function of the nuclear coordinates [30] - a parametrisation of the position of the nuclei of the chromophore. When unexcited, the chromophore geometry is the ground-state geometry, the ground-state being denoted in the rest of this thesis as the S_0-state. This geometry corresponds to the minimum of the ground-state potential energy parabola. In the frame of the Born-Oppenheimer approximation, the nuclei motions are slow compared to the electrons (see Section 2.3 for more details), and as a consequence the absorption transition is vertical: the geometry of the chromophore does not undergo any change during the photon-absorption or emission process. In the rest of this thesis, all transitions will be vertical: they take place without immediate molecular geometry change, as sketched in figure 1.3. Just after photo-absorption the chromophore is in the first excited-state (or any higher excited state, depending on the photon energy), that we will call in the rest of this thesis the S_1-state, and the potential energy surface of the molecule has changed due to the presence of the excitation, leading to a different combination of the oscillator modes (see figure 1.3). Due to the coupling between the chromophore and its environment (solution, phonons), the chromophore will consequently relax from the S_0 geometry to the S_1 geometry, corresponding to the minimum of the S_1 potential energy surface. This relaxation is fast, typically 100 fs [31,32]. Radiative decay mechanisms will then be responsible for the emission of a photon at the emission energy, vertically from the S_1 to the S_0 potential energy surface. This will be followed by the relaxation of the molecule from the S_1 geometry back to the ground-state S_0 geometry.

This is illustrated in figure 1.3. From this figure it is clear why the absorption energy is always higher than the emission energy (the difference between the absorption and emission energies is usually called "Stokes-shift" [14]). For an ensemble of

chromophores, due to thermal energy, the chromophores will individually experience a number of geometrical configurations leading to a broadening of the equilibrium absorption energy. This phenomena is defined as "inhomogeneous broadening of the spectra".

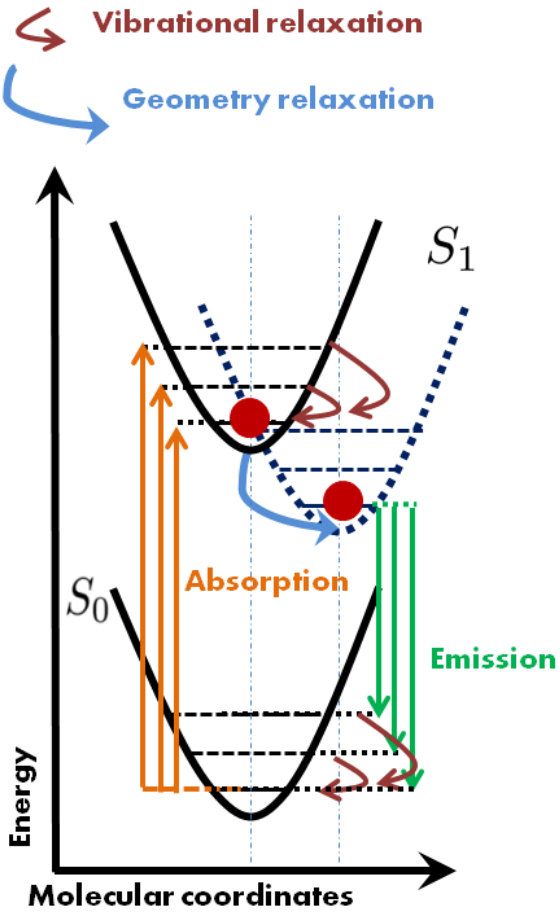

Figure 1.3: Sketch of the processes involved in the photo-excitation of a chromophore.

All these photo-physical processes do not change the orientation of the electronic spins. The excitation, when created, is always a singlet because the pair of electrons in the HOMO have opposite spins. Therefore, in the description above, only a singlet exciton is considered. Change of orientation of the spins can nonetheless occur, following a mechanism called inter-system crossing [14] and this results in the creation of triplet excitons. The mechanisms for the creation of these triplet excitons are generally slow (typically on the nanosecond timescale [33–35]) so in the rest of the thesis, where the focus will be on the pico- and sub-picosecond excitation dynamics, we will consider only singlet excitons.

In polymers, due to the strong π-orbital overlap arising from the closely spaced neighbouring atoms of the monomeric units, the exciton wavefunction usually extends over several of these monomers [20]. As previously stated, the extent of this wavefunction is called the conjugation length [21]. It is theoretically possible for the

exciton to be extended over chains belonging to neighbouring polymers because of intrachain interactions, and the resulting multichain exciton is called an exciplex [36]. However, the significant disorder in polymer films makes this delocalisation very unlikely; as a result the formation of exciplexes will be ignored in the rest of this thesis.

Non-radiative decay mechanisms also exist. A measure of the fraction of these non-radiative decays is given by the photoluminescence quantum yield (PLQY). The PLQY is defined as the ratio of the number of photons emitted over the number of photons absorbed [14]. Values range from close to 0% to almost 100% quantum efficiency, meaning that in the latter case almost all excitons follow the recombination path described above.

1.2.2 Molecular vibrations: Impact on photophysics

A more realistic model includes vibrations; indeed molecules made of hundreds of atoms possess numerous degrees of freedom, leading to vibrations arising because of thermal energy and photo-excitation [30]. Due to thermal energy, the energy of the chromophore will actually not necessarily be the minimum of the ground-state potential energy surface, but could have a range of values, depending on where the vibrational modes are energetically situated. The transitions to the excited-state which will be dominant are the ones reaching a vibrational state of the excited-state energy potential [30]. Detailed mathematical treatment of the absorption probability between electronic and vibrational states is given by the Franck-Condon principle, which is developed in Section 2.4. These vibrations are very evident in the absorption and emission spectra of a single chromophore, provided the homogeneous linewidth (the spectral broadening appearing from the dephasing time of the excitation, see Section 2.4) is not too wide.

1.2.3 Multiple chromophores: Exciton transfer

Once the exciton is created, its transfer to another chromophore is possible. This transfer can be realised by simple photoluminescence from one chromophore, and re-absorption of the emitted photon by another chromophore. However, the radiative lifetimes of the fluorene-bases molecules we investigated in this thesis are longer than 100 ps [37], whereas we are interested in the picosecond and sub-picosecond dynamics of such molecules. In the rest of this work, our interest will therefore be restricted to non-trivial exciton transfer mechanisms, involving no photon-emission and re-absorption.

We can distinguish two kinds of exciton transfer: either the exciton has reached a chromophore of the same molecule or it has transferred into the chromophore of an-

other molecule. The first case corresponds to "intrachain" exciton transfer whereas the second case is called "interchain" exciton transfer [38]. Interchain transfer requires close neighbouring molecules and therefore does not take place in well diluted solutions with small concentrations of organic semiconductors, nor in gas-phases.

Exciton transfer mechanisms lead to the transfer of excitation to low energy chromophores. This phenomena plays a major role in the ultra-fast photo-physics processes in organic semiconductors, by governing which subset of chromophores of the whole ensemble is most likely to become excited after photo-excitation. This is of crucial importance in devices such as organic light emitting diodes (OLEDs) and organic photovoltaic cells (OPV), where the the device characteristics are based on both the photo-physics and charge transport properties (see detailed device descriptions in Section 1.3). It can also lead to the transfer of either the electron or the hole only, creating a separated electron and hole pair - a quasi-particle which is known as a "polaron" [36]. However such separation requires one to overcome the strong exciton binding energy, typically 0.5 eV in polyfluorenes [12], and therefore requires a specific structure and blend or semiconducting molecular species, as used in organic photovoltaic cells (see Section 1.3). As we will only study pure-phase samples of molecules without charge transfer character in this thesis, we will assume that polaron formation is non-existent at the time-scale we are interested in. This is also supported by the lack of observed polaron signatures seen during the realisation of the experiments presented in Chapters 3, 4 and 6.

The need for a theory enabling the excitation transfer in organic materials appeared in the middle of the twentieth century, when it was observed that the PQLY of dye species were significantly different whether they were in solution or in solid phase [39, 40]. One of the explanations at this time was that the excitation was transferred to lower energy molecules in films (in diluted solutions, non-aggregated molecules behave like isolated molecules), and if these molecules to which the excitation transferred were not fluorescent (dark), this resulted in the observed PLQY loss [41].

Energy transfer processes are intimately linked to the interactions between chromophores. In the following work, we will present three interaction regimes: the weak, intermediate and strong coupling regimes. These regimes are determined by the comparison of two distinct timescales [30]: the vibrational relaxation time τ_{relax} and the exciton transfer time $\tau_{transfer}$. τ_{relax} is the time it takes for an excited chromophore to return to the thermal equilibrium of the excited-state from the "hot" out-of equilibrium vibrations induced by the vertical photo-induced electronic transition. It is intrinsically linked to the decoherence time, because such vibrational relaxation induces dephasing. Therefore a system with fast relaxation times will loose its quantum coherence quickly. $\tau_{transfer}$ is simply the typical time associated

with the movement of one exciton from an excited chromophore to a non-excited chromophore in the ground-state; it is directly linked with the interaction strength between these two chromophores, and with their spectral matching. All exciton transfers arise from the following Hamiltonian [42]:

$$H = H_0 + H_{el} + H_{el-vib} \ , \tag{1.1}$$

with H_0 being:

$$H_0 = \sum_n \varepsilon_n \left|n\right\rangle \left\langle n\right| + \sum_{n,k} \hbar\omega_{n,k} b^\dagger_{n,k} b_{n,k} \ , \tag{1.2}$$

where $|n\rangle$ is an excitation created in the n-th chromophore site, ε_n its associated energy, $\hbar\omega_{n,k}$ is the energy of the k-th vibrational state of the n-th chromophore, with $b^\dagger_{n,k}$ and $b_{n,k}$ being respectively its bosonic creation and annihilation operator. H_{el} describes the intermolecular electronic coupling:

$$H_{el} = \sum_{m>n} \sum_n J_{m,n} \left(\left|n\right\rangle \left\langle m\right| + \left|m\right\rangle \left\langle n\right|\right) \ , \tag{1.3}$$

with $J_{m,n}$ being the electronic coupling between chromophores m and n. $H_{el-bath}$ represents the electronic interaction with the bath.

$$H_{el-bath} = \sum_n \sum_k g_{n,k} \left(b^\dagger_{n,k} + b_{n,k}\right) \left|n\right\rangle \left\langle n\right| \ , \tag{1.4}$$

where $g_{n,k}$ is the coupling of the k-th vibrational mode of the n-th chromophore with the phonon bath.

The ratio between the energy difference and the electronic coupling of two chromophores ($|\varepsilon_m - \varepsilon_n|/J_{m,n}$) defines the localisation of the excited state [42].

The comparison of the electronic coupling between two chromophores and their coupling with the phonon bath determines if the transfer is coherent or not. Indeed, the electronic coupling is linked to the exciton transfer rate $\tau_{transfer}$, whereas the chromophore-phonon bath coupling relates to τ_{relax} [30].

We can therefore distinguish three cases, depending on the comparison between these characteristic times [30, 42, 43]:

- $\tau_{relax} \ll \tau_{transfer}$, in such a case the exciton transfer take place when the chromophore is totally relaxed to the excited-state equilibrium geometry, and therefore the coherences do not exist any more. This case is thus called incoherent transfer, or the weak coupling limit.

- $\tau_{relax} \gg \tau_{transfer}$. In this situation, coherence is long lived compared to the transfer, so the exciton is a quantum mechanical wave packet. It can in conse-

quence move almost freely from chromophore to chromophore. Such transfer is therefore called coherent transfer, or transfer in the strong coupling limit.

- $\tau_{relax} \approx \tau_{transfer}$. This case is not trivial, as the exciton motion is at the border between coherent and incoherent. Additionally, the definition of such a system is not straightforward: if the molecular sample is made of aggregates, it is possible that the exciton motion in an aggregate is coherent, whereas the motion between aggregates is not. This regime is called partially coherent, or the intermediate coupling limit.

In particular, the assumption that incoherent transfer is the dominating transfer mechanism is consistent with the assumption that excitons are localised on one chromophore - the weak coupling limit. We assume that in fluorene-based molecules, $|\varepsilon_m - \varepsilon_n| \gg J_{m,n}$, so that the exciton is localised on only one chromophore and that weak coupling applies. This confirmed by results from Chapters 4 and 6.

The electronic coupling V between the acceptor and donor molecules can be partitioned into two coupling mechanisms [43]: one coupling arising from the Coulombic interaction between the charged particles, V_C, and one associated with the degree of overlap between the molecular orbitals of the donor and acceptor, the exchange-interaction V_X.

$$V = V_C + V_X \ . \tag{1.5}$$

Two theories have developed to describe incoherent energy transfer, depending on which coupling energy is dominant. If the coupling energy is dominated by Coulomb coupling, the associated coupling is called Förster transfer and is based on resonant, dipole-induced energy transfer. Conversely, if the main coupling mechanism is the overlap between molecular orbitals, the transfer is Dexter-type and relies on electron exchange. Therefore, Förster transfer deals with long-range energy transfer whereas Dexter transfer deals with short-range energy transfer.

1.2.4 Förster theory: Incoherent exciton transfer

It was first proposed that excitation transfer in organic semiconductors was similar to energy transfer in coupled oscillators [42]: if one excites a spring which is weakly coupled to another one, it is possible to see the oscillation spreading and being transferred to the other coupled spring. In the case of chromophores, the coupling is between the transition densities of each chromophore. Indeed, if these charges are spatially distributed so that light interaction with the chromophore is possible, an oscillating dipole is created on the chromophore, conceptually analogous to an oscillating spring. In this frame, the coupling energy between chromophores is therefore approximated as $V \approx V_C$. Knowing the wavefunction of state i of

chromophore X, $\phi_i(\boldsymbol{x_1}, \boldsymbol{x_2}, ..., \boldsymbol{x_N})$, where $\boldsymbol{x_j}$ is the coordinate of electron j, the transition density between the ground and first excited states is given by [30]:

$$n_{01}^X(\boldsymbol{r}) = N \int \phi_0(\boldsymbol{x_1}, \boldsymbol{x_2}, \ldots, \boldsymbol{x_N}) \phi_1^*(\boldsymbol{y_1}, \boldsymbol{y_2}, \ldots, \boldsymbol{y_N}) d\boldsymbol{x_2} \ldots d\boldsymbol{x_N} d\boldsymbol{y_2} \ldots d\boldsymbol{y_N} \ , \quad (1.6)$$

where $\boldsymbol{r} = \boldsymbol{x_1} - \boldsymbol{y_1}$. These transition densities are coupled to each other by Coulombic interaction, leading to the following interaction energy between the acceptor and donor chromophores A and D:

$$V_C = \frac{e_0^2}{4\pi\varepsilon_0} \int \frac{n_{01}^D(\boldsymbol{r_1}) n_{10}^A(\boldsymbol{r_2})}{|\boldsymbol{r_1} - \boldsymbol{r_2}|} d\boldsymbol{r_1} d\boldsymbol{r_2} \ . \quad (1.7)$$

If the distance between the chromophores is larger than the spread of the transition, then the dipole approximation can be used and the transition density distribution can be reduced to a linear dipole [44].

It was also found experimentally, in 1948, that the efficiency of the excitation transfer in molecular samples depends strongly on the absorption and emission energies [42]; more precisely, on the emission spectrum of the excitation donor and the absorption of the acceptor. This is fundamentally the expression of the energy conservation rule, and of the resonant character of these transfers. These experimental findings motivated Förster to undertake theoretical work to predict these observations. Using the Fermi Golden rule with second-order perturbation theory treatment of the electronic coupling between donor and acceptor, Förster derived an expression of the excitation transfer rate [44, 45]:

$$k_{Förster} = \frac{2\pi}{\hbar} V_C^2 \int g(\hbar\omega) \ d\hbar\omega \ , \quad (1.8)$$

where $\hbar\omega$ is the excitation energy, $g(\hbar\omega)$ is the overlap between the normalised fluorescence spectra of the donor and the normalised absorption spectra of the acceptor and V_C the interaction energy between the chromophores. This interaction energy depends on the photon energy through the dielectric screening of the Coulombic interaction. The spectra used in the spectral overlap calculation need to include vibrations as well [44, 45].

Förster used the point-dipole approximation to obtain a simplified expression of this rate [43]:

$$k_{Förster}(R) = \frac{1}{\tau^r} \left(\frac{R_0}{R} \right)^6 \ , \quad (1.9)$$

where τ^r is the radiative decay of the donor chromophore, R the centre to centre separation and R_0 the Förster radius, defined as the distance for which the transfer

rate is equal to the radiative decay rate of the donor:

$$k_{Förster}(R_0) = \frac{1}{\tau^r} \ . \tag{1.10}$$

It can be shown that this Förster radius R_0 is, within the point-dipole approximation [43]:

$$R_0^6 = \frac{9000\kappa^2\eta g(\hbar\omega)\ln 10}{128\pi^5 N_A n^4} \ , \tag{1.11}$$

with η the photoluminescence quantum yield, N_A Avogadro's number, n the refractive index and κ the orientation factor arising from the dipole-dipole interaction, defined as:

$$\kappa = \boldsymbol{d_A} \cdot \boldsymbol{d_D} - 3\left(\boldsymbol{d_A} \cdot \boldsymbol{R}\right)\left(\boldsymbol{d_D} \cdot \boldsymbol{R}\right) \ , \tag{1.12}$$

where $\boldsymbol{d_A}$ ($\boldsymbol{d_D}$) is the direction of the dipole of the acceptor (donor) chromophore and $\boldsymbol{R}$ is the acceptor centre to the donor centre vector. In the case of an ensemble of spatially randomly oriented linear chromophores, we can calculate that an average value for κ is 2/3 [41].

The expression of equation (1.9) highlights the separation dependence of the Förster energy rate, in $1/R^6$.

The use of the term "Förster energy transfer" usually implies a transfer rate following the expression derived by Förster in the limit of the point-dipole approximation. However, the use of the point-dipole approximation is subject to a number of conditions which are not fulfilled in standard organic semiconductor films. Numerous approximations to "improve" Förster theory, consisting for instance of higher dipole expansion [46], quantum electrodynamic theory [47–49] or transition density cubes obtained by quantum chemistry calculations [50–52], have been proposed since. A complete review of these methods, and, in particular, the dipole approximations, as well as an accurate and efficient Coulombic interaction calculation method, will be presented in Chapter 5. In the rest of this thesis, "Förster energy transfer" designates the incoherent exciton hopping given by the rate of equation (1.8), whatever the method used for the calculation of the Coulombic coupling is (it will clearly be stated when necessary). The other assumptions of Förster theory are that only one electronic state of each of the two chromophores is involved in the process, that the quantum coherence has vanished and that the bath around the chromophores varies incoherently.

1.2.5 Dexter theory: Incoherent exciton transfer

The other incoherent exciton transfer mechanism which can take place was first formulated by Dexter [46]. He stated that at short distance, $V \approx V_X$ and therefore the main mechanism responsible for energy transfer is the electron exchange interac-

tion. This interaction arises from the symmetrisation of the electronic wavefunctions. In consequence, if two molecular species are very closely separated, their molecular orbitals can overlap, leading to electron transfer from the donor to the acceptor. Dexter stated that, as the molecular orbital tails decay exponentially (typically, the tail T is proportional to $\exp(-\alpha R)$, α being in the range of 1.2-2.0Å^{-1}) [42], therefore the electronic coupling V_X varies as $V_X \propto \exp(-2\alpha R)$, R being the centre-to-centre separation of the molecular orbitals [53]. The Dexter electron transfer rate is the same as for the Förster exciton transfer rate (it depends on the overlap of the absorption spectra of the acceptor with the fluorescence spectra of the donor, and on the square of this interaction energy), but the interaction energy is now derived from the molecular orbital overlap [46]:

$$k_{Dexter} = \frac{2\pi}{\hbar} V_X^2 \int g(\hbar\omega) d\hbar\omega \ . \tag{1.13}$$

This interaction is quite weak compared to the dipole-dipole interaction, except at short distances, typically for separations less than 5Å, where Dexter transfer dominates [42].

However, the original Dexter theory deals with electron transfer, not exciton transfer. Indeed, the transfer of an exciton requires the hole to be transferred from the donor to the acceptor as well. This means that the electron in the LUMO of the exciton donor must be transferred to the LUMO of the exciton acceptor, and in parallel, the spin-matching electron of the HOMO of the exciton acceptor must relocate to the HOMO of the exciton donor [54], as sketched in figure 1.4. This results in the expression of the transfer rate being somewhat more complex than the rate formulae presented in equation (1.13), but as a first approximation we can assume that dependence of the rate with the centre-to centre separation ($V_X \propto \exp(-2\alpha R)$) is still valid. A more precise treatment is given in reference [54].

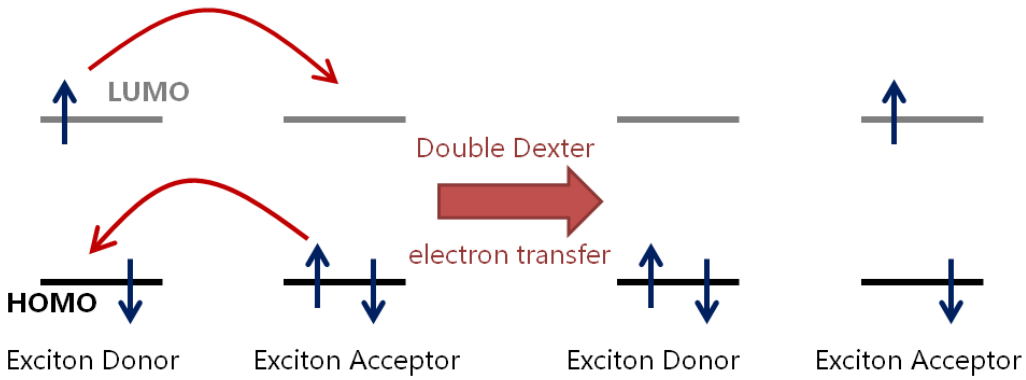

Figure 1.4: Sketch of the two electron transfers resulting in exciton transfer in the frame of Dexter theory.

Förster and Dexter transfer are therefore characterisable in real systems, as long

as we can measure the distance dependence of the exciton transfers. Indeed, we have shown that Förster transfer varies approximately in $1/R^6$, whereas Dexter transfer varies as $\exp(-2\alpha R)$. In theory molecular systems can exhibit both behaviours [42], depending on how close the chromophores are, and how they are arranged. In the rest of this thesis, we however exclude Dexter transfer, as we believe fluorene based-chromophores are not so closely packed that they are within the range of application of Dexter transfer. Indeed, we show evidence in this thesis that Dexter theory is not necessary to model exciton transfer in solutions of fluorene-based star-shaped molecules (Chapter 4) and in polyfluorene films (Chapter 6).

1.2.6 Beyond Förster-Dexter theory: Incoherent exciton transfer

Recent corrections have been proposed to the original incoherent Förster-Dexter energy transfer theories. Förster based his theory on the Coulombic effect, neglecting the magnetic effects arising from the magnetic field associated with any electric field. In most cases, this magnetic field is negligible; however when inter-chromophore distances are comparable with the excitation wavelength $2\pi c/\omega$, where c is the speed of light and ω the angular frequency of the excitation exchanged between the chromophores, the full electromagnetic coupling should be taken into account, and not only the Coulombic coupling [47, 55]. However, due the conditions on the virtual photon exchanged and the distance between the two involved chromophores (the wavelength of the photon has to be typically a few nanometers), this applies only for high energy photons, such as photons in the ultraviolet range [54], and is mostly relevant for biological systems exposed to such radiations, such as nucleic acids in DNA [56]. As the fluorene-based molecules we present in the rest of this thesis emit in the visible spectra, we will be not using this correction to the Förster theory in our work. More details about this correction to the Förster theory, called "photon-mediated energy transfer", are available in the literature, for instance in reference [54].

Another long-range correction is "bridge-mediated energy transfer" [57,58]. This correction is based on the idea that the transfer of energy from the donor chromophore to the acceptor chromophore can be mediated by one or more "intermediate" chromophores. For instance, if the donor and acceptor are different species which are very different energetically, direct Förster transfer between these two chromophores will be unlikely. However, if a neighbouring chromophore with an energy between the energies of the donor and acceptor species exists, the excitation could transfer more efficiently from the donor to to this intermediate chromophore, and then from there to the final acceptor chromophore. Because we use pure-phase fluorene-based molecular samples in the rest of this thesis, we neglect any bridge-mediated energy transfer theory to calculate "improved" Förster rates. For refer-

ence, detailed theoretical results concerning this correction are given in reference [54]. Additionally, this corrective transfer is intrinsically included in the model of Förster based exciton transfer that we present in Chapter 6, and an "improved" Förster rate is not necessary in this case. We will also demonstrate, in Chapter 6, that in pure fluorene-based materials, none of these corrections are necessary to predict the experimentally observed exciton transfer.

1.2.7 Coherent exciton transfer

In the strong coupling limit, energy transfer is coherent and excitons are delocalised over several chromophores, so that the incoherent Förster-Dexter theories are not applicable any more. Coherent effects are pure quantum mechanical effects, the excitation being described by wavefunctions whose phases are conserved [42]. This means that quantum interferences can occur, exactly like in the Young slits experiment, because multiple pathways exist for the transfer of excitation from one delocalised site to another one. These interferences imply oscillatory dynamics of the electronic eigenstates, which are coupled to each other by the coherences. In the basis of the chromophores (where the excitation is described as the excitation density on each chromophoric site), coherent effects are characterised by the spread of an exciton over many of these chromophores, with local oscillations of the exciton density on a particular chromophoric site, coupled with other sites. The only way to deal accurately with the modelling of such quantum coherent excitations is the utilisation of the density matrix approach, combined with a master equation [42]. However, the modelling of the interaction between a molecular exciton and the surrounding bath is still a theoretical challenge, even though some relatively satisfying treatments exist (based on a small-polaron transformation for instance [59–61]) beyond the scope of this thesis. A detailed presentation of density matrix theory, used in conjunction with a particular master equation approach (the optical Bloch equations), can be found in Chapter 2.

Coherent energy transfer has long been neglected because of the belief that coherence was very-short lived compared to any other typical time-scales in molecular semiconducting systems (typically less than a hundred femtoseconds) [62–64]. However, recent experiments seem to indicate that quantum coherent superposition of states occur over much longer times than originally thought [65–68], and that therefore quantum coherent energy transport phenomena could play an important role in the overall energy transfer process. Many of the systems where such long-lived coherences have been observed are biological light-harvesting systems [42]; in fluorene based molecules, to the best of our knowledge, no indication of long-lived coherent effects has been demonstrated, and we therefore neglect coherent exciton transfer mechanisms in the rest of this thesis.

1.2.8 Partially-coherent exciton transfer

When the molecular coupling is of the same order as the coupling of the excitons to the bath, the energy transfer regime is intermediate between coherent and incoherent. This case is particularly challenging, as it covers a lot of different scenarios [30, 42]. For instance, the relative strengths of these two couplings can be similar over the whole chromophoric ensemble, or different depending on the region, due to the local order of chromophores for instance. In this latter example, the exciton will be delocalised and its transfer will be coherent within the locally ordered chromophores, but become incoherent when the exciton reaches another region of space. For this reason, it is still a challenge to establish a reliable theory describing this regime, as no theory is currently satisfying, and the recent attempts [69–71] need further investigation.

1.3 Principles of the operation of organic semiconducting devices

Conjugated organic materials are the subject of intensive research for a range of optoelectronic applications. These include light sources such as light-emitting diodes [5], light-emitting field-effect transistors [72] or lasers [12], as well as photodetectors [73] and photovoltaics [74]. In this Section we will review the principles of three common devices most relevant to our research, that can currently be fabricated from organic semiconductors: lasers, light emitting diodes and photovoltaic cells. We will highlight how organic semiconductors are used in these devices, and what particular challenges and advantages are associated with the use of these materials for these devices.

1.3.1 Lasers

The first laser using organic semiconductors was built in 1967 [10]. However, as with inorganic lasers, it required growing high quality crystals, which is a difficult, expensive and demanding process. The great stride forward in the field of organic lasers came with the realisation of a laser made of a polymer in solution, in 1992 [13], which opened up the possibility of fabricating lasers much more easily than conventional inorganic lasers [12].

Lasers are made of two distinct components: a cavity and a amplifier (or optical gain material) [75]. The cavity is made of two reflecting surfaces, usually mirrors, so that light can travel back and forth between the two mirrors. It acts as a light resonator and therefore selects a certain number of possible optical modes. The amplifier is inside this cavity. Its role is to emit the light and compensate for the losses light suffers during its reflection inside the cavity. This leads to a coherent emitted light, which can have an extremely well defined frequency and a very narrow

beam. The active part of the amplifier is the organic semiconducting material, as it emits additional photons through stimulated emission by incident photons. Energy is provided to the amplifier material by an external power source. In the rest of this Section, we will focus on gain materials, as this is the laser component which can be realised from organic materials.

The first generation of organic amplifiers were made of crystals of small molecules, such as anthracene [76] (see figure 1.5). The discovery that film amplifiers could be fabricated by simpler processes such as evaporation of small molecules (for example aluminium tris(quinolate) [12]) or spin-coating and ink-jet printing techniques for conjugated polymers (such as poly(phenylene-venylenes) (PPV) [77, 78] or polyfluorenes (PFO) [79] - see figure 1.5), resulted in numerous advances in the field of organic lasers [12]. Hybrid molecular structures also exist, such as the dendrimers [80]. In contrast to the conjugated polymers which are linear, the dendrimers are branched structures. They consist of a core and branched conjugated arms, the dendrons, with attached surface groups. The core and the conjugated arms are responsible for the main electronic properties, whereas the surface groups ensure very good solubility of the molecule. For this last reason, they are nowadays also commonly used as laser amplifiers [81, 82].

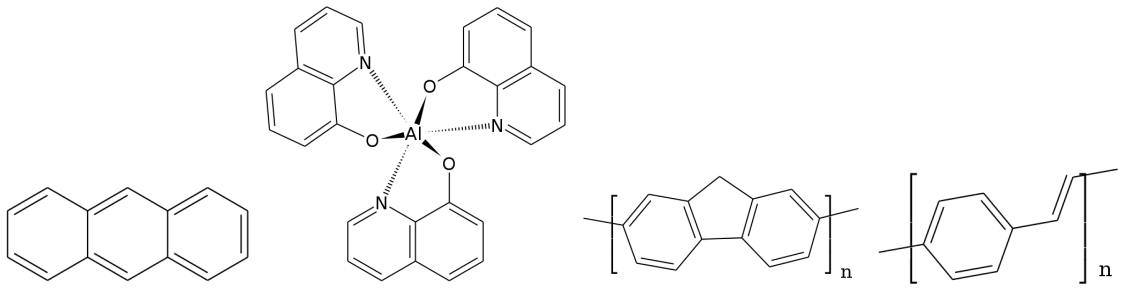

Figure 1.5: Sketch of the anthracene, aluminium tris(quinolate) (Alq_3), polyfluorene (PFO) and poly(phenylene-venylenes) (PPV) molecules, from left to right. These molecules are commonly used as laser materials.

The principle of an optical amplifier is to emit photons through stimulated emission [75]: once a site (chromophore) has absorbed a photon, an incoming photon will trigger the emission of an additional photon, of the same phase, energy and direction as the latest incident photon, giving rise to an amplified coherent light beam. Inversion of population is required for stimulated emission to take place. In a ensemble of two-level systems, this requires most of the chromophores to be in the excited state, and therefore strong intensities, which are difficult to generate and which can damage the materials, in addition to intrinsic excitonic effects, such as exciton-exciton annihilation (see Chapter 6), which will prevent high excitation densities from being long-lived.

However, real chromophores behave more like a model four-level system. Indeed,

we have seen in Section 1.2, and illustrated in figure 1.3, that the excitation of a chromophore involves a vertical transition to a vibrational level, before relaxation of the molecule to the equilibrium geometry of the excited state. A photon is then emitted by the transition from the equilibrium geometry of the excited state to a vibrational state of the ground-state, before relaxation from this vibrational state to the equilibrium geometry takes place. Therefore, it is possible to obtain significant population inversion between the equilibrium excited-state geometry and the vibrational mode of the ground-state geometry, even if a small fraction of the ensemble of chromophores is excited [12]. In addition, this process results in stimulated emission occurring at the emission energy, distinct from the absorption energy; this guarantees minimum re-absorption of the coherent beam to be amplified - if the system is well tuned [12].

The difference between the absorption and emission energies is further increased by the energy transfer processes which lead to localisation of the excitons to low energy sites. If two species of different energies are mixed together, it is possible to further enlarge this energy difference and even control it, by judicious choice of the low energy species. This clear distinction between absorption and emission energies results in even lower threshold lasing operation. By performing transient absorption measurements, it has been demonstrated that some organic materials could reach high optical gains [83, 84], making them particularly suitable for lasers. One additional reason for this high gain is that organic materials absorb strongly (a 100 nm thick film can absorb 90% of the incoming light [85]): if absorption is strong, stimulated emission will be strong as well, and only a small quantity of material is necessary.

Compared to inorganic lasers, organic lasers possess a much lower charge carrier mobility [86] and much higher exciton binding energy [27–29], creating issues for electrical pumping (see below). However, their advantages are their relative insensitivity to temperature change (due to the localised character of the excitons [87]), compared to inorganic lasers, the wide range of materials with emission energy in the visible spectra [88, 89] and the ease of the processing techniques [24]. These advantages make organic lasers particularly suited for displays, spectroscopy, sensing and data communication [12]. Compared to dye lasers, organic semiconductors do not need to be at low concentrations in solid state to offer high photoluminescence quantum yield, resulting in increased optical gain. Dye lasers cannot transport charges, so the possibility of electrical pumping does not even exist [12].

The inability to electrically pump organic lasers is the main drawback limiting the commercial development of these promising devices, and this limitation is the subject of intense research efforts. The low mobility of charges in organic materials is one of the main reasons explaining the impossibility of pumping lasers electrically:

this would require very high current densities, which would overheat and destroy the device [12]. High densities of excitation would create additional losses by high-order processes such as exciton-exciton annihilation. Triplet formation and contacts would be responsible for further losses.

1.3.2 Photovoltaic cells

Solar photovoltaic cells are a major field of application of organic semiconductors. They potentially play a role in meeting the challenge of increasing the world production of electric energy from renewable sources, at a low cost per final unit of energy produced.

The first inorganic, silicon solar cell appeared in 1954 and had an efficiency of 6% [8], whereas the first organic cell (with an efficiency of around 1%) was produced in 1986 [9]. Currently, the best inorganic cells have over 40% efficiency (Multi-junction cells [90]), with common commercial photovoltaic cells having an efficiency of around 20% [91]. Recently, organic cells with efficiencies greater than 10% have been demonstrated [92], increasing the hope for future research developments of very efficient cells. However, the real commercial efficiency measure is the cost per unit of energy produced [91], and the prospect of organic cells potentially having a better commercial efficiency than inorganic cells is the main reason for the current research interest in them, as we shall see in this Section.

The fundamental aim of any solar cell is to absorb photons from the Sun and convert them into electricity. For this purpose, a material which can create charges following photon absorption is necessary - these materials are typically semiconductors. Once the excitation is created, it is necessary to overcome the exciton binding energy in order to separate the electron and hole and thus create free charge carriers, which need to be collected by two specific electrodes and therefore create an electric field and current. In inorganic semiconducting materials, charges are separated by the utilisation of two oppositely doped materials, forming a "p-n junction" [8]. In organic semiconductors, where band theory is not applicable, there is no such junction, but instead a blend of two materials. One molecular species is the "electron acceptor", and the other one the "electron donor" [24]. MEH-PPV, P3HT or PCDTBT (see figure 1.6) are some of the common hole conductors [93], or equivalently electron donors. Fullerene (C_{60} or C_{70}), with its high mobility and ultrafast photo-induced charge transfer is considered the best acceptor [94] and is very often the acceptor material under the PCBM molecular structure (see figure 1.7).

Current generation from solar energy is achieved in four steps [95]. First, the incident light must be absorbed by the solar cell to create an exciton. As we have seen above, organic semiconductors possess very good absorption properties, and therefore thin-film layers of typically 100 nm [96] are thick enough for absorption

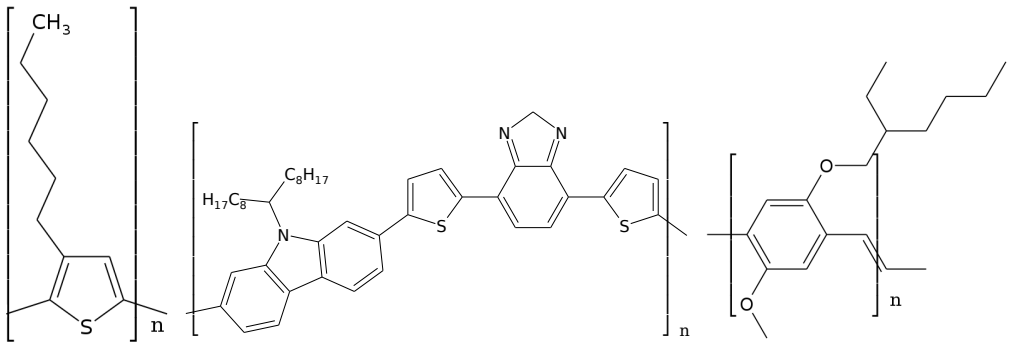

Figure 1.6: Sketch of the electron donors P3HT, PCDTBT and MEH-PPV, from left to right.

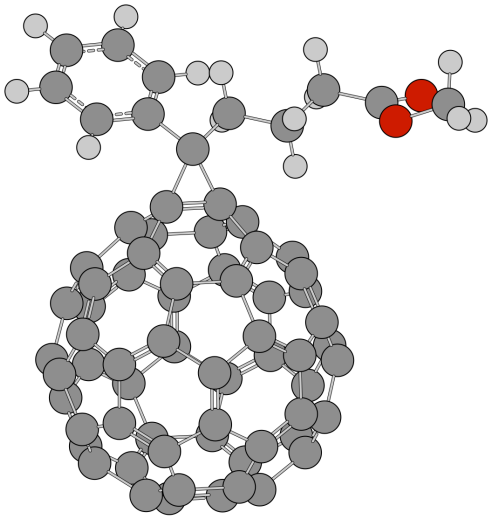

Figure 1.7: Sketch of the electron acceptor PCBM.

of most of the incident photons. It is crucial to choose organic materials with absorption energies matching the solar spectra for efficient energy conversion from the sunlight. With many materials possessing large absorption bands in the visible spectra, organic semiconductors are well suited for this purpose [24].

Once the exciton is created, numerous mechanisms exist for the exciton to transfer away from the chromophore where it was first created, as highlighted in Section 1.2. The exciton will therefore diffuse until de-excitation or until it reaches an interface between the electron donor and the electron acceptor, where the charges will separate with an efficiency of almost 100% [93] (if the donor and acceptors are well designed). Therefore, the longer the exciton diffusion length, the more likely the exciton will successfully be separated into free carriers. However, in organic materials, the exciton diffusion length is typically around 10 nm [97], much shorter than the thickness of the film.

The last step, after charge separation, is charge transport to the electrodes. This process can lead to exciton formation and therefore loss of overall efficiency. In

organic materials, due to the low charge mobilities (from 10^{-5} to 10^{-2} $cm^2 \cdot V^{-1} \cdot s^{-1}$ [86]), the charge collection length is also less than 100 nm, making it difficult for this process to occur in a typical solar cell.

Common device architectures are presented in figure 1.8. The morphology of the films plays an important role. For instance, increased overall efficiency (due to better energy transport) is achieved in cells where the acceptor and donor chromophores are mixed together (mixed phase cell), in an optimised way, compared to devices where the acceptor and donor materials are layered on top of each other (for instance, a bilayer cell) [98].

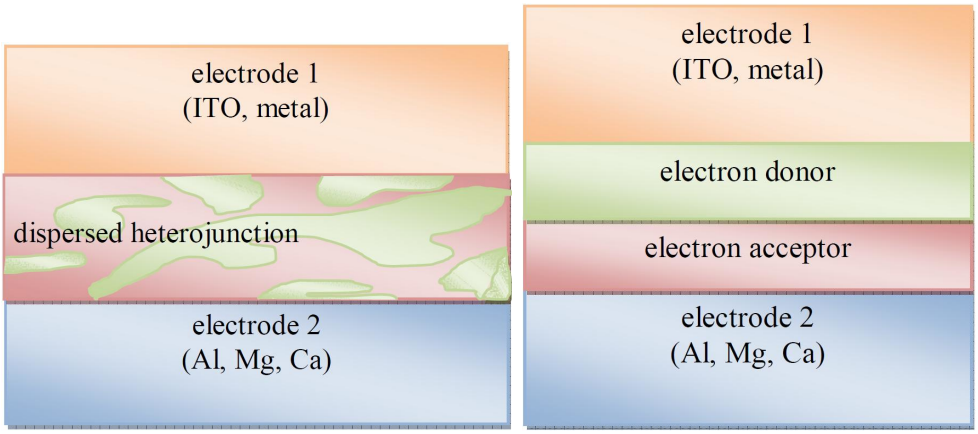

Figure 1.8: Sketch of a mixed phase cell (left) and a bilayer cell (right) (from reference [17]). ITO stands for indium-titanium oxide.

The main advantages of organic solar cells compared to inorganic cells are, as for all organic devices, the possibility of using simple fabrication techniques, such as roll-to-roll printing, in addition to being lightweight and flexible [24] - this facilitates the integration of solar cells in buildings and other common accessories, such as clothes. However, serious issues remain. The two main drawbacks that limit the cells being available on the market are the low carrier mobility and their lifetime [99]. The low carrier mobility (and small exciton diffusion length) makes the design of efficient devices particularly challenging. The stability problems come from the interactions between the molecular material and oxygen and water (vapour, etc.), and also from the chemical reactions with the electrodes. We have shown here that organic photovoltaic cells suffer from a certain number of drawbacks, which need to be solved for their viable commercialisation. If these problems can be overcome, considering their potential major advantages, they should meet commercial success in the future.

1.3.3 Organic light emitting diodes (OLEDs)

The most commercially successful device to date is without question the organic light emitting diode (OLED) [24]. Electrolumiscence was achieved in organic crystals in 1965 [100], but the first thin-film OLED created by vacuum deposited molecular materials dates from 1987 [5], and the first OLED from solution processed polymers was realised in 1990 [101]. After the demonstration of these functioning devices, research has been focused on using OLEDs for displays, and such displays can already be found on the market. In addition, since the beginning of the twenty-first century, numerous researchers have investigated the utilisation of OLEDs for lighting purposes [102–105].

The fundamental principles of OLEDs are in many respects the same as for a photovoltaic cell, except that an OLED operates in "reverse-mode". Indeed the injection of electric energy into an OLED creates an emission of photons. The steps leading to light emission are [106]: application of an external voltage for the injection of free charges through the electrodes of the OLED, transport of these free charges in the device, leading to exciton formation, and finally radiative decay of this exciton.

The injection of the free carriers is realised by two electrodes situated at opposite sides of the device. As for solar cells, at least one of these electrodes needs to be transparent. ITO (indium-titanium oxide) is very commonly used as the anode [107], as it is a high work-function transparent metal. After injection of the holes at the anode, the holes will fill the HOMOs of the chromophores of a conduction layer, the hole-transport layer. This layer needs a high mobility to guarantee efficient transport of the holes away from the anode. TPD, α-NPD, PEDOT:PSS and S-TAD are common materials used for hole transports [106] (see figure 1.9). Similarly, electrons are injected from the cathode (usually made of aluminium, magnesium or silver [107]), before being transported further away by the electron transport layer, where the electrons will fill the LUMOs of the semiconductors of this region. Materials used for electron transport are for instance Alq_3, BCP or BPhen [106] (see figure 1.10). Having these extra electron or hole transport layers could be seen as problematic for the overall efficiency of the device; however, this in fact enables an efficiency improvement if all the layer materials and thickness are well chosen and tuned [106]. After transport of the free charges through the transport layer, the free charges reach the recombination region where they need to "meet" (enter their Coulombic attraction region) in order to form excitons. Due to the multiplicity of three of the triplet states, three quarters of the excitons formed in this way will be triplets states, with only one quarter being singlet excitons [108]. Therefore, the molecular species in the recombination region need to be efficient phosphorescent materials (radiative decay from a triplet state) rather than fluorescent (light emission

from a singlet exciton) to ensure efficient light production [109]. In addition, systems possessing short triplet lifetimes (to minimise the probability of non-radiative bi-excitonic quenching processes) and efficient inter-system crossing (conversion of a singlet exciton to a triplet exciton) will lead to the most efficient semiconducting organic materials [107]. Finding molecular species which can match all these criteria and make a consistent ensemble of layered species, in addition to being stable, is a challenging issue. Heavy-metal centred metal organic complexes have been shown to be good candidates [110–112] (examples provided in figure 1.11), with the main issues remaining stability, in addition to the availability of the raw compounds [106].

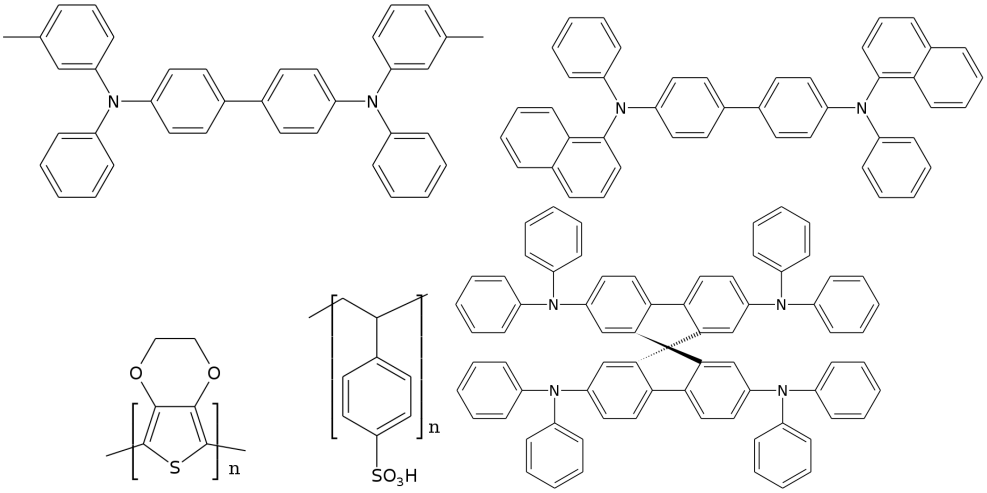

Figure 1.9: Sketch of some common hole transport materials: TPD, α-NPD, PEDOT, PSS and S-TAD, from left to right, top to bottom.

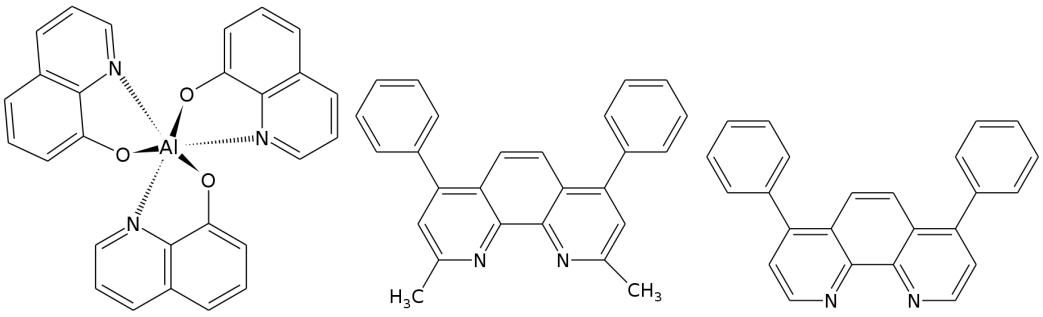

Figure 1.10: Sketch of some common electron transport materials: Alq_3, BCP and BPhen, from left to right.

One of the main advantages of OLEDs compared to LEDs is the possibility of making flexible and efficient devices by using simple fabrication techniques [24]. In addition, as organic semiconducting emitters possess an intrinsically broad luminescence spectrum, by combining several layers of various materials it is possible to create efficient white light OLEDs [102, 113]. These are particularly suitable for lighting applications as a replacement for the less efficient incandescent and flu-

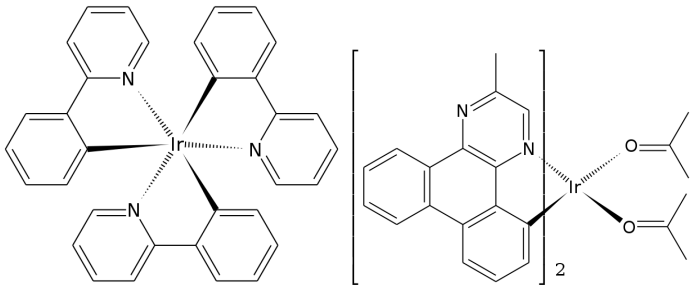

Figure 1.11: Sketch of a green phosphorescent emitter, $Ir(ppy)_3$ and of a red phosphorescent emitter, $Ir(MDQ)_2(acac)$, from left to right.

orescent light bulbs as general lighting sources. Another advantage is that when small organic molecules are used as the emitting molecules, the light source can be quite focused ("point-like") [106], whereas when polymers are used as emitters, the light source is delocalised over a large surface area, creating large, uniform light sources [106] which can have many more applications than usual light bulbs. Such complex "white OLED" devices need also to be carefully designed: for instance, energy transfer needs to be accounted for carefully, to ensure that the excitons dissociate in the right regions of the device and can lead to the emission of photons of various energies from all the emitter layers.

We have shown that OLEDs possess numerous advantages over conventional LEDs, which explain their current commercial success in display applications. Applications for these devices as light sources are also undergoing tremendous research, driven by the promise of significantly improved light sources compared to the current, commercially available light bulbs. However, the most critical remaining challenge is the stability of these devices and their materials, with degradation resulting from a variety of processes, from chemical transformations in the recombination region to effects originating from energy transfer [114].

In the previous Sections we have given an overview of the current knowledge of ultra-fast processes in organic semiconductors, and of the state-of-the-art organic devices, with the challenges still associated with their commercialisation. We have shown that these challenges are linked with the fundamental ultra-fast intrinsic physics of these materials. In the next Section, we will further expand on the current research challenges in the field, to guide our research work for the rest of this thesis.

1.4 Current challenges

We have demonstrated in this introduction the importance of organic electronics for the realisation of a new generation of promising electronic devices. Nevertheless, most of these devices are not commercially available yet, with the exception

of OLEDs which are available in only one area of their two possible uses. From the introduction, it is clear that the current research challenges are numerous and particularly arduous for the route to mass-produced, commercially available devices. These challenges cover a wide area of science, with physics, chemistry and engineering being the fundamental disciplines that enable the understanding and improvement of these materials. For instance, it is crucial to develop new materials with improved intrinsic properties, such as an increased charge mobility or charge-transfer character [115], in addition to being easy to synthesise and to process, with widely available, cheap compounds [115]. These materials and device structures also need to be stable under repeated electrical- or photo-excitations, and to not chemically react with other species (such as oxygen or water) in a time-span which should ensure a good device life-time [115]. Control of the fabrication processes also needs to be improved [115] to avoid batch to batch variations, and to realise more efficient device morphologies. Indeed, fundamental questions about morphologies still remain (what is a typical polymer morphology in films, and how does this affect its semiconducting properties?). The way electron donor and acceptor polymers are blended in solar cells is still not clear [116], for instance. Similarly, the role of interfaces in the efficiency of a device is very complex and far from being elucidated.

More generally, very fundamental physics issues remain. One major issue is the role of energy transfer in organic systems, and the difficulties in modelling such processes - as highlighted in Section 1.2.3, these mechanisms are complex and involve many parameters and approximations - for instance identifying the appropriate transfer regime. Analytical models are still emerging and are far from being able to simulate the physics of a real system [117], especially as in-depth observation of energy transfer is not often directly accessible experimentally. However, the availability of such analytical models, and, for instance, the understanding of the role of coherent versus incoherent regimes in energy transfer, would definitely help to improve devices. In addition, coherent effects are still not well understood, and extensive research remains to be undertaken to understand the early stage of exciton creation, such as to what extent the coherent exciton is delocalised and where and how the exciton localises when decoherence appears [31]. More generally, many ultra-fast physical processes (exciton creation, charge separation, molecular relaxation and energy transfer, among others) take place in typically sub-picosecond time-scales [118–122], making experimental probes of such processes particularly challenging, and consequently, theoretical formulations are not easily verifiable by experiments.

Excited-state processes are also very difficult to model and therefore theoretical knowledge of such processes is very limited [123]. However, they play an important role in the physics of the device, through phenomena like, among others, excited-

state absorption, damages by ionisation or exciton-exciton annihilation.

1.5 Aim of the thesis

We have shown the importance of organic semiconducting materials for the realisation of a new generation of devices which are extremely promising as a replacement for conventional, inorganic semiconductor devices. We have seen that the challenges facing the fabrication of commercially-ready organic devices are still numerous, and require the collaboration of many disciplines, such as process engineering for improving the actual fabrication steps of the devices, to fundamental physics to understand the mechanisms responsible for the intrinsic properties of the materials.

In this thesis, to address some of these challenges, we will focus on the fundamental physical aspects, and study the theory of exciton transfer in a single, star-shaped molecule (Chapters 3 and 4) and in an ensemble of chromophores mimicking a polymer thin-film (Chapters 5 and 6). These star-shaped molecules are a novel class of fluorene-based materials that increase the ease of experimental processing. The polymer is polyfluorene, currently very often used because of its good physical properties, and because it constitutes a good model system (see Chapter 2). We will confront these theoretical studies with experimental results from our collaborators at the university of St Andrews. We aim to model exciton transfer in a realistic way to obtain useful knowledge about the important mechanisms that govern such transfers.

In the next Chapter, we present the theoretical methods that we will use to achieve these goals.

Chapter 2

Methods

In this Chapter, we introduce the methods that are used in the rest of the research presented in this thesis. Indeed, in order to successfully model and understand the theory of ultra-fast photo-physics in organic semiconductors, reliable methods and a study of preliminary basic concepts are necessary to underpin any deep theory work.

2.1 Introduction

In the field of organic semiconductor theory, there are some well-established theoretical methods which describe the quantum effects regulating the properties of small molecular systems, or the structure-related properties of larger systems. They are usually referred to as "Quantum Chemistry" (QC) [124], and will be presented in Sections 2.2 and 2.3. In this thesis, if not indicated otherwise, "system" designates an isolated ensemble of atoms, for instance one molecule (typically, a "small system") or an ensemble of thousands of interacting molecules (a "large system").

However, the description of the photophysics of a large system is a much more complex problem, and an important current research topic [125]. Two main approaches prevail in modelling the photo-physics of organic semiconductors: a method based on the Monte-Carlo simulation of charges or quasi-particles (such as excitons) moving around in the system [126–134]; and a method based on a master-equation type approach, which enables the calculation of the evolution of exciton densities at the microscopic level [125, 135–138]. The approach used in this work being much closer to this latter method, the Monte-Carlo method will not be developed in this Section. A simple master-equation type approach, the "Optical Bloch Equations" (OBE), is presented in Section 2.4 to introduce some generic approximations and results that will be used in the rest of this thesis.

We are interested in the photo-physics of molecular systems. Therefore we aim to calculate molecular transition properties, such as energy, dipole and density, and time-dependent excitonic properties, such as polarisation or the exciton densities of large ensembles of molecules. The former quantities will be obtained by the electronic structure methods presented in Section 2.3 and the later time-dependent properties will be calculated by the OBE, as presented in Section 2.4.

2.2 Quantum chemistry

2.2.1 Large-scale atomistic systems methods

These methods, for the investigation of a large atomistic system (thousands of atoms), usually enable either access to information on the structural properties or predict the time-dependent photo-physics of an ensemble of chromophores. The methods used to obtain the structural details are generally referenced under the name "Molecular Dynamics" (MD) or sometimes "Molecular Mechanics" (MM). They are mostly based on classical physics: they use a force-field to obtain the electronic energy as a function of the position of the nuclear coordinates, and use Newton's Law to describe the nuclear motions [124, 139]. These methods therefore enable time-dependent simulations of the interactions between a large number of atomistic and molecular components at low computational cost. They enable, for instance, the calculation of geometries, relative energies (such as torsional or bending energies) and energy barriers for interconversion between different conformations. They have been applied successfully in biology and biophysics to study large-scale processes, such as protein folding or interactions [140, 141], but their application to organic semiconductors is more recent [142] and their reliability is therefore not as well-established. Indeed, the correct force field for such components is usually not known. For this reason, these methods have not been used at any stage of the research work presented here and so will not be described in more detail in this thesis.

2.2.2 Small-scale atomistic systems methods

The methods dealing with a small-scale atomistic system are usually described under the generic term "electronic structure methods" [124, 143]. This term covers common methods such as the Hartree-Fock approximation or Density-Functional Theory (DFT), and are typically used for calculating the electronic and vibrational properties of a single molecule. We have been using these methods extensively in our research to predict the electronic properties of a number of polyfluorene-based molecules. For this reason, in Section 2.3, we will review, in detail, the basics of electronic structure methods calculations, and how they have been used to produce some of the results presented later in this thesis.

2.3 QC: Electronic structure methods

2.3.1 Background

Electronic structure methods encompass a very wide range of methods, approximations and techniques, with the aim of predicting, as accurately and efficiently as possible, the quantum-related properties of any molecule (including geometric or electronic properties [124]). The goal is simply to calculate the solution of the M-particle Schrödinger equation $\hat{H}\phi_i(\boldsymbol{r_1}, \boldsymbol{r_2}, \ldots, \boldsymbol{r_M}) = \varepsilon_i\phi_i(\boldsymbol{r_1}, \boldsymbol{r_2}, \ldots, \boldsymbol{r_M}, t)$, where $\hat{H}$ is the Hamiltonian of the system, ϕ_i the M-body wavefunction of the i-th excited-state and ε_i its energy, from which it is possible to derive all other system properties. The Hamiltonian is the sum of the kinetic and potential energy terms: $\hat{H} = \hat{T} + \hat{V}$, the potential energy $\hat{V}$ being the Coulomb interaction between each pair of charged entities, and the kinetic energy $\hat{T}$ being the sum of the individual kinetic energies of each particle in the molecule.

Unfortunately, for molecules it is impossible to solve this Schrödinger equation exactly. The electronic structure methods aim at making this solution tractable with modern computers, at the price of some approximations. These electronic structure methods are divided into three categories [143]: semi-empirical methods, ab-initio methods and Density Functional Theory (DFT).

Two approximations are common to any electronic structure method [144]: the adiabatic approximation and the Born-Oppenheimer approximation. In the adiabatic approximation [145], the coupling between different electronic states is neglected; systems involving these electronic states coupling are photochemical reactions and beyond the scope of this work. The Born-Oppenheimer approximation goes further than the adiabatic approximation, by stating that, as the nuclei are much heavier than the electrons (by at least a factor of a few thousand), the movements of the nuclei can be neglected compared to the movement of the electrons [146]. The kinetic energy of the nuclei is thus assumed to be zero and the electronic motion is described as occurring in a field of fixed nuclei. This means that the total Hamiltonian for the M-particle system can be rewritten as $\hat{H} = \hat{H}_{elec}$, $\hat{H}_{elec}$ depending only on the N electrons in the system. It is also important to note that the particles are considered as non-relativistic.

The further principles and differences between the three methods are presented in the following Subsections, with a particular emphasis on DFT, as this is the method we have been using to obtain our theoretical knowledge of the fluorene-based molecules presented in the rest of this thesis.

Semi-empirical methods

Semi-empirical methods are based on a series of experimental parameters, to simplify the solution of the Schrödinger equation [144], but nonetheless keeping it realistic. Examples of common methods include the Austin Model 1 (AM1) or Modified Neglect of Diatomic Overlap (MNDO). However, these methods are by essence very sensitive to the system they are employed for [144]. Indeed, they are parametrised from experimental data for a system of molecules, and the results they produce can only be trusted if the system studied theoretically is very "close" to the experimental system which parametrised the method - "close" being difficult to quantify. Despite being computationally inexpensive, we decided not to use these methods because of this aforementioned limitation: for instance, the star-shaped truxene-cored molecules we investigated, presented in the next Chapter, have not been extensively studied and they have been relatively recently synthesized [37]; therefore parametrising a semi-empirical method would have been challenging and without any guarantee of success.

Ab-initio methods

Ab-initio methods, on the other hand, do not involve any experimental results in their algorithms, but are based solely on the laws of quantum mechanics and theoretical properties obtained using these laws [144]. The most popular methods in this category are the Configuration Interaction method (CI), the Møller-Plesser perturbation theory (MP) and the Coupled Cluster Methods such as CCSD and CCSD(T). These methods are better than the semi-empirical methods in the sense that, as they do not rely on experimental data, they can be used on any kind of system [124]. However, the computational cost of such methods is much higher than for semi-empirical methods [144], making then less practical for large molecules (more than 10 atoms for CCSD(T), more than a hundred for CI). For this reason, we have not been using any of these ab-initio methods, but instead used the more recent DFT, which offers a good compromise between computational cost and accuracy, and is for this reason already very popular.

Density Functional Theory

Rather than directly calculating the wavefunction from the Schrödinger equation, like the semi-empirical methods and ab-initio methods do, DFT calculates the charge density of the system, from which it is possible to obtain the wavefunctions. Indeed, DFT is based on the theorem demonstrated by Hohenberg and Kohn [147]. This theorem states that the potential of an interacting system is fully determined by its electronic density, and that there is a functional expressing the total energy

as a function of the electronic density, valid for any potential. For a particular potential, the energy minimising the functional is the energy of the ground state, and its associated density is the ground state density.

The main advantage of this theorem is that the many-body problem (N electrons and therefore $3N$ variables) can be simplified into a single-body problem with only three variables, as only the one-particle probability density is necessary to obtain all the information about the ground-state. This single-particle probability density $n(\boldsymbol{r})$ is defined as:

$$n(\boldsymbol{r}) = N \int ... \int |\phi_i(\boldsymbol{r}, \boldsymbol{r_2}, \ldots, \boldsymbol{r_N})|^2 \, d^3r_2 \ldots d^3r_N \ . \tag{2.1}$$

The difficulty is now to obtain the one-particle density of the system. This can be done relatively easily by the Kohn-Sham algorithm [148]. The work realised by Kohn and Sham consists of separating the total electronic energy $\hat{H}_{elec}[n]$ into the kinetic energy $\hat{T}_{elec}$ and the electronic potential energy $\hat{V}[n]$, itself divided into the series of following terms ($[n]$ designates a functional of n):

$$\hat{H}_{elec}[n] = \hat{T}_{elec} + \hat{V}[n] = \hat{T}_{elec} + \hat{V}_{nn} + \hat{V}_{en} + \hat{V}_{ee} + \hat{V}_{XC}[n] \ , \tag{2.2}$$

where $\hat{T}_{elec}$ is the kinetic energy of the electrons, given by:

$$\hat{T}_{elec} = -\sum_i \frac{\hbar^2}{2m} \nabla_i^2 \ , \tag{2.3}$$

$\hat{V}_{nn}$ is the Coulomb interaction between the nuclei. In the frame of the Born-Oppenheimer interaction, this term is constant.
$\hat{V}_{en}$ is the nuclear-electron Coulomb interaction, and of course depends on the electron density $n(\boldsymbol{r})$:

$$\hat{V}_{en} = \frac{e^2}{4\pi\varepsilon_0} \sum_i \int \frac{Z_i n(\boldsymbol{r})}{|\boldsymbol{R_i} - \boldsymbol{r}|} d\boldsymbol{r} \ , \tag{2.4}$$

where Z_i is the charge of nuclei i and $\boldsymbol{R_i}$ its centre. $\hat{V}_{ee}$ is the electron-electron Coulomb interaction, depending on $n(\boldsymbol{r})$:

$$\hat{V}_{ee} = \frac{e^2}{4\pi\varepsilon_0} \sum_i \frac{1}{2} \int \int \frac{n(\boldsymbol{r}) n(\boldsymbol{r'})}{|\boldsymbol{r} - \boldsymbol{r'}|} d\boldsymbol{r} d\boldsymbol{r'} \ . \tag{2.5}$$

$\hat{V}_{XC}[n]$ is the exchange-correlation term, which can be further decomposed into the exchange term $\hat{V}_X[n]$ and the correlation term $\hat{V}_C[n]$ [143]: $\hat{V}_{XC}[n] = \hat{V}_X[n] + \hat{V}_C[n]$. $\hat{V}_X[n]$ is the exchange energy arising from the antisymmetry of the electronic wavefunctions and $\hat{V}_C[n]$ is the dynamic correlation in the motions of the individual

electrons. This term $\hat{V}_{XC}$ is the functional that gave its name to DFT. It is a functional in the sense that it is a function of a function. Indeed, this potential $\hat{V}_{XC}[n]$ is not known exactly and therefore many alternatives exist to calculate it. They will be detailed in Section 2.3.2.

In practice, the steps of the Kohn-Sham algorithm, which enables the calculation of the electronic density and therefore the electronic wavefunctions, are the following [143]:

1) Guess of an initial electron density $n(\boldsymbol{r})$.

2) Calculation of the effective potential $\hat{V}[n] = \hat{V}_{nn} + \hat{V}_{en} + \hat{V}_{ee} + \hat{V}_{XC}[n]$.

3) Solving the Schrödinger equation:

$$\hat{H}_{elec}[n]\left(\boldsymbol{r_1}, \cdot, \boldsymbol{r_N},\right)\phi_i\left(\boldsymbol{r_1}, \ldots, \boldsymbol{r_N},\right) = \epsilon_i \phi_i\left(\boldsymbol{r_1}, \ldots, \boldsymbol{r_N},\right) \ , \tag{2.6}$$

which provides the electronic wavefunctions $\phi_i\left(\boldsymbol{r_1}, \cdot, \boldsymbol{r_N},\right)$ and energies ϵ_i.
4) Calculation of the new electronic density using:

$$n^*\left(\boldsymbol{r}\right) = \sum_i^N \left|\phi_i\left(\boldsymbol{r}\right)\right|^2 \ . \tag{2.7}$$

5) If the new electronic density $n^*\left(\boldsymbol{r}\right)$ is very close to $n\left(\boldsymbol{r}\right)$, then the problem is solved; otherwise we iterate starting from step 2) until convergence is achieved.

This method would therefore be exact (with the exception of approximations such as the Born-Oppenheimer approximation mentioned previously) if we knew how to express the exchange-correlation potential. This is not the case, and this is the main limitation of DFT: knowing how to express this exchange-correlation potential and thus which functional to use. The inclusion of such a corrective term is still a strong point of DFT, compared for instance to methods such as Hartee-Fock, where the correlation is calculated on average, using a mean-field electron density, and the way it is included in the theory means it is much more computationally efficient than ab-initio methods. This explains the popularity of DFT: almost obtaining the accuracy of ab-initio methods, at only the computational cost of semi-empirical methods.

It is worth noting that this method deals with the ground-state only. However, most phenomena relevant for the photo-physics study of molecules are excited-state processes. Fortunately, a method based on DFT was recently developed to

enable such excited-state studies: Time Dependent - Density Functional Theory (TD-DFT). This is the subject of the next Section.

Time Dependent - DFT (TD-DFT)

DFT aims to solve the stationary Schrödinger equation to obtain the ground-state electronic properties of the system; the purpose of TD-DFT is to solve the time-dependent Schrödinger equation [149]:

$$i\hbar\frac{\partial\phi_i}{\partial t} = \hat{H}\phi_i\left(\boldsymbol{r_1},\ldots,\boldsymbol{r_N},t\right) \ , \tag{2.8}$$

to obtain the excited-state electronic properties. The electronic Hamiltonian contains similar terms as previously, except that they are now time-dependent:

$$\hat{H}_{elec}(t)[n] = \hat{T}(t) + \hat{V}(t)[n] + \hat{W}(t) \ , \tag{2.9}$$

with $\hat{W}(t) = \sum_{i=1}^{N} w(\boldsymbol{r_i},t)$ being an external potential. w is often written as [150]:

$$w(\boldsymbol{r},t) = \theta(t-t_0)w_1(\boldsymbol{r},t) \ , \tag{2.10}$$

where w_1 is the initial external potential at t_0 and $\theta(t-t_0)$ is a Heaviside function ($\theta(t-t_0)$=1 if $t > t_0$, $\theta = 0$ otherwise), so that the time-dependent potential is switched-on at $t = t_0$.

Additionally, the continuity equation regulates the electronic density $n(\boldsymbol{r},t)$ [151]:

$$\hbar\frac{\partial n}{\partial t}(\boldsymbol{r},t) = -\nabla\boldsymbol{j}(\boldsymbol{r},t) \ , \tag{2.11}$$

with the current $\boldsymbol{j}$ being defined as

$$\boldsymbol{j}(\boldsymbol{r},t) = 1/2i\sum_{i}^{N}\left[\phi_i\left(\boldsymbol{r},t\right)^*\nabla_i\phi_i\left(\boldsymbol{r},t\right) - \phi_i\left(\boldsymbol{r},t\right)\nabla_i\phi_i\left(\boldsymbol{r},t\right)^*\right] \ . \tag{2.12}$$

The time-dependent equivalent to the Hohenberg-Kohn theorem is the Runge-Gross theorem. This theorem states that two electronic systems in the same initial state, but undergoing different time-dependent external potentials, will result in the systems in two different states [152]. Therefore, similarly to the Hohenberg-Kohn theorem, we can write the time-dependent potential $v(t)$ of the system as a functional of the density and the initial state ϕ_0:

$$v(\boldsymbol{r},t) = v[n,\phi_0](\boldsymbol{r},t) \ . \tag{2.13}$$

We can observe that in the case where the initial state is the ground state, as

the Hohenberg-Kohn theorem asserts that the ground-state wavefunctions are a functional of the density only, then the time-dependent potential is a function of the density only as well. The time-dependent Kohn-Sham algorithm is almost the same as for DFT [150], now using time-dependent densities and potentials, and solving $i\hbar\frac{\partial\phi_i}{\partial t} = \hat{H}_{elec}(t)[n]\phi_i\left(\boldsymbol{r_1}, \cdot, \boldsymbol{r_N}, t\right)$ instead of $\hat{H}_{elec}[n]\left(\boldsymbol{r_1}, \cdot, \boldsymbol{r_N},\right)\phi_i\left(\boldsymbol{r_1}, \cdot, \boldsymbol{r_N},\right) = \epsilon_i\phi_i\left(\boldsymbol{r_1}, \cdot, \boldsymbol{r_N},\right)$. When the algorithm has provided a self-consistent density, the excited-state of the system is determined.

Using the linear-response function of the system it is possible to obtain the excitation energies of the system [150]. The idea of linear response theory is to treat the time-dependent external potential v_1 as a perturbation potential, and using perturbation theory, calculate the first-order resulting change in the ground-state density (for in depth analysis of linear response theory, see for instance reference [149]). Doing this, it is possible to obtain self-consistently the eigenmodes of the oscillations in the system, where the only perturbation is considered to be the density itself, resonating self-consistently at the excitation energies of the system.

2.3.2 DFT: Choice of functional and basis-sets

Functional

As shown in Section 2.3.1, DFT requires the knowledge of a functional for the calculation of the exchange-correlation potential. In this Section, we will give an overview of the general principles of functionals, and then will focus on the functionals used in the rest of this work.

There are two main categories of approximations for the exchange-correlation functional [144]; one based on the Local Density Approximation (LDA), where the system is assumed to be a uniform electron gas, and the other one based on the GGA (Generalized Gradient Approximation) where the gradient of the density is also taken into account.

In the LDA case, the local exchange function has the form [144]:

$$E_X^{LDA} = \frac{e^2}{4\pi\varepsilon_0}\frac{3}{2}\left(\frac{3}{4\pi}\right)^{1/3}\int n(\boldsymbol{r})^{4/3}d\boldsymbol{r}\ , \tag{2.14}$$

whereas a GGA functional, as developed by Becke in 1988 [153], has a corrective gradient term:

$$E_X^{GGA} = E_X^{LDA} - \gamma\frac{e^2}{4\pi\varepsilon_0}\int \frac{n(\boldsymbol{r})^{4/3}N(\boldsymbol{r})^2}{1+6\gamma\sinh^{-1}N(\boldsymbol{r})}d\boldsymbol{r}\ , \tag{2.15}$$

with $N(\boldsymbol{r}) = n(\boldsymbol{r})^{-4/3}\left|\nabla n(\boldsymbol{r})\right|$ and γ being a fitting parameter, obtained thanks to the known exchange energy of noble gases. Similarly, local or gradient-corrected

formulations exist for the electronic correlation potential [154].

Hybrid functionals are a very popular class of functional, based on either local or gradient-corrected approximations. They are called hybrid as their exchange term is calculated as a mixture of DFT and Hartree-Fock theory exchange energies [124]: $E_X^{Hybrid} = c^{HF} E_X^{HF} + c^{DFT} E_X^{DFT}$ where c^{HF} and c^{DFT} are constants defined by the functional. In the theory presented in the rest of this thesis, three functionals have been used, because they are found to be accurate for the materials we investigated: B3LYP, CAM-B3LYP and M06-2X.

Indeed, B3LYP is the functional most commonly used to study semiconducting molecules. It yields very good results compared to experimental measurements on fluorene-based molecules; B3LYP is therefore the functional we used the most. The B3LYP acronym stands for Becke, 3 parameters, Lee, Yang and Parr and designates a hybrid functional which was developed in 1992 [155]. CAM-B3LYP and the M06 series of functionals, and especially the M06-2X functional, are more recent but are growing in popularity. CAM-B3LYP is based on B3LYP, with the correction added by CAM, meaning Coulomb Attenuating Method. It takes into account longer-range Coulombic effects, such as charge transfer, and therefore is believed to increase the accuracy of B3LYP [156]. M06 is a new range of functional designed by Zhao et al. [157]. It claims to be the most efficient amongst all the functionals in many common situations. In particular, the functional M06-2X is said to be the best functional to date for Time Dependant-DFT (TD-DFT) calculations with charge transfer phenomena.

We shall compare the accuracy and range of application of these three functionals on fluorene-based star-shaped molecules in Chapter 3.

Basis Set

In addition to the functional, another parameter of importance has to be chosen to perform a DFT calculation (or any other electronic structure method): the basis set. Indeed, most electronic structure methods involve an assumption regarding the molecular orbitals: they are approximated as a linear combination of one-electron functions. These functions are called basis functions, they are normalised, and are similar to molecular orbitals in the sense that they are centred on the nuclei. It is therefore necessary to decide which kind of functions to use as basis functions and how to apply them. The "basis set" refers to this choice for a given calculation.

As for functionals, lots of basis sets exist, but we can highlight some extensively used ones, the so-called Gaussian basis sets, created in the seventies by John Pople and co-workers [158,159]. They are the basis sets we utilised to produce the quantum chemistry results presented in this thesis. They are obviously based on Gaussian functions. Their nomenclature typically has the form: X-YZ G, where X, Y and

Z are numbers. G indicates that the functions are Gaussians, the number of digits on the left of the hyphen is the number of functions describing the core orbitals, and on the right the number of functions describing the valence orbitals, the actual digits being the number of Gaussians used in the basis set. These basis sets are commonly 3-21G, 6-31G and 6-311G. For instance, the first basis set means there is one function made of three Gaussians to describe the core orbital and two functions made of two and one Gaussians to respectively describe the valence orbitals.

Extra functions have been developed to describe more accurately polarisation and diffusion effects. Extra "polarisation functions" are necessary for accurate chemical bonding calculations, polar molecules and molecules made of heavy atoms [160]. Diffusion effects are important in the case of weakly bound anions [161]. To signify their use, extra polarisation functions are denoted by one or two * symbols after the G, and extra diffusion functions by one or two + symbols before the G [162]. Of course, the more functions the basis set contains, the more accurate it is going to be, but this will obviously incur a greater computational cost and slow down the calculations significantly. Once more, a careful choice of the basis set is therefore required.

As the 6-31G basis set has shown very good results compared to experiments and there is no variation in the results for more extended basis sets for oligofluorene molecules [163], if not otherwise specified, it is the basis we used for all the quantum chemistry results presented in this thesis.

2.3.3 Calculation scheme

Gaussian09

All the quantum chemistry work presented in this thesis has been carried out using a commercial package called Gaussian09 [164], which has been developed since the seventies by John Pople [165], the scientist who introduced the Gaussian basis-sets - hence the name of the program. This software package is used by a large percentage of the molecular quantum chemistry community. It provides a huge number of trusted implementations of ab-initio, semi-empirical and DFT methods, and, since the 2009 version of the software, TD-DFT. This package was therefore a natural choice for us. I used the common bundled graphical user interface, called GaussView [166], which has been used to prepare all the geometries, visualise the electronic properties of the molecules, and produced all the quantum chemistry figures that are displayed in this thesis.

The rest of this Section shows how Gaussian enables the calculation of the electronic properties presented in this thesis and what parameters we used in the program. It will feature some preliminary results showing evidence that Gaussian09

functions perform as well as expected and that we can have confidence in the way we run the Gaussian09 calculations, and therefore the results we obtain.

Calculation steps

To gain relevant knowledge of the photo-physics of the molecules, we performed DFT calculations to determine their ground-state geometries, and then TD-DFT calculations to calculate their excited-state properties: absorption and emission energies and dipoles, and excited-state geometries.

First of all, for the study of a molecule by the means of quantum chemistry, the molecule needs to be "built" numerically. For this we used GaussView. The molecule should be built in a realistic way (as the chemist would expect it to look), but there is no need to know all the geometric parameters exactly. Indeed, quantum chemistry methods aim to calculate the equilibrium geometries of the investigated molecules.

For this purpose, the algorithm used in Gaussian is the following [162]. The location and number of electrons of each atom is specified, and after having chosen an electronic structure method (in our case, DFT), the package calculates the energy of the molecule (in our case, by using the Kohn-Sham algorithm), and then computes the internal atomic forces to estimate a new possible and likely position of the atoms. The energy of this new geometrical configuration is calculated, and comparison with the energy and atomic forces of the previous configuration is made to determine if this new configuration is closer to or further from a local ground-state. This is repeated until some convergence criteria are met. In Gaussian09, there are five convergence criteria: the relative variation of the total energy, the relative variation of the total atomistic displacements, the maximum atomistic displacement, the relative variation of the total atomic forces, and the maximum strength of the atomic forces. The first criteria and three out of the four latter criteria need to be met for Gaussian09 to consider that a local minimum has been reached; the current geometry is then believed to be the ground-state geometry. This minimum is not necessarily the global minimum, and depends on the initial guess made about the molecular geometry, hence the importance of building the molecule as close to the global minimum as possible. Sometimes, it can be worth building various initial geometrical configurations to check which resulting local minimum produced by Gaussian09 is most likely to be the global minimum. Additionally, it is worth noting that in most cases, the convergence criteria used are the Gaussian09 default values, unless a detailed geometrical study is necessary, in which case the convergence criteria are the tightest allowed by Gaussian09. Once we are in possession of a molecular ground-state geometry, a TD-DFT calculation gives the corresponding absorption energies and dipoles. Using TD-DFT once more, now for a geometry optimisation,

it is possible to obtain the excited-state geometry of the molecule, corresponding to the excited-state of interest (it is not necessarily the lowest excited-state, depending on whether it is bright or not). To guarantee meaningful results during the optimisation of the molecule into the excited-state geometry, the initial geometry must be the ground-state geometry. Finally, a TD-DFT calculation for this geometry gives the emission properties.

All these calculation steps are summarised under the form of a sketch in figure 2.1. It is important to conduct all these steps at the same level of theory (functional and basis set) to ensure consistency of the results.

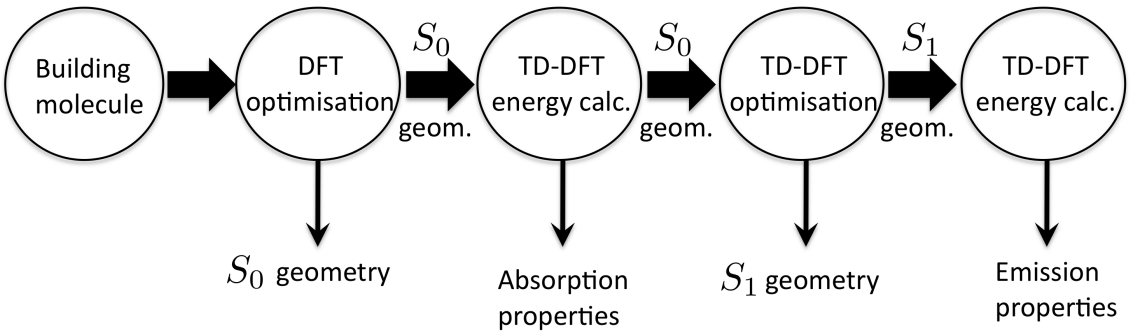

Figure 2.1: Sketch of the series of steps followed to conduct a full calculation of photophysics properties of a molecule.

Later in this thesis, some figures show a "transition density plot". This plot has been obtained by subtracting the electron density of the excited-state from the electron density of the ground-state. The resulting textures are therefore the places where the electrons are moved from or to during photo-absorption or emission.

Unless otherwise specified, no solvent has been used for these calculations, meaning that they are conducted in the gas-phase, at zero temperature. Gaussian09 can perform calculations in solution using the polarisable continuum model (PCM). However, as the solvent used by the experimental team is non-polar, it is believed that gas-phase calculations should accurately reproduce the experimental conditions for molecular solutions. This has been checked with the star-shaped molecules presented in Chapter 3. In addition, in Chapter 4, we have investigated the effects of molecular geometry changes, as would occur in the presence of solvent, and found the effects of such changes to be very small in oligofluorenes.

Most of the time, there are few difficulties arising from these quantum chemistry calculations. However, issues can be present from time to time, and the difficulty the quantum chemist faces is to detect and solve them. These issues can be very varied, from difficulty in finding a reasonable optimised molecular geometry to the non-convergence of the Kohn-Sham algorithm. Experience and the use of the online Gaussian09 user's guide taught us how to detect and solve these issues.

Preliminary Results: Oligofluorenes

Some preliminary results are highlighted in this Section, showing evidence that the choice of functional and basis set is good, in the sense that the results obtained for some well-studied molecules agree with the literature. We performed these preliminary calculations on a series of oligofluorene molecules. Indeed, all the molecules we investigated and presented in this thesis are fluorene-based. This is why it is important to demonstrate that the method we applied for the quantum chemistry calculations of oligofluorenes are judiciously chosen, in order that any new results for fluorene-based molecules can be trusted. Numerous articles presenting electronic properties exist for oligofluorenes already, for instance in references [163, 167–171]. The aim with these preliminary results is not to contribute further to the research on these molecules but instead to ensure that we were able to use Gaussian09 to reproduce these already published results.

We decided to use the B3LYP functional together with the 6-31G basis set to investigate the electronic properties of a series of fluorene oligomers, as results obtained with this choice of functional and basis set have previously shown very good agreement with experiments [163, 168, 169]. We compared the results of our quantum chemistry calculations with the experiments published by N. Montgomery et al. [163]; their experiments were realised on F8 oligomers - this abbreviation means that the monomer units possess side chains made of eight carbon atoms. A fluorene unit (monomer) is sketched in figure 2.2.

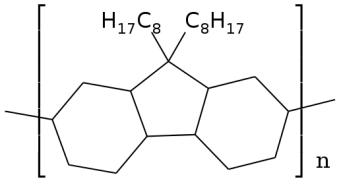

Figure 2.2: Sketch of a F8 fluorene monomer unit.

In all the quantum chemistry calculations involving fluorenes in this thesis, the C_8H_{17} side chains attached to the fluorene arms have been replaced by shorter CH_3 chains. This reduction of the structure is an approximation significantly reducing the computational costs of the calculations, without diminishing the accuracy of the results, as it is commonly understood that side chains are largely uninvolved in the electronic excitations of the molecules [163]. We have explicitly validated this for the benzene-dendrimer B2 (a fluorene-based star-shaped molecule, presented in the next Chapter) for which we have carried out the calculation including the full C_8H_{17} side groups as well. Compared to the calculation with the shorter CH_3 groups, the change in absorption energy and dipole is 0.6% and 2.4%. This comparison clearly demonstrates that side-chains are not contributing to electronic transitions.

If the side-chains are replaced by an hydrogen atom only, the variation is 1.7% in absorption energy and 3.6% for the absorption dipole moment, compared to the full chains. Therefore, CH_3 chains are the best compromise to allow for accurate results and efficient computation.

Following this approximation, the O4 (fluorene quadrimer) we built, for instance, is represented in figure 2.3. Some of the results we obtained, compared to the

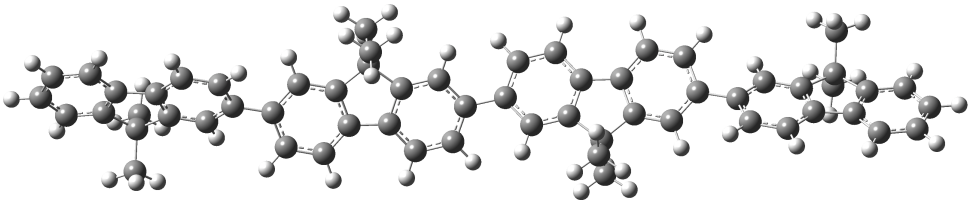

Figure 2.3: Fluorene quadrimer, as used in the quantum chemistry calculations.

theoretical values published by S.Schumacher et al. [163], are displayed in table 2.1.

		Absorption Energy (eV)	Absorption Dipole (eÅ)	Emission Energy (eV)	Emission Dipole (eÅ)
O1	This work	4.70	0.8	4.18	1.07
	Schumacher et al.	4.70	0.7	4.24	1.1
O3	This work	3.47	2.63	2.91	3.08
	Schumacher et al.	3.51	2.7	2.98	3.1
O8	This work	3.13	4.65	2.70	4.74
	Schumacher et al.	2.86	5.0	2.69	4.7

Table 2.1: Comparison of the theoretical results obtained from the literature, by Schumacher et al. [163] and some of our results for a series of α-phase oligomer molecules, calculated using B3LYP 6-31G.

All of our results are extremely similar to the theoretical results in reference [163], even though not identical. The reason for this discrepancy comes from the length of the side chains. Indeed, where we used longer $-CH_3$ groups, only an hydrogen atom has been used by S. Schumacher et al. [163]. We have validated this explanation on the O5 and O3 molecules: we built molecules with only an hydrogen atom per side chain, and the results were identical to the ones of S. Schumacher et al. We have also checked that the geometries of the molecules we computed correspond to the current knowledge about oligofluorenes. The ground-state geometries we obtained are the global energy minima of the molecular structure, with the dihedral angle between two fluorene units being about $+36°$, resulting in a helix-shaped molecule, in agreement with references [163, 168].

Additionally, comparative checks with an extended basis set (6-31G*) were made, and the final values always varied by less than 2%. Similar conclusions were also reached in references [163, 169].

These preliminary results enabled us to gain confidence and expertise in the use of quantum chemistry methods for oligofluorenes. The excellent agreement between theoretical and experimental transition dipoles and energies, as shown in reference [163], is obviously preserved by our results. This demonstrates that DFT and TD-DFT calculations performed at the B3LYP 6-31G level of theory can accurately describe the physics of oligofluorenes, and therefore fluorene-based molecules.

In summary, we have highlighted the principles of DFT, shown some examples of the application of this theory with the B3LYP functional, and shown that some common basis sets obtain good results compared with experiments. This enables the calculation of the transition dipoles and vertical energies, and the visualisation of the molecular orbitals, the transition densities and the geometries.

DFT is useful to obtain the properties of single molecules. These properties can then be utilised for realistic dynamics studies of a few molecules, using the Optical Bloch Equations (OBE).

2.4 Bloch equations

2.4.1 Background

The optical Bloch equations (OBE) are a version of the original Bloch equations, which were first developed by Bloch to describe the magnetic resonant effect of nuclear spin rotation [172]. These were then successfully applied to other physical systems, for instance predicting the dynamics of a two-level system interacting with an optical field [173], for inorganic semiconductors [174] and for molecules [175].

The OBE can be written in many ways. We will start by expressing the OBE as an explicit system of coupled differential equations, to better explore what these equations govern and imply. Following this we will use the more compact and practical, but less physically direct, density matrix approach to express the same equations. The OBE govern the excitation population n_i^X of the fermionic level i of a multi-level system X. Typically, the systems we are interested in are chromophores. The fermionic levels i and j of the same chromophore X are coupled through the polarization term p_{ij}^X. Two chromophores X and Y can also be coupled through the OBE.

In the next Section, we will present how the OBE can be used in practice to model the photo-physics of organic semiconductors. We will start by presenting the equation for a simple single two-level system, before introducing a more realistic six-level system to model an oligofluorene molecule in the next Subsection. Finally,

we will present results for systems of these coupled chromophores.

2.4.2 Application for the photo-physics of organic semiconductors

The OBE have been successfully applied to organic systems, for instance for the modelling of non-interacting oligofluorenes [125] or for the modelling of interacting light harvesting complexes, such as LHC II [176]. The main advantages of the OBE is that they include coherences (defined as the off-diagonal term of the density matrix, such as polarisation), and can therefore model coherent effects. They enable one to gain exact knowledge of the exciton population in a system including virtually any kind of interaction effects (such as exciton diffusion and exciton-exciton annihilation), and vibrational levels and their relaxation - providing we know all the necessary parameters (coupling energies, relaxation times, etc.).

The work by Richter et al. [176] consists of modelling the LHC II chromophores by two-level systems, and then simulating the interactions between fourteen of these two-level systems. It can predict the ultra-fast photo-physics of such a system, even at high intensities where Pauli blocking and exciton-exciton annihilation play a major role in the photo-dynamics. However, real systems of organic semiconductors cannot be described by such a small number of chromophores. Indeed, organic films are large-scale systems of interacting chromophores and require, at the very least, thousands of model chromophores in order to be modelled accurately.

In addition, Schumacher et al. [125] have shown that a two-level model does not accurately describe an oligofluorene chromophore, as a two-level model does not account for vibrations. Instead, they used six-level systems, but did not couple them together, as this would be too computationally expensive.

In the next Section, we will show how to apply the OBE to model organic electronic systems, introduce results showing the fundamental processes that are important in such systems, and demonstrate how to implement them accurately in the OBE. We will also show that an exact formulation of the OBE cannot be utilised to model large-scale system. However, the OBE still enable one to understand the theoretical concepts that are needed to establish a simplified yet accurate model. This simplified model, derived from the OBE, will be the subject of Chapter 6.

2.4.3 Preliminary results

A single two-level system

The Hamiltonian $\hat{H}$ of a two-level system with energies ε_0 and ε_1, $\varepsilon_1 > \varepsilon_0$, with optical pumping, is, using the usual second quantisation operators:

$$\hat{H} = \varepsilon_0 c_0^\dagger c_0 + \varepsilon_1 c_1^\dagger c_1 + \left(c_1^\dagger c_0 d_{01} E(t) + c_0^\dagger c_0 d_{10}^* E^*(t) \right) \ . \tag{2.16}$$

c_x is the fermionic annihilation operator of state x, whereas $c_x^\dagger$ is the fermionic creation operator of state x. $E(t)$ is the excitation field. d_{xy} is the transition dipole for the transition from level x to level y.

This system can be described by two state-variables: the polarisation $p = \left\langle c_1^\dagger c_0 \right\rangle$, and the probability of occupation of the level 1, $n_1 = \left\langle c_1^\dagger c_1 \right\rangle$. Indeed, the knowledge of the occupation density n_0 of level 0 is directly linked to n_1, as $n_0 + n_1 = 1$

The equations of motion are derived using the Heisenberg's equation ($\mathrm{d}A/\mathrm{d}t = i/\hbar\,[H, A]$, where A is an non-explicitly time-dependent observable [173])

$$\frac{\mathrm{d}p}{\mathrm{d}t} = \frac{\mathrm{d}}{\mathrm{d}t}\left\langle c_1^\dagger c_0 \right\rangle = -\frac{i}{\hbar}\left\langle \left[c_1^\dagger, H\right] c_0 + c_1^\dagger \left[c_0, H\right] \right\rangle \ , \tag{2.17}$$

$$\frac{\mathrm{d}n_i}{\mathrm{d}t} = \frac{\mathrm{d}}{\mathrm{d}t}\left\langle c_i^\dagger c_i \right\rangle = -\frac{i}{\hbar}\left\langle \left[c_i^\dagger, H\right] c_i + c_i^\dagger \left[c_i, H\right] \right\rangle \ . \tag{2.18}$$

Expressing the commutators and using $c_i^2 = 0$ and ${c_i^\dagger}^2 = 0$ for fermions, we derived the resulting equations:

$$i\hbar\frac{\mathrm{d}p}{\mathrm{d}t} = -\Delta\varepsilon p - (1 - 2n_1) d_{01} E(t) \ , \tag{2.19}$$

$$\hbar\frac{\mathrm{d}n_1}{\mathrm{d}t} = 2\mathrm{Im}\left[d_{01} p E^*(t)\right] \ , \tag{2.20}$$

where $\Delta\varepsilon = \varepsilon_1 - \varepsilon_0$.

However, in reality, any system will have a polarisation dephasing constant, also called "pure dephasing" [177], $\gamma = \hbar/T_2$, T_2 being the dephasing time, and a radiative decay time [14] T_1. Adding these extra terms empirically, the system can be rewritten as:

$$i\hbar\frac{\mathrm{d}p}{\mathrm{d}t} = (-\Delta\varepsilon - i\gamma) p - (1 - 2n_1) d_{01} E(t) \ , \tag{2.21}$$

$$\hbar\frac{\mathrm{d}n_1}{\mathrm{d}t} = 2\mathrm{Im}\left[d_{01} p E^*(t)\right] - \frac{\hbar}{T_1} n_1 \ . \tag{2.22}$$

The linear susceptibility χ can be easily derived (assuming linear regime, and therefore $(1 - 2n_1) = 1$):

$$\chi(\omega) = \frac{P(\omega)}{E(\omega)} = \frac{d_{01}}{\hbar\omega - \Delta\varepsilon - i\gamma} \ , \tag{2.23}$$

capital letters denoting Fourier coefficients and ω being a photon angular frequency. The susceptibility shows that the polarisation is resonant with the field when the field energy $\hbar\omega$ is equal to $\hbar\omega_0 = \Delta\varepsilon$. For field energies far-off $\hbar\omega_0$, the response of the two-level system is therefore strongly attenuated. Knowing this, and by

rewriting a real sinusoidal field of energy $\hbar\omega$, $E(t) = E_0 \cos(\omega t)$ as:

$$E(t) = \frac{E_0}{2}\left(\mathrm{e}^{i\omega t} + \mathrm{e}^{-i\omega t}\right) = \widetilde{E}(t)\,\mathrm{e}^{i\omega_0 t} \ , \tag{2.24}$$

with

$$\widetilde{E}(t) = \frac{E_0}{2}\left(\mathrm{e}^{i(\omega-\omega_0)t} + \mathrm{e}^{-i(\omega+\omega_0)t}\right) \ , \tag{2.25}$$

we remark that this $\widetilde{E}(t)$ has two characteristic angular frequencies, one at $\omega - \omega_0$ and one at $\omega + \omega_0$. As we are interested in angular frequencies ω near the resonant angular frequency ω_0 of the system only, the response of the system being almost null if ω is far-off ω_0, we can neglect the fast oscillatory term $\mathrm{e}^{-i(\omega+\omega_0)t}$ of $\widetilde{E}(t)$, compared to the much slower $\mathrm{e}^{i(\omega-\omega_0)t}$ term. This approximation is commonly called the Rotating-Wave-Approximation (RWA) [177]. Under the RWA, the real electric field can thus be simply approximated as:

$$\widetilde{E}(t) = \frac{E_0}{2}\mathrm{e}^{i(\omega-\omega_0)t} \ . \tag{2.26}$$

The advantage of this approximation is that for angular frequencies ω near ω_0, this field $\widetilde{E}(t)$ is slowly varying. And if we observe that, as $\widetilde{E}(t) = E(t)\,\mathrm{e}^{i\omega_0 t}$ and $pE^* = \widetilde{p}\widetilde{E}^*$, we can rewrite the system of the OBE as:

$$i\hbar\frac{\mathrm{d}\widetilde{p}}{\mathrm{d}t} = (\hbar\omega_0 - \Delta\varepsilon - i\gamma)\,\widetilde{p} - (1-2n_1)\,d_{01}\widetilde{E}(t) \ , \tag{2.27}$$

$$\hbar\frac{\mathrm{d}n_1}{\mathrm{d}t} = 2\mathrm{Im}\left[d_{01}\widetilde{p}\widetilde{E}^*(t)\right] - \frac{\hbar}{T_1}n_1 \ . \tag{2.28}$$

We have therefore obtained an expression for the OBE that depends only on these slowly varying envelope terms, enabling a significant reduction of the computational cost of numerically solving this system of coupled differential equations.

Taking $\gamma = 0$ and $\hbar/T_1 = 0$ and a monochromatic source of angular frequency ω, it is easy to analytically calculate the population of the highest energy level:

$$n_1 = \frac{\Omega_R^2}{\Omega^2}\sin^2\frac{\Omega t}{2} \ , \tag{2.29}$$

where $\Omega = \sqrt{\Omega_R^2 + (\omega-\omega_0)^2}$, Ω_R being the Rabi frequency [173] defined as $\Omega = d_{01}E/\hbar$. This expression shows that if the monochromatic pump pulse is resonant with the energy difference between the two levels, both levels will oscillate between being totally depleted and totally occupied, at any pump intensity. The pump magnitude regulates the period of these oscillations only. For instance, when $\omega = \omega_0$, we can use the formula $E = \hbar\pi/d_{01}t$ to choose the pump intensity so that we obtain oscillations of 1 ps. The resulting calculated excited state occupations are shown

in figure 2.4. These results have been obtained by numerical solution of the OBE, using a 4-th order Runge-Kutta algorithm [178]. It is the algorithm which has been used for numerical solving of all differential equations in this thesis. Also presented in figure 2.4 are population oscillations resulting from pump excitations at energies slightly off the resonance energy. At an energy of only 99% of the resonance energy, the system barely responds, which validates the RWA. Additional calculations have been carried out with the optical field being written mathematically as a real field, and without using the RWA. Apart from the need to use much smaller time-steps for the numerical resolution of the equations, no differences in the results have been noticed. Therefore, we utilised the RWA in the rest of the work on the Bloch equation.

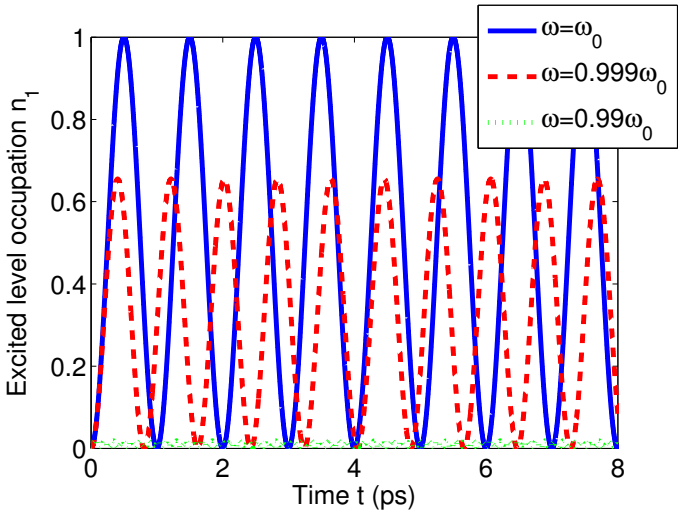

Figure 2.4: Excited-state population n_1 calculated using equation (2.27), without the dissipative terms, for different pump excitation energies.

If we now assign a value to the dissipative terms, either γ or $\hbar/T_1$, the oscillations become damped. We keep $\hbar/T_1 = 0$, as this term is simply an overall time-constant for depopulating the electronic state, but assign different values to the pure-dephasing, as its role is not as obvious as for T_1. We use the polarisation dephasing time literature values of 44 fs [125], but also much higher values, to observe their effect. As we expected, the slower the dephasing time is, the more pumping is achieved at constant pump intensity, as displayed in figure 2.5.

Obviously, pure monochromatic sources do no exist in real life. Instead, ultrafast lasers typically create a Gaussian-like pump, of the form:

$$E(t) = A \exp\left[-\left(\frac{t-t_0}{\alpha \Delta t}\right)^2\right] \cos(\omega t) \ , \tag{2.30}$$

with $\alpha = 1/\sqrt{2\ln 2}$ and Δt the Full Width at Half Maximum (FWHM) of the pump

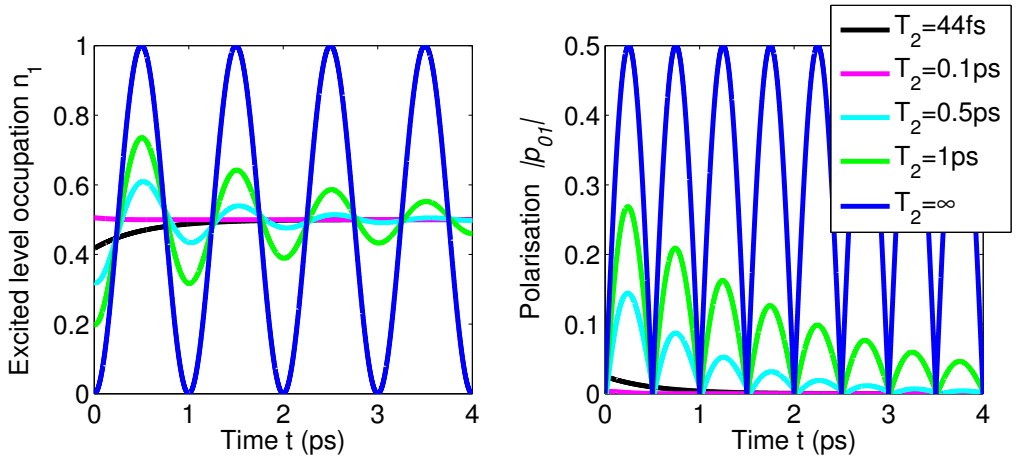

Figure 2.5: Excited-state population n_1 calculated using equation (2.27) with $T_1 = \infty$ and various values for the pure-dephasing γ, for sinusoidal pump excitation at $\omega = \omega_0$, starting at t=0. The system response is therefore a transient response, converging to the steady-state response.

intensity (the square of the pump field).

To solve equation (2.27), the pump field in the frame of the RWA is:

$$\widetilde{E}(t) = \frac{A}{2} \exp\left[-\left(\frac{t-t_0}{\alpha \Delta t}\right)^2\right] \mathrm{e}^{i(\omega-\omega_0)t} \ . \tag{2.31}$$

Results using Gaussian pumps are presented in figure 2.6, for various pump intensities. We notice that at high pump intensities oscillations appear due to the Pauli exclusion principle, before the two levels become equally occupied. At low intensities, no such non-linear phenomena occur.

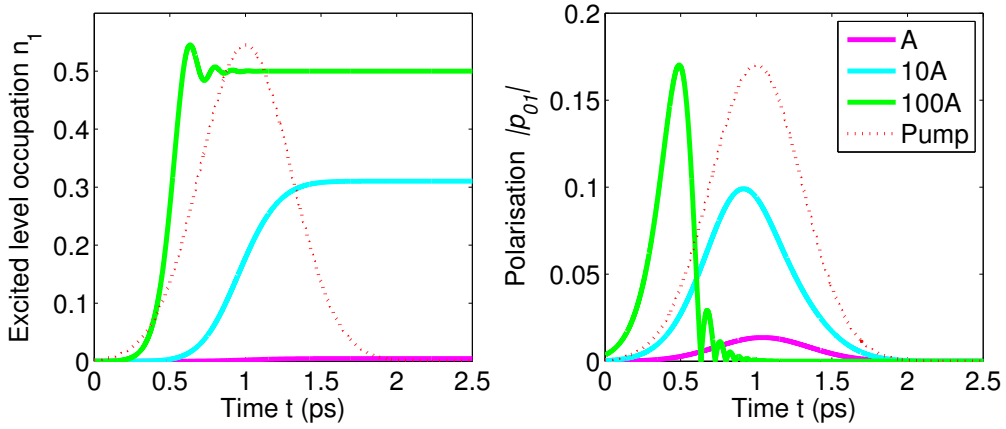

Figure 2.6: Excited-state population n_1 calculated using equation (2.27) with Gaussian pumps of various amplitudes.

Such Gaussian pumps are used in the rest of this thesis to model the ultra-fast laser pulses.

A single six-level system

A two-level system is certainly not a very realistic model of a chromophore. Indeed, a chromophore usually possesses numerous excitable ("bright") electronic levels, in addition to a multitude of associated vibrational levels [14]. Bright electronic excited states are usually separated from the ground electronic states by bandgaps of a few electronvolts (typically 3 eV for polyfluorene) and are similarly far apart from each other, so that we can neglect any other electronic state that is not tuned with the pump excitation. However, vibrational levels are usually energetically close to electronic levels (typically 0.1 eV in polyfluorenes) and therefore can play an important role in the photo-physics of molecules. Schumacher et al. [125] have shown that, from the point of view of the photo-physics, a 6-level model is a very good approximation of an oligofluorene molecule. In this part we will show how the OBE are modified to include six levels instead of only two, and highlight some particular results of interest.

According to Schumacher et al. [125], the four additional levels to include in the model correspond to two vibrational levels for each electronic level. The levels of the same electronic state are dipole forbidden and therefore are not optically coupled, so that the ground state levels are only optically coupled with the excited states. The energy of these six levels is taken from the values published by S. Schumacher [125]. It is assumed that the transition dipoles are the same between any vibrational level of the same electronic state, the corrections to this being given by the Franck-Condon factors (see below).

A sketch of the system is presented in figure 2.7. The same method as for the two-level model is used to derive the OBE for this six-level system. The Rotating Wave Approximation is used as well. As in the previous Subsection, extra empirical terms have been included in the equations. They are the pure dephasing γ_{dephas}, the vibrational relaxation γ_{relax} and the Franck-Condon factors $F_{v,v'}(n)$. γ_{relax} is a term which takes into account the fast-relaxation of excited vibrational states into the lower electronic state; it therefore depletes the vibrational states to the benefit of electronic states, and induces dephasing to the polarisation. The Franck-Condon factors $F_{v,v'}(n)$ give, for each vibrational mode, the overlap between the vibrational state v of S_0 with the vibrational state v' of S_1 [179]:

$$F_{v,v'}(n) = \mathrm{e}^{-\frac{\beta_n^2}{2}} \sqrt{\frac{v!}{v'!}} \beta_n^{v'-v} L_v^{v'-v}\left(\beta_n^2\right) \ , \tag{2.32}$$

with $L_v^{v'-v}\left(\beta_n^2\right)$ the Laguerre polynomial:

$$L_v^{v'-v}\left(\beta_n^2\right) = \sum_{i=\max(0,v-v')}^{v} \frac{(-1)^i v'! \left(\beta_n^2\right)^i}{i!(v-i)!(v'-v+i)!} \ , \tag{2.33}$$

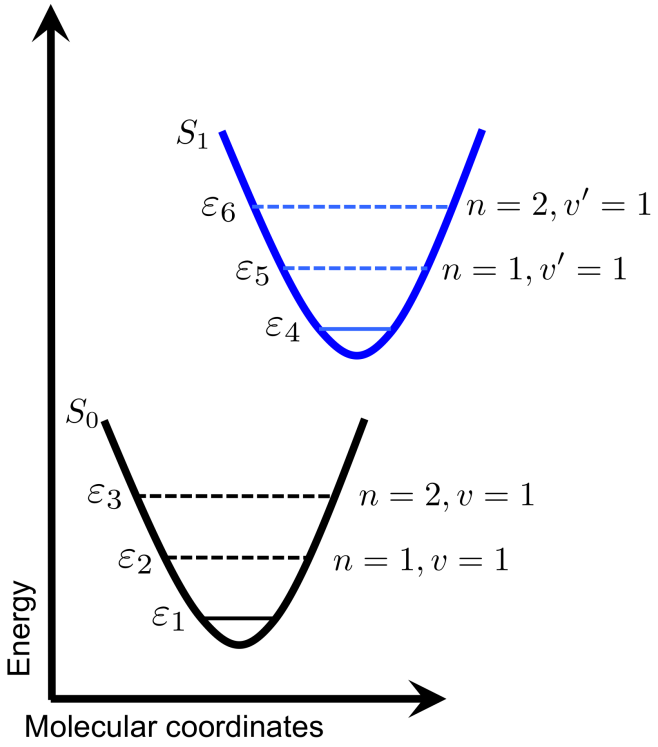

Figure 2.7: Sketch of the model six-level system. The black parabola represents the ground-state, the blue one the excited state. The solid lines are electronic states, the dashed lines vibrational modes (only the first level of two vibrational modes are considered. The values for n, v and v' are used for determining the Franck-Condon factors. Optical transitions are allowed between one level and the three levels of the other state. Vibrational levels relax directly to the lowest level of the state.

and $\beta_n^2 = R_n$ with R_n being the Huang-Rys factors for each oscillator mode n. The Huang-Rys factor is simply the oscillator displacement for the mode n, compared to the electronic state [179]. The model six-level systems include two vibrational modes, each of which has only one vibrational state, so that $n = 1$ or $n = 2$ and $v, v' = 0$ or $v, v' = 1$.

The Huang-Rys factors can be obtained by standard vibration calculations using DFT, and S. Schumacher has published them for the two vibrational modes that we consider in the model [125]: $\beta_1 = 0.45$ and $\beta_2 = 0.42$. The Huang-Rhys factor is a dimensionless relative displacement between two potential energy surfaces, $R_n = (g_e(n) - g_g(n))^2$, with g_e (g_g) being the dimensionless shift of the potential energy surface of the excited-state (ground-state), $g_e(n) = -\sqrt{\frac{\omega_n}{2\hbar}} q_n^e$, ω_n and q_n^e being respectively the angular frequency and wave-function of the n oscillator mode of the excited-state (ground-state) [30].

The vibrational relaxation time is taken to be $\tau_{relax} = 100\,\text{fs}$ and the pure-dephasing time to be $T_2 = 44\,\text{fs}$, following the results published by Schumacher et al [125].

There are six differential equations for the population (one for each level), and

nine equations for the polarisation (three for the interactions between each ground state level and the three excited-state levels). For instance, the equation governing the population of the electronic excited state, f_4, is:

$$\hbar\frac{\mathrm{d}n_4}{\mathrm{d}t} = 2\mathrm{Im}\left[d\left(F_{0,0}(1)F_{0,0}(2)\widetilde{p}_{14} + F_{1,0}(1)F_{0,0}(2)\widetilde{p}_{24} + F_{0,0}(1)F_{1,0}(2)\widetilde{p}_{34}\right)\widetilde{E}^*(t)\right] + \gamma_{relax}\left(n_5 + n_6\right) \ . \quad (2.34)$$

The level referenced as number 4 is the electronic excited-state (see figure 2.7), which is coupled to the electronic ground state (level 1) and to the first and second vibrational ground-state modes (level 2 and 3). The Franck-Condon factors are, for level 1 to 4, $F_{0,0}(1)F_{0,0}(2)$, as no vibrational states are involved. For level 2 to 4, the Franck-Condon factors are $F_{1,0}(1)F_{0,0}(2)$. Indeed, this transition is from the first vibrational ground-state mode to an electronic state, hence the use of $F_{1,0}(1)$. The second vibrational mode is not involved, therefore the second factor is $F_{0,0}(2)$. The last term, $\gamma_{relax}\left(n_5 + n_6\right)$, describes an excitation migration from the excited-vibrational modes to the electronic excited-state through vibrational relaxation.

Similarly, the equation governing the population of the first vibrational mode of the excited state, f_5, is:

$$\hbar\frac{\mathrm{d}n_5}{\mathrm{d}t} = 2\mathrm{Im}\left[d\left(F_{0,1}(1)F_{0,0}(2)\widetilde{p}_{15} + F_{1,1}(1)F_{0,0}(2)\widetilde{p}_{25} + F_{0,1}(1)F_{1,0}(2)\widetilde{p}_{35}\right)\widetilde{E}^*(t)\right] - \gamma_{relax}n_5 \ . \quad (2.35)$$

This equation is similar to the previous equation, with a notable difference in the last term, $-\gamma_{relax}n_5$, as this vibrational mode (level 5) relaxes into the electronic excited-state. The higher vibrational mode (level 6) also relaxes directly into level 4, and not through the lower vibrational mode, level 5.

The equations for the polarisation follow an analogous principle. For instance, the equation for the polarisation between the level of the first excited-state vibrational mode (level 5) and the electronic ground-state level (level 1), is:

$$i\hbar\frac{\mathrm{d}\widetilde{p}_{15}}{\mathrm{d}t} = \left(\varepsilon_5 - \varepsilon_1 + \hbar\omega_0 - i\gamma_{dephas} - i\frac{1}{2}\gamma_{relax}\right)\widetilde{p}_{15} - F_{0,1}(1)F_{0,0}(2)\left(n_1 - n_5\right)d_{01}\widetilde{E}(t) \ . \quad (2.36)$$

We observe that this polarisation is created when the levels 1 and 5 have different occupations, and that the vibrational relaxation affects the polarisation of the system, following the quantum decoherence idea - this polarisation being a purely quantum coherent effect.

Similarly, the equation for the polarisation between the levels representing the

two different states of the first vibrational mode is:

$$i\hbar\frac{\mathrm{d}\widetilde{p}_{25}}{\mathrm{d}t} = \left(\varepsilon_5 - \varepsilon_2 + \hbar\omega_0 - i\gamma_{dephas} - i\gamma_{relax}\right)\widetilde{p}_{25} - F_{1,1}(1)F_{0,0}(2)\left(n_2 - n_5\right)d_{01}\widetilde{E}\left(t\right) \quad . \tag{2.37}$$

Again, it is important to note the difference from the previous equation concerning the factor describing vibrational relaxation.

This model enables prediction of phenomena that the two-level system would not describe well at all, such as optically pumping the system with a pump pulse tuned to the first excited vibrational mode. Comparison between this model and the two-level model is presented in figure 2.8, and clearly shows the superiority of the six level model in this case.

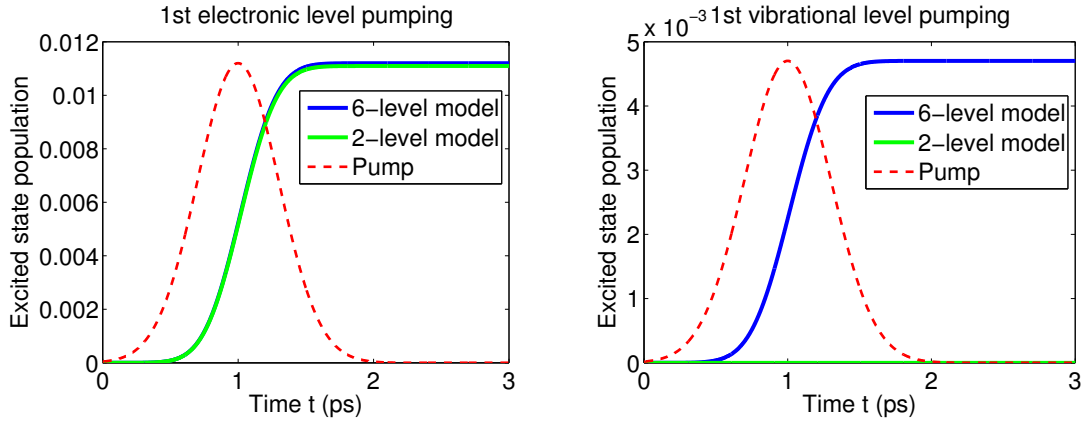

Figure 2.8: Comparison of the excited-state populations obtained by using the 2- and 6- level models, for pump excitation to the electronic excited state (left) and to the 1st vibrational level of the 1st vibrational mode of the excited state (right).

Even though this six-level system is better for describing an oligofluorene molecule than the two-level system, these simulations concern only one molecule. To make them appropriate for describing real systems, we need the molecules to interact with each other by mechanisms such as Coulomb coupling. This is why the model needs to be extended.

Two coupled two-level systems

We began by using a couple of two-levels models to represent two molecules. A sketch of this model is presented in figure 2.9. The model uses a two-level system to describe each of the two molecules, these molecules being able to interact through electronic coupling, so that excitation can transfer from one two-level system to the other [43]. The Bloch Equations account for both coherent and incoherent energy transfer, as they are derived from the full Hamiltonian and the Schrödinger equation.

Instead of writing implicitly the differential equations, from now on we will use the density matrix formalism to keep them more compact and tractable. In practice,

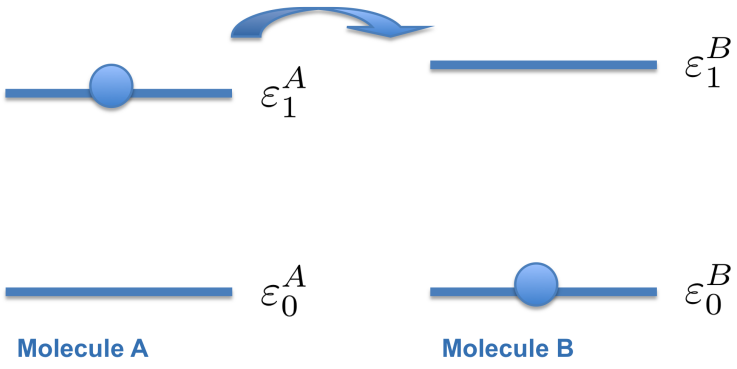

Figure 2.9: Sketch of the two coupled two-level systems. Excitation can hop between the two systems due to electronic coupling.

this means that the OBE are solved by calculating the density matrix ρ at each step, as the time-evolution of density matrix is given by the equation:

$$\frac{\mathrm{d}\rho}{\mathrm{d}t} = -\frac{i}{\hbar}\left[\rho, H_{coupled}\right] \ , \tag{2.38}$$

with $H_{coupled}$ being the Hamiltonian of the coupled system. It can be written in the following form:

$$H_{coupled} = \begin{pmatrix} \varepsilon_0^A + \varepsilon_0^B & d_{01}^A E^A(t) & d_{01}^B E^B(t) & 0 \\ d_{10}^A E^A(t)^* & \varepsilon_1^A + \varepsilon_0^B & V_{AB} & d_{01}^B E^B(t) \\ d_{10}^B E^B(t)^* & V_{AB}^* & \varepsilon_0^A + \varepsilon_1^B & d_{01}^A E^A(t) \\ 0 & d_{10}^B E^B(t)^* & d_{10}^A E^A(t)^* & \varepsilon_1^A + \varepsilon_1^B \end{pmatrix} \ , \tag{2.39}$$

with ε_0^X the electronic ground state energy of molecule X and ε_1^X its electronic excited state energy. $E^X(t)$ is the optical field seen by molecule X, d_{01}^X the transition dipole between its two states, and V_{AB} the interaction energy between both two-level molecules. In the frame of Förster theory, the electronic coupling energy is simply the Coulomb coupling between the two molecules, the short-range coupling coming from the molecular orbitals being ignored [43].

The density matrix $\rho(t)$ for this Hamiltonian $H_{coupled}$ contains all the information about all the polarisation and occupation probabilities. For instance, the polarisation $p^A(t)$ between the states of molecule A will be given by the sum: $p^A(t) = \rho_{12} + \rho_{34}$. ρ_{22} will be the probability of occupation of the excited state of molecule A and of the ground state of molecule B, so the probability of occupation of the excited state of molecule A alone will be given by: $n_1^A = \rho_{22} + \rho_{44}$.

The Rotating Wave Approximation is used and pure dephasing is empirically

implemented, so the time-evolution equation is actually:

$$\frac{\mathrm{d}\rho}{\mathrm{d}t} = -\frac{i}{\hbar}\left([\rho, H_{coupled}] + L\rho\right) \ , \tag{2.40}$$

with the matrix L being:

$$L = \begin{pmatrix} 0 & \hbar\omega_0 - i\gamma_{dephas} & \omega_0 - i\gamma_{dephas} & 0 \\ \omega_0 + i\gamma_{dephas} & 0 & -i2\gamma_{dephas} & \omega_0 - i\gamma_{dephas} \\ \omega_0 + i\gamma_{dephas} & i2\gamma_{dephas} & 0 & \omega_0 - i\gamma_{dephas} \\ 0 & \omega_0 + i\gamma_{dephas} & \omega_0 + i\gamma_{dephas} & 0 \end{pmatrix} \ . \tag{2.41}$$

This simple model enables us to illustrate energy transfer effects. In figure 2.10 we have plotted the time-evolution of the excited population of molecule A and molecule B, with $\Delta\varepsilon^A = \varepsilon_1^A - \varepsilon_0^A = 3\,\mathrm{eV}$ and $\Delta\varepsilon^A = \varepsilon_1^A - \varepsilon_0^A = 3.1\,\mathrm{eV}$. The pump is resonant with A. When the two molecules are not coupled, molecule B is barely excited. We observe that the excitation transfer from molecule A to molecule B becomes faster with increasing electronic coupling. The values of the electronic coupling used are typical of Coulombic interaction between chromophores in films [180]. The effect of the excitation is very significant; energy transfer mechanisms are indeed dominant mechanisms which cannot be ignored for standard chromophore interactions in films.

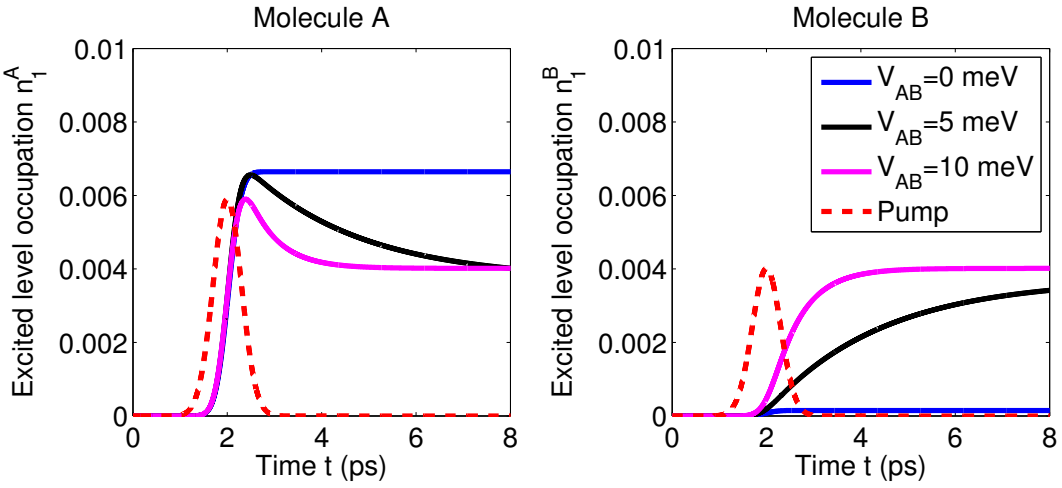

Figure 2.10: Excited-state occupation of molecule A (left) n_1^A and of molecule B (right) n_1^A for different coupling strengths, when molecule A is preferentially excited by the pump.

In addition, this model allows us to observe the effect of electronic coupling on the absorption spectra of the system. The absorption spectra $A(\omega)$ is given by [177]:

$$A(\omega) = \frac{4\pi\omega}{n_r c}\mathrm{Im}\left[P(\omega)/E(\omega)\right] \ , \tag{2.42}$$

with $P(\omega)$ and $E(\omega)$ being the Fourier transform of the polarisation and the pump respectively, c the velocity of light in vacuum and n_r the refractive index of the propagation medium. Using a very short pump pulse, the Fourier transform of this pump is wide enough to accurately calculate the ratio $P(\omega)/E(\omega)$. The results of this calculation for two identical two-level systems coupled through electronic coupling are presented in figure 2.11. As predicted, when the two-level systems are not coupled, the absorption spectra is simply a Lorentzian of width equal to the dephasing rate, centred on the absorption energies $E_{abs} = \varepsilon_1^A - \varepsilon_0^A = \varepsilon_1^B - \varepsilon_0^B$ of the two-level systems. When the systems are coupled, the absorption spectra features two peaks, situated at $E_{abs} - V_{AB}$ and $E_{abs} + V_{AB}$. The Hamiltonian H of two identical oscillators of energy E, coupled by the coupling energy V, can be written as

$$H = \begin{pmatrix} E & V \\ V & E \end{pmatrix} . \tag{2.43}$$

It is easy to calculate that the eigenvalues of this Hamiltonian, and therefore the energy modes of the system, are $E - V$ and $E + V$. However, as shown in figure 2.11, only one of these two transitions is optically active (has a non-zero dipole): either the lowest one if $V_{AB} < 0$ (such coupling corresponds, for instance, to two chromophores aligned on the same line [180]) or the highest one if $V_{AB} > 0$ (such coupling corresponds, for instance, to two parallel chromophores on top of each other [180]). A low energy shift of the absorption corresponds to a J-aggregate whereas the higher energy shift corresponds to an H-aggregate arrangement [181, 182].

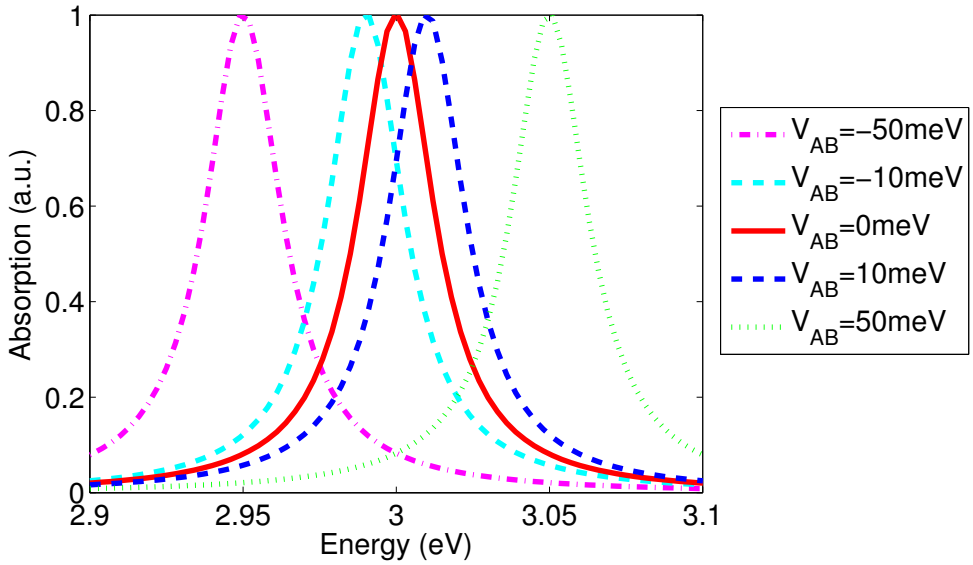

Figure 2.11: Absorption spectra calculated according to the equation (2.42) for two identical two-level systems coupled together through various Coulomb energies.

It is clear that this model predicts realistic results for two-level systems. Nev-

ertheless, to obtain realistic results for the simulation of two coupled oligofluorene chromophores it is necessary to use a much more realistic model: the six-level model instead of the two-model.

Two coupled six-level systems

The model for the two six-level systems coupled to each other is presented in figure 2.12. We used the same methods as previously described: the equations are

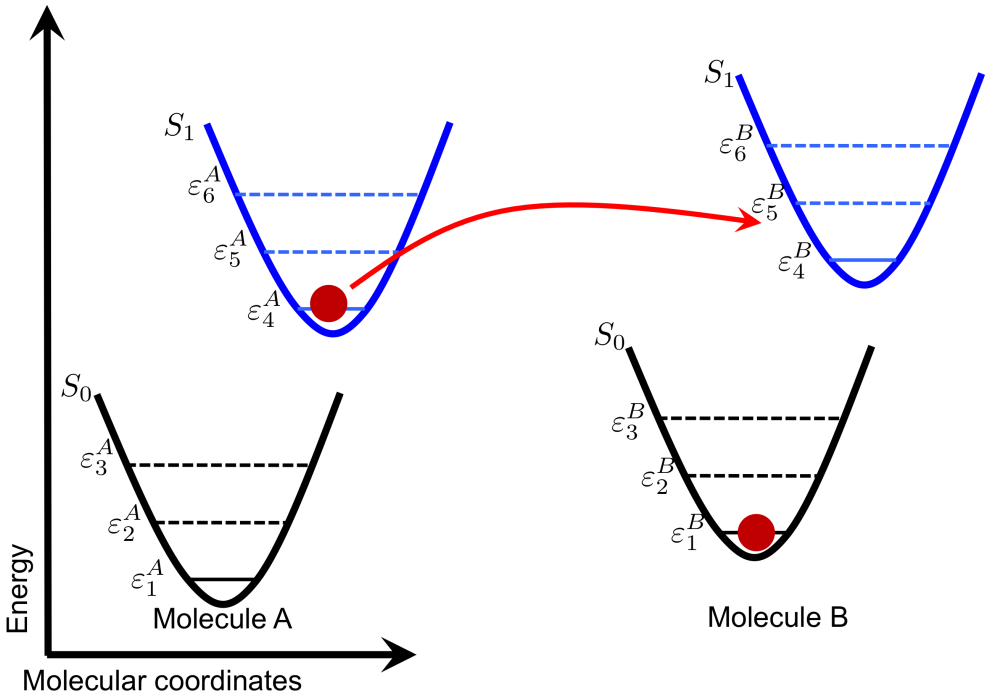

Figure 2.12: Sketch of the model for two coupled six-level molecules. The black parabola represents the ground-state, the blue one the excited state. The solid lines are electronic states, the dashed lines vibrational modes (only the first level of two vibrational modes are considered). Optical transitions are allowed between one level and the three levels of the other state. Vibrational levels relax directly to the electronic level of the state. Excitation can transfer from one level to any other level. Franck-Condon factors are implemented to take into account the different transition probabilities due to the different vibrational overlaps.

derived using the density-matrix theory. Franck-Condon factors, pure dephasing, vibrational relaxation and the RWA are implemented. The Hamiltonian of the system is now a 36×36 matrix; there are 666 free coupled differential equations describing the system. We chose to write the Hamiltonian in this way, to make things tractable: the first six diagonal terms of the Hamiltonian correspond to all the possibilities of the energy levels of B for the first level of A, the six next diagonal term correspond to the six level of B for the second level of A, and so on. These levels are then coupled through the appropriate off-diagonal terms, either optically or through electronic coupling.

Results for a system of two six-level molecules are presented in figure 2.13. Both molecules are identical to the single 6-level model molecule presented earlier, except that the excited-state energy levels of molecule A are shifted by the vibrational energy of the first vibrational mode, so that the electronic excited state level of molecule A (level 4) is resonant with the first vibrational mode of the excited state of molecule B (level 5). Such energy difference between otherwise identical molecules can happen in real systems due to conformational disorder. The pump pulse is resonant with the electronic excited-state of molecule A (and therefore the level 5 of B), and the molecules are coupled by an energy of 10 meV. We observe a quick transfer of excitation from molecule A to molecule B, mediated by vibrational relaxation of molecule B, leading to oscillations during the pumping process. On the other hand, assuming all other parameters being identical, such phenomena do not appear if we do not account for the vibrational levels (2-level systems), as shown in figure 2.13.

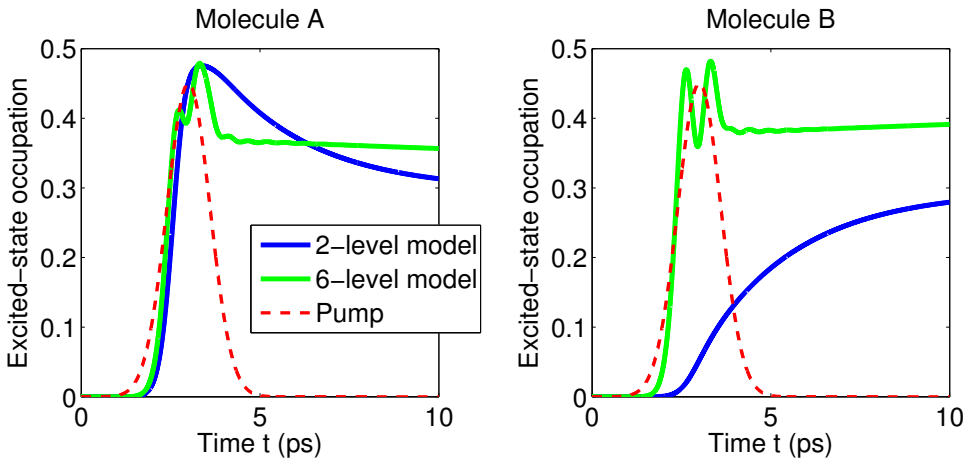

Figure 2.13: Comparison of the excited-state population obtained by using the 2- and 6- level models, for two molecules of different energies - see details in the text.

However, the RWA does not seem to be useful any more. We now clearly need very small time steps to have the same precision as obtained before with larger time steps.

2.4.4 Limitations of this approach

This model has also been extended to three coupled 6-level model molecules. The Hamiltonian is in this case a 216×216 matrix (and so can be expanded by the density matrix theory into 23 436 free coupled differential equations). The execution time of the program has thus been multiplied by approximately a factor of a hundred (which takes two days on a standard computer). Even if the numerical code could be further optimised, it certainly means that without approximation, this model

could not be extended to four molecules. In term of memory, limits would also be reached quickly.

Real systems are typically made of 10^{23} (Avogadro's number) chromophores, and each chromophore interacts with tens of other chromophores. It is therefore impossible to extend the formalism of the Optical Bloch Equations to a real-life system. However, these results constitute the basics of a development of a simplified, but yet accurate model to predict the excitation dynamics of real-life system. It will be presented in the last Chapter of this thesis.

2.5 Conclusion

In this Chapter, we have detailed the methods that we are going to use in the rest of this thesis, in order to gain knowledge about ultra-fast photo-physics of fluorene-based straight and star-shaped molecules. We have chosen to perform quantum chemistry calculation by the means of DFT, at the B3LYP 6-31G level of theory (unless specified otherwise), in order to learn about the single ground- and excited-state properties of the fluorene-based molecules we investigated. Such excited-state properties are useful to describe molecular relaxation, and therefore exciton transfer, in star-shaped molecules. This will be demonstrated in Chapters 3 and 4. Single molecule properties, such as transition energy and dipoles, are also necessary to calculate the inter-molecular interactions playing a major role in the photo-physics of a large molecular ensemble. This will be discussed in Chapter 5 where some molecular interaction models will be investigated and improved, leading to the complex large-scale energy transfer dynamics model presented in Chapter 6. This model will be based on the OBE we have presented here, and will describe the exciton dynamics arising from interactions between numerous multi-level systems. Indeed in this Chapter we have shown the importance of interactions between multi-level systems in accurately describing the ultra-fast photo-physics processes, such as exciton transfer, between oligofluorene molecules.

Chapter 3

Optical properties of fluorene-based C_3-symmetric molecules

In this Chapter, we present a detailed combined experimental and theoretical study of the low energy optical transitions in two families of star-shaped molecules. Both families have three-fold rotational symmetry ("C_3-symmetry") with oligofluorene arms attached to a central core. This study of the fundamental optical and electronic properties of these star-shaped molecules is essential if one wants to understand the mechanisms of exciton transfer in these branched molecules. The results presented in this Chapter are necessary to gain detailed knowledge of intra-molecular exciton transfer in this family of molecules, which will be presented in Chapter 4.

3.1 Background: why are star-shaped molecules important?

As highlighted in Chapter 1, the most widely studied solution-processable, organic semiconducting materials are conjugated polymers. However, we have also seen that several other small molecular geometries can be utilised, including dendrimers [183], spiro-compounds [184] and star-shaped molecules [185]. The influence of the shape of the molecules on their light absorption and emission properties is therefore an important issue if one wants to design new and efficient devices with these less known materials. Star-shaped molecules also make for an excellent model system to study intra-molecular exciton transfer because, contrary to polymers, their geometry is known accurately in solution, and is therefore of particular interest in our studies.

Star-shaped molecules have several advantages over the established polymer materials such as no polydispersity, increased solubility and improved morphology in films. This results in overall easier experimental processing. They have been shown to exhibit many desirable properties such as high solid state photoluminescence quantum yield (PLQY) or high non-linear absorption coefficients [82,186–190]. Nevertheless, despite increasing interest in star-shaped molecules for technological purposes, little has been done to understand how their shape influences their photophysical properties, and previous experimental studies of truxene-cored molecules have been limited to basic spectral properties [191]. Compared to straight polymer chains with no particular symmetry, star-shaped molecules possess a C_3 point-group symmetry, making their photo-physics more complex. The one previous theoreti-

cal study of the truxene-cored molecules, with either no or two fluorene units per arm, focused on Raman spectroscopy and electronic structure in the ground state geometry [192]. We therefore decided to further the research on these star-shaped molecules by considering a wider range of molecular lengths and by investigating excited-state properties as well.

The structures of the two families of star-shaped molecules we studied are shown in figure 3.1. The arms of these star-shaped molecules consist of oligofluorenes func-

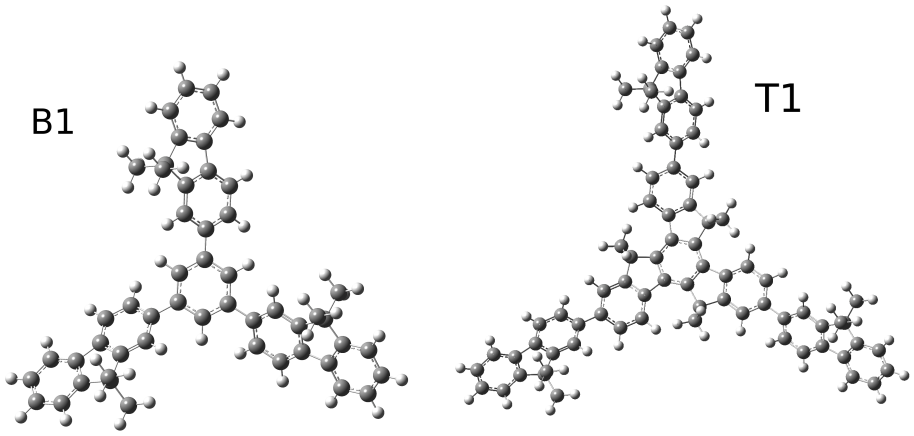

Figure 3.1: Representation of the benzene-cored molecule with one fluorene unit per arm (B1 - left) and truxene-cored molecule with one fluorene unit per arm (T1 - right), shown with reduced methyl side-chains instead of hexyl chains.

tionalised with two hexyl side groups per repeat unit. One star-shaped molecular family consists of truxene-cored molecule with these fluorene arms [191, 193]. These materials have been used in applications such as laser gain materials [82, 194], field effect transistors [195], light emitting devices [196] and for fluorescence probes [197]. The other family of star-shaped materials investigated are benzene-cored molecules [192] with three oligofluorene arms attached at the meta positions of the core. The results are then compared with linear oligofluorenes [163, 168] to show the effect of the star-shape on the properties of the material. The materials are labelled here by the core and number of fluorene units in each arm: the benzene-cored molecules are B1-B4, the truxene centred molecules are T0-T4 and the oligofluorenes O1-O5.

In this Chapter we demonstrate the dependence of transition energies and transition dipole moments in star-shaped truxene- and benzene-cored molecules on the length of their arms (with up to four repeat units in each arm) by combining experiments (steady-state and time-resolved spectroscopy) from co-workers in St Andrews with our time-dependent density functional theory calculations.

3.2 Methods for the optical and electronic studies of star-shaped molecules

3.2.1 Quantum chemistry calculations: methods

We used the methods and procedures described in Section 2.3.3 to perform the quantum chemistry calculations. In particular, the B3LYP exchange-correlation functional together with the 6-31G basis set was used unless noted otherwise.

We are interested in "bright states" only, as opposed to "dark states". We consider that any state with a transition dipole less than around 0.1 eÅis dark. In the calculations, all the fluorene arms are attached to one of the cores and are of helix type [163], that is the dihedral angle between each pair of adjacent fluorene units has the same sign. In the optimized ground state geometries, this dihedral angle is found to be about 35°. In their most symmetric conformations, the optimized ground state geometries of the benzene dendrimers and of the truxenes both show C_3-symmetry. Generally, the C_3 point-group supports singly and two-fold degenerate irreducible representations. Thus, the excited state potential gradient is non-totally symmetric, due to the Jahn-Teller theorem, which states that the ground-state electronic degeneracy of a molecular component is removed by a symmetry breaking to result in a lower energy configuration [198]. Consequently, in the excited state geometry optimization a slight initial symmetry breaking was introduced, such that geometry optimization to the lowest excited state is seeded.

In agreement with previous studies [163, 169] and the results and methodology presented in the Section 2.3.2, the use of a larger basis set does not significantly change the results for the types of molecules investigated here. For instance for B1, we have found that in absorption, using an extra polarisation function in the basis set 6-31G* or an extra diffusion function 6-31+G decreases the lowest transition energies by less than 2% and increases the dipole strength by slightly more than 1%, when compared to the 6-31G basis set.

For some of the molecules studied in this work, the functionals CAM-B3LYP and M06-2X, with the basis set 6-31G, have been used for comparison. In the comparisons, both the geometry optimizations and the transition energies were calculated with these functionals. For T0, T1 and B1 we find that different functionals predict a different ordering of the two lowest excited singlet states. A detailed comparison for T0, T1 and B1 is given in tables 3.1 and 3.2. With both M06-2X and CAM-B3LYP, the first transition in absorption is bright in contrast to the B3LYP result. For all the longer star-shaped molecules and straight oligofluorenes, the lowest absorption transition is bright, whatever the functional is. We can therefore speculate that B1 and T1 also possess a bright lowest absorption transition. If this is the case, CAM-B3LYP and M06-2X would give more physically accurate results than B3LYP on these relatively small molecules. However, results in table 3.3 show that B3LYP

T1 (T0)	B3LYP 6-31G	CAM-B3LYP 6-31G	M06-2X 3-31G
Absorption Energy (eV)	3.62 (4.34)	4.25 (4.89)	4.23 (4.89)
Absorption Dipole (eÅ)	2.37 (1.03)	2.61 (1.15)	2.63 (1.15)
Absorption transition number	2 (3)	1 (1)	1 (1)
Emission Energy (eV)	3.13 (4.16)	3.48 (4.19)	3.5 (4.25)
Emission Dipole (eÅ)	2.69 (1.07)	2.63 (1.08)	2.66 (1.04)
Emission transition number	1 (3)	1 (2)	1 (2)

Table 3.1: Results for T1 and T0 (given in parentheses) with different exchange-correlation functionals, with the 6-31G basis set. All the presented transitions are the first electronic bright transitions.

B1	B3LYP 6-31G	CAM-B3LYP 6-31G	M06-2X 3-31G
Absorption Energy (eV)	4.03	4.58	4.57
Absorption Dipole (eÅ)	1.72	1.97	2.01
Emission Energy (eV)	3.51	3.79	3.83
Emission Dipole (eÅ)	2.05	2.04	2.07

Table 3.2: Results for B1 with different exchange-correlation functionals, with the 6-31G basis set. All the transitions are the first electronic transitions, except for the absorption calculated with B3LYP where it is the second (but lowest bright transition).

gives overall better agreement with experiments than CAM-B3LYP and M06-2X, and this is why we use B3LYP as the functional of reference for these molecules.

For T0, none of the predicted lowest emission transitions are bright. This agrees with the low experimental PLQY value measured for T0 (see experimental results in figure 3.6), and can be explained by the lack of fluorene units in this molecule. This highlights that fluorene arms play a crucial role in the provision of good optical properties.

For all the longer star-shaped molecules and straight oligofluorenes, we find qualitatively similar results for all functionals. We also observe that CAM-B3LYP and M06-2X give very similar quantitative results, showing evidence that these two functionals capture essentially the same physical processes, and that they could therefore be the most accurate functionals for describing these star-shaped molecules. However, the transition energies calculated with B3LYP are significantly lower and give better overall quantitative agreement with the experimental data than with CAM-B3LYP and M06-2X. CAM-B3LYP and M06-2X also give a slightly larger transition dipole in absorption than B3LYP.

We have also checked in the polarisable continuum model (PCM) that inclusion of the solvent (tetrohydrofuran, dielectric constant of 6.97) in the calculations does

not change the overall qualitative and quantitative results.

In the calculations the C_6H_{13} side chains attached to the fluorene arms have been replaced by shorter CH_3 chains, as it is believed the side chains play a very minor role in the electronic properties of fluorene-based molecules [163]. This has explicitly been validated for B2 for which we have carried out the calculation including the full C_6H_{13} side groups (the resulting molecule is displayed in figure 3.2). Compared

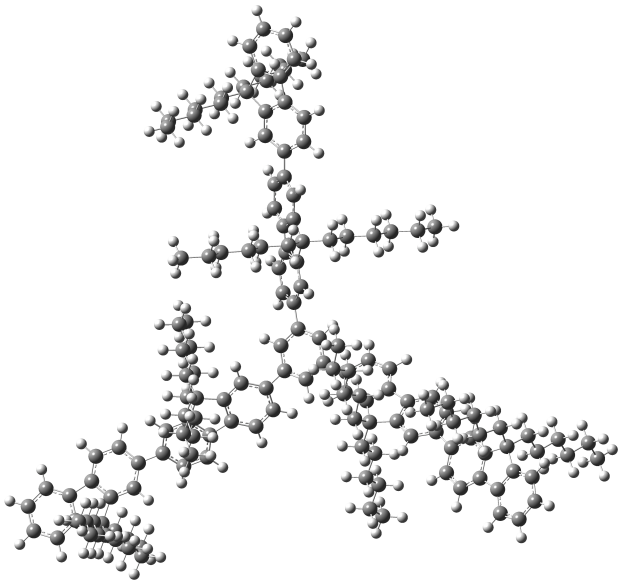

Figure 3.2: B2 molecule with full hexyl side-chains.

to the calculation with the shorter CH_3 groups, the change in absorption energy and dipole is 0.6% and 2.4%, respectively (at the B3LYP, 6-31G level of theory). This comparison clearly demonstrates that the C_6H_{13} side chains are largely uninvolved in the electronic excitations of the molecules. However, their presence guarantees excellent solubility of the star-shaped molecules, and they are therefore of significant experimental importance.

3.2.2 Experimental methods

All the experiments reported in this Chapter have been performed by our collaborators at the university of St Andrews.

All the measurements presented in this Chapter were conducted in solution. The solutions were prepared in either tetrohydrofuran or toluene. Spectroscopic measurements (photoluminescence and absorption) were performed, all at room temperature. The oligofluorene PLQY was reported previously in reference [163]. The fluorescence lifetimes were measured using a streak camera with a 3 ps time resolution and the sample was excited using a 100 fs pulse from a laser at excitation wavelength 375 nm, except for B1 and T0 which were excited at 266 nm.

The vertical transition energies E_{vert} for the molecules in absorption (abs) and emission (em) were estimated from the recorded spectra using the formulae from reference [199]. The absorption and fluorescence transition dipole $|d_f|$ were determined using the absorption coefficient and fluorescence intensities following the methods in references [200, 201]. The degeneracy of the absorption levels and the broken-symmetry of the excited-geometry (see Section 3.4) is carefully accounted for.

For greater experimental details, please see the complete description in our reference [37].

3.3 Comparison between theoretical and experimental results

The photoluminescence and molar absorption spectra, in solution for all three families of molecules, are presented in figure 3.3. The spectra show that for all families there is a red-shift in absorption and emission with increasing arm length, as one expects (a more extended wavefunction results in a decrease of its energy). This is the case for the theoretical results as well, as shown in figure 3.4 and table 3.3.

Table 3.3 summarises all theoretical and experimental results obtained with B3LYP 6-31G for the two families of star-shaped molecules studied and the straight oligofluorenes. This table enables a comparison of the experimental and theoretical transition energies and dipoles.

Figure 3.4 displays the experimental and theoretical transition energies for all three families of materials. Values obtained from experiments and TD-DFT show good agreement and demonstrate the validity of quantum chemistry calculations at the B3LYP 6-31G level of theory. For each family the transition energies in both absorption and emission decrease with increasing arm length. For two to four fluorene units the transition energies of linear oligofluorenes, and both star-shaped molecules, show a much smaller change in both emission and absorption. For a single fluorene unit there is a substantial change in transition energies depending on the molecule. This is due to the cores, where present, being a relatively large fraction of the molecule. The energies in both star-shaped families are red-shifted with respect to the oligofluorenes, with the size of the red-shift dependent upon the size of the core. Truxene-cored molecules have absorption and emission characteristics similar to $n + 1$ number of oligofluorene units when compared to the oligofluorene data. This is because the conjugation extends through an extra fluorene unit which is part of the core. The benzene-cored molecules also show a slight red-shift from the corresponding arm length oligofluorene chains, because of conjugation to the central benzene unit at the core. Due to the smaller size of the benzene core this shift is

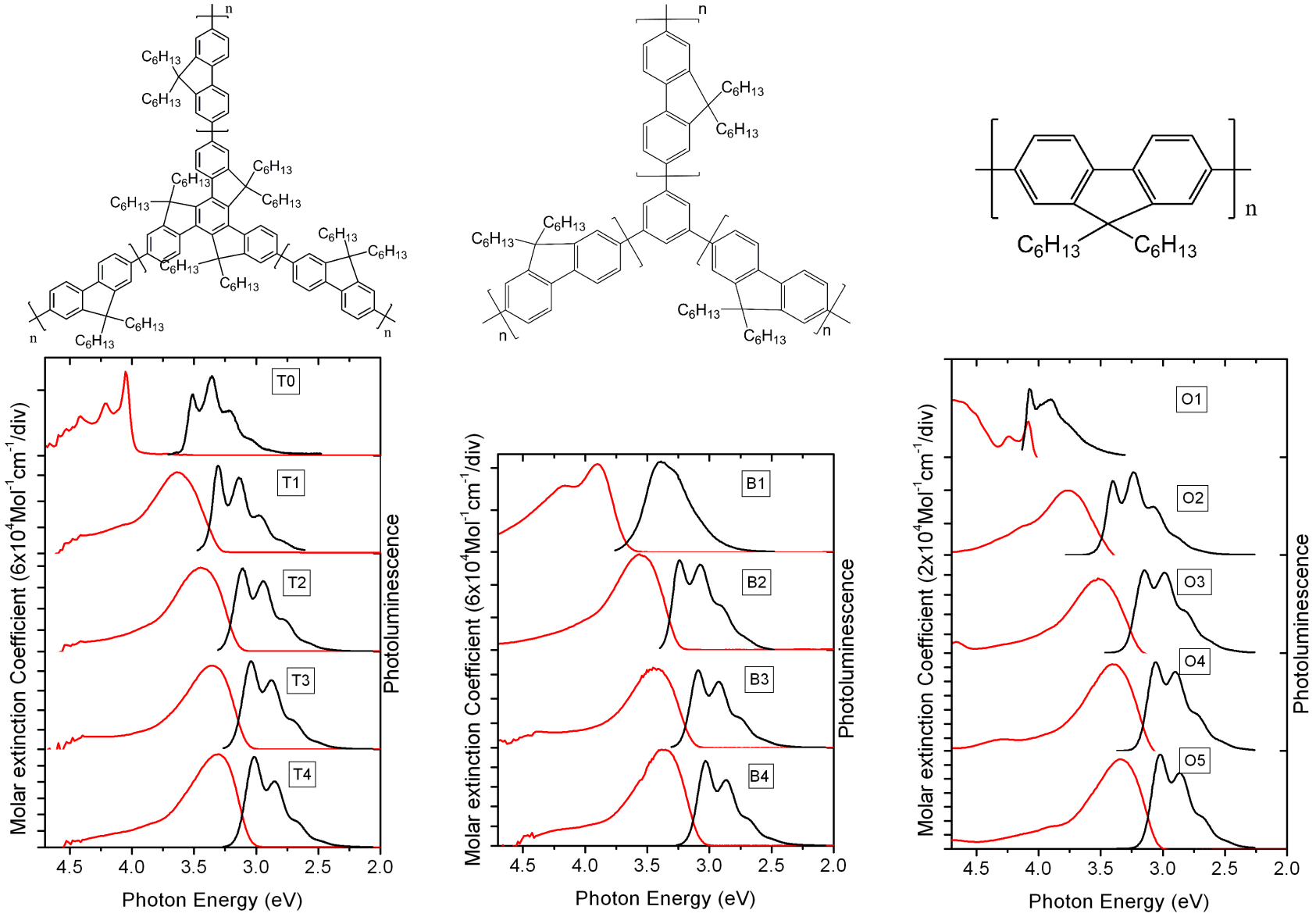

Figure 3.3: Structures and spectra of (a) truxene-cored (b) benzene-cored and (c) oligofluorene molecules. The molar extinction coefficient is given by the red lines and the emission by the black lines. Note the change in vertical scale in (c) (from our reference [37]).

	Vertical transition energy (eV)				Transition dipole (eÅ)					
	Absorption		Emission		Absorption		Emission			
Arm Length	Experiment	Theory	Experiment	Theory	Experiment	Theory	Experiment	Theory	τ_{rad} (ns)	Molar extinction coefficient ($Mol^{-1}cm^{-1}$)
Benzene-cored										
B1	4.16	4.03	3.31	3.51	2.3	1.72	0.3	2.05	42	0.126
B2	3.73	3.53	3.07	3.01	2.7	2.95	2.3	3.14	1.2	0.176
B3	3.54	3.33	2.95	2.82	3.2	3.72	3.3	3.74	0.75	0.197
B4	3.42	3.24	2.90	2.74	3.4	4.29	3.7	4.15	0.64	0.295
Truxene-cored										
T0	4.25	4.34	3.31	4.16	1.2	1.03		1.07	400	0.077
T1	3.66	3.62	3.14	3.13	2.5	2.37	2.0	2.69	1.9	0.186
T2	3.57	3.37	2.97	2.86	2.9	3.4	3.0	3.56	0.74	0.235
T3	3.49	3.25	2.91	2.75	3.2	4.08	3.3	4.05	0.7	0.256
T4	3.38	3.19	2.89	2.71	3.4	4.62	3.6	4.39	0.63	0.341
Straight oligofluorene										
O1	4.64	4.7	3.91	4.18	0.9	0.8	0.2	1.07	23	0.011
O2	3.9	3.81	3.25	3.23	1.9	1.97	2.1	2.33	1.4	0.040
O3	3.65	3.47	3.00	2.91	2.5	2.63	2.7	3.08	1.1	0.080
O4	3.52	3.31	2.95	2.78	3.1	3.13	2.9	3.60	1.0	0.124
O5	3.41	3.24	2.93	2.72	3.2	3.55	3.4	4.00	0.75	0.128

Table 3.3: Theoretical and experimental vertical transition energies E_{vert} and transition dipole moments $|d|$, and experimental radiative lifetimes and molar extinction coefficients, for the series of benzene-cored material B1 to B4, truxene-cored material T0 to T4 and oligofluorene O1 to O5.

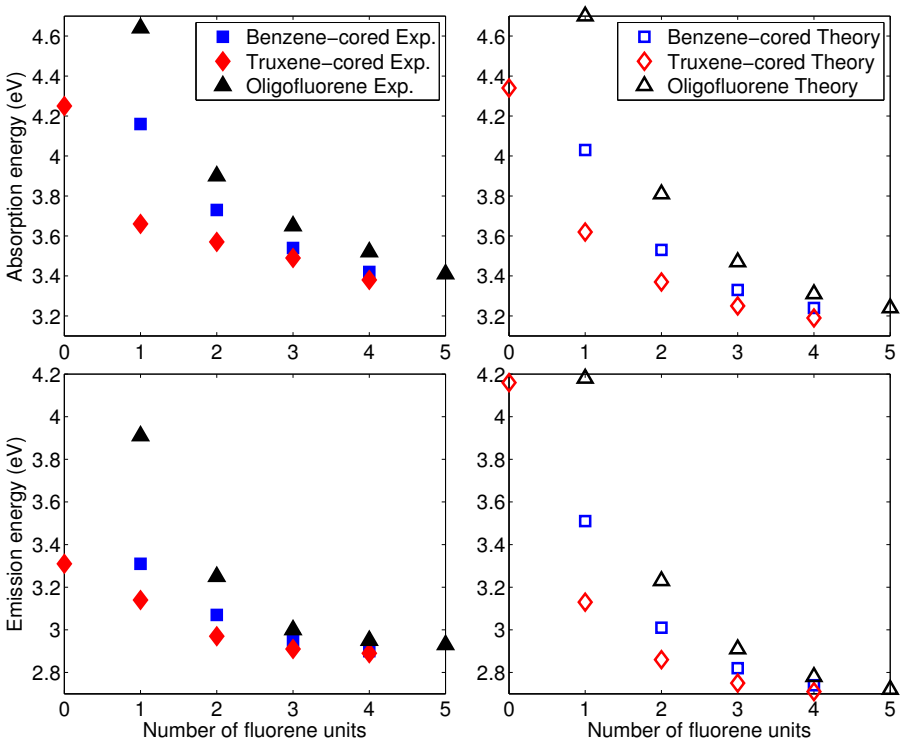

Figure 3.4: Vertical absorption (top row) and emission (bottom row) energies, measured experimentally (left column) or calculated by TD-DFT at the B3LYP 6-31G level of theory (right column).

less pronounced. The red-shift of the truxene molecule from the oligofluorene is also clearly seen in the figure 3.4.

In figure 3.5 we present the transition dipole moments for all the molecules on a semi-logarithmic scale, to display in an obvious fashion any power-law relationship between the transition dipoles and the molecular length. The TD-DFT results shown in figure 3.5 correspond to the energetically lowest optically active transitions. For most of the molecules this is the transition from the ground state into one of the two lowest excited electronic singlet states. For B1 and T1 only we have found that the lowest energy singlet transition in absorption is dark (in agreement with reference [193]) so that the lowest bright transition is the transition from the ground state into the degenerate second and third excited singlet states. For T0 we find both in absorption and emission that the lowest bright transition is from the ground state into the third excited singlet state. Again, good agreement between the theoretical and experimental values is observed.

All the families show an increase in the absorption and fluorescence transition dipole moments with increasing arm length. In both families of star-shaped molecules both experimental and theoretical transition dipole moments are larger than their corresponding straight chain oligofluorene molecules due to the extra conjugation between the oligofluorene arms and the core. The theoretically calculated

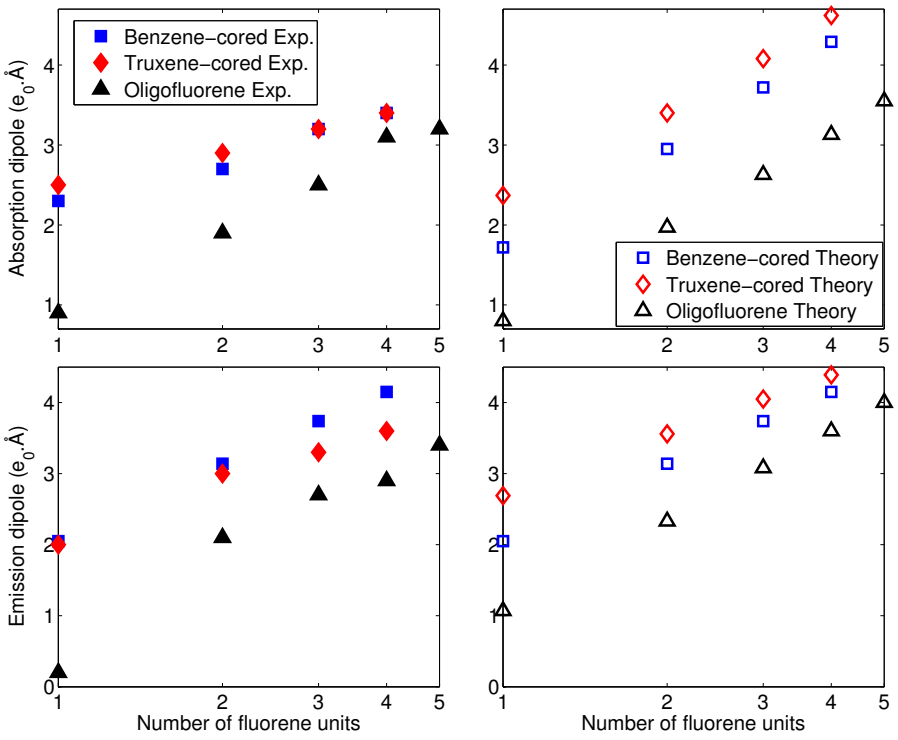

Figure 3.5: Absorption (top row) and emission (bottom row) dipoles, measured experimentally (left column) or calculated by TD-DFT at the B3LYP 6-31G level of theory (right column).

transition dipole moments for both the benzene-cored and truxene-cored molecules show an approximate $\sqrt{n}$ dependence on the arm length, as highlighted by the semi-logarithmic scale of figure 3.5. This same dependence was previously found for the linear oligofluorene molecules in frozen solution at 77 K [163]. The experimental measurements in this work show a weaker increase of the transition dipole moment in both absorption and fluorescence, which is likely to be due to the effects of conformational disorder on these molecules at room temperature in solution.

Experimental photoluminescence quantum yield (PLQY) and lifetime data for all the molecules is presented in figure 3.6 (a) and (b) respectively. The PLQY for all families increases with arm length, with the truxene-cored molecules having consistently high PLQY across the entire family, with a slight increase from 78% for T1 to 87% for T4. This is consistent with the calculations, showing that the lowest transition state in the S_1 geometry is bright for all molecules except for T0, where only the third transition of the S_2 geometry is bright, as shown in Section 3.2. The same conclusion is observed experimentally, with only the T0 (truxene core) having a low PLQY of 7% (not shown). Benzene-cored molecules show a much greater change in PLQY, increasing from 36% for B1 to 86% for B4. The increasing PLQY of the benzene-cored molecules follow a similar trend to the oligofluorene molecules, but are always higher. The PLQY for the star-shaped molecules with

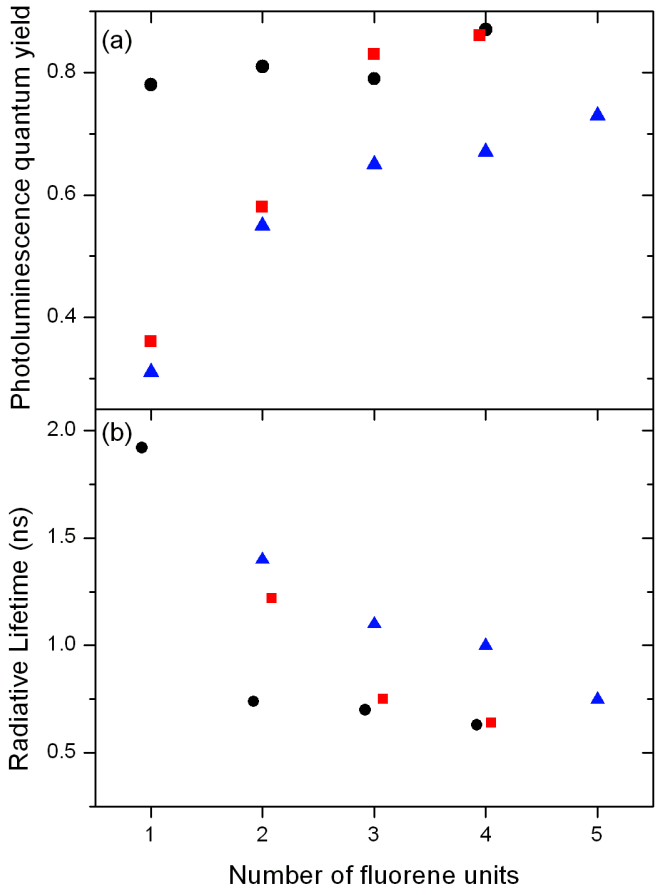

Figure 3.6: Photoluminescence quantum yield (PLQY) (a) and lifetime (b) for truxene-cored molecules (black circles), benzene-cored molecules (red squares) and oligofluorene (blue triangles). Lifetime and PLQY measurements for the oligofluorene were reported in ref. [163] (from our reference [37]).

three and four repeat fluorene units are similar, suggesting that the photo-physics of the larger molecules is dominated by their arms. The radiative lifetime determined using $\tau_{rad} = \tau/PLQY$, where $PLQY$ is the photoluminescence quantum yield and τ is the measured fluorescence lifetime, is presented in figure 3.3 (b). The radiative lifetime decreases with increasing arm length.

3.4 Exciton localisation and symmetry breaking

The good qualitative and quantitative agreement between the theoretical and experimental results validates the theoretical results obtained by the quantum chemistry calculations and enables us to learn more about the exciton localisation in the star-shaped molecules studied.

As we have shown, the C_3-symmetry of these star-shaped molecules is responsible for the existence of degenerate transitions and electronic states. For instance, the Highest Occupied Molecular Orbital HOMO and HOMO-1 of B2 are degenerate.

This means that they are the linear combination of any two non-collinear molecular orbitals which form a base. A pair of two "base molecular orbitals" randomly picked up by Gaussian09 are plotted in figure 3.7. They obviously cover only a fraction of the molecules. However, if we were to add them, they would extend over the whole molecule and exhibit C_3-symmetry as well. On the contrary, the Lowest Unoccupied Molecular Orbital LUMO+ 2 is not degenerate and extends over the whole molecule. Figure 3.8 shows TD-DFT calculations of the change in the electron density by

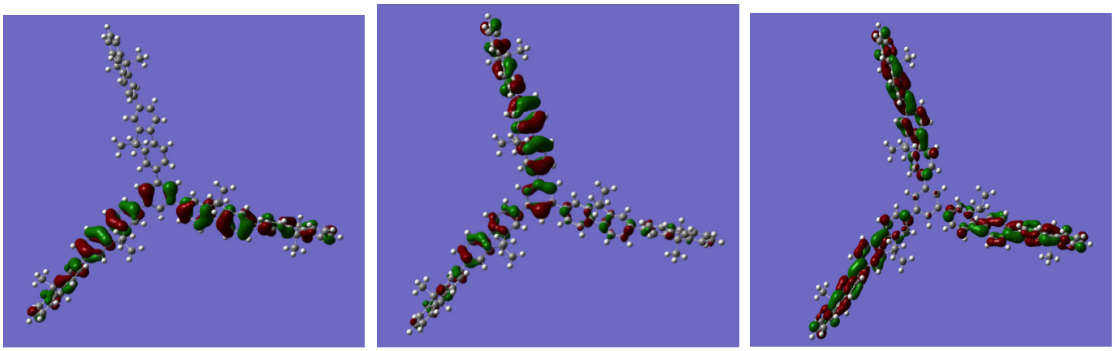

Figure 3.7: Visualisation of the HOMO-1 (left); HOMO (centre) and LUMO+2 molecular orbitals in the B2 molecule.

absorption of a uniform excitation, for instance a circularly polarized light, and by fluorescence in B2. The change in the electron density during both transitions is greatest in the middle of the arms, however, absorption transitions are delocalised over the entire star-shaped molecule, while fluorescence transitions are localised on a single arm. The absorption is made of two degenerate perpendicular levels (involving the HOMO-1 and HOMO of figure 3.7) and is therefore extended over the whole molecule in case of isotropic excitation such as circularly polarised light. This agrees with the measured molar absorption coefficient, presented in figure 3.3. Indeed, for all families this measured absorption coefficient increases with increasing arm length, and for a given length, the molar absorption coefficient is similar for the truxene-cored and benzene-cored star-shaped molecules. For molecules with 2-4 fluorene units in the arms, the molar extinction coefficient is approximately three times larger than that of the equivalent oligofluorene arm. This difference can be explained by the star-shaped molecules absorbing light across all three fluorene arms.

For B1 and B2 we have run a series of calculations with a variety of different initial (small) symmetry breakings in the excited state, however, only three different minima on the excited state potential energy surface were found. In each of these three excited state geometries, the excitation is localized on one of the molecule's three arms. The symmetry is broken due to the well-known Jahn-Teller effect, i.e., vibronic coupling between the degenerate components of an electronic state via non-totally symmetric vibrations, leading to three equivalent minima on a "tricorn" potential [202], as represented in figure 3.9. In both benzene-cored and

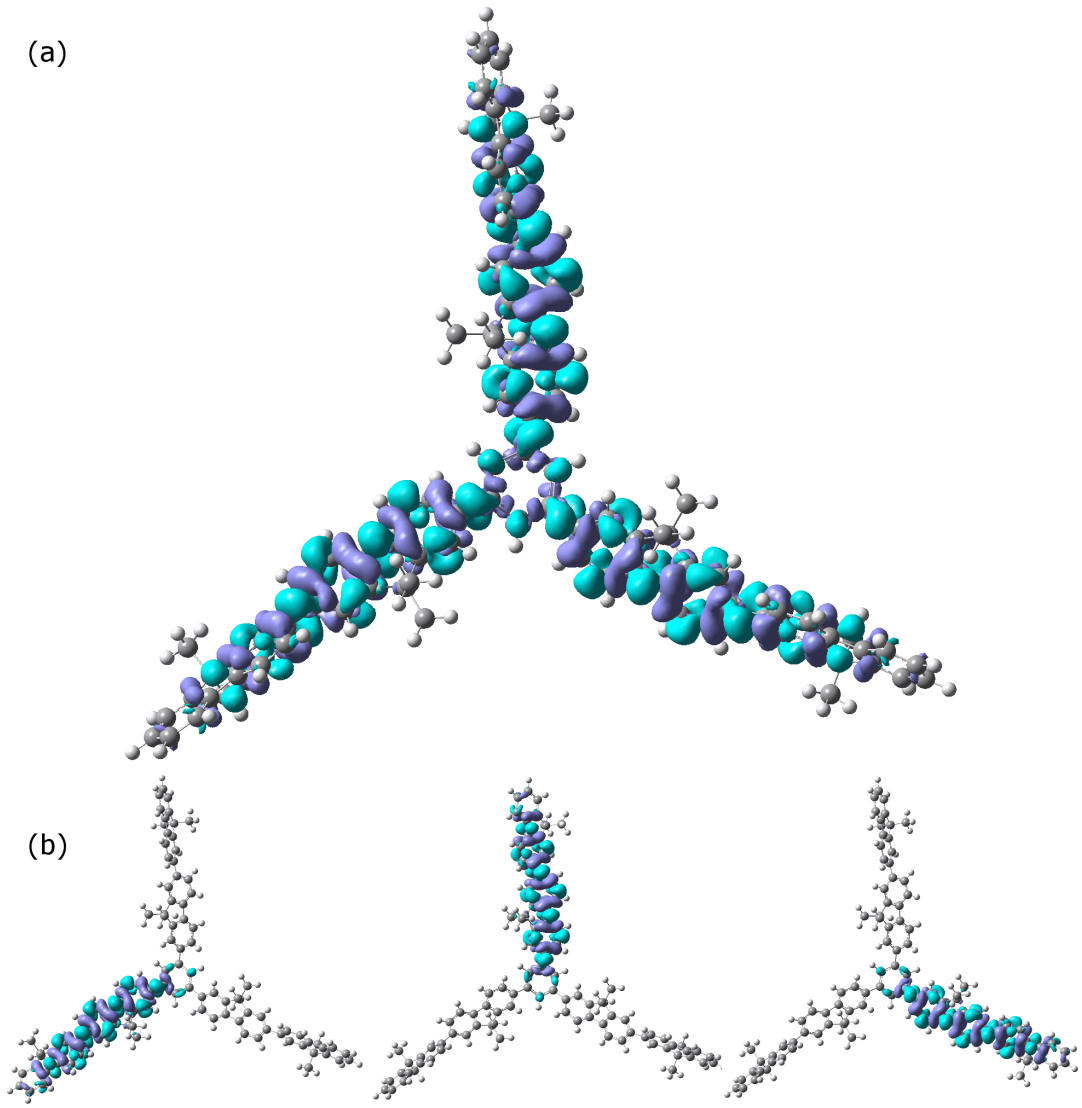

Figure 3.8: Visualisation of the calculated change in electron density for the B2 molecule in absorption (a), emission (b). Shown are the three possible emission states for the B2 molecule. In absorption, circular polarization is assumed for light incident on the molecule from on top; the emission dipole is oriented along the respective fluorene arm from which it originates.

truxene molecules there are three stable emission states which allow the emission to radiate from any one of the three arms. The excited state relaxation process occurs in a qualitatively similar way for both families of star-shaped molecules, and for a range of arm lengths. Physically, following the absorption process there is a change in the geometry such that the C_3-symmetry is spontaneously broken and the excitation is localized on one of the arms. Similar to linear oligofluorenes [163] the equilibrium geometry of the arm on which the excitation localises is planarised by the excitation. This process is illustrated in figure 3.9: after photo-excitation, the C_3 symmetric molecule is situated at an unstable local maximum of the potential energy, surrounded by three local minima. The molecule is going to relax to one of these three points, corresponding in our case to the planarisation of one of the three oligofluorene arms of the star - the resulting actual "chosen" minimum being dependent on subtle initial symmetry-breakings.

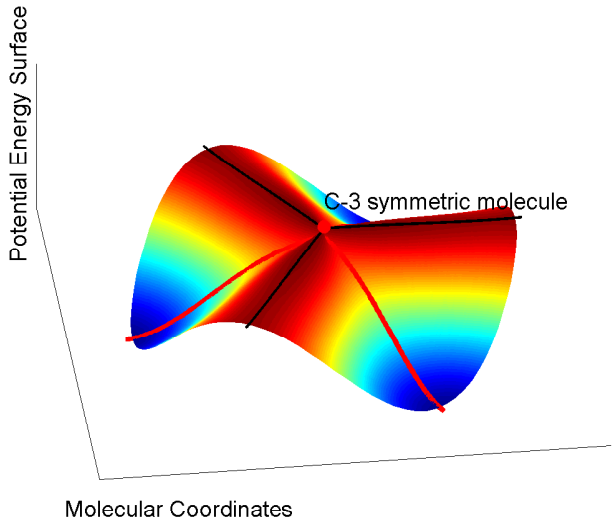

Figure 3.9: Sketch of the "tricorn" excited-state potential seen by the star-shaped molecule.

3.5 Conclusion

In order to gain knowledge on exciton transfer in star-shaped molecules, ideal candidates to conduct a study of intra-molecular excitation transfer due to their accurately known geometries, it is important to have an understanding of the underlying optical transitions, the effects of the core, and the effect of the length of the arms upon the properties and efficiency of the molecule. this could also result in the discovery of improvements in the application of these molecules in devices. Theoretical results show that that there is a red-shift in the emission and absorption energies due to the extra conjugation of the core, and that the transition dipole

moments in both absorption and emission are slightly larger for the star-shaped molecules than linear oligofluorenes. These theoretical results are complimented by the experimental results which provide a good quantitative agreement of the absorption and emission energies and dipole moments. The calculations also show that the absorption of light in both families of star-shaped molecules generates delocalised excitons over the whole molecules. This result confirms that when inferring the transition dipole moment from measurements it is important to correctly account for the number of involved transitions, which, due to rotational symmetry, is two for the star-shaped molecules in absorption. In contrast the calculations show that the emission is localised on a single arm due to an excited state relaxation process. The photo-physical excitation process of a single star-shaped molecule is summarised in figure 3.10. We have also shown that the transition dipole moments in the star-

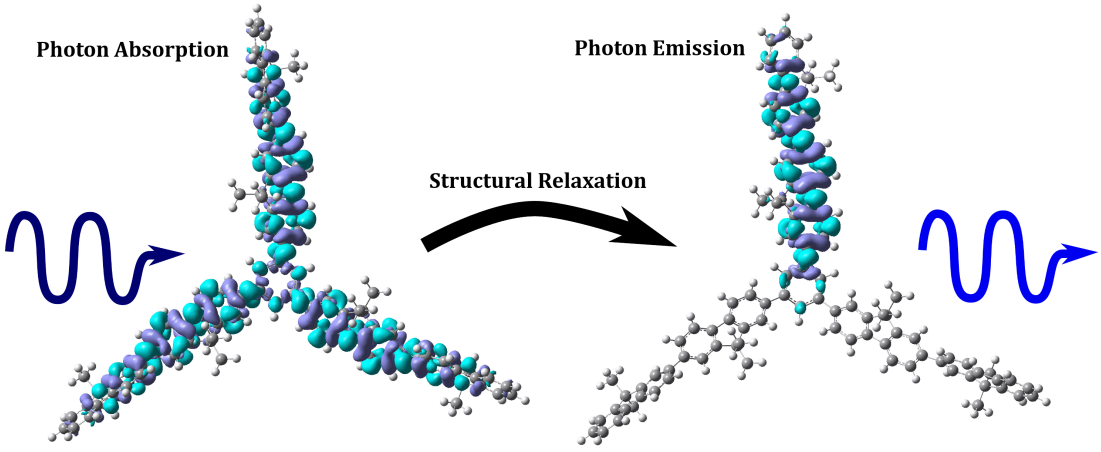

Figure 3.10: Transition density following isotropic photo-excitation, resulting in exciton localisation on one arm.

shaped molecules increase with a $\sqrt{n}$ dependence on arm length which is the same as in the oligofluorenes. The increase is slightly weaker for the experimental results suggesting that there is some conformational disorder in the larger molecules. The experimental results also show that the star-shaped molecules have higher PLQYs than oligofluorenes with equivalent arm lengths. The large molar absorption coefficients and high PLQY of these molecules makes them attractive for light-emitting devices, especially optically pumped lasers.

We have presented the theoretical and experimental photo-physical properties of star-shaped molecules. We can now use this knowledge to understand the specific exciton transfer mechanisms in such star-shaped molecules. This is the object of the next Chapter.

Chapter 4

Intra-molecular exciton transfer in C_3-symmetric molecules

Star-shaped molecules are of growing interest as organic optoelectronic materials. In addition, the known geometry of these molecules makes them particularly useful in understanding intra-molecular exciton transfer. We have gained valuable knowledge about the optical and electronic properties of some star-shaped molecules, as seen in the previous Chapter. Based on these results, we report in this Chapter a detailed theoretical study of the time-resolved photo-physics of the truxene-cored molecules presented in Chapter 3, combined with experiments through the use of fluorescence depolarisation. This combined experimental and theoretical study enables us to gain valuable knowledge about the mechanisms responsible for exciton migration in solutions of these star-shaped molecules.

4.1 Background

We have shown in Chapter 3 that star-shaped molecules are of research interest due to their ease of experimental processing. In addition, branched conjugated molecules in general show attractive properties such as directional energy transfer [203], enhanced two photon absorption [204–206], and high photoluminescence quantum yield in the solid state [81, 207]. These properties make them useful in light harvesting systems for solar energy conversion [203, 208, 209], fluorescence sensors [210, 211], organic light emitting diodes [183, 212] and organic lasers [81, 82]. In order to design efficient light-harvesting antennae which would absorb light and funnel energy to a desired location, it is important to understand exciton localisation and energy transfer.

A number of experimental and theoretical studies investigating exciton localisation have been carried out on branched molecules with different chemical structures, observing their fluorescence [213, 214] or transient absorption [215]. The depolarisation of fluorescence also provides complementary information about energy transfer, as it shows the change in orientation of the emission dipole from the absorption dipole. Molecules with a nitrogen core [65, 213–216] show a very fast energy transfer between branches on a 30 fs time scale and subsequent localisation on one branch [215]. In contrast the molecules with benzene [217–219], carbon and adamantine cores show much slower depolarisation which implies that excitation localises

quickly on one branch [218] and subsequently transfers to other branches via Förster hopping [219].

For the truxene- and benzene-cored star-shaped molecules presented in Chapter 3, there has been a small amount of work carried out on their fluorescence dynamics, in a study of the picosecond planarisation process of the branches [220]. However, there has yet to be a study of energy transfer and exciton localisation in truxene- and benzene-cored molecules. This work is the subject of this Chapter. We believe that, regarding the photo-physics results presented in Chapter 3, the benzene- and truxene-cored star-shaped molecules behave in a qualitatively similar fashion, and we thus restrict our study to truxene-cored molecules.

4.2 Fluorescence anisotropy theory

4.2.1 Background to fluorescence anisotropy

The fluorescence anisotropy technique provides an experimentally accessible measure of the relative orientation of the fluorescence dipole compared to the absorption dipole. The principle lies in the excitation of a sample by a linearly polarised pulse, and by then recording separately the intensities emitted by the excited sample in the directions parallel and perpendicular to the linearly polarised excitation pulse. It is thus possible to monitor the average transition dipole angle and rotation (due to, for instance, molecular relaxation, Förster transfer or molecular movement), with respect to the excitation pulse [221].

The quantitative measure of the fluorescence anisotropy, usually denoted as r, is given by the following formula [221]:

$$r = \frac{I_{\parallel} - I_{\perp}}{I_{\parallel} + 2I_{\perp}} \ , \tag{4.1}$$

where $I_{\parallel}$ and $I_{\perp}$ are the fluorescence intensities respectively parallel and perpendicular to the linearly polarised pump. Polarisation-independent fluorescence dynamics, the intensity recorded at the "magic angle" m, is, in our work, reconstructed from the parallel and perpendicular intensities using:

$$m = \frac{I_{\parallel} + 2I_{\perp}}{3} \ . \tag{4.2}$$

In the rest of this thesis, "magic angle" will be used to refer to this quantity, which is the polarisation-independent fluorescence intensity.

4.2.2 Fluorescence anisotropy theory for "rod-like" molecules

In this Subsection we deal with molecules which possess only one, straight, absorption dipole which can be excited at the particular excitation energy of the pump, with no rotation of this transition dipole due to molecular relaxation. Such molecules are referred to as "rod-like molecules" in the rest of this thesis. It is known that the initial anisotropy of a sample made of randomly oriented rod-like molecules is [221]: $r = 2/5 = 0.4$. Once the fluorescence anisotropy has disappeared (molecules are all equally likely to be excited), the measured anisotropy is $r = 0$. We now derive this well-known result and then extend it for the case where the molecules possess two orthogonal absorption dipoles, as this is the case in the truxene-cored star-shaped molecules.

We parametrise a rod $\boldsymbol{r}$ in a spherical coordinate system, with the usual polar angle θ and azimuthal angle ϕ, as sketched in figure 4.1. In the Cartesian system

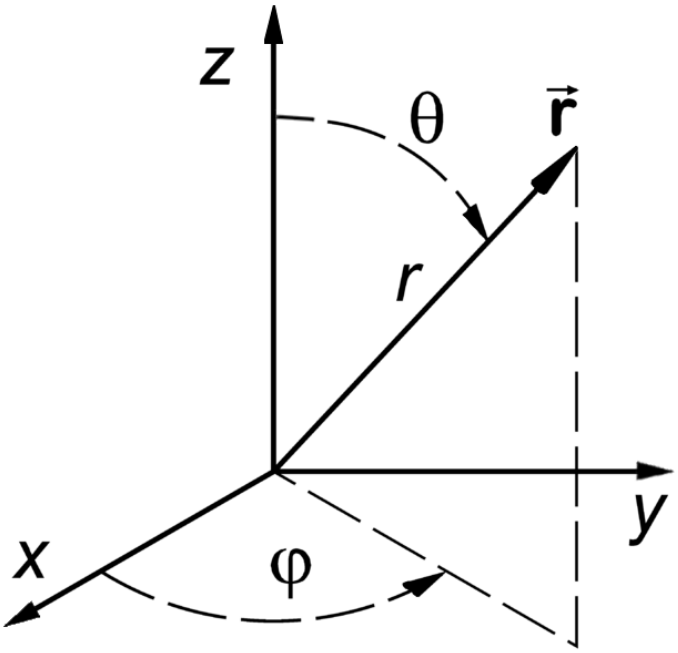

Figure 4.1: Sketch of the parametrisation of a rod $\boldsymbol{r}$ in a spherical coordinate system (from reference [17]).

$(O; \boldsymbol{x}, \boldsymbol{y}, \boldsymbol{z})$, $\boldsymbol{r}$ can be parametrised as:

$$x = \sin\theta\cos\phi, \tag{4.3}$$

$$y = \sin\theta\sin\phi, \tag{4.4}$$

$$z = \cos\theta. \tag{4.5}$$

The ensemble of all possible dipole positions $\boldsymbol{r}$ is a half sphere, so ϕ can take its values between 0 and π and θ between $-\pi/2$ and $\pi/2$.

We consider a pump polarised in the $\boldsymbol{z}$-direction. In such a case, the intensity absorbed by the dipole $\boldsymbol{r}$ is $I \propto \cos^2\theta$. Therefore the emitted intensities can be derived: $I_x \propto \cos^2\theta \sin^2\theta \cos^2\phi$ and $I_z \propto \cos^4\theta$. We calculate the averages of the intensities over all possible dipole orientations by multiplying them by $|\sin\theta|$ and assuming a uniform distribution of the molecules in space ($|\sin\theta|$ being the differential surface element in a spherical coordinate system (θ, ϕ) with fixed r):

$$I_\perp = \langle I_x \rangle = \frac{\int_{-\frac{\pi}{2}}^{\frac{\pi}{2}} \int_0^\pi \cos^2\theta \sin^2\theta |\sin\theta| \cos^2\phi \; d\theta d\phi}{\pi \int_{-\frac{\pi}{2}}^{\frac{\pi}{2}} |\sin\theta| \; d\theta} = \frac{1}{15}, \tag{4.6}$$

$$I_\parallel = \langle I_z \rangle = \frac{\int_{-\frac{\pi}{2}}^{\frac{\pi}{2}} \int_0^\pi \cos^4\theta |\sin\theta| \; d\theta d\phi}{\pi \int_{-\frac{\pi}{2}}^{\frac{\pi}{2}} |\sin\theta| \; d\theta} = \frac{1}{5}. \tag{4.7}$$

The denominators $\pi \int_{-\frac{\pi}{2}}^{\frac{\pi}{2}} |\sin\theta| \; d\theta$ are normalisation constants. We obtain the expected result for the anisotropy $r = (I_\parallel - I_\perp)/(I_\parallel + 2I_\perp) = 2/5 = 0.4$.

4.2.3 Fluorescence anisotropy theory for star-shaped molecules

The star-shaped molecules, such as the truxene-cored family of molecules, are different from the rod-like molecules in the sense that instead of having only one excitable absorption dipole, they possess two orthogonal absorption dipoles due to the degeneracy of the absorption states arising from the C_3 symmetry of the molecules, as it has been demonstrated in Chapter 3. In consequence, the absorption transitions always allow a dipole parallel to the optical polarization to be induced by exciting a linear combination of the degenerate states. This strong initial dipole leads to an anisotropy different from the rod-like case.

Considering absorption properties from the symmetry point of view, these C_3 symmetric molecules can be modelled as a disk. This is true for any molecule with two degenerate absorption transitions. In the following we establish the fluorescence anisotropy value to expect from these "disk-like" molecule, arising either from the absorption dipole or the emission dipole.

We parametrise the disk-like molecules in the following way: the normal to the disk of the molecule is $\boldsymbol{n}$ (corresponding to $\boldsymbol{r}$ in figure 4.1), parametrised by θ and azimuthal angle ϕ. The last degree of freedom of the disk-like molecule, its rotation around this normal vector $\boldsymbol{n}$, is parametrised by the angle α, defined as the angle between the projection of $\boldsymbol{z}$ in the plane of the disk and the vector $\boldsymbol{OM}$, representing the (non-degenerate) emission dipole of the molecule. Thus the star-shaped molecules are parametrised by the three degrees of freedom: (α, θ, ϕ), as drawn in figure 4.2. The ensemble of all possible positions for $\boldsymbol{n}$ are included in a half-sphere (due to symmetry), and therefore $(\theta; \phi) \in [-\pi/2; \pi/2] \times [0; \pi]$. The

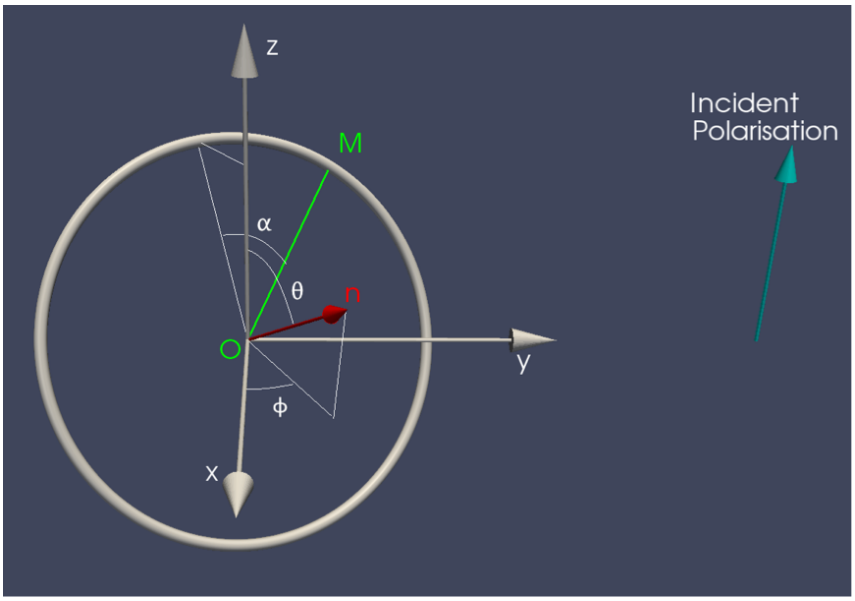

Figure 4.2: Sketch of the parametrisation of an arm $\boldsymbol{OM}$ of a disk-like, star-shaped molecule.

vector situated at $\alpha+\pi$ on the disk is equivalent, in the point of view of the emission dipole, to vector $\boldsymbol{OM}$, at the angle α on the disk. Therefore, the problem is fully described with values of α between $\pi/2$ and $\pi/2$.

In the Cartesian coordinate system $(O; \boldsymbol{x}, \boldsymbol{y}, \boldsymbol{z})$, the arm $\boldsymbol{OM}$ is parametrised by:

$$x = -\cos\alpha\cos\theta\cos\phi - \sin\alpha\sin\phi, \tag{4.8}$$

$$y = \sin\alpha\cos\phi - \cos\alpha\cos\theta\sin\phi, \tag{4.9}$$

$$z = \cos\alpha\sin\theta. \tag{4.10}$$

The pump pulse, along $\boldsymbol{z}$, is absorbed by the quantity $I \propto \sin^2\theta$ as the degeneracy of the S_0 state means that the absorption dipole created by the pump will always have the largest projection possible on the z axis, while on the plane of the molecule. This corresponds the absorption dipole $\boldsymbol{OM}$ at the position $\alpha = 0$.

As demonstrated in Chapter 3, after molecular relaxation the excitation gets localised on one arm. The arm where the dipole localises corresponds to $\boldsymbol{OM}$. This emission dipole emits an intensity proportional to the projection of $\boldsymbol{OM}$ on the $\boldsymbol{x}$ and $\boldsymbol{z}$ axis, and to the strength of the dipole created by the pump. Therefore the emitted intensities are given by $I_x \propto \sin^2\theta(\cos\alpha\cos\theta\cos\phi + \sin\alpha\sin\phi)^2 \propto \cos^2\alpha\sin^2\theta\cos^2\theta\cos^2\phi + \sin^2\alpha\sin^2\theta\sin^2\phi + 2\sin\alpha\cos\alpha\cos\theta\sin^2\theta\cos\phi\sin\phi$ and $I_z \propto \cos^2\alpha\sin^4\theta$.

We calculate the average intensities emitted by the emission dipole over all possible geometrical configurations, where the emission dipole can rotate on the disk from its position at $\alpha = 0$ up to an angle α_{max}. Indeed, this will enable us to quickly evaluate the fluorescence anisotropy of plausible cases, as we will see below. We assume that the rotation of this dipole can occur with equal probability to any angle α between $-\alpha_{max}$ and α_{max}. The average intensities over all possible configurations, in function of α_{max}, are therefore:

$I_\perp = \langle I_x \rangle = I + J + 2K$ with:

$$I = \frac{\int_{-\alpha_{max}}^{\alpha_{max}} \int_{-\frac{\pi}{2}}^{\frac{\pi}{2}} \int_0^{\pi} \cos^2\alpha \sin^2\theta \cos^2\theta |\sin\theta| \cos^2\phi \; d\alpha d\theta d\phi}{\frac{\pi}{3}\pi \int_{-\frac{\pi}{2}}^{\frac{\pi}{2}} |\sin\theta| \; d\theta} , \tag{4.11}$$

$$J = \frac{\int_{-\alpha_{max}}^{\alpha_{max}} \int_{-\frac{\pi}{2}}^{\frac{\pi}{2}} \int_0^{\pi} \sin^2\alpha \sin^2\theta |\sin\theta| \sin^2\phi \; d\alpha d\theta d\phi}{\frac{\pi}{3}\pi \int_{-\frac{\pi}{2}}^{\frac{\pi}{2}} |\sin\theta| \; d\theta} , \tag{4.12}$$

$$K = \frac{\int_{-\alpha_{max}}^{\alpha_{max}} \int_{-\frac{\pi}{2}}^{\frac{\pi}{2}} \int_0^{\pi} \sin\alpha \cos\alpha \cos\theta \sin^2\theta |\sin\theta| \cos\phi \sin\phi \; d\alpha d\theta d\phi}{\frac{\pi}{3}\pi \int_{-\frac{\pi}{2}}^{\frac{\pi}{2}} |\sin\theta| \; d\theta} = 0 , \tag{4.13}$$

and

$$I_\parallel = \langle I_z \rangle = \frac{\int_{-\alpha_{max}}^{\alpha_{max}} \int_{-\frac{\pi}{2}}^{\frac{\pi}{2}} \int_0^{\pi} \cos^2\alpha \sin^4\theta |\sin\theta| \; d\alpha d\theta d\phi}{\frac{\pi}{3}\pi \int_{-\frac{\pi}{2}}^{\frac{\pi}{2}} |\sin\theta| \; d\theta} . \tag{4.14}$$

We observed, and analytically verified, that because of the symmetry of the problem, the average intensities $\langle I_x \rangle$ and $\langle I_y \rangle$ are equal.

These average intensity results lead to the fluorescence anisotropy:

$$r(\alpha_{max}) = 0.3 \frac{\sin 2\alpha_{max}}{\alpha_{max}} + 0.1 . \tag{4.15}$$

The variation of anisotropy with increasing maximum emitting dipole rotation angle α_{max} is illustrated in figure 4.3:

Non-relaxed excited molecules

In the case where the molecules have not yet relaxed, very shortly after photo-excitation, we have $\alpha_{max} = 0$. Indeed, the emitting dipole is still the absorption dipole created by photo-excitation at $\alpha = 0$, and which did not undergo any further rotation. Therefore the fluorescence anisotropy very shortly after photo-excitation is $r(0) = 0.3 \times 2 + 0.1 = 0.7$.

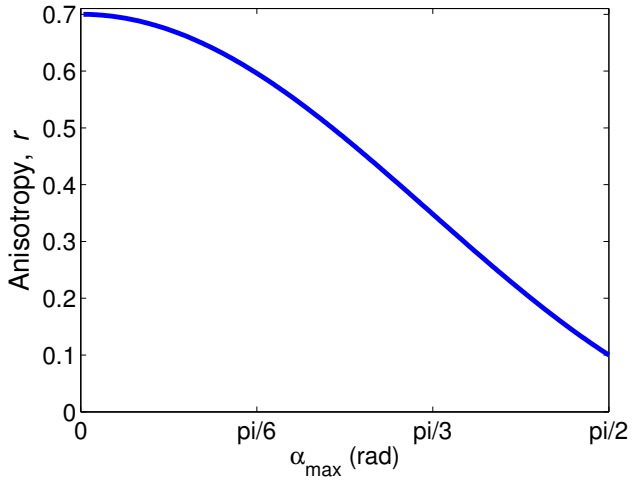

Figure 4.3: Anisotropy in function of the angle α_{max}.

Relaxed molecules

We have shown in Chapter 3 that the exciton relaxes to one of the arms of the star-shaped molecule. Two cases seem possible regarding this arm where the exciton localises: either the dipole created by the pump relaxes to the arm closest to where it has been created, or it is randomly relaxed on any one of the three arms of the molecules. If the exciton localisation occurs to the closest arm, the maximum dipole rotation angle will be $\alpha_{max} = \pi/6$, yielding the fluorescence anisotropy $r(\pi/6) = 9\sqrt{3}/(10\pi) + 0.1 \approx 0.6$. In the second case, it is clear that $\alpha_{max} = \pi/2$ and therefore the fluorescence anisotropy is $r(\pi/2) = 0.1$.

It is important to notice that it is known that the initial fluorescence anisotropy [222] or pump-probe anisotropy [223, 224] of a molecule with degenerate states is expected to be 0.7, and decrease to 0.1 due to a symmetry-breaking relaxation and dephasing. However, to the best of our knowledge, the possibility of the excitation relaxing to the closest arm where the excitation has been created (in a branched molecule) has never been discussed.

Experimental fluorescence anisotropy realised in solution of truxene-cored star-shaped molecules should enable one to identify the actual relaxation process from these two possibilities.

4.3 Comparison with experimental results

All the experiments presented in this Chapter have been performed by our collaborators at the university of St Andrews.

4.3.1 *Experimental methods*

The experiments have been conducted on the T2 and T4 molecules: the truxene-cored star-shaped molecules with either two or four fluorene units per arm respectively (see insert in figure 4.4). To identify the effect of the core and the C_3 symme-

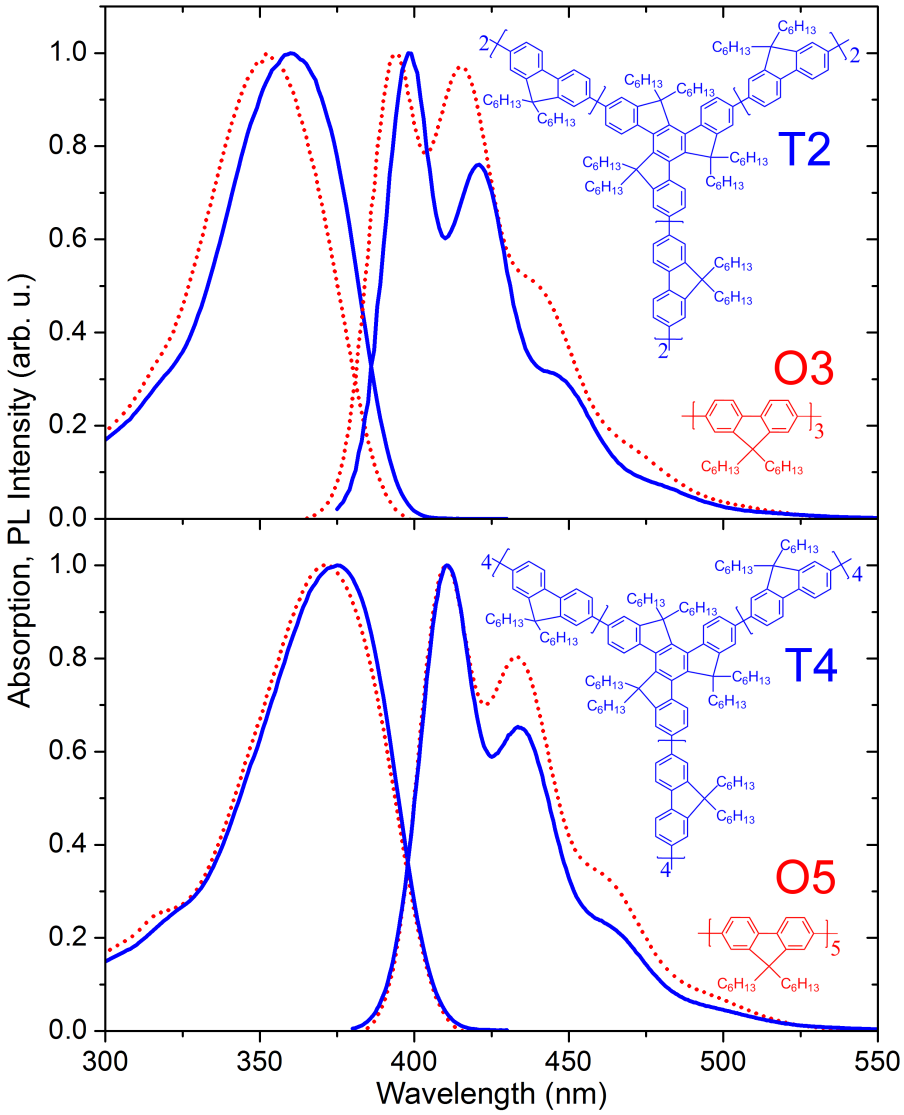

Figure 4.4: Absorption spectra (left) and emission spectra (right) of (a) truxene T2, and oligofluorene O3 (b) truxene T4, and oligofluorene O5. Truxenes are the blue solid lines and oligofluorenes the red dotted lines. The molecular structures are shown in the inset (from our reference [225]).

try of the star-shaped molecules the results are compared with linear oligofluorene molecules of three and five units in length (denoted O3 and O5 respectively). The oligomers are chosen to be directly comparable to a single spoke of the oligofluorene-truxene molecules. For example, the T2 molecules arm consists of two fluorene units in the arm in conjugation with one fluorene unit of the core, so we compare it with O3.

Ultra-fast photoluminescence dynamics were measured using fluorescence spectroscopy. The emitted intensities are filtered by a narrow bandwidth filter (less than 5 nm wide), centred around a given detection wavelength. The pump source has pulses of full-width half-maximum (FWHM) 100 fs. The photolumiscence (PL) is recorded in the direction perpendicular and parallel to the excitation to derive the fluorescence anisotropy. The temporal shifts in recorded PL between parallel and perpendicular excitation were obtained by recording the water Raman signal for both polarisations and finding the shift between the two. The shifts were 39 fs at 380 nm, 32 fs at 400 nm and 38 fs at 420 nm excitation: all anisotropy data were corrected for this temporal shift before fitting.

Fitting was carried out using the impulse reconvolution method [226]. This involves firstly fitting a convolved function to the reconstructed magic angle data $I_{\parallel} + 2I_{\perp}$, denoted as the sum fit. The fitting parameters are then multiplied by the trial function for the anisotropy decay and convolved with the instrument response function (IRF). This function is compared with the numerator of the anisotropy equation $I_{\parallel} - I_{\perp}$, the so-called difference fit. A full description of fitting is given in reference [225].

It was checked that the kinetics and anisotropy decays were concentration independent, in the low-concentration range used, when detecting the fluorescence at the 0-1 vibronic peak and longer wavelengths.

The excitation wavelength λ_{ex} was chosen such that it is as close to the peak of the absorption as the experimental setup would allow, whilst the detection wavelength λ_{det} was chosen to be on the red side of the 0-1 peak to remove any effects of self-absorption on the recorded dynamics. It was found that the observed anisotropy decay was independent of detection wavelength, a result that has previously been noted in reference [227].

4.3.2 Experimental results

Figure 4.4 shows experimental absorption and time integrated fluorescence spectra of the branched molecules T2 and T4 and of the linear molecules O3 and O5.

The upper panels of figure 4.5 show the reconstructed fluorescence kinetics at the magic angle for all of the studied molecules, with $\lambda_{ex} = 380$ nm and $\lambda_{det} = 420$ nm (O3 and T2) and $\lambda_{ex} = 380$ nm and $\lambda_{det} = 440$ nm (O5 and T4). The lower panels show the corresponding anisotropy decays calculated using equation (4.2).

Magic angle kinetics for both branched and linear molecules show a finite rise of ~ 90 fs which is more clearly visible when compared against an instantaneous rise with a magnified scale shown in the insets. Both branched and linear molecules show an initial anisotropy of 0.4 but only the branched molecules show fast depolarisation on a sub-picosecond time scale. The T2 anisotropy shows a fast initial decay from 0.4

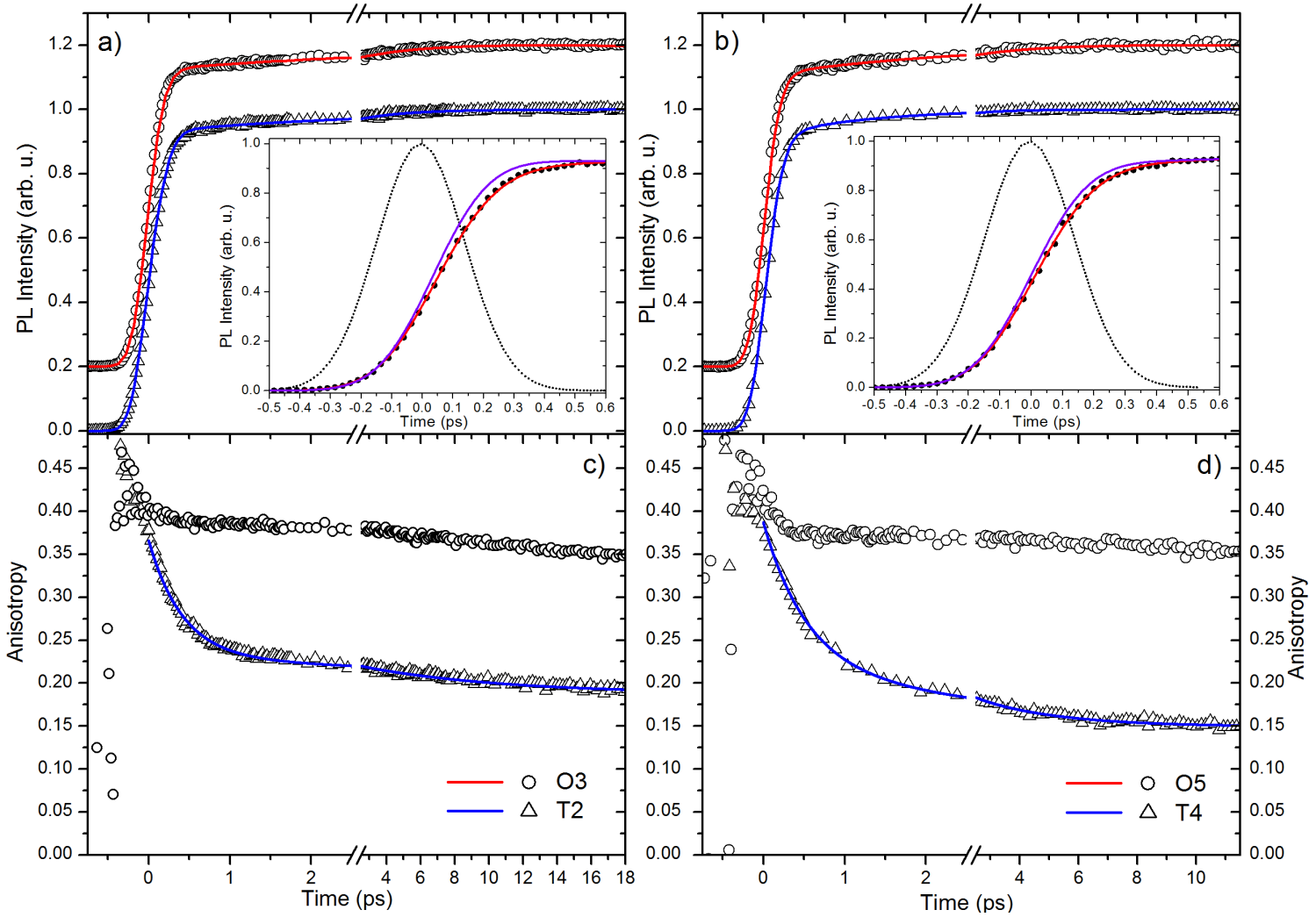

Figure 4.5: Fluorescence magic angle (top panels) and anisotropy (bottom panels) data and fits for the four studied molecules. The data on the left panels (a and c) contain comparisons between O3 and T2, while those on the right (b and d) contain comparisons between O5 and T4. The magic angle data are offset vertically for clarity. Inset to the magic angle kinetics are the early time magic angle data, showing the rise-time that is observed in the fluorescence when comparing against an instantaneous formation (purple line), the instrument response function is also shown for information (dotted line) (from our reference [225]).

to 0.25 and a slower decay component which reduces the anisotropy further to 0.2. The T4 anisotropy shows similar dynamics, with a fast initial decay from 0.4 to 0.225 and then a second, slower decay to a final anisotropy value of 0.15. Two exponential decays and a long-lived offset were needed to describe the depolarisation dynamics. The solid lines shown in figure 4.5 are the fits to the magic angle data and a simulated decay of anisotropy using fitting parameters given in table 4.1. The anisotropy decay

Molecule	λ_{ex} (nm)	λ_{det} (nm)	R_0	τ_1 (ps)	A_1	τ_2 (ps)	A_2	R_{inf}
T2	380	420	0.37	415	0.76	8.4	0.24	0.19
T4	380	440	0.39	513	0.67	2.9	0.33	0.15
T4	400	500	0.38	520	0.60	5.2	0.4	0.18
T4	420	500	0.38	520	0.34	7.9	0.66	0.24

Table 4.1: The fitting times for the anisotropy decay in the truxene molecules. R_0 is the initial anisotropy, τ_1 is the first time constant of the decay and A_1 is the pre-exponential factor of this decay. τ_2 is the second decay time constant with A_2 being the pre-exponential factor of this decay, and R_{inf} is the anisotropy at time t$>$ 15 ps.

in the branched molecules is well described using two time constants, a fast 400-500 fs and a slower 4-8 ps component. Time-resolved fluorescence measurements on a longer time scale using a streak camera gave depolarisation times greater than 100 ps for the linear O3 and O5 molecules, which we attribute to rotational diffusion.

The observed anisotropy in branched molecules with the truxene core shows two interesting features. Firstly, the initial anisotropy is 0.4, not the expected value of 0.7, and secondly, there are at least two different depolarisation mechanisms which are both significantly faster than those observed in the linear molecules. To explore these features further, we investigated the effect of the excitation wavelength on the anisotropy dynamics in T4. The results are presented in figure 4.6. Three excitation wavelengths were chosen: 380, 400 and 420 nm, and dynamics observed at λ_{det} = 440 nm (λ_{ex} = 380 nm) and at λ_{det} = 500 nm for λ_{ex} =400 and 420 nm. The upper panel of figure 4.6 shows the magic angle kinetics, where a $\sim$ 90 fs rise-time of the PL was observed. Inset to the magic angle data is a logarithmic plot of T4 absorption and the spectra of the laser excitation wavelengths that were used in this study. The chosen excitation wavelengths cover the low-energy side of the T4 absorption spectrum. It is clear that when exciting with 420 nm we are accessing the very red edge of the absorption. The anisotropy results are shown in the lower panel of figure 4.6. All three show an initial anisotropy value of $\sim$ 0.4 and all show a two-exponential decay. The initial decay is always fast with a time constant of $\sim$ 500 fs and reduces in amplitude as one moves excitation to the red edge of the absorption. The second slower component has a time constant of 4-8 ps with an amplitude that remains fairly constant across all three excitation wavelengths. Full fitting parameters are shown in table 4.1.

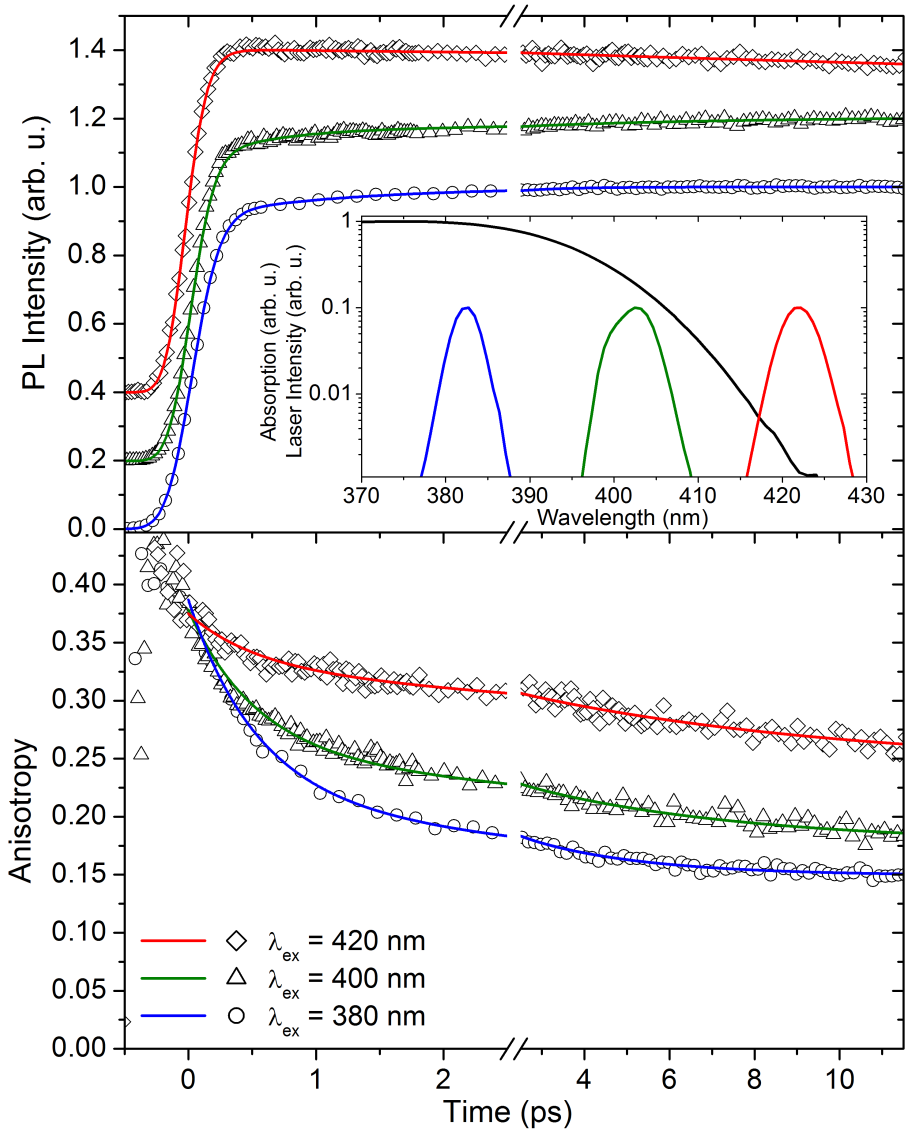

Figure 4.6: Excitation wavelength dependence of the magic angle (top panel) and anisotropy (bottom panel) kinetics for T4. The fits for both the magic angle and anisotropy are shown by solid lines over the data. The magic angle data are offset vertically for clarity. The 380 nm data are the open circles with the blue solid line, 400 nm is the open triangles and green line and the 420 nm shows the open rectangles with the red solid line. The inset to the top panel shows the excitation laser linewidths and wavelengths in comparison with the absorption spectra (black line) (from our reference [225]).

The observed anisotropy values differ greatly from the values we predicted in Section 4.2.3. Indeed, assuming perfect symmetry of the star-shaped molecules and therefore degenerate absorption energies, we had calculated that the initial value of the anisotropy should be 0.7, and that it should then decay to either 0.6 or 0.1 due to the molecular relaxations. These final anisotropy values depend on two possible scenarios: either the excitation is transferred to the arm closest to where the excitation was created ($r = 0.6$), or to a random arm ($r = 0.1$). However, none of these predicted values are observed experimentally. We will examine possible explanations to explain this discrepancy, until one of these explanations fully resist the comparison with experiments. This is the purpose of the rest of this Chapter.

4.4 Proposed theory I: two-step exciton transfer in "disk-like" molecules

The presented anisotropy measurements are detected in the emission wavelength range of the molecules, therefore they correspond to a molecule in its relaxed excited state. A value of the anisotropy between 0.1 and 0.6 is thus expected. We observe experimental values between these two values, and a fast decay. In this Section we present theoretical results in order to verify if the discrepancy between the fluorescence anisotropy results we observed and the results we expected for "disk-like" molecules is coming from rotation of the transition dipole from the arm closest to where it was created to any of the other arms, and from experimental artefacts. Indeed, the IRF, pulse length, and the anisotropy decay have comparable time-scales, so we must carefully account for the inter-mixing convolution of these effects, which could lead to measured results different from expected.

4.4.1 Method

We assume that the star-shape molecules behave like the "disk-like" molecules of Section 4.2.3. As the anisotropy is detected around the emission energy, we assume that all the star-shaped molecules have relaxed to their excited-state geometries when the anisotropy is detected. It follows that the excitation is relaxed to an actual arm of the molecule, as we have seen in Chapter 3. We make the assumption that this arm is the closest to where the excitation has been created (otherwise the fluorescence anisotropy would stay constant at $r = 0.1$). We believe that the excitation can transfer to one of the other two arms from there (otherwise no decay of anisotropy would be observed). These assumptions being established, we can build a model to formalise them and take into account the effects of the pump pulse width and the experimental IRF. We have therefore constructed a set of equations to model the early time-dynamics of excitations:

$$\frac{\mathrm{d}n_1}{\mathrm{d}t} = I(t) - 2\frac{n_1}{\tau} + a\frac{n_2}{\tau} + a\frac{n_3}{\tau} \ , \tag{4.16}$$

$$\frac{\mathrm{d}n_2}{\mathrm{d}t} = \frac{n_1}{\tau} - 2a\frac{n_2}{\tau} + a\frac{n_3}{\tau} \ , \tag{4.17}$$

$$\frac{\mathrm{d}n_3}{\mathrm{d}t} = \frac{n_1}{\tau} + a\frac{n_2}{\tau} - 2a\frac{n_3}{\tau} \ , \tag{4.18}$$

where n_1 is the population on the arm closest to where the transition dipole has been originally created ("arm 1"), and n_2 and n_3 are the populations on each of the two other arms of the molecule ("arm 2" and "arm 3"). τ is the time constant for the transfer process from one arm to the other. $I(t)$ is the pulse of width t_p, taken as a $\mathrm{sech}^2(t/t_p)$ form. From symmetry we clearly have $n_2 = n_3$ so we can rewrite the system more simply:

$$\frac{\mathrm{d}n_1}{\mathrm{d}t} = I(t) - 2\frac{n_1}{\tau} + 2a\frac{n_2}{\tau} \ , \tag{4.19}$$

$$\frac{\mathrm{d}n_2}{\mathrm{d}t} = \frac{n_1}{\tau} - a\frac{n_2}{\tau} \ . \tag{4.20}$$

$$n_2 = n_3 \tag{4.21}$$

From the exciton densities, we can calculate the emitted intensities: $I_\perp = n_1 I_{\perp,close} + 2n_2 I_{\perp,far}$ where $I_{\perp,close}$ is the intensity perpendicular to the pump pulse, emitted when the transition dipole is on arm 1, and $I_{\perp,far}$ when it is either on arm 2 or 3. Similar expressions exist for $I_\parallel$. We calculate $I_{\perp,close}$ and $I_{\parallel,close}$ using equations (4.11) to (4.14) with $\alpha_{max} = \pi/6$. We find that $I_{\perp,close} = 1/5 - \sqrt{3}/5\pi$, $I_{\parallel,close} = 4/5 + 2\sqrt{3}/5\pi$. We obtain $I_{\perp,far}$ and $I_{\parallel,far}$ using the same equations, but with integration over α from $\alpha = -\pi/2$ to $\alpha = -\pi/6$ and from $\alpha = \pi/6$ to $\alpha = \pi/2$. The results are $I_{\perp,far} = 1/5 + \sqrt{3}/10\pi$ and $I_{\parallel,far} = 4/15 - \sqrt{3}/5\pi$.

a is a factor that allows for the possibility of the final populations on arms 1, 2 and 3 not being the same. This possibility is necessary to obtain the expected final anisotropy value r_∞. It is clear that in steady-state, $n_{2,\infty}/n_{1,\infty} = a$. Knowing this and that:

$$r_\infty = \frac{n_{1,\infty}\left(I_{\parallel,close} - I_{\perp,close}\right) + 2n_{2,\infty}\left(I_{\parallel,far} - I_{\perp,far}\right)}{n_{1,\infty}\left(I_{\parallel,close} + 2I_{\perp,close}\right) + 2n_{2,\infty}\left(I_{\parallel,far} + 2I_{\perp,far}\right)} \ , \tag{4.22}$$

we can from there show that:

$$a = \frac{9\sqrt{3} - 20\pi(r_\infty - 1/10)}{9\sqrt{3} + 40\pi(r_\infty - 1/10)} \ . \tag{4.23}$$

Therefore, knowing the experimental steady-state fluorescence anisotropy value r_∞ enables one to obtain a. For instance, in the case of the detection wavelength

$\lambda_{detect} = 400\,\text{nm}$ we observe $r_\infty = 0.2$, so we need $a = 1.77$.

The experimental IRF is fitted by a Gaussian, which is then used to convolve the calculated intensities to mimic the ones observed experimentally. Finally the fluorescence anisotropy is calculated from these convoluted intensities. Like in the experiments, the time $t = 0$ is such that the calculated magic angle reaches $m = 0.5$.

4.4.2 Results

We present the fluorescence anisotropy and magic angle results for two meaningful values of τ, compared to experiments for T4, with excitation at $\lambda_{ex} = 400\,\text{nm}$, in figure 4.7, and excitation at $\lambda_{ex} = 380\,\text{nm}$, in figure 4.8. In these figures we also display the time-dependent densities on each of the arms.

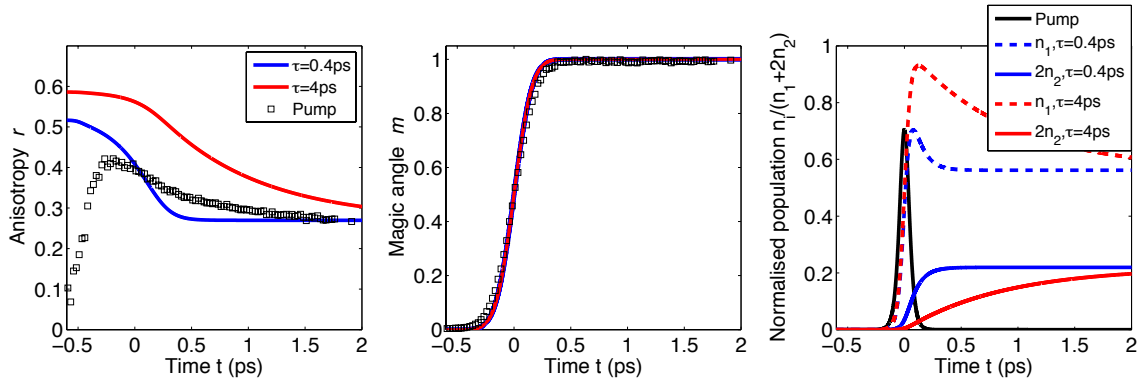

Figure 4.7: Comparison of the predicted anisotropy (left) and magic angle (centre) values with the T4 experimental results, with excitation at $\lambda_{ex} = 400\,\text{nm}$, for two values of τ. The ratio of density on each arm is also presented (red).

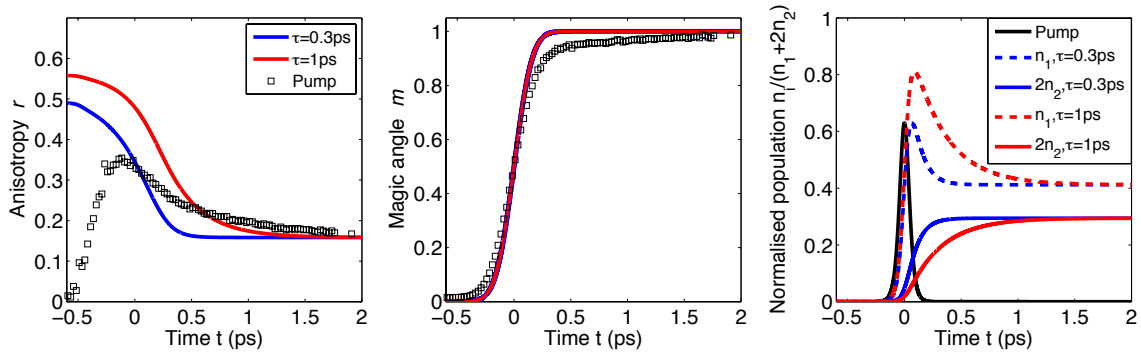

Figure 4.8: Comparison of the predicted anisotropy (left) and magic angle (centre) values with the T4 experimental results, with excitation at $\lambda_{ex} = 380\,\text{nm}$, for two values of τ. The ratio of density on each arm is also presented (red).

From figures 4.7 and 4.8 we observe that it is impossible to obtain both the experimental initial anisotropy value and comparable anisotropy decay rates. Therefore, because of the initial fluorescence anisotropy value of $r = 0.4$, we believe that the

star-shaped molecule could behave like a rod-like molecule. That would mean that, as a consequence of a slight geometrical symmetry-breaking defect, the molecules are "not C_3-symmetric enough" for the degeneracy of the absorption level to exist. An existing explanation for such low fluorescence anisotropy values is that in fluorescence the molecule has already undergone a fast relaxation into a localised emitting state [215]. Others have also discussed issues of polarity of solvents breaking the symmetry of the molecules so that the degeneracy is lifted [227] (it is important to note that the solvent used experimentally here is non-polar). This possibility of the existence of symmetry-broken star-shaped molecules as a way to explain a lower value of the measured fluorescence anisotropy is discussed in the next Section.

4.5 Proposed theory II: influence of symmetry-breaking defects

4.5.1 Method

To explore the degree by which the symmetry of the molecule might be broken by thermally excited conformers, thereby inducing a splitting of the degenerate lowest transition, we have conducted a series of quantum chemistry calculations on the truxene molecule for a variety of conformational distortions. If we can find distortions which produce a sufficiently large splitting at an energy cost of less than k_BT then in our room temperature experiments different ensembles of conformers will be excited at different wavelengths. Hence their subsequent relaxation pathways may be different. These calculations were performed on T2 and T4 molecules for non-symmetric conformations. We started with the C_3-symmetric S_0 geometries described in Chapter 3. Some other stable configurations corresponding to local minima also exist, for example, where some fluorene units of one arm are flipped over by 180°. The energy of these configurations is not much higher than the C_3-symmetric case (typically, 5 meV higher) but the energy barrier is estimated to be more than 45 meV. The resulting energy splitting is quite small, less than 1 nm, because the π-conjugation between the fluorene units does not change much by a 180° twist. Here we are interested in out-of-equilibrium configurations, showing that thermal energy can easily create, from these local minima, some symmetry-breaking defects having a non-negligible effect on the degeneracy of the absorption states. In the rest of the quantum chemistry calculations presented in this chapter, we use the global minima as the equilibrium position, but the reasoning is valid from the other local minima as well. This optimised equilibrium geometry was then slightly distorted by us in a variety of ways as described below to create a "defect" breaking the perfect three-fold rotational symmetry. After this defect is introduced no further geometry optimisation is performed, as this "defect" is treated as an out-of-equilibrium configuration. Therefore, to estimate the formation cost of

the conformational change introduced, the total energy was calculated for this new geometry by DFT and compared with the symmetric ground-state energy. Linear response Time-Dependent DFT (TD-DFT) was then used to calculate the resulting absorption energy splitting and to obtain the S_1 excited state geometry, following the method developed in Chapter 2. For all calculations, the B3LYP functional and the 6-31G basis set were used, and the C_6H_{13} side groups attached to the fluorene arms have been replaced by shorter CH_3 groups in all the calculations, for the reasons we have exposed in Chapters 2 and 3.

4.5.2 Fast depolarisation component

The fluorene units are planar, but the arms are not, as there is a dihedral angle of approximately 36.5° between two consecutive fluorene units all along the arm. The arms are 1.8 nm and 3.4 nm long from the truxene core for T2 and T4 respectively. In table 4.2 we show the degeneracy splitting versus the cost of formation of the symmetry-breaking defects for nine different realisations of possible defects, representative of the kinds of "defects" that can be realised at reasonable energetic cost (compared to thermal energies at room temperature). We observe that

Case	Formation cost (meV)	Degeneracy splitting (nm)	1st absorption (nm)
1	7	1.96	369.95
2	15	3.98	372.01
3	18	3.24	367.88
4	29	4.41	367.85
5	16	4.87	373.21
6	50	0.19	367.95
7	16	1.19	369.16
8	62	7.11	375.39
9	30	6.2	371.66

Table 4.2: Results of the quantum chemistry calculations for T2, using TD-DFT at B3LYP 6-31G level of theory, for some of the calculated broken-symmetry defects. The formation cost is the difference between the total electronic energy calculated for each symmetry-broken configuration and the total energy of the fully symmetric ground state of the molecule. For each case, the resulting splitting of the first two excited states is given, as well as the wavelength of the energetically lowest transition in absorption. Cases 1 to 4 -Twists of a fluorene unit, by -5°, -10°, +10°, +15° at the end of an arm and Case 5, by -10° at the beginning of an arm. Case 6, rotation of a fluorene unit at the end of an arm, by +5° in the plane of the molecule and Case 7 rotation by -5° out of the plane of the molecule. Case 8, combination of a twist of a fluorene unit at the end of an arm by -10° and a rotation of the same arm by -10° out of the molecular plane. Case 9, combination of a twist of a fluorene unit at the end of an arm by -10° and a twist of a fluorene unit at the end of another arm by +10°.

the only symmetry-breaking defects with formation cost close to thermal energies

at room temperature, which give a significant splitting, are the ones which twist a fluorene unit within an arm (cases 1 to 5 of table 4.2). Twisting an entire arm in a way such that the symmetric star-shaped configuration is lost is very costly in terms of formation energy and only results in very small energy splitting (cases 6 and 7). Thus, in these molecules, the observed symmetry-breaking is not likely to be a major distortion of the star-shape of the molecules, but corresponds to twists of selected fluorene units within the fluorene arms. These symmetry breakings can even be combined on a single molecule to increase the splitting: in case 9, two fluorene units on two separate arms have been twisted; the cost of each one of those twists is around 15 meV, and the resulting splitting is greater than 6 nm.

In order to understand the effect of the symmetry-breaking "defects" on the excitation wavelength dependence observed on T4, in figure 4.9 we display the calculated changes in charge density upon photoexcitation for a selection of representative scenarios for this molecule: in case A, the dihedral angle between the second and third fluorene units in the middle of one arm is reduced by 10°; in case B this angle is increased by +10°. Case C shows both twists applied to a single molecule with one of the arms being twisted by +10° and another by -10°. The defect of case A costs 20 meV and leads to a splitting of 4.2 nm, case B results in a splitting of 2.7 nm for a cost of 18 meV and case C costs 30 meV and the resulting splitting is 5.9 meV.

In case A, one of the arms is more planar than in the symmetric ground state of the molecule. The energy cost for this structural modification in the electronic ground state is 20 meV and leads to a splitting of the lowest optically bright transition of 4.2 nm. As a result, the first electronic transition in absorption at 3.157 eV is lower in energy than in the symmetric case (3.191 eV) and corresponds to excitation localised on the distorted arm, figure 4.9 (a). This arm being more planar, the π-conjugation is increased within the arm and therefore the excitation now shows less localisation on the arm, compared with the symmetric case, thus reducing its energy. The second transition at 3.191 eV leads to localisation on the other two, non-distorted arms, figure 4.9 (b), and closely resembles one of the transitions in the fully symmetric case. On the other hand, if we twist a fluorene unit between the second and third fluorene units of an arm by +10° such that the dihedral angle increases, the π-conjugation between these two fluorene units gets reduced (case B). Therefore the 1st transition in this case resembles one of the two transitions in the degenerate case, at 3.191 eV, exciting the two undistorted arms, figure 4.9 (c). The 2nd transition, for which the excitation is mainly localised on the distorted arm, has an increased energy of 3.214 eV, figure 4.9 (d). The cost of this symmetry-breaking is 18 meV and leads to a splitting of 2.7 nm. If we combine these two distortions on one molecule but on two different arms (case C), then the 1st absorption transition has an energy of 3.159 eV, and involves excitation of the distorted,

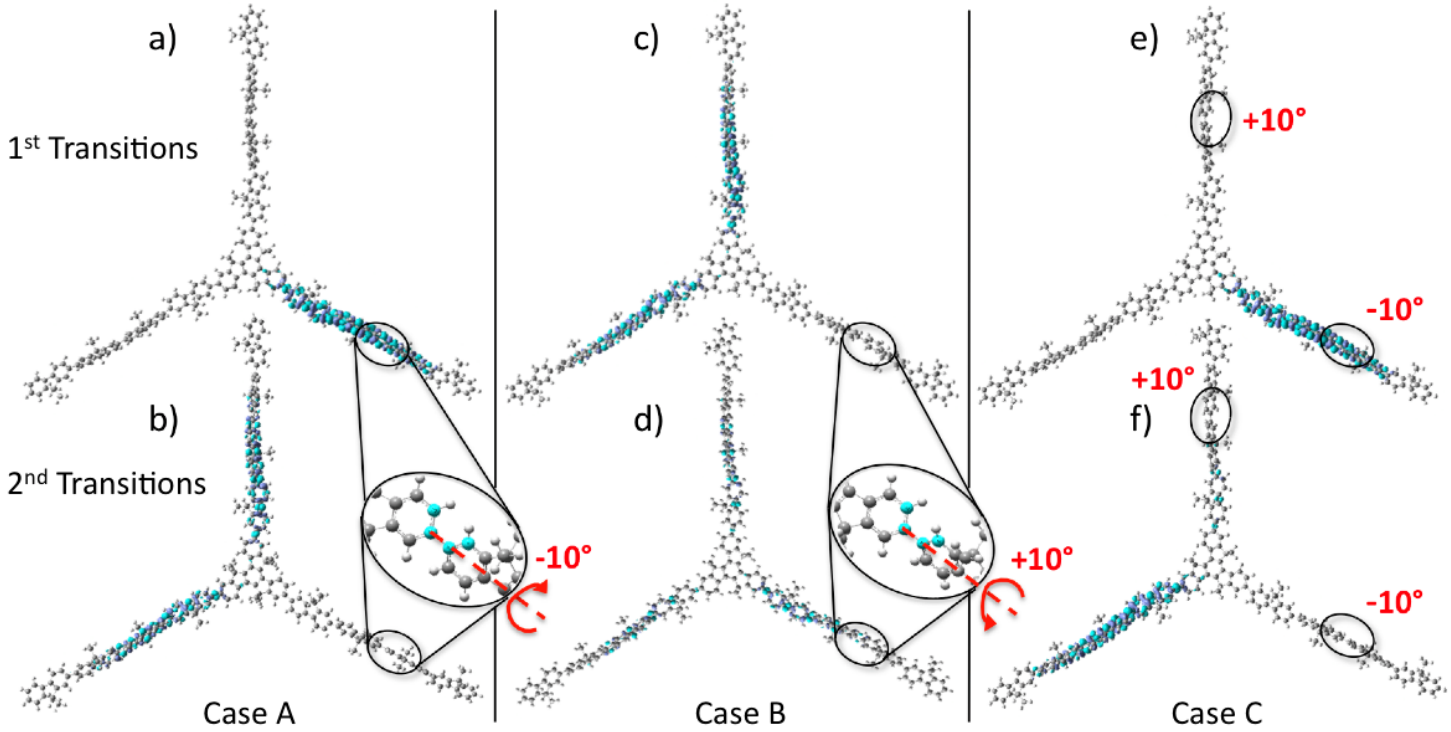

Figure 4.9: Change of the electron density upon photo-excitation of molecules with rotational twists slightly breaking their symmetry. Case A corresponds to a rotational twist clockwise of 10° of the 3rd fluorene unit. Case B represents an anti-clockwise twist of 10° of the third fluorene unit and Case C is a combination of the two. Below the cases are the S_1 emission geometries for the lowest t transitions. The defects have been introduced on the arms as indicated in the figure.

more planar arm, figure 4.9 (e), and the 2nd absorption transition is the excitation of the undistorted arm, with a small contribution on the distorted, less planar arm, with an energy of 3.207 eV, figure 4.9 (f). The total cost of these two distortions is 30 meV and the resulting splitting is 5.9 meV. The third excited state in absorption (at about 3.28 eV), which is totally dark for the symmetric molecule, now carries some oscillator strength. However, it remains significantly darker than the two first quasi-degenerate transitions, with a transition dipole less than 2 eÅ (compared to more than 4.4 eÅ for the first two transitions). These splittings ensure that, when photo-excited with a spectrally narrow beam, on very short timescales after the initial excitation, the star-shaped molecules behave more like rod-like molecules rather than disk-like (with at least three-fold rotational symmetry) molecules and thus lead to an initial anisotropy value of 0.4. Due to the "defect-induced" finite energy splitting between excited states that are degenerate in the fully symmetric (C_3-symmetry) conformation of the molecules, only one of the two dipoles gets selectively excited by the spectrally narrow light beam. Then, in contrast to the fully symmetric case, the initial orientation of the transition dipole is to a large extent determined by molecular properties and spatial orientation of the molecules (as is the case for rod-like molecules) rather than the polarisation state of the light used for excitation (expected for molecules with C_3-symmetry and thus fully degenerate levels).

In the above discussion, based on cases A, B, and C of figure 4.9 we have reasoned that if exciting at low energy (long wavelength), predominantly those molecules of cases A and C get excited, where the lowest excitation possible is strongly localised on a single fluorene arm which was slightly planarised by introducing a "defect" (thermally induced in the real system at finite temperature). Thus the actual absorption in the sample corresponds mainly to cases (a) and (e) of figure 4.9. In those cases, the excited-state-geometry relaxation merely leads to further planarisation of the already more planar arm [163], as shown in figure 4.9. Thus, the excitation gets trapped on this particular arm where the initial excitation occurred. As a result, the rotation of the transition dipole due to the relaxation from the S_0 to the S_1 geometry is very small (calculated at 1.7° for case A, and 7.2° for case C). That is why at the lowest excitation wavelength, we experimentally observe an initial anisotropy of 0.4 (at time zero), exactly as for a rod-like molecule, and we hardly observe any contribution due to the fast decay of the anisotropy. This simple scenario changes when we excite at shorter wavelength (higher energy). In this case a new depolarisation mechanism comes into play, which is almost absent if exciting into the low-energy tail of the absorption (corresponding to the scenario discussed in the above). For higher excitation energy, a larger fraction of molecules gets excited in which the lowest excitation is extended over two arms of the molecule, as in figure 4.9 (c). In

addition, in those molecules, where the lowest excitation is predominantly localised on one arm only, the next higher-lying transition also gets excited, as in figure 4.9 (b) and (f). In both cases, when the molecule relaxes into its excited state equilibrium geometry, the excitation gets localised (trapped) on only one of the arms, as illustrated in figure 4.9. This process gives rise to significant and fast rotation of the transition dipole (our calculations giving 30.1°). The experimental data indicates that we observe this relaxation process, which manifests itself as rapid reduction of the total anisotropy in the sample at early times after the excitation process.

4.5.3 Slower depolarisation component

Now we turn our attention to the slow decay on the 5-8 ps timescale which we assign to resonant energy transfer between arms. We have calculated the time constant of Förster energy transfer between the branches in a weak coupling limit, using the equation presented in Chapter 1:

$$\frac{1}{\tau_{Förster}} = \frac{2\pi}{\hbar} g \left| sV \right|^2 \ , \tag{4.24}$$

where V is the electronic coupling energy between donor and acceptor chromophores and s is the dielectric screening of the interaction by the surrounding medium. g is a spectral overlap between the homogeneous spectral profiles of donor fluorescence $f^{hom}(E)$ and acceptor absorption $a^{hom}(E)$, which have each been normalised to unit area on an energy scale, $g = \int_0^{E_{max}} f^{hom}(E) a^{hom}(E) dE$ and E_{max} is the upper energy of the vibronic progression in $S_1 \leftarrow S_0$ absorption [43]. We use $s = 1/n^2$, where $n = 1.5$ is the refractive index of the solvent, which follows from the dipole approximation, and the measured steady state fluorescence and absorption spectral profiles assuming that homogeneous broadening dominates at room temperature.

The electronic coupling V can be determined using the DFT calculations. Indeed, in the ground-state geometry, each of the three arms is interacting with the other two. Each individual arm has an energy E_0 and interacts with a strength V. Therefore, the Hamiltonian of the system, H, is:

$$H = \begin{bmatrix} E_0 & V & V \\ V & E_0 & V \\ V & V & E_0 \end{bmatrix} \ . \tag{4.25}$$

We call ε_1, ε_2, ε_3 the three transition energies of the molecule. They are the eigenvalues of the Hamiltonian of the molecule, and the quantities calculated by quantum chemistry. We can easily calculate that $\varepsilon_1 = \varepsilon_2 = E_0 - V$ and $\varepsilon_3 = E_0 + 2V$.

Therefore V is determined as $V = (\varepsilon_3 - \varepsilon_1)/3$, where ε_1 and ε_3 are the transition energies from ground state to the lowest energy excited state S_1 and to the dark

state S_3 respectively calculated using DFT in the ground state geometry. These results are presented in table 4.3. These calculations predict $\tau_{Förster} = 15$ ps for the T2 molecule and $\tau_{Förster} = 8$ ps for the T4 molecule which are similar to the values we found for the slower depolarisation component. For comparison we also used a Förster point-dipole approximation to estimate $\tau_{Förster}$ with a point dipole being placed in the centre of each branch using:

$$k_{Forster} = \frac{1}{\tau_D} \frac{9000(\ln 10)\kappa^2 \phi_D I}{128\pi^5 N n^4} \frac{1}{R^6} \ , \tag{4.26}$$

where τ_D is the donor lifetime, ϕ_D is the fluorescence quantum yield, N is Avogadro's number, n is the refractive index, I is the spectral overlap and R is the centre-to-centre separation [43]. We observe in table 4.3 that this approach gives a similar value $\tau_{Förster} = 13$ ps for T2 but a much longer $\tau_{Förster} = 54$ ps for T4. The point dipole approximation underestimates coupling strength in T4, showing that for the chromophore size of four fluorene units and larger one has to go beyond the point dipole approximation.

Molecule	V (meV)	g (meV^{-1})	$\tau_{Förster}$ (ps)	τ_1 (ps)	τ_2 (ps)
T2	23 (25)	0.063	15 (13)	0.4	8.3
T4	25 (10)	0.10	8 (54)	0.5	5

Table 4.3: Coupling energies and exciton transfer rates. V is the electronic coupling calculated from the excited state splitting using DFT, g is the spectral overlap, $\tau_{Förster}$ is the calculated resonant energy transfer time and τ_1 and τ_2 are the experimentally measured decay times. The values in parenthesis are obtained using a point-dipole approximation.

4.6 Assignment of depolarisation processes

Above we have presented our experimental and theoretical results. The combination of both enables us to assign the depolarisation timescales observed to different physical depolarisation mechanisms. The 500 fs anisotropy decay and its dependence on excitation wavelength can be explained by a fast dipole reorientation because of adiabatic geometry changes within the molecules. In the case of a perfectly C_3-symmetric molecule, in a simplified manner, the excited state potential-energy surface (PES) resembles a so-called "Mexican hat" as depicted in figure 4.10 (a) (see reference [228] for general symmetry considerations). Excitation with high energy photons brings the system near the maximum of the PES (indicated by the red dot in the figure) and starting from this unstable situation the excitation can then take different relaxation pathways, down the potential energy hill which end in different equilibrium excited state geometries. For these equilibrium geometries the spatial orientation of fluorescence dipoles are very different as these are each oriented along

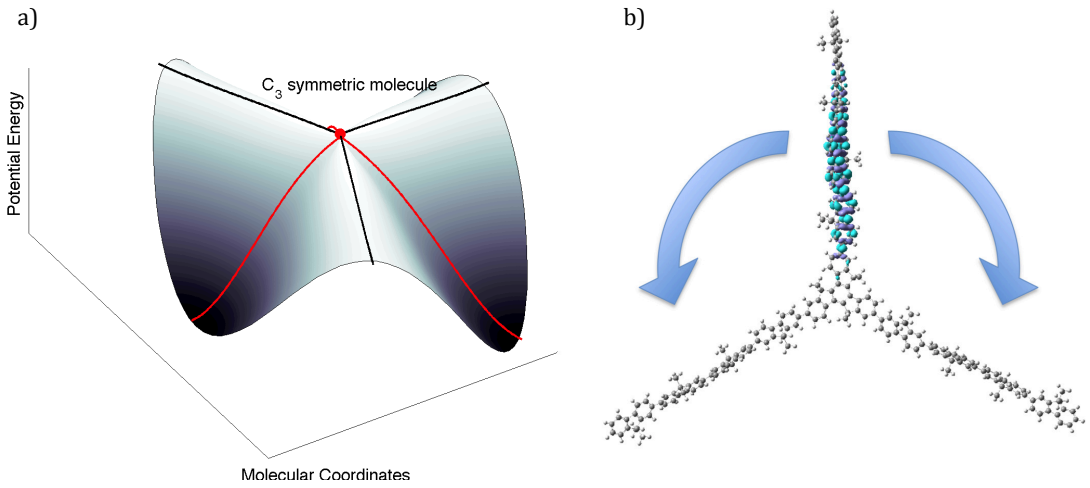

Figure 4.10: Illustration of the two mechanisms leading to the decay of polarisation anisotropy on two different timescales. Left: mechanism that explains the initial fast (500 fs) decay of polarisation anisotropy. Shown is a simplified illustration of the excited state potential-energy surface on which the initial relaxation takes place right after the excitation process. Right: illustration of the Förster-type hopping from arm to arm on a timescale of 4-8 ps.

one of the three arms of the molecule, thus, relaxation leads to depolarisation. For small initial distortions of the molecule from its perfectly threefold-symmetric geometry in the ground-state this picture still qualitatively holds and the relaxation on the nearly degenerate lowest excited-state potential energy surfaces still gives rise to fast de-polarisation (500 fs in our experiments). Excitation with low-energy photons populates the states closer to one of the potential energy minima, such that only one of the relaxation pathways is available for further geometrical relaxation. In this case the fast 500 fs process does not contribute to the depolarisation dynamics. A different mechanism is responsible for the slower decay in anisotropy (~ 5 ps timescale) and is attributed to Förster-type resonant energy transfer (RET) between different arms of a single molecule as illustrated in figure 4.10 (b) in good agreement with calculated transfer rates. Our results show that excitons are delocalised for about 500 fs in these materials which is about 10 times longer than previously observed in branched conjugated molecules based on amino-styrylbenzene dendrimer repeat units [65, 216]. Delocalised excitons can transfer energy to an acceptor faster and more efficiently. This property of branched oligofluorene materials in combination of their large molecular extinction coefficients can be used to design molecular systems to collect light and transfer its energy.

4.7 Conclusion

In this Chapter we have presented a combined theoretical study of ultra-fast fluorescence depolarisation and energy transfer in truxene-cored branched molecules

with oligofluorene arms, supported by experiments performed by our collaborators, and compared the observed dynamics with corresponding linear oligofluorenes. The anisotropy decay process is found to be bi-exponential with an initial fast 500 fs localisation followed by a slower 2-8 ps resonant energy transfer between branches. The fact that it takes 500 fs for exciton localisation to occur can be exploited in the design of new antennae for efficient light harvesting.

The initially observed polarisation anisotropy value of 0.4 suggests a thermally induced small symmetry breaking in these nominally symmetric molecules. Calculations based on density-functional theory confirm that in solution there is enough thermal energy at room temperature to create a splitting of greater than 5 nm between the two nominally degenerate lowest optical transitions which allows for their selective excitation with spectrally narrow light pulses. Our experimental and theoretical data indicate that after photo-excitation the molecules undergo a two-stage relaxation energy transfer process. A fast decay of polarisation anisotropy is found on a 400-500 fs timescale and is attributed to a fast initial relaxation within the nearly degenerate potential energy surfaces of the lowest excited states. The relative strength of this process is larger for shorter wavelength excitation, and is explained by calculations of the excitations generated. The second process is an excitation-energy independent 5-10 ps decay which we attribute to resonant energy transfer between different arms of a single molecule. Our results show that oligofluorene-based materials can support long-lived delocalised excitons which may mediate efficient energy transfer.

We have so far considered exciton migration in solutions of fluorene based molecules. However, understanding exciton dynamics processes in films of such molecules is also of theoretical and practical importance. First, a reliable model for chromophore interaction is necessary before any further exciton dynamics can be modelled in a closely packed ensemble of molecules, such as in films. This is the subject of the next Chapter.

Chapter 5

Dipole approximations to calculate intermolecular interactions

In this Chapter we examine the use and limits of transition dipole theory, both point- and line-dipole models (used to quantify Förster hopping rates). We then compare their results with related sets of quantum chemistry calculations for interacting molecules. We demonstrate that the line-dipole model breaks down for long molecules at separations typical of organic thin-films, whatever the number of sub-dipoles used. Finally, we present an improved way of distributing the sub-dipole moments of the line-dipole that overcomes the limits of the usual line-dipole approximation, providing excellent agreement with the quantum chemistry benchmarks.

5.1 Introduction

We have so far investigated excitonic transfer in fluorene-based molecules in diluted solutions only. However, organic semiconducting thin-films are widely used in electronic devices such as displays, solar cells, lasers and LEDs. Quantifying the interactions between excitations in organic chromophores in such thin-films is key to optimizing the performance of these devices [12, 79, 102, 229]. It has long been appreciated that the dominant inter-molecular interaction of excitations arises from a dipole (Förster) coupling [44, 230–232].

Due to the complex morphology of the thin films used in such applications [233, 234] it is also crucial to be able to model this dipole coupling on the basis of a simple dipole-dipole interaction model rather than using an *ab initio* quantum chemical method for the whole sample [51,235]. With this in mind, it is interesting to ask what the range of validity is of such dipole-dipole models and how the dipole moments and intermolecular distances can be related to quantum chemistry calculations whilst retaining an accurate description of the interaction. The influence of the geometric configurations of two molecules has been explored through quantum chemistry [236–239], but to the best of our knowledge, the limits of the line-dipole model have never been explored in depth.

This knowledge is a necessary basis for the development of the exciton dynamics model that we present in Chapter 6, and will also enable future studies which explore the effect of morphology and phase aggregation on organic thin films. It will also underpin dynamics studies in relatively large systems, for example, using a quantum

Monte-Carlo approach [132–134], or within the Ehrenfest approximation [135, 136].

We study in this Chapter the modelling of interactions between oligofluorene molecules, as, *in fine*, we aim at modelling excitation dynamics in fluorene-based thin-films (Chapter 6). We have demonstrated in Chapters 2 and 3 that density-functional theory (DFT) and time-dependent DFT (TD-DFT) provide an accurate photo-physical description of isolated oligofluorenes. In the present study we also show that it can be effectively used to calculate the transition dipole-dipole interaction energy between pairs of fluorene molecules. In this Chapter we start by comparing these results with simpler dipole-dipole interaction models where we analyse in detail the effect of the relative orientation of the two transition dipoles and their relative distance as well as changing the number of sub-dipoles within the line-dipole approach [238, 239]. We show that the line-dipole model does not perform as well as expected and propose a new alternative dipole model.

5.2 Background: dipole models

In the following Section we investigate the interaction energy between two transition dipoles located on a pair of neighbouring linear chromophores. This interaction energy is, for example, a crucial ingredient in the calculation of resonant energy transfer efficiency between the two molecules in a Förster-type transfer picture [44]. In bulk polymer systems bimolecular interactions occur between molecules with all possible relative orientations. A direct way to calculate the interaction energy between transition dipoles in the two molecules would be to calculate the transition densities of the respective transition in each molecule and then to compute the Coulomb interaction between these two transition charge densities [38, 51, 235, 237, 240, 241]. This approach is accurate and intuitive but it is also computationally very expensive [238] and difficult to apply to a large number of different molecular orientations, as may be needed for the microscopic modelling of truly extended multi-chromophoric systems. For this purpose it would be desirable to have a simpler phenomenological approach that still allows a sufficiently reliable prediction of inter-molecular interaction energies.

The simplest such model is obtained when the inter-molecular interaction is treated as the interaction between two point dipoles. The point dipoles then carry the total respective transition dipole of molecules A and B, $\boldsymbol{\mu}_A$ and $\boldsymbol{\mu}_B$, and the relative distance is given by the centre-to-centre separation, $\boldsymbol{d}_{AB}$, of the two molecules. The interaction energy is then:

$$E_{\mathrm{PD}} = \frac{\boldsymbol{\mu}_A \cdot \boldsymbol{\mu}_B}{|\boldsymbol{d}_{AB}|^3} - 3\frac{(\boldsymbol{\mu}_A \cdot \boldsymbol{d}_{AB})\,(\boldsymbol{\mu}_B \cdot \boldsymbol{d}_{AB})}{|\boldsymbol{d}_{AB}|^5}\,. \tag{5.1}$$

Whilst easy to evaluate, this approximation breaks down, and over-estimates the interactions [242], when the separation of the molecules is of the order of their length or smaller. This limits the applicability of the point dipole approximation to dilute molecular systems, a limit that is typically not fulfilled, for example, in organic thin-films.

In a typical fluorene film [234], the mass density is of the order of 1 g/cm^3, which, assuming an isotropic distribution, implies an average intermolecular separation of 1.7 nm. This is significantly smaller than the ~ 6.8 nm length of the O8 chromophore so such an isotropic morphology is over-simplified. If we assume that molecules are all lying parallel to the $x-y$ plane and arranged in parallel lines, sited on a square lattice, the square lattice spacing is 0.9 nm. Therefore, for such a system, we would not expect the point-dipole approximation to give accurate results. In what follows, we use the point-dipole model only as a reference at large inter-molecular separation.

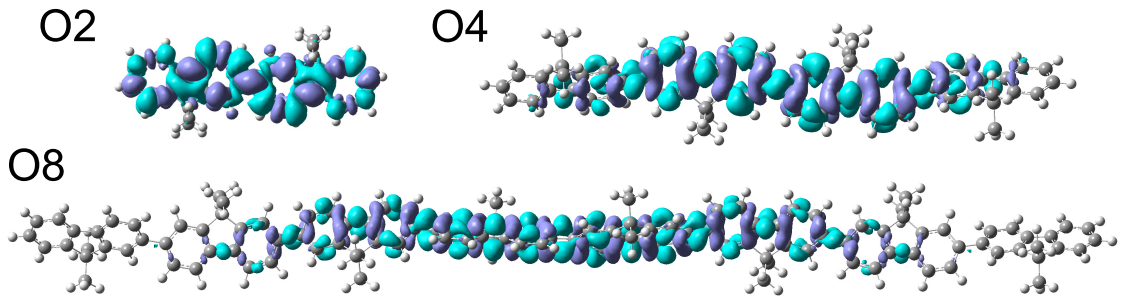

Figure 5.1: Shown is the change of charge density upon photon absorption in the fluorene dimer, O2, quadrimer, O4, and octamer, O8, respectively. Note that for O2 the absorption takes place over the whole molecule, whereas for O8 it takes place on about six fluorene units only.

A more accurate approximation has been applied to polythiophenes [238]. Each of the molecular transition dipoles $\boldsymbol{\mu}_A$ is replaced by N weaker sub-point-dipoles $\boldsymbol{\mu}_{A_i}$, arranged along the backbone of the linear molecular chains. The inter-molecular interaction energy is then given by:

$$E_{\mathrm{LD}} = \sum_{i,j}^{N} \frac{\boldsymbol{\mu}_{A_i} \cdot \boldsymbol{\mu}_{B_j}}{|\boldsymbol{d}_{A_i B_j}|^3} - 3\frac{(\boldsymbol{\mu}_{A_i} \cdot \boldsymbol{d}_{A_i B_j})(\boldsymbol{\mu}_{B_j} \cdot \boldsymbol{d}_{A_i B_j})}{|\boldsymbol{d}_{A_i B_j}|^5} \,. \tag{5.2}$$

For the lowest optical transition from the ground-state, the sub-dipole moments are modulated with a sinusoidal distribution [238]. Taking $i = 1$ at one end of the molecule, to $i = N$ at the other end, we then have:

$$\boldsymbol{\mu}_{A_i} = \frac{\sin\left(\frac{i\pi}{N}\right)}{\sum_j \sin\left(\frac{j\pi}{N}\right)} \quad \boldsymbol{\mu}_A \,, \tag{5.3}$$

with $\sum_i^N \boldsymbol{\mu}_{A_i} = \boldsymbol{\mu}_A$ by construction. This approach has been successfully applied

to estimate incoherent (Förster) transfer rates, for instance in polythiophene solutions [242] or in supramolecular nanoassemblies [134]. The total length, L, of the interacting dipoles can be roughly estimated from the spatial extent of the chromophores studied. However, more accurately, it should be related to the actual spatial extent of the electronic transition induced. An example of the change in electronic density induced in a series of fluorene molecules upon photo-excitation from the S_0 to the S_1 electronic state is shown in figure 5.1. For instance, the change in density in the octamer, O8, is extended over about six fluorene units which gives a rough estimate of the relevant total dipole length associated with this excitation. This estimate is in good agreement with the value extracted from more detailed quantum chemistry calculations as discussed below.

5.3 Method: calculation of interaction energies by quantum chemistry

In order to quantify the intermolecular interaction from first principles, we have performed TD-DFT calculations of the electronic excitations in a pair of two spatially close molecules. As a specific example, we study pairs of interacting fluorene oligomers. These molecules can, for example, serve as efficient emitters in a variety of devices, and they have been extensively studied in the recent past [171] such that their single-molecule properties are rather well understood. We have investigated in detail the interaction between short fluorene dimers, O2, and longer fluorene octamers, O8. Previous studies have shown that eight fluorene units roughly correspond to the observed conjugation length in fluorene oligomers [163] and with this should also represent typical properties of chromophores in polyfluorene chains reasonably well.

In the calculations, we place two identical oligomers close to each other (cf. figure 5.2) and compute the lowest excitation energies from the electronic ground state. The mutual interaction of the two molecules leads to a splitting of the lowest transition energies compared to the transition energies obtained for each of the molecules independently. This splitting between the two lowest transitions can be identified as twice the inter-molecular interaction strength [182,238]. This condition holds provided all other significantly bright transitions are far off resonance (on the energy scale of the interaction strength, which is the case here). In terms of coupled oscillators, the eigenvalues of the Hamiltonian matrix are $E = E_{\text{single}} \pm E_{\text{int}}$, where E_{single} is the oscillator energy (transition energy) of a single, isolated molecule and E_{int} the interaction energy between the two interacting oscillators (molecules).

To calculate the lowest optical transitions in single molecules and in the coupled molecular system, we use linear response time-dependent density-functional theory (TD-DFT) with the B3LYP functional and 6-31G basis set, which have pre-

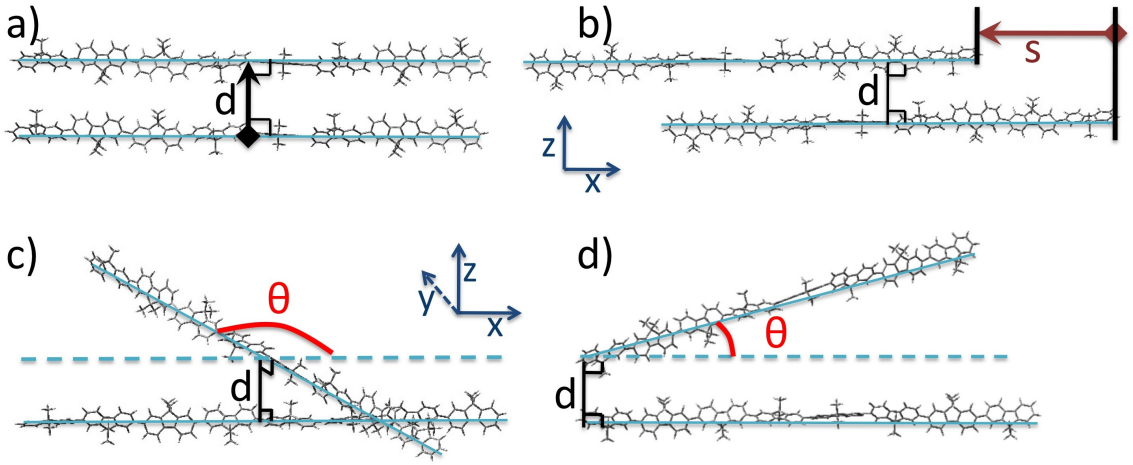

Figure 5.2: Schematic of coupled fluorene octamers with different relative distances and orientations. In (a), the two molecules are parallel. (b) is same as (a), but with a translation of the molecular centres by s as indicated. In (c), both molecules lie in the xy plane, with their centres separated by a fixed distance d, and a variation in the angle of rotation θ about the molecular centres. In (d), both molecules also lie in the xy plane and a variation in the angle of rotation about the end of the molecules, θ, is indicated.

	Physical Length (nm)	Dipole Length L (nm)	Dipole moment μ (eÅ)
O2	1.7	1.5	1.97
O4	3.3	2.8	3.13
O8	6.8	5.7	4.66

Table 5.1: Parameters for the three oligomers of different lengths as used in the dipole-dipole modelling. Details for the fluorene dimer, O2, and octamer, O8, are discussed in the text. Parameters for the quadrimer, O4, are included for comparison.

viously been shown to perform well for prediction of transition energies and oscillator strengths of oligofluorenes. [163] The molecular geometries have been optimized for each molecule in the electronic ground state separately, only the transition energies are calculated for the coupled system. The optimized geometries have finite dihedral angles between adjacent fluorene units (corresponding to the fluorene α-phase) and the conformation is such that the sign of dihedral angles alternates while going along the chain.

From the TD-DFT calculations for the coupled system, we extract the interaction energy as explained above from the splitting of the two lowest transitions. We then compare the results obtained from the full quantum chemistry calculations, with the interaction energies obtained from the simplified dipole-dipole interaction models to assess their accuracy and applicability. The value used for the total transition dipole moment of each molecule is taken directly from the TD-DFT calculations for a single molecule. Values obtained are summarized in Table 5.1. We obtain the length of the dipole, L, needed in the line-dipole model by fitting the calculated line-dipole interaction energy to the interaction calculated by quantum chemistry

for parallel molecules (figure 5.2(a)) at medium-range separation (d between 1 and 2 nm for O2 and between 3 and 5 nm for O8). As expected, these values are slightly smaller than the overall length of the molecules and are also consistent with the spatial extent of the transition density shown in figure 5.1.

In molecular systems of practical interest, bimolecular processes are (in a Förster-type picture) mediated by interaction matrix elements of the type discussed above. However, typically the interaction is between different molecular states (as in e.g. exciton-exciton annihilation processes), or between absorption and emission dipoles of molecules (as in excitation transfer where one emission dipole and one absorption dipole contributes), or even between different molecular species.

However, in the quantum chemical approach discussed above, the interaction energy can only easily be identified in the symmetric case when both molecules are identical. This is why here all the calculations are performed for the absorption (S_0) geometries of the two molecules. By comparing with this symmetric scenario, we will learn how a simple dipole-dipole model can be applied to accurately predict interaction energies between two line dipoles.

After we have identified the limitations of these simpler models, they can then be reliably applied to more complicated scenarios of interest. In the following Section, we will show that even the line-dipole approximation described above breaks down in some of the scenarios discussed such that it can not safely be used to predict interaction energies in certain parameter ranges. To resolve this issue, we then propose an improved model which gives good agreement with the quantum chemistry in all scenarios studied.

5.4 Results and discussion

In the following we analyse in detail the interaction energy between two identical fluorene oligomers. In figure 5.2, the various different scenarios for the relative orientation of the two molecules we consider are defined. One molecule is fixed in space with the molecular backbone along the x-axis. The other molecule, whose position is being varied, always lies in the $x-y$ plane without loss of generality. These configurations are particularly relevant in the case of spin-coated films, where the molecules lie in parallel planes. The distance between the two molecules is d, and the angle between the two molecules, in the $x-y$ plane, is θ, independent of the centre of rotation. In figure 5.2(a) and (b), we have $\theta = 0$ whereas in cases (c) and (d) $\theta \neq 0$. In case (b), we shift the centre of one molecule by the distance s on the x-axis. The rotation in case (c) is around the centre of the molecule, whereas in case (d), it is around one end of the molecules. Below, we study two different molecular lengths in detail (fluorene dimer and octamer). We complement these two

limiting cases of *short* and *long* molecules with additional modelling parameters for the intermediate case of a fluorene quadrimer (cf. figure 5.1 and table 5.1).

5.4.1 Short molecules – the O2 dimer

We first present results for a short molecule, O2, the oligomer made of two fluorene units where at all but the closest separations we expect the point dipole approximation to work reasonably well.

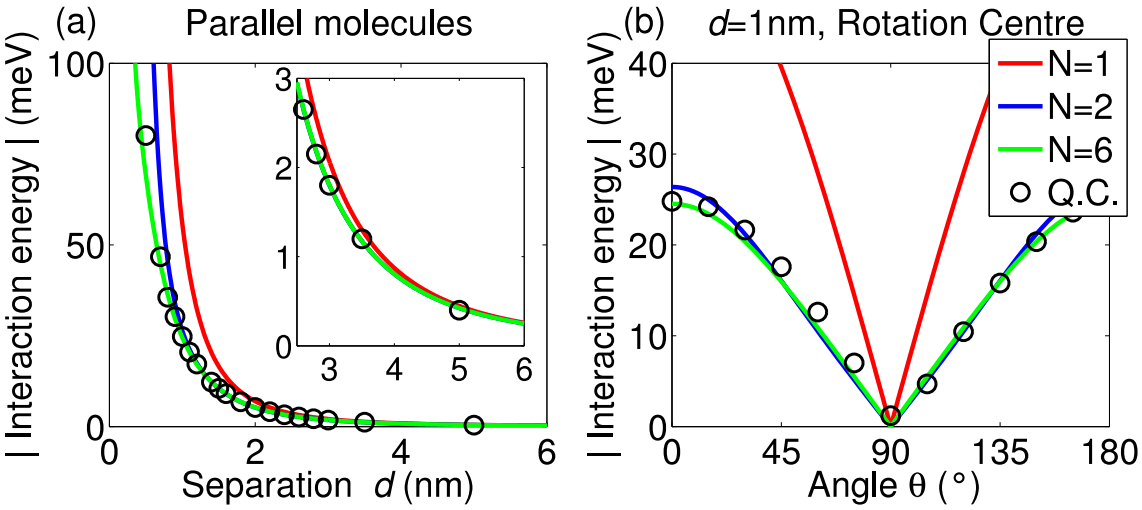

Figure 5.3: The O2 interaction energies obtained by the point and line-dipole approximations are compared to the TD-DFT (Q.C.) results. The two line-dipoles lie in parallel planes with N sub-dipoles per line: (a) for parallel dipoles as a function of the separation, d, between the two line-dipoles [figure 5.2(a)] and (b) as function of θ when $d = 1\,\text{nm}$ (figure 5.2(c)). The inset (magnification of the graph (a) for $2\,\text{nm} < d < 6\,\text{nm}$) shows the very good agreement of all the different approximation schemes for separations $d > 2.5\,\text{nm}$.

In figure 5.3(a) the effect of varying the separation between the two parallel molecules [cf. figure 5.2(a)] on the interaction strength is shown. At separations $d > 0.5\,\text{nm}$ a line-dipole with only two sub-dipoles is sufficient to obtain excellent agreement between the splittings calculated by quantum chemistry and the line-dipole interaction energy, with the average discrepancy being 2% in the case of six sub-dipoles. Fluorene molecules have a finite width of around 0.25 nm and cannot be closer than this. As expected, at large separations ($d > 2\,\text{nm}$) even the point-dipole approximation is excellent.

In figure 5.3(b) we show the interaction energy for two molecules lying in parallel planes separated by $d = 1\,\text{nm}$, with a rotation angle θ around their centres, as described in figure 5.2(c). At this relatively small separation the line-dipole approximation works well at all angular orientations for line-dipoles made of at least two sub-dipoles (the average error is 3.3% in the case of six sub-dipoles). The point-dipole approximation, $N = 1$, is poor for all non-perpendicular angles. For perpendicular orientation ($\theta = 90°$) the interaction strength within the line- (and

point-) dipole approximation is strictly zero. In the quantum chemistry calculations it shows some very small residual interaction due to the finite width of the molecule (which is not taken into account in the simpler models).

The overall good performance of the line-dipole approximation demonstrated above clearly shows that it is quite safe to model interactions of neighbouring fluorene dimers (even at small separations as in thin films) using a simple line-dipole approach. We now turn our attention to a more challenging case, molecules significantly longer than their separation.

5.4.2 Long molecules – the O8 octamer

Figure 5.4 shows the interaction energy between two fluorene octamers, O8, aligned in a parallel configuration as depicted in figure 5.2(a). We note that the

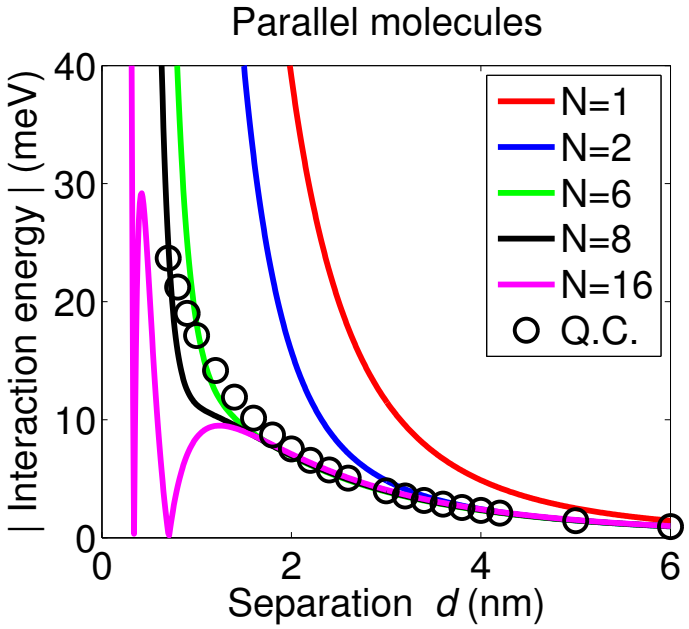

Figure 5.4: The O8 interaction energy obtained by the point and line-dipole approximations are compared to the TD-DFT results. The two parallel line-dipoles lie in parallel planes with N sub-dipoles per line as a function of their separation, d (figure 5.2(a)).

minimum separation for which it was possible to unambiguously extract the intermolecular interaction energy from the quantum chemistry calculations was ~ 0.8 nm. For separations smaller than this, the structure of electronic transitions started to deviate significantly from a simple dipole-dipole interaction picture of the two molecules. This aspect might be worthwhile studying in more detail in future work.

For the longer O8 molecules, the point-dipole approximation clearly breaks down at separations less than ~ 5 nm (to be compared with the length of the chromophore dipole at 5.7 nm).

At separations larger than 1 nm, good agreement, having an average discrepancy of 5%, with the quantum chemistry is found when the line-dipole is made of six sub-dipoles. However, at smaller separations and when the number of sub-dipoles per line is at least sixteen, we observe a change of sign of the O8 interaction energy and correspondingly a very poor prediction of values for the interaction strength. (Note that in the figure we compare the absolute values of the interaction energy). The origin of this sign change lies in the change in dominant character of the dipole interaction from repulsive to attractive and can be understood as follows. From equation (5.2) it is clear that two parallel dipoles [configured as in figure 5.2(a)] will experience a repulsive interaction ($E_{LD} = \boldsymbol{\mu}_A \cdot \boldsymbol{\mu}_B / |\boldsymbol{d}_{AB}|^3$), whereas two parallel dipoles arranged end on will experience an attractive interaction ($E_{LD} = -2\boldsymbol{\mu}_A \cdot \boldsymbol{\mu}_B / |\boldsymbol{d}_{AB}|^3$).

Physically this attraction arises from the dominant contribution of the two nearest ends of the dipoles which are oppositely charged. Considering now the line dipole approximation as used in figure 5.4, at small separations with many sub-dipoles, the unphysical switch to an attractive interaction arises from the large number of sub-dipole pairs which are aligned almost end on. Clearly, real molecules do not possess such a series of very small sub-dipoles such that modelling with very small sub-dipoles does not reflect the interactions between the molecules in a physically meaningful fashion. We find that this sign-change behaviour limits the applicability of the usual line-dipole approximation as for small inter-molecular distance with increasing number of sub-dipoles convergence is not reached at the correct interaction strength.

In figure 5.5, the separation, d, between the molecules is fixed at 1 or 2 nm, respectively, with a rotation of angle θ either about the centre or the end of the molecules.

Seen from above, this results in a +-shaped or an L-shaped configuration, respectively (cf. figure 5.2(c) and (d)).

We observe that when the separation between the molecules is large (2 nm), then the quantum chemistry and dipole-modelling agree well, as long as we use more than six sub-dipoles. This is also true for rotation around the end of the molecule. At smaller separation (1 nm), for line-dipoles made of about six sub-dipoles, the results agree qualitatively for both rotations, but not quantitatively for the rotation about the centre. The latter represents the configuration for which the molecules are closest to each other, such that clearly the limit of the dipole-modelling is reached. In this case all the dipole results are relatively far from the quantum chemistry results. At $d = 1$ nm, it is clear that the line-dipole model starts losing its validity with worsening quantitative agreement for increasing number of sub-dipoles.

Finally, in figure 5.6, the molecules are parallel ($\theta = 0$), but the centre of one molecule is shifted with respect to the centre of the other molecule by a distance,

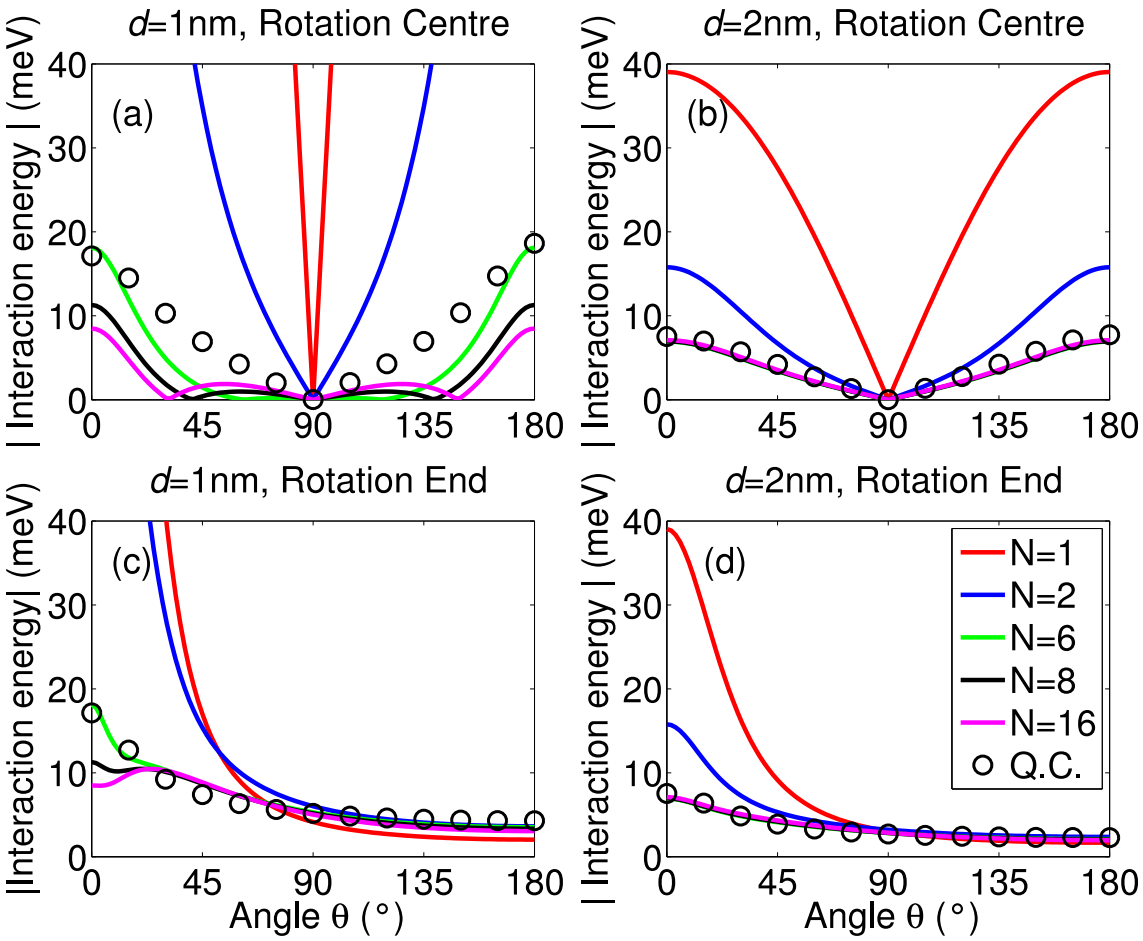

Figure 5.5: Comparison of the O8 interaction energy obtained by the line-dipole approximation with the quantum chemistry results, for a range of number, N, of sub-dipoles per line-dipole, with the two line-dipoles lying in parallel planes, separated by either $d1$ nm - (a) and (c) - or $d = 2$ nm - (b) and (d) - , and as a function of θ, which denotes the angle of rotation around the centre of the molecules -(a) and (b) [cf. figure 5.2(c)]- or around the end of the molecules - (c) and (d) [cf. figure 5.2(d)].

s, along the molecular length as sketched in figure 5.2(b). The quantum chemistry results give a smooth trend for the interaction energies with a change in sign as the shift reaches about half the chromophore length at ~ 3 nm. The reason again is that the molecules are getting almost aligned on the same line when the shift of the centre becomes large enough. This is consistent with previous calculations presented for OP and OPV molecules, where the transition from H-aggregates to J-aggregates occurs when the shift becomes bigger than half the length of the chromophores. [237]

The results for the dipole modelling are very different depending on the number of sub-dipoles used (they reach convergence at about 16 sub-dipoles). More importantly, however, for a smaller number of sub-dipoles, e.g. for 6 or 8 sub-dipoles, which gave good results for the scenarios studied in figures 5.4 and 5.5, the predicted interaction energies undergo unphysical oscillations and changes in sign (again, the absolute value is plotted). With an average deviation from the quantum chemistry

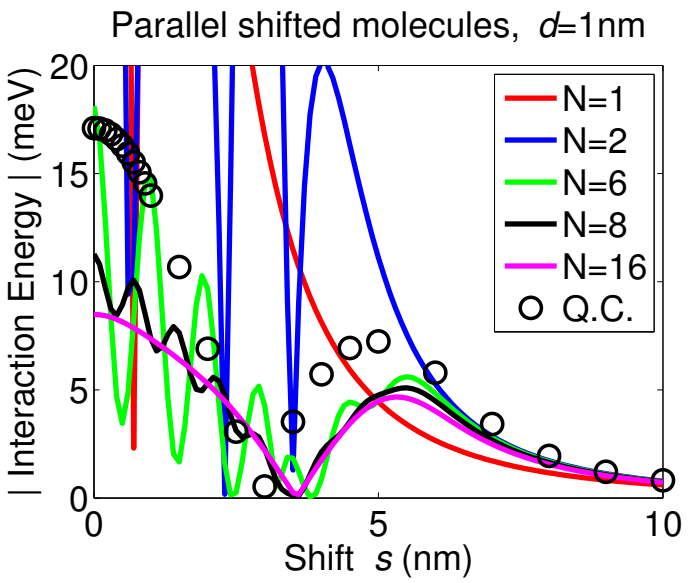

Figure 5.6: Comparison of the O8 interaction energy obtained by the line-dipole approximation with the quantum chemistry results, for a range of number N of sub-dipoles per line-dipole, with the two parallel line-dipoles, separated by 1 nm, as function of the shift s between the two molecules (as in figure 5.2(b)).

of 23% for six sub-dipoles, these results are in poor agreement with the quantum chemistry. The source of these oscillations is rooted in the discrete character of the line-dipole when the number of sub-dipoles is too small. As we shift one line made of discrete sub-dipoles, the interaction between the sub-dipoles of the two lines varies considerably. For instance, if two sub-dipoles, aligned in the same direction, are on top of each other, the interaction between them will be repulsive.

However, if we shift one of these two sub-dipoles by half of the length of the sub-dipoles, the dominant interaction will become much smaller, before increasing again as we shift again by half the length of the sub-dipoles. These oscillations disappear when the lines are made of many sub-dipoles, because the line of sub-dipoles is continuous again. This mechanism is illustrated in figure. 5.7. In the O8 molecules, the excitation is localized on approximately six fluorene units, as shown in the transition density plot of figure 5.1. The results obtained so far for O2 and O8 indicate that the optimal number of sub-dipoles to use for the usual line-dipole approximation is roughly the number of active monomer units (apart from the scenario studied in figure 5.6). Nevertheless the interaction energies calculated with this line-dipole do not always give results in good agreement with the quantum chemistry and can sometimes cause unphysical artefacts, as in figure 5.6. For the results in figure 5.6 this can partly be fixed by introducing more and more sub-dipoles. On the other hand, however, the number of sub-dipoles needed in figure 5.6 does not agree with the number of sub-dipoles giving good results and physical

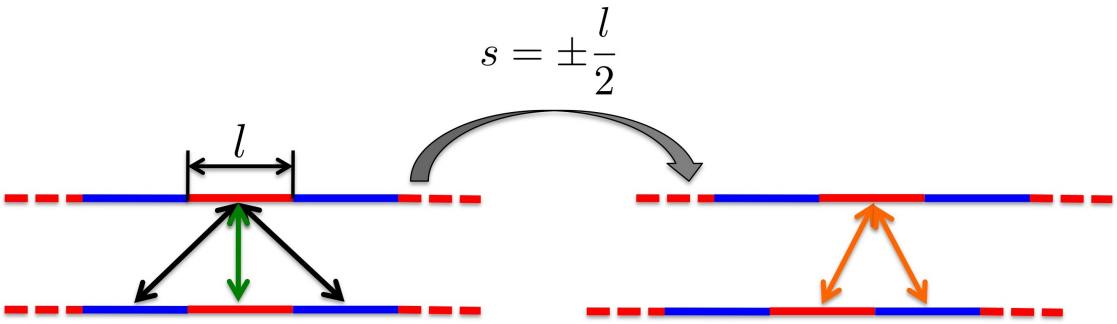

Figure 5.7: Illustration of the origin of the oscillations in the interaction of figure 5.6. With no shift (left), the strongest interaction between sub-dipoles is given by the green arrow. l is the length of the sub-dipoles. If we shift one molecule by $l/2$ (right), then the interaction between the sub-dipoles is strongly reduced as the strongest one is now given by the orange arrows. If we shift again the molecule by a half of the length of the sub-dipoles, we are back to the situation with strong interactions (left) (neglecting end effects).

meaningful behaviour in figures 5.4 and 5.5. Unfortunately, this dilemma can not be fixed for the system parameters studied here at distance of ~ 2 nm or below. This severely limits the applicability of the usual line-dipole approximation to situations of great interest, e.g. thin films made from polyfluorene or other materials where extended chromophores are densely packed. In the following Section we propose an improvement of the usual line-dipole approximation that resolves this issue.

5.5 An improved line-dipole approximation

Above we have demonstrated that the line-dipole approximation in its usual form [238, 242] does not always give physically meaningful results for extended chromophores at separations smaller than their length, as is typically the case in thin films. In this Section, we develop a slightly different formulation of the line-dipole approximation designed to resolve these issues. We then show that this new approximation scheme can safely be applied to calculate interaction energies also in molecular systems with extended chromophores that are densely packed.

Instructed by the structure of the density changes upon photo-excitation as shown in figure 5.1, we modify the line-dipole approximation [equations (5.2) and (5.3)], such that we introduce additional nodes to the distribution of sub-dipoles along the backbone of the molecule, as shown in equation (5.3). The new formulation for the distribution of sub-dipoles then reads:

$$\boldsymbol{\mu}_{A_i} = \frac{\left|\sin\left(\frac{iP\pi}{N}\right)\right|}{\sum_j \left|\sin\left(\frac{jP\pi}{N}\right)\right|} \; \boldsymbol{\mu}_A, \tag{5.4}$$

where P is the number of antinodes of the distribution function. In the following

we demonstrate that this new approach more accurately represents the nature of the transitions as unphysical behaviour even at small inter-molecular distances can completely be avoided if applied correctly.

For the example of a fluorene octamer O8, in figure 5.8(a), we identify about five microscopic dipoles per fluorene unit (the figure shows a magnification of the centre of the fluorene octamer in figure 5.1). Guided by this observation, with the

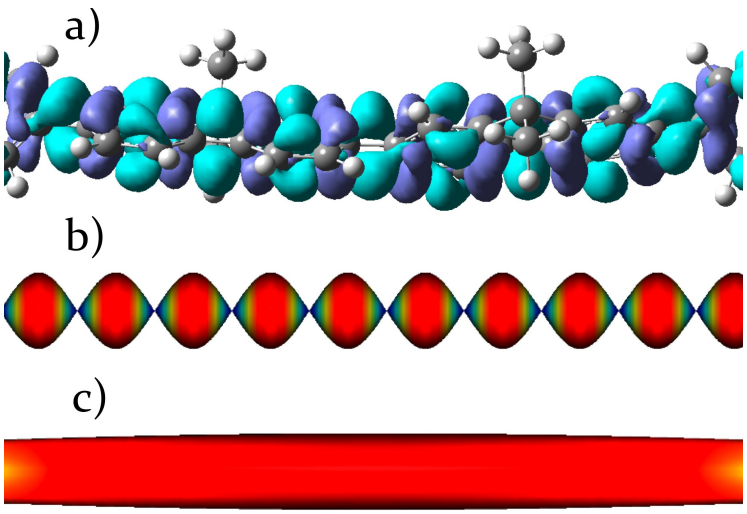

Figure 5.8: (a) Magnification of the two central fluorene units in O8 of the transition density plot (figure 5.1). (b) Corresponding part of the sub-dipole distribution of the associated line dipole representation with the improved model ($P = 30$). The red parts have a high dipole moment, the blue parts a low one. The sub-dipole bumps mimic the distribution of pairs of negative and positive charges on the molecule. (c) Corresponding part of the sub-dipole distribution of the associated line dipole representation with the usual model.

excitation being extended over about six fluorene units in O8, we would expect that inclusion of about thirty antinodes in the dipole distribution of the line-dipole approximately reflects the nature of this transition. A part of such a line-dipole is illustrated in figure 5.8(b): roughly each pair of negative and positive charges in space is associated with a maximum of the sub-dipole distribution. To highlight the difference in construction, this is compared with the usual line-dipole approximation in figure 5.8(c), where there is just a continuum of sub-dipoles representing about the same total dipole moment. The results discussed in the following clearly show that the microscopic physics of the actual charge distribution is mimicked more accurately by our new line-dipole approach. In the following, we chose to include $N = 50$ sub-dipoles and vary the number of antinodes P in the distribution function to study its influence on the results.

Figure 5.9 shows the results for varying separation, d, in the parallel molecule case, as studied before in figure 5.2(a). We notice, as expected, that the cases $P = 1$ and $P = 50$ approximately correspond to the case of the usual line-dipole

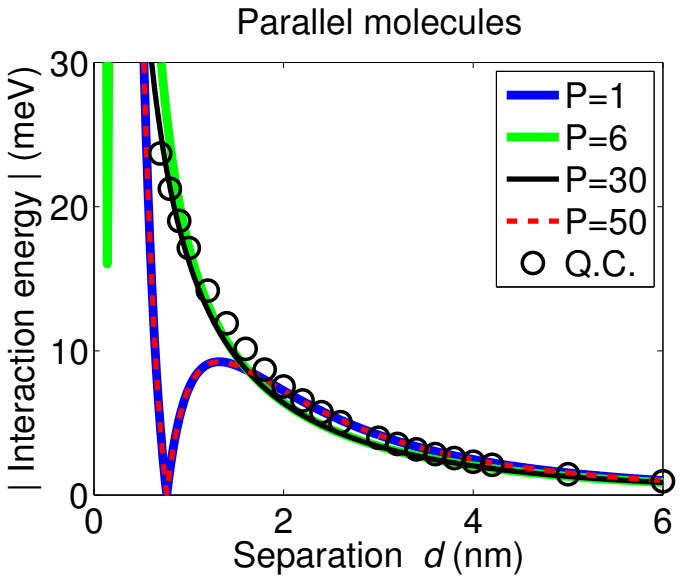

Figure 5.9: Results for O8, in the case of figure 5.2(a) (parallel molecules), for a series of number of antinodes P in the distribution of sub-dipoles. The line-dipoles are made of $N = 50$ sub-dipoles each, therefore $P = 1$ corresponds to the usual line-dipole approximation.

approximation. The results for $P = 6$ and $P = 30$ are essentially identical, and we do not find the unphysical change of sign at $d \approx 0.8$ nm any more (in the case of $\theta = 0$). This indicates that the results are quite insensitive to the exact number of nodes included.

These results are now only 2.6% away on average from the quantum chemistry results, in good agreement over the full range of values of d studied, including those small values of d where the usual line-dipole approximation failed - the largest error is now only 6%, compared to more than 80% previously. In figure 5.10, results are presented for the rotation around the centre - (a) and (b) - and the end - (c) and (d) -of the molecules (cf. figure 5.2(c) and (d)), respectively, for the case where the molecules are separated by $d = 1$ nm - (a) and (c) - and $d = 2$ nm - (b) and (d). The results for $P = 6$ and $P = 30$ show much better agreement with the quantum chemistry than any of the energies obtained previously with the usual line-dipole approximation. Good agreement is reached for all angles, with a maximum error of 15%. Figure 5.11 displays the result for a shift s between the two parallel molecules (cf. figure 5.2(b)). The unphysical oscillations observed previously when the number of sub-dipoles was too small are eliminated (cf. figure 5.6), and the results for $P = 6$ and $P = 30$ are now in good agreement with the quantum chemistry, with the average error being now only about 12%.

The results shown in figures 5.9 to 5.11 clearly demonstrate the strength of our new formulation of a line-dipole approximation. In particular, we show that it can be applied to scenarios where the usual line-dipole approximation led to

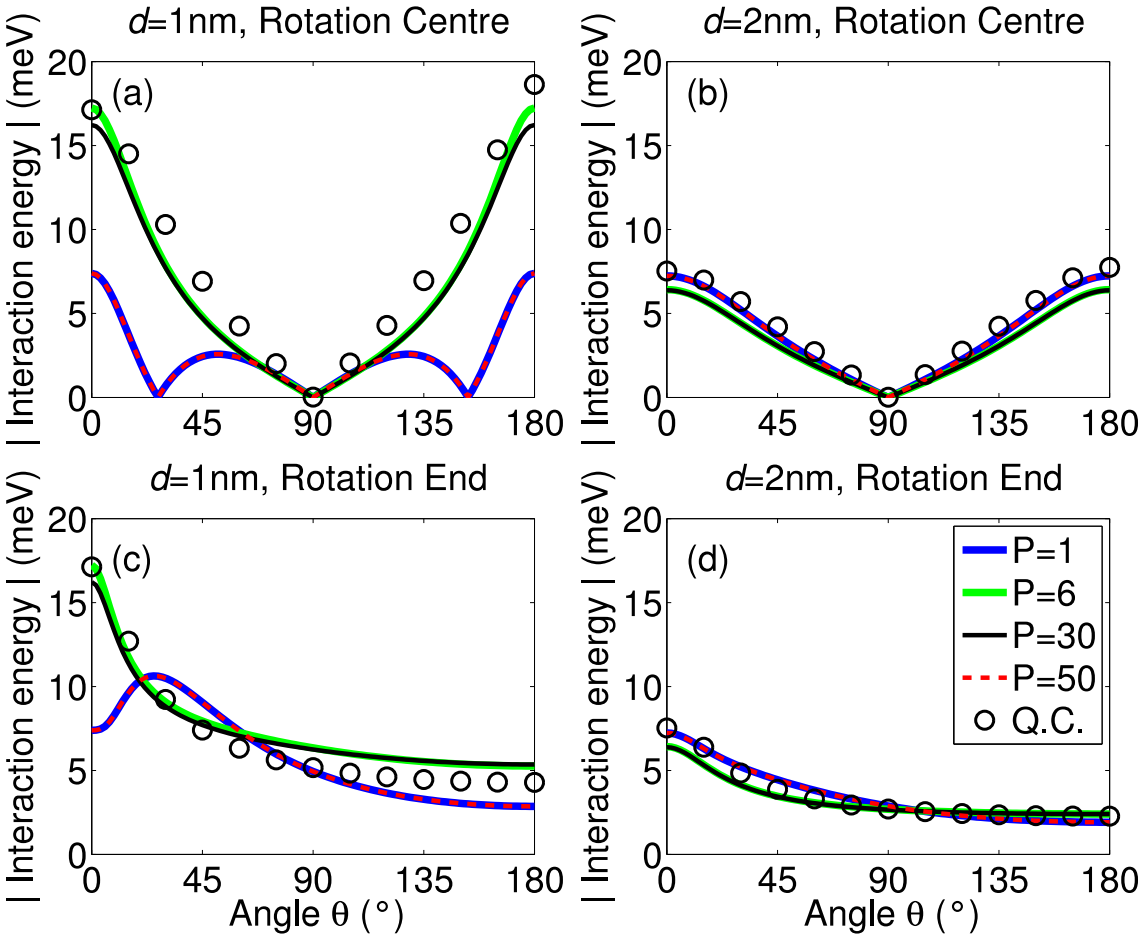

Figure 5.10: Results for O8, in the case of figure 5.2(c) and case of figure 5.2(d) (rotation around the centre - (a) and (b) - or around the end - (c) and (d) -, for a set of different numbers of antinodes P in the distribution of sub-dipoles. Here either $d = 1$ nm - (a) and (c)- or $d = 2$ nm - (b) and (d). The line-dipoles are made of $N = 50$ sub-dipoles each, therefore $P = 1$ corresponds to the usual line-dipole approximation.

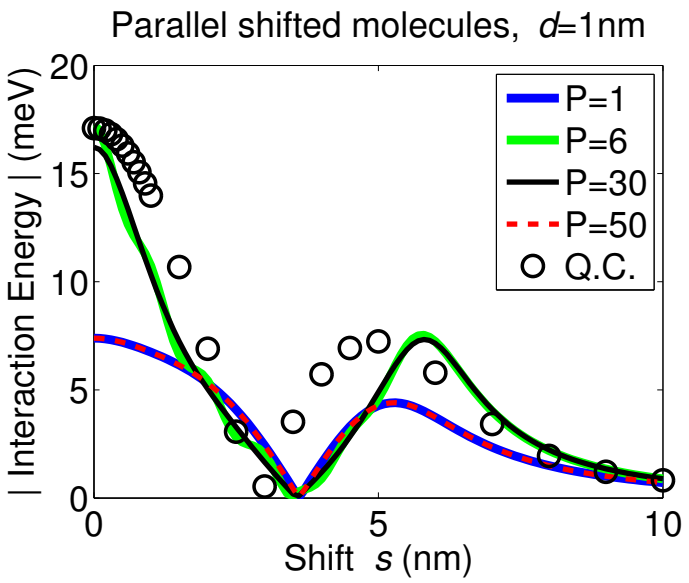

Figure 5.11: Results for O8, in the case of figure 5.2(b) (parallel molecules with a shift s of one molecule along the x axis) for a series of number of antinodes P in the distribution of sub-dipoles. The line-dipoles are made of $N = 50$ sub-dipoles each, therefore $P = 1$ corresponds to the usual line-dipole approximation.

quantitatively poor results or even unphysical behaviour, namely those cases where the inter-molecular distance is significantly smaller than the spatial extension of each of the interacting chromophores. This case is particularly interesting as it is typically realized in molecular thin films. Apart from this small-distance case, our approach can equally well be applied to larger intermolecular separations and smaller molecules (such as O4) where we have checked that it also produces accurate results.

5.6 Conclusion

In the first part of this Chapter, we have shown that for short molecules, like the fluorene dimer studied, the line-dipole model provides a very accurate approximation to the inter-molecular interaction energy. With a line-dipole made of two sub-dipoles only, the calculated interaction energy is in excellent agreement with the quantum chemistry calculations for the full range of separations studied, ranging from typical distances relevant to both dilute solutions and thin films.

We demonstrated in the second Section of this Chapter that the usual line-dipole model breaks down for longer molecules, where the inter-molecular separation is similar to or smaller than the molecular length. In certain parameter ranges which are very relevant to the description of molecular thin films, we have found unphysical behaviour of the interaction strength calculated such that the usual line-dipole approximation can not be safely applied to these scenarios.

In the last part of this Chapter we presented a new formulation of the line-dipole approximation which enables us to overcome these limitations. This new formulation of the interaction of transition dipoles includes nodes in the distribution of sub-dipole moments in addition to the simple line-dipole approximation. Results obtained are then in excellent quantitative agreement with the TD-DFT calculations for all spatial separations and relative orientations considered.

This new line-dipole model enables us to calculate efficiently and accurately the interactions between pairs of oligofluorenes. In the next Chapter we present a microscopic model taking advantage of this improved line-dipole approximation to simulate accurately the exciton dynamics in polyfluorene films.

Chapter 6

A microscopic model of exciton dynamics in polyfluorene films

In this Chapter we present a combined experimental and theoretical study of exciton dynamics in polyfluorene films. The observed sub-picosecond fluorescence anisotropy decay leads us to use the efficient and reliable chromophore interaction energy calculation method presented in Chapter 5 for the construction of a microscopic dynamics model. This model demonstrates that if film morphology, both physical and spectral, is properly accounted for, dipole mediated hopping is sufficient to fully explain the observed sub-picosecond dynamics.

6.1 Introduction

Understanding the photo-physics of ensembles of organic semiconductor molecules is essential if progress towards more efficient and functional devices is to be made [243–246]. We have shown in Chapter 1 that one fundamental process that underpins the operation of devices is energy transfer through the material, and that numerous research efforts are still ongoing to fully understand the fundamental energy transfer processes. Förster first proposed his incoherent energy transfer theory more than six decades ago [44]. Since then many extensions to this theory have been developed [46, 47, 54–58], and new theories to describe coherent or partially-coherent energy transfer have also emerged [42, 65–68] - we give a more detailed overview of these theories in Chapter 1. In devices, the combined additional influence of, amongst others, sample morphology [233, 234], molecular conformations [37, 247, 248], packing and traps [71, 249], exciton hopping and exciton annihilation makes the problem of device optimization even more challenging, as it involves a wide range of energies, timespans and difficult to access parameters. Unpicking one from another is challenging and requires a combination of both experimental and theoretical approaches. Simulations of large-scale systems are usually conducted in the framework of a Monte-Carlo approach [128, 132–134] or a Master-Equation-type approach [125, 136, 250–252], whereas experiments often investigate spectral- and time-resolved photo-luminescence decay [14, 234, 253] or pump-probe spectroscopy [14, 254] to monitor ultra-fast photo-physics. Rather than investigating the dynamics of excitons in organic systems, many of the theoretical simulations model charge-separated excitations [126, 127, 129–131, 255], as this is particularly

relevant to devices such as photovoltaics and LEDs. However, even in these systems, knowledge of exciton dynamics is fundamental to understand and predict the early-time dynamics of the solar generated excitations.

We have studied ultra-fast exciton dynamics in solutions of fluorene-based star-shaped molecules and of oligofluorenes in Chapter 4. In this Chapter, we focus on films of polyfluorene (PF8). Using fluorescence ultra-fast anisotropy experiments, as in Chapter 4, we measure how long the initial photo-induced dipole orientation survives, and infer from that a hopping time for excitonic excitations. As we shall show, an analysis based on simple mean field hopping rates fails to account for the measured sub-picosecond anisotropy decay. We therefore develop a detailed microscopic model of the dynamical processes involved which is able to correctly describe the experimental findings. Finally, we use this model to further explore the detailed physics underlying these results and answer a number of open questions about the importance of inhomogeneous versus homogeneous broadening, exciton localization, and the typical number of hops an exciton undergoes before becoming localized.

6.2 Experiments: fluorescence anisotropy in PFO films

All the experiments presented in this Chapter have been performed by our collaborators at the university of St Andrews.

6.2.1 Experimental methodology

Films of PF8 were prepared using a spin-coating technique. It was ensured that only glassy phase polyfluorene was formed. The films were pumped by a 100 fs (full-width half-maximum) laser pump pulse at an excitation wavelength of 400 nm. Ultrafast luminescence was measured at a detection wavelength of 475 nm. Fluorescence dynamics parallel ($I_{\parallel}$) and perpendicular ($I_{\perp}$) to the excitation were measured. The instrument response function (IRF) was also recorded, and was found to be 380 fs FWHM. Having measured fluorescence dynamics parallel and perpendicular to the excitation polarisation the anisotropy can be reconstructed, where the anisotropy, r, is defined as in Chapter 4:

$$r = \frac{I_{\parallel} - I_{\perp}}{I_{\parallel} + 2I_{\perp}} \ . \tag{6.1}$$

The "magic angle" (polarisation-independent fluorescence dynamics) is also defined in the same way as in Chapter 4: $m = (I_{\parallel} + 2I_{\perp})/3$.

As in Chapter 4, fitting of the depolarisation kinetics was performed using the impulse reconvolution method [226] which enables deconvolution of the instrument

response function from the decay. The fitting methodology involves convolving a sum of exponentials with the IRF and then fitting the results with the magic angle m. The best-fit for the magic angle kinetics can then be convolved with a trial function representing the depolarisation and also convolved with the IRF. Iteration of the trial function to give a good fit to the numerator of equation (6.1) (the so-called difference fit) enables the depolarisation to be fitted with full account taken of the instrument response function.

6.2.2 Experimental results

The ultra-fast fluorescence kinetics in the polyfluorene file (PF8) are shown in figure 6.1(a). In the "magic angle" kinetics of the photoluminescence (PL) at the 475 nm (on the 0-2 vibronic) peak we are able to fit fast and slow exponential rise-times of 200 fs and 2 ps, with 0.76 amplitude assigned to the fast component and 0.19 assigned to the slow, with the remaining 0.05 contribution essentially instantaneous following the pump. As expected, on the red-side of the PL spectrum we observe an increase in PL intensity over the first few picoseconds, a rise attributed to electronic and geometry relaxation (e.g. bond lengths, torsional angles). These processes, however, cannot easily be disentangled from the energy transfer between chromophores (on or between polymer chains) that is occurring when just looking at the ensemble magic angle dynamics alone. Consequently, we have monitored the depolarisation of the fluorescence by recording fluorescence kinetics parallel and perpendicular to the laser field to obtain information on the change in the angle of the dipole moment of the exciton on an ultra-fast timescale. The fluorescence anisotropy of PF8 at a detection wavelength of 475 nm is shown in figure 6.1(b). We have chosen a detection wavelength on the red-side of the PL spectrum to ensure that there is absolutely no contamination of the recorded signal with the excitation laser field or any prompt higher energy emission from PF8. The instrument response does not enable us to resolve the initial anisotropy of 0.4 that we might expect (as demonstrated in Chapter 4); instead, around $t \leqslant 0$, we observe noisy anisotropy values as the intensity recorded is very low. Using the anisotropy fitting procedure as described in the experimental methodology we find that the depolarisation fits to time constants of 680 fs and 5 ps with depolarisation amplitudes (i.e. loss of anisotropy) of 0.24 and 0.09 respectively. These values are considerably different from the fitted time constants of the magic angle kinetics and show that as well as electronic and geometric relaxation, dipole reorientation is occurring on fast and slower timescales. To the best of our knowledge this is the first time that the ultra-fast fluorescence depolarisation has been investigated in films of polyfluorene. The observation of such fast depolarisation is not necessarily unexpected in films of conjugated polymers (for instance sub-picosecond fluorescence anisotropy decay has been measured

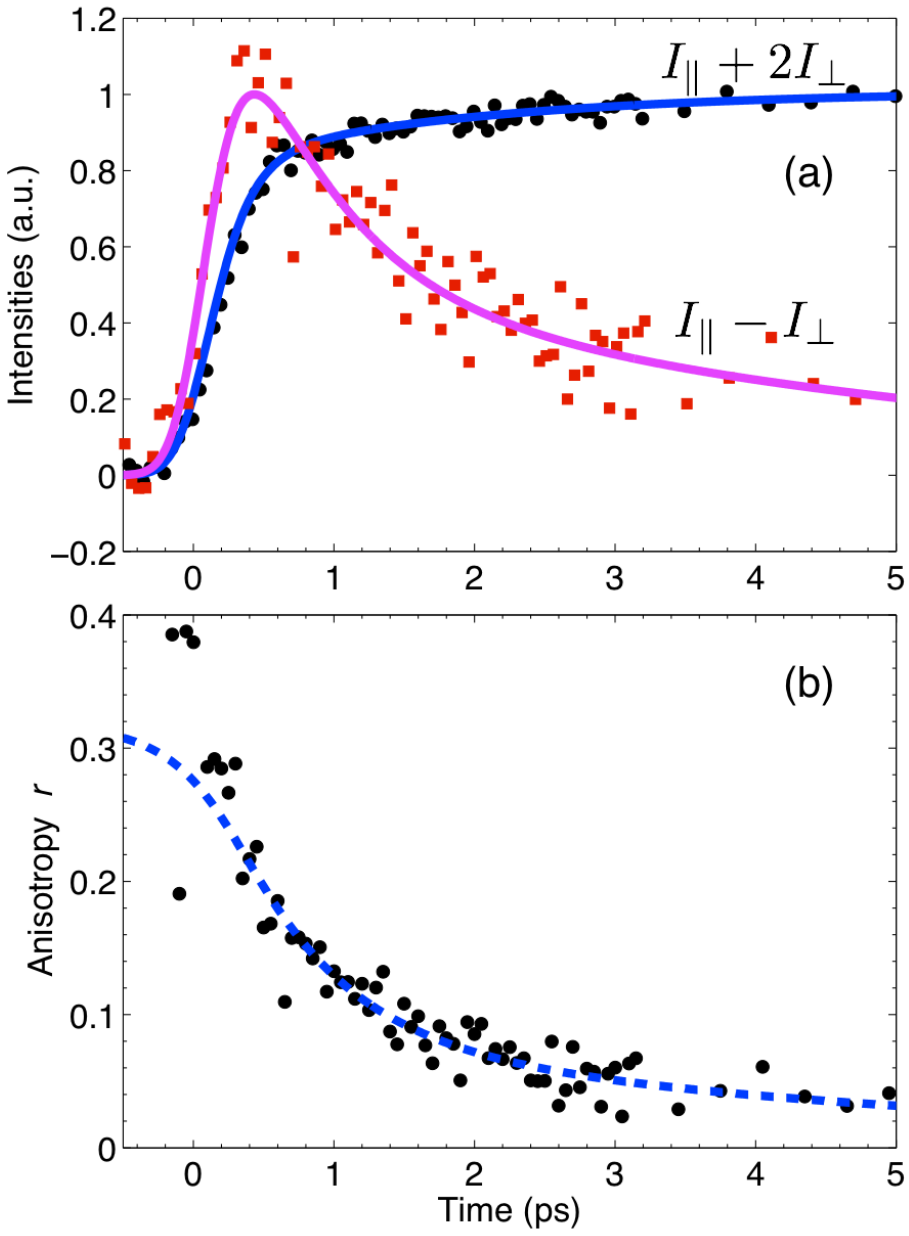

Figure 6.1: Experimental (a) magic angle and intensity difference results and (b) anisotropy decay measured for PF8 films. The discrete data points are experimental raw results and lines are the fitted experimental traces from which reported decay times are extracted.

in MEH-PPV [256]), but the timescales and nature of such depolarisation is still an area of active investigation.

6.2.3 Macroscopic description

The decay of the anisotropy arises from the hopping of excitons from the chromophore on which they were photo-excited to nearby chromophores oriented in a different direction. To try and understand our measurements we calculate the typical Förster rate for exciton hopping in the following macroscopic, simple model.

As introduced in Chapter 1, the Förster hopping rate $\gamma_F = 1/\tau_F$ between two chromophores i and j is [42, 230]: $\gamma_F = 2\pi/\hbar \times |g_{ij}| \left|V_{ij}^F\right|^2$. g_{ij} is the spectral overlap between the exciton donor and acceptor chromophores which we obtain from the measured spectral overlap between the normalised film absorption, $\mathcal{A}(\hbar\omega)$, and emission, $\mathcal{E}(\hbar\omega)$, spectra.

$$|g_{ij}| = \frac{\int \mathcal{A}(\hbar\omega)\mathcal{E}(\hbar\omega)\ d(\hbar\omega)}{\int \mathcal{A}(\hbar\omega)\ d(\hbar\omega) \quad \int \mathcal{E}(\hbar\omega)\ d(\hbar\omega)}. \tag{6.2}$$

We calculate a spectral overlap of $|g_{ij}| = 0.296\,\text{eV}$, from the experimental spectra presented in figure 6.2. V_{ij}^F is the coupling energy between donor and acceptor chromophores i and j. We have see in Chapter 5 that the most tractable approach to obtain this interaction energy is based on the line-dipole approximation [238,242], which can show very high accuracy at very low calculation cost, particularly when using the improved line-dipole model introduced in Chapter 5. We do not use the point-dipole approximation as we know that this approximation is not valid for separations typical of films [180, 242]. V_{ij}^F is calculated using:

$$V_{ij}^F = \sum_{i,j}^{N} \frac{\boldsymbol{\mu}_{A_i} \cdot \boldsymbol{\mu}_{B_j}}{|\boldsymbol{d}_{A_iB_j}|^3} - 3\frac{\boldsymbol{\mu}_{A_i} \cdot \boldsymbol{d}_{A_iB_j} \quad \boldsymbol{\mu}_{B_j} \cdot \boldsymbol{d}_{A_iB_j}}{|\boldsymbol{d}_{A_iB_j}|^5}\ , \tag{6.3}$$

with $\boldsymbol{d}_{A_iB_j}$ being the vector between the centres of the sub-dipoles $\boldsymbol{\mu}_{A_i}$ for chromophore A and $\boldsymbol{\mu}_{B_j}$ for chromophore B. The sub-dipole moment $\boldsymbol{\mu}_{A_i}$ is given by:

$$\boldsymbol{\mu}_{A_i} = \frac{\left|\sin\left(\frac{iP\pi}{N}\right)\right|}{\sum_j \left|\sin\left(\frac{jP\pi}{N}\right)\right|} \quad \boldsymbol{\mu}_A, \tag{6.4}$$

and similarly for $\boldsymbol{\mu}_{B_i}$.

The usual line-dipole approximation [238, 242] corresponds to $P = 1$ and $N > 1$ and for the improved line-dipole approximation we take $P = 30$ and $N = 50$, following the results presented in Chapter 5. What remains is to specify the size, separation and orientation of the molecules. Typical values of the polyfluorene conjugation length [163] correspond to around eight monomer units so we view the

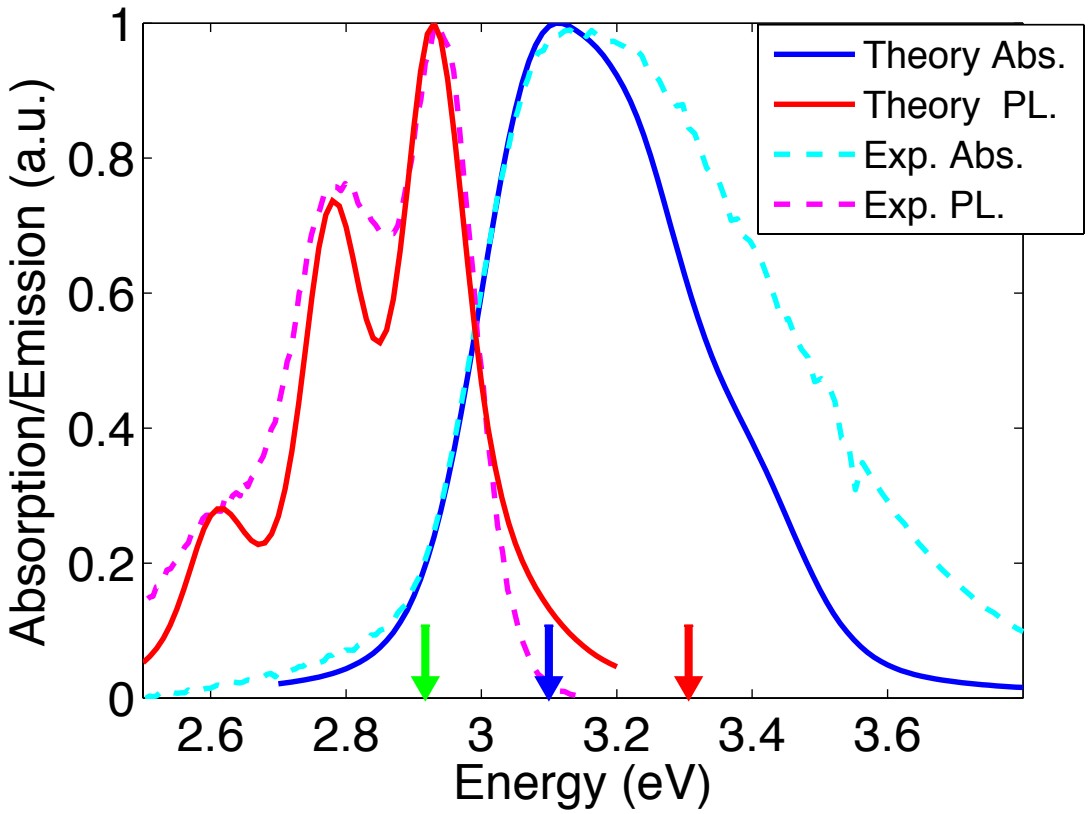

Figure 6.2: Comparison of the experimental absorption and emission spectra (dotted lines) with the reconstructed spectra used to set input parameters for the dynamical simulations. The blue arrow represents the excitation at 400 nm, the red one at 375 nm and the green one at 425 nm.

polyfluorene film as an ensemble built of these octamers. the experimental team in St Andrews measured a film density of 0.54 g/cm^3 for PF8. The molar mass of the PF8 octamers is $M = 3106$ g/mol, thus the mean separation between the chromophores can be estimated as $a = 2.12$ nm. For the purposes of this simple estimate we assume that the chromophores are all separated by this average spacing.

Hops between parallel molecules will lead to no change in the anisotropy, while within the line dipole approximation hops between molecules which are perpendicular have zero dipole coupling so no hopping occurs. To get a lower bound on the hopping time we assume a mean angle between all chromophores of $\frac{\pi}{4}$. (Note, we have checked that doing the angle average correctly leads to only a tiny correction to this much simpler assumption). The transition dipole length l and dipole moment d are obtained from the quantum chemistry calculations presented in Chapter 5. They are, for absorption, $l_{abs} = 5.4$ nm and $d_{abs} = 4.65$ eÅ, and for emission $l_{em} = 4.3$ nm and $d_{em} = 4.74$ eÅ.

The calculated interaction strength per pair and corresponding Förster hopping rates τ_F (allowing for interactions with the six nearest neighbours) from this mean-

Dipole model	Interaction per pair (meV)	τ_F (ps)
Line-dipole	5.54	12.1
Improved line-dipole	3.97	23.5

Table 6.1: Interaction energies estimates for the simple model, for a pair of chromophores and for a chromophore interacting with its six closest neighbours, and hopping times estimates for this last case.

field type model are given in table 6.1. It can be seen that, even using the largest interaction strength, this mean-behaviour model predicts a hopping time much larger (twenty times slower) than the experimentally observed 0.68 ps anisotropy decay. The reason for the failure of this simple intuitive model is that the interactions which dominate the decay are not well captured in a model based on the average properties of the film, as we shall see in the next Section.

6.3 Microscopic theory of exciton diffusion in PFO films

6.3.1 The microscopic model

The simple estimate presented above is not able to correctly explain the observed time-scales for the anisotropy decay in polyfluorene films. Indeed, it underestimates the decay rate by a factor of over thirty. Therefore we introduce a more detailed model where the microscopic hopping dynamics and sample geometry are more accurately captured. This model will allow us to simulate the exciton dynamics in a large ensemble of chromophores. In what follows we will adopt a number of simple but sufficient assumptions to avoid the need for "fitting" parameters in such a model. To this end we use the combined insight from our experimental measurements and quantum chemistry calculations to obtain all the necessary parameters. In this sense the model is predictive and not merely a complex fitting procedure.

In this Subsection we introduce this model and its assumptions. Its formalism is developed in the next Subsection. The choice of parameters, illustrated by, but not restricted to, the simulation of polyfluorene films, will be the subject of Subsection 6.4.

We simulate the excitation occupation probability on each chromophore of an ensemble of chromophores, and thereby gain knowledge of exciton dynamics on both a microscopic and macroscopic scale. Each chromophore has its own spatial (location, orientation) and energetic (absorption and emission energy) characteristics. Exciton dynamics arises from inter-molecular Förster transfer.

The description of the excitation, hopping and relaxation processes included in the model are summarised in figure 6.3. The excitation is represented by two exciton occupation probabilities on each chromophore: n_i^0, the molecular exciton occupation probability when the chromophore is in its ground state geometry S_0, and n_i^1 when

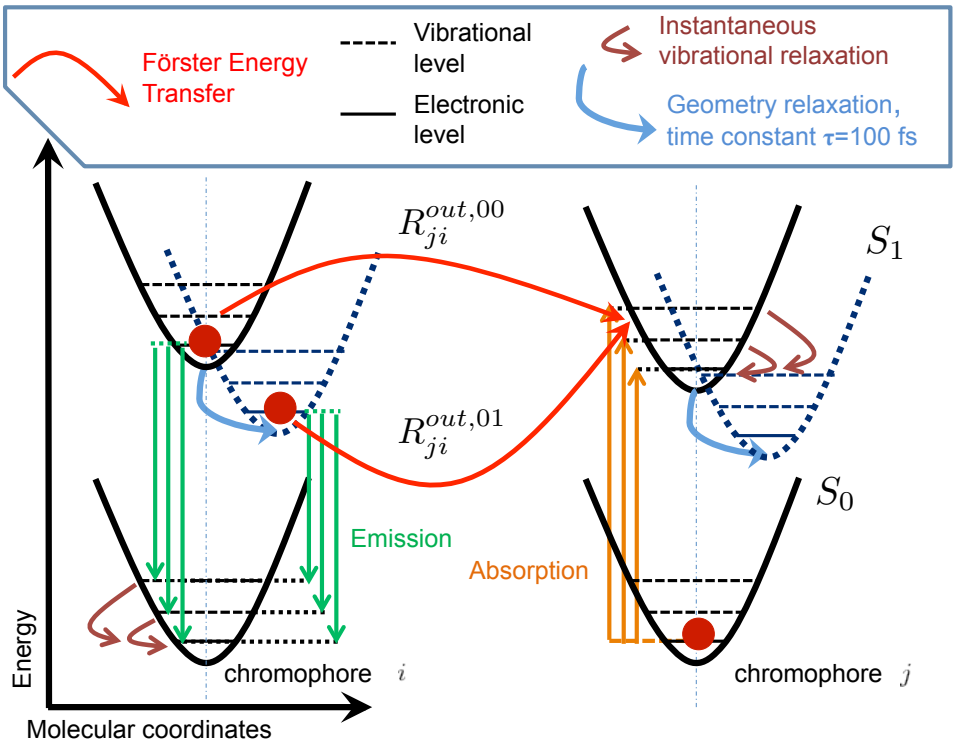

Figure 6.3: Schematic of the mechanisms included to describe the Förster type energy transfer between two chromophores i and j.

the chromophore is relaxed into the electronic S_1 state.

As in the experiments, the system is pumped by a short pulse of defined energy, temporal width, propagation direction and polarisation state. This pumps the chromophore directly to the excited electronic state (and the vibrational levels) of the unrelaxed S_0 geometry, thereby increasing the exciton probability n_i^0. In the weak coupling regime, we can assume that relaxation from higher lying vibrational states is very fast compared to the time-scales of interest [43] here, and for simplicity we consider vibrational relaxation to be instantaneous by considering only the electronic populations. An excited chromophore relaxes to the relaxed excited state (S_1 geometry, exciton probability n_i^1), with a time constant $\tau^x = 1/\gamma^x$. This is represented by the displaced excited-state energy surface in figure 6.3.

Excitons in both S_0 and S_1 can hop to an unexcited chromophore j by the Förster-type mechanism, increasing the exciton probability in the non-relaxed excited-state n_j^0. The exciton emits directly from either the non-relaxed S_0 or fully relaxed S_1 chromophore to a vibrational level of the electronic ground-state, which is taken into account in the spectral overlap of the hopping rate..

We neglect coherent effects which typically occur only on a 100 fs timescale. We include Pauli blocking, as this is very straightforward to implement and does not require knowledge of any additional parameters.

6.3.2 *Exciton dynamics*

Within this model, the rate-equations giving the change of excitation probabilities n_i^0 and n_i^1 on each chromophore i are:

$$\begin{aligned}\frac{dn_i^0}{dt} &= \mathcal{I}_i^{pump} - \left(\gamma^x + \gamma^r + \sum_{j\neq i} R_{ji}^{out,00}\right) n_i^0 \\ &\quad + \sum_{j\neq i} \left(R_{ji}^{in,01} + R_{ji}^{in,00}\right)\left(1 - n_i^1 - n_i^0\right), \qquad (6.5)\\ \frac{dn_i^1}{dt} &= \left(\gamma^x - \gamma^r - \sum_{j\neq i} R_{ji}^{out,01}\right) n_i^1 - \sum_{j\neq i} R_{ji}^{XX} n_i^1 n_j^1. \qquad (6.6)\end{aligned}$$

The first term of equation (6.5) is the source term for the pumping of the chromophore i of dipole moment $\boldsymbol{d}_i$ by the field $\boldsymbol{E}$:

$$\mathcal{I}_i^{pump} = \left(1 - n_i^1 - n_i^0\right) \Gamma_i\left(\hbar\omega\right) \left|\boldsymbol{d}_i \cdot \widetilde{\boldsymbol{E}}\left(t\right)\right|^2. \qquad (6.7)$$

As the sample is a thin film we can neglect propagation effects in the optical field [125]. Equation (6.7) is derived from the linear response of a chromophore system assuming a low pumping intensity and using the Rotating Wave Approximation (see Appendix for details). $\widetilde{E}\left(t\right) = E\left(t\right)\mathrm{e}^{i\omega_0 t}$, is the envelope of the pump pulse with photon energy $\hbar\omega_0$ and Γ_i is proportional to the spectral overlap between the chromophore absorption and the source:

$$\Gamma_i(\hbar\omega) \propto \int E(\hbar\omega)\mathcal{A}_i(\hbar\omega)d\left(\hbar\omega\right), \qquad (6.8)$$

$\hbar\omega$ is the photon energy, $E\left(\hbar\omega\right)$ the Fourier Transform of the field $E(t)$ and $\mathcal{A}_i\left(\hbar\omega\right)$ the absorption lineshape of molecule i (see equation (6.12) below). In equation (6.7), $(1 - n_i^1 - n_i^0)$ describes the Pauli blocking which limits each chromophore to only one exciton.

The second term of equation (6.5), and the first term of equation (6.6), corresponds to the relaxation from the S_0 geometry to the S_1 geometry. The γ^r term, describes the exciton radiative decay $\gamma^r = 1/\tau^r$, with τ^r the radiative lifetime. The following terms of the equations are the Förster hopping-in and -out rates. $R_{ji}^{out,0p}$ corresponds to exciton hopping from a chromophore i in geometry S_p, with $p = 0$ or 1, onto an unexcited chromophore j in its ground state geometry S_0, whereas $R_{ji}^{in,0p}$ deals with hopping from an excited chromophore j in the S_p geometry to the chromophore i, in its ground-state. The last term R_{ji}^{XX}, the exciton-exciton annihilation

rate, will be detailed later in this Subsection. $R_{ji}^{out,0p}$ and $R_{ji}^{in,0p}$ are given by:

$$R_{ji}^{out,0p} = \frac{2\pi}{\hbar}\left(1 - n_j^1 - n_j^0\right)\left|g_{ji}^{0p}\right|\left|V_{ji}^{0p}\right|^2, \tag{6.9}$$

$$R_{ji}^{in,0p} = \frac{2\pi}{\hbar} n_j^p \left|g_{ij}^{0p}\right|\left|V_{ij}^{0p}\right|^2, \tag{6.10}$$

with V_{ij}^{0p} being the Coulombic (line-dipole) interaction between the excitons on chromophore i, in the ground state, and on chromophore j, in the excited state and in the S_p geometry. We use the improved line-dipole approximation presented in Chapter 5 to calculate this interaction, as presented in the previous Section by equation (6.3). We use the appropriate transition dipoles, absorption dipole of chromophore i and emission ($p = 1$) or absorption ($p = 0$) dipole of chromophore j. g_{ij}^{0p} is the overlap between the normalised emission lineshape of chromophore j, in the S_p geometry, with the normalized absorption lineshape of chromophore i. As highlighted in Chapter 1 (Section 1.2.4) and in reference [42], it is essential these lineshapes contain the vibronic structure on top of the purely electronic transitions.

The spectral overlaps g_{ij}^{0p} are calculated for each pair of chromophores. Each chromophore possesses its own absorption transition energy, to mimic inhomogeneous broadening. This energy is randomly generated in a Gaussian distribution of width σ (the inhomogeneous broadening), centred around the electronic absorption peak, E_i^{abs}. In addition, vibrational peaks are included for each molecule. The spectrum of a single chromophore is therefore the sum of several Lorentzian line shapes weighted for the vibrational peaks. These Lorentzian lines have a width γ, the homogeneous broadening. The calculated absorption spectrum of the film, integrated over all polarisation directions, is the sum of these Lorentzian line-shapes over the chromophore ensemble:

$$\mathcal{A}(\hbar\omega) = \hbar\omega \sum_i \mathcal{A}_i, \tag{6.11}$$

$$\mathcal{A}_i = L(E_i^{abs}, \hbar\omega) + \sum_k \alpha_k^{vib} L(E_i^{abs} + \delta E_k^{vib}, \hbar\omega). \tag{6.12}$$

α_k^{vib} and δE_k^{vib} are the strength and energetic offset of the k-th vibrational level respectively and $L(x, \hbar\omega)$ a normalized Lorentzian lineshape,

$$L(x, \hbar\omega) = \frac{1}{\pi}\frac{\gamma}{\gamma^2 + (x - \hbar\omega)^2}. \tag{6.13}$$

The emission spectra is time-dependent, reflecting the exciton dynamics, and is

calculated using the expression:

$$\mathcal{E}(\hbar\omega, t) = \hbar\omega \sum_i I_i(\hbar\omega, t), \tag{6.14}$$

with I_i the time- and energy-dependent intensity emitted by chromophore i:

$$I_i(\hbar\omega, t) = n_i^1(t)\ \mathcal{E}_i(E_i^{em}, \hbar\omega) + n_i^0(t)\ \mathcal{E}_i(E_i^{abs}, \hbar\omega), \tag{6.15}$$

where $\mathcal{E}_i(x, \hbar\omega)$ is the emitted spectrum for the i-th chromophore,

$$\mathcal{E}_i(x, \hbar\omega) = L(x, \hbar\omega) + \sum_k \alpha_k^{vib} L(x - \delta E_k^{vib}, \hbar\omega). \tag{6.16}$$

To calculate the spectral overlap for the hopping rates between the i-th and j-th chromophores in equations (6.9) and (6.10), g_{ij}^{00} and g_{ij}^{01}, we use equation (6.2), but with the calculated single chromophore absorption and emission lineshapes, rather than the sample spectra. It is important to note that in the most general case, $g_{ij}^{0p} \neq g_{ji}^{0p}$ and $V_{ij}^{0p} \neq V_{ji}^{0p}$; however the conservation of the exciton probability during hopping is ensured by the fact that $R_{ji}^{out,0p} n_i^p = R_{ij}^{in,0p} \left(1 - n_j^1 - n_j^0\right)$ for all i, j.

We have modelled exciton-exciton annihilation, through the inclusion of the R_{ji}^{XX} term, for high pump intensity calculations. Indeed, exciton-exciton annihilation plays a major role in high exciton density regimes and has been studied in polyfluorene films [234]. When an exciton-exciton annihilation event takes place, one exciton loses its energy and goes back to the ground-state, while the exciton of another chromophore absorbs this energy and is promoted to a higher energy level. R_{ji}^{XX} represents the annihilation of an exciton on chromophore i due to the presence of an exciton on chromophore j. It is assumed that the exciton on chromophore j absorbs instantly the exciton energy of chromophore i and then undergoes immediate relaxation back to the S_1 geometry. This results in no change of the exciton probability of chromophore j. We also assume that this mechanism occurs only between excited molecules in their S_1 geometries, because we believe annihilation processes happen on a longer timescale than the S_0 to S_1 relaxation. R_{ji}^{XX} is given by:

$$R_{ji}^{XX} = \frac{2\pi}{\hbar} \left|g_{ji}^{XX}\right| \left|V_{ji}^{XX}\right|^2, \tag{6.17}$$

where V_{ji}^{XX} is, in the frame of the improved line-dipole approximation, the Coulomb interaction energy between the emission dipole of chromophore i and the excited-state absorption dipole of chromophore j. g_{ji}^{XX} is the spectral overlap between the emission lineshape of chromophore i and the excited-state absorption lineshape of chromophore j. All these quantities are calculated in the same way as for the Förster

rates, but with the excited-state absorption properties instead of the absorption properties.

6.3.3 Fluorescence anisotropy

From this model, one can calculate the time-dependent fluorescence anisotropy r and the magic angle m. m is defined as $m = (I_{\parallel}+2I_{\perp})/3$, where $I_{\parallel}(I_{\perp})$ is the emitted intensity (perpendicular) to the pump, and so m is the total intensity emitted by the sample. Anisotropy is defined as $r = (I_{\parallel} - I_{\perp})/3m$ and reflects any change of the average orientation of the fluorescing dipoles. For a perfectly random sample of chromophores, without rotation of the transitions dipoles, we have $r = 0.4$. The emitted intensity in the perpendicular and parallel directions $I_{\perp}$ and $I_{\parallel}$ are calculated separately by reconstructing their emission spectra . We have:

$$I_{\parallel} \propto \sum_i I_i(\hbar\omega, t) {d_i^{\parallel}}^2, \tag{6.18}$$

where $d_i^{\parallel}$ is the emission dipole component of chromophore i parallel to the pump, and similarly for perpendicular emission.

As in the experiments, a Gaussian spectral filter of standard deviation $\sigma_{detect} = 7$ meV and centred at the emission peak (at 10 ps) is applied to the calculated emission spectra. This integrated emission intensity then is convoluted by the instrument response function of the experimental detection device, and, finally, the time origin is determined using the same algorithm as for the experimental results, so that the comparison between theoretical and experimental results is meaningful.

6.4 Parameter selection - low pump intensity

A number of quantities are necessary to predict the exciton dynamics in a specific film from the above model. The Förster mechanism requires knowledge of the morphology of the sample and of the transition dipole moments and lengths to calculate the interaction energies, and some knowledge of the global spectral properties to infer the individual absorption and emission energies of each chromophore and to calculate the spectral overlaps. In the following, we discuss how all these parameters are fixed, using either theoretical or experimental results. Our approach is, as far as possible, to use only parameters which are supported by independent experimental measurements. At low pump intensity, exciton-exciton annihilation does not play any role on the exciton dynamics. We discuss the relevant parameters for exciton-exciton annihilation in Section 6.6; up to this Section, only low pump intensities are used.

6.4.1 Geometrical parameters

In this Chapter we model spin-coated polyfluorene (PFO) films. We assume a conjugation length of eight monomers in agreement with previously published studies [163, 180]. Therefore we choose to take oligofluorene octamers as the typical PFO chromophore and represent the film as a closely packed ensemble of octamer molecules. We show in Section 6.5 that the choice of octamers is judicious in that using longer chromophores leads to essentially the same results.

To achieve the correct volume density of chromophores in our modelled film the octamers are initially positioned on a tetragonal lattice and then their locations randomly moved by up to one third of the lattice spacing to mimic the amorphous nature of the film. The lattice constant in the $\boldsymbol{z}$ direction, the direction of stacking of the layer, is taken to be $a = 0.9\,\text{nm}$, unless specified otherwise. Each $(\boldsymbol{x}, \boldsymbol{y})$ layer is a square lattice, of lattice constant $b = 3.25\,\text{nm}$, so that the average volume density of the film is the measured value of $0.54\,\text{g/cm}^3$. The rods are each randomly oriented in the $(\boldsymbol{x}, \boldsymbol{y})$ plane, but their projection on the $\boldsymbol{z}$ plane cannot be more that the z-lattice constant a. In this way, the chromophores are preferentially lying in the $(\boldsymbol{x}, \boldsymbol{y})$ plane, as we would expect for a spin-coated film.

To take into account the finite width of the chromophores, the minimum distance between the two rods is 0.3 nm. This means that if two chromophores are at any point at a distance closer than 0.3 nm, one of these two chromophores is repositioned and reoriented randomly again until they are separated by at least 0.3 nm, to take into account the actual width of the chromophores and make the ensemble realistic.

A representation of our ensemble of packed chromophores is shown in figure 6.4. It is important to note that we have checked that by taking a minimum molecular separation of 0.2 nm or 0.4 nm, we obtained the same fluorescence anisotropy as for 0.3 nm, showing an insensitivity of the results to this parameter for realistic values. Similarly a maximum (random) movement of either a quarter or a half of the tetragonal lattice spacing gives virtually identical results as for a third. Periodic boundary conditions are used to repeat the "box" of model chromophores, so that excitons can hop from one side of the "box" to the opposite side, thus eliminating interface effects.

The simulations include 125 000 chromophores. Each chromophore can interact within the cube centred on it, with edges of 7 lattice spacings (making $7^3 - 1 = 342$ nearby chromophores); any interactions involving a Förster rate slower than 200 ps are neglected in calculating the dynamics. This number of chromophores and interacting neighbours guarantees convergence of the dynamics - any two runs with randomly assigned geometries and energies but otherwise identical parameters are found to give the same results.

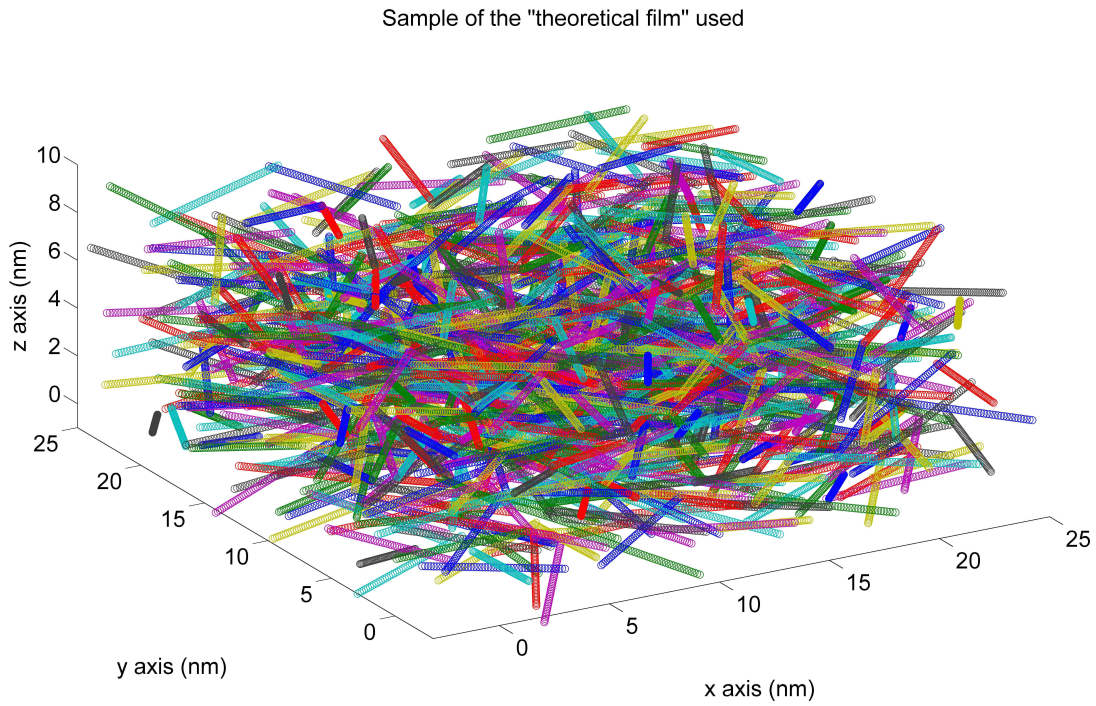

Figure 6.4: Sketch of a small portion (less than 1%) of the molecular ensemble used in the calculations. Note the geometrical anisotropy, with chromophores lying preferentially in the $(\boldsymbol{x}, \boldsymbol{y})$ plane.

6.4.2 Spectral Parameters

The absorption energy, homogeneous (dephasing time) and inhomogeneous broadening are obtained by reproducing the experimental absorption and emission spectra with the model calculations (see figure 6.2). The spectra for an individual chromophore consists of a sum of three Lorentzian functions of the same width, to mimic the lowest three vibrational peaks of PFO. We found that for a fixed homogeneous broadening, only one value of inhomogeneous broadening can give a good fit between the theoretical and experimental absorption spectra. The electronic emission peak, the vibrational peak position, relative to the electronic peak, and strength are obtained by fitting the computed emission spectra at 10 ps to the experimental spectra. The vibrational parameters are the same for all the chromophores. Each chromophore has its own emission energy, linked by a linear relationship: $E_i^{em} = 0.48 E_i^{abs} + 1.50$, to its absorption energy. The slope of this linear relationship is obtained by linear fit of the absorption energies with emission energies for various oligomer lengths, using the quantum chemistry values calculated by Schumacher et al. [163]. The intercept is obtained by placing the calculated emission peak at the observed experimental emission peak. This relationship basically implies that the emission inhomogeneous broadening is half of the absorption inhomogeneous broadening. We have noticed, by comparison with the experimental

	Length	Abs. Dipole Length	Emiss. Dipole Length	Abs. Dipole Moment	Emiss. Dipole Moment
O6	4.98	3.9	3.5	3.96	4.30
O8	6.64	5.4	4.3	4.65	4.74
O10	8.30	6.8	4.9	5.30	5.02

Table 6.2: Dipole lengths (nm) and transition dipole moments (eÅ) for absorption and emission in oligofluorenes O6, O8 and O10, obtained by (TD)-DFT calculation using B3LYP, 6-31G.

spectra, that the inhomogeneous broadening indeed needs to be smaller in emission than in absorption. This can be explained physically by the fact that an exciton self-trapping process occurs in polyfluorenes [163]. Thus the exciton is localised on a smaller part of the chromophore in emission than in absorption, it is less sensitive to chromophore geometry distortions than in absorption, resulting in a reduced inhomogeneous broadening.

In addition, most of the pairs of homogeneous and inhomogeneous broadening values which can fit the experimental absorption spectra do not give good agreement between experimental and theoretical emission spectra. The only pair of inhomogeneous and homogeneous broadening values which give a reasonable fit simultaneously for both absorption and emission spectra is a dephasing time of $T_2 = 20\,\text{fs}$ (leading to $\gamma = 33\,\text{meV}$) and $\sigma = 70\,\text{meV}$. The resulting fit is displayed in figure 6.2. Even if the detailed link between absorption and emission energies and of homogeneous and inhomogeneous broadening values is not certain, the important outcome is to be able to reproduce the macroscopic dynamics using microscopic properties, derived from quantum chemistry calculations and fits to the experimental absorption and emission spectra. In this context, the comparison of our theoretical spectral model used, as an input parameter, and the experimental results is very satisfying, as shown in figure 6.2.

For the radiative lifetime, we have taken the measured experimental value of $\tau^r = 110\,\text{ps}$, taken from the experimental data published by Shaw et al. [234]. The relaxation from the S_0 to S_1 geometry in the excited state is taken to be $\tau^x = 100\,\text{fs}$, a typical time for such systems [31,32]. The dipole moments and dipole lengths of the fluorene octamers in absorption and emission geometries (Table 6.2) have been calculated using Time Dependent-Density Functional Theory (TD-DFT) calculations for oligomers, at the B3LYP 6-31G level of theory [180].

The ensemble is excited by a linearly polarized pulse of defined wavelength and temporal width and propagates perpendicularly to the plane of the film, unless otherwise stated. Excitation is spatially uniform across the sample. The temporal full width at half maximum (FWHM) of the Gaussian input pulse intensity is 100 fs (cor-

responding to 41 meV or about 5 nm around the 400 nm excitation wavelength), and three different excitation wavelengths are used in the calculations: 375 nm (3.30 eV), 400 nm (3.10 eV), and 425 nm (2.92 eV) (the absorption peak being at 3.07 eV).

6.5 Results and discussion: low pump intensity

In this Section, we present results calculated for a low exciton density, so that exciton-exciton annihilation does not play any role in the exciton dynamics. The experimental data we compare our results to were also obtained at low pump intensity, and do not exhibit any measurable exciton-exciton annihilation mechanism.

6.5.1 Fluorescence anisotropy

As shown in figure 6.5, this microscopic model prediction of the anisotropy is in a very good agreement with the experimental results, especially given that no explicit fitting parameter has been used in the model at low pump intensity; the prediction is obtained after having independently fixed all the parameters, as described in the previous Section. Both a fast sub-picosecond initial decay and the slower decay at longer times are seen in the simulations. These results demonstrate the validity of this microscopic model to predict Förster-type hopping mechanisms, indicating indeed that the Förster-type energy transfers happen between specific interacting molecules whose properties can not be simply traced to the average properties of the sample. Furthermore, this demonstrates that no mechanisms other than incoherent Förster energy transfer need to be invoked to explain the sub-picosecond anisotropy decay observed. Were we to adjust in an ad-hoc fashion some of the model parameters no doubt an improved agreement would be possible but this brings no deeper understanding of the underlying physics.

It is important to note that the anisotropy, both experimental and theoretical, does not start at $r = 0.4$, for the simple reason that the experimental instrument response is too slow to obtain an accurate measurement of the initial fast anisotropy decay. Nevertheless, the "raw" theory results coming directly from the rate equation model (without convolution with the instrument response function) obviously resolve this decay and an initial value of $r = 0.4$ is observed (figure 6.5).

6.5.2 Insights into spectral and spatial energy migration

Having validated the model we now use it to obtain additional insights into the spatio-temporal dynamics not available from macroscopic models or experiments. We have calculated the time-resolved emission spectra, as presented in figure 6.6. We observe a very fast (a few hundreds of femtoseconds) low energy shift of the

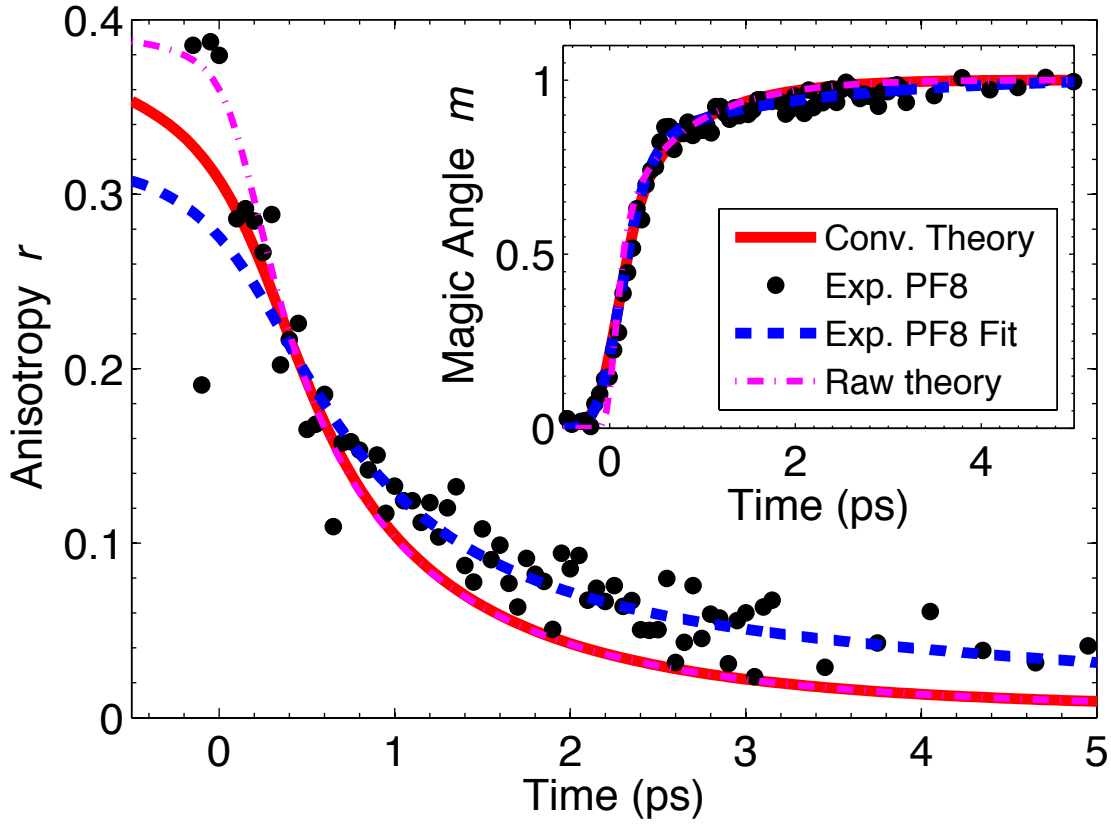

Figure 6.5: Comparison of the predicted fluorescence anisotropy and magic angle dynamics (inset) with the observed experimental decay (the discrete data points are raw results, whereas the experimental line comes from separate fits to the numerator and denominator of equation (6.1)). The "Conv. Theory" results correspond to the theory results convoluted with the instrument response function, for a meaningful comparison with experiments, whereas the "Raw theory" results are unconvoluted.

emission peak, the steady state spectra being reached after approximately two picoseconds. This is consistent with the time-scales obtained for the anisotropy decay. The high energy emission peaks at very early times correspond to emission from excited chromophores in the S_0, non-relaxed geometry. Such unrelaxed chromophores have a strong spectral overlap with the absorption of unexcited chromophores which can lead to efficient hopping at early times.

Figure 6.7 shows the exciton occupation probability for given chromophore emission energies. We clearly see at the earliest times the image in emission of the pump process, exciting molecules at well defined energies, and we then see the migration of these excitons to low energy molecules, where the exciton probability gets more and more localised. Note, we show only 1000 chromophores out of 125 000 as if all points were plotted the details of the figure are masked by overlapping points. Visualising this process on a 3D plot is also possible, to get spatial information, as shown in figure 6.8. This figure illustrates that, whereas the chromophores initially excited are numerous and quite close to each other, as the excitation gets trapped on lower

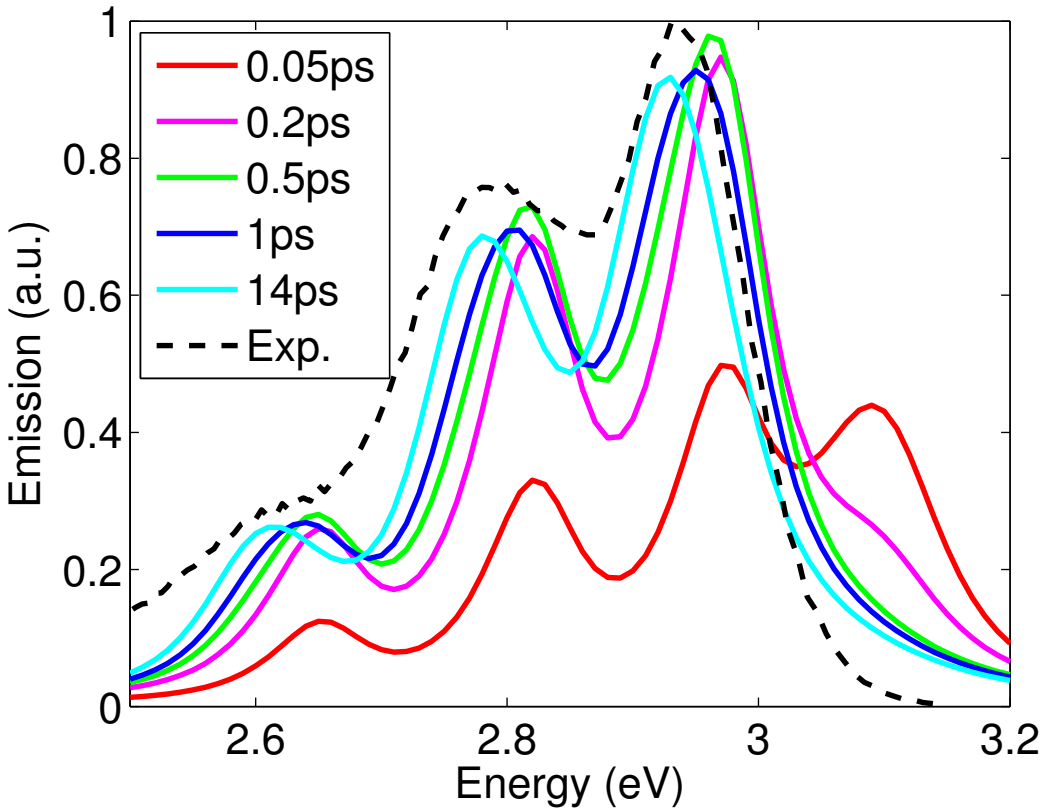

Figure 6.6: Time-resolved emission spectra, compared with the experimental emission spectrum at 10 ps .

energy chromophores, these excited chromophores are spread far apart from each other.

The spectral overlap is responsible for the preferential hopping of excitons to the low energy sites. The exciton hopping rate includes the spectral overlap between the donor emission spectra and the acceptor absorption spectra. For chromophores of the same energy, the energy difference between the peaks of these two curves is about 0.3 eV, larger than both the homogeneous and inhomogeneous broadenings. Hopping from a donor to a low energy acceptor is thus favoured. Only very few acceptors will be at sufficiently low energy to match the resonance condition with any emitting chromophores.

We have calculated that the average exciton energy decreases from 3.07 eV to 2.95 eV in about 1 ps, and that after 5 ps, the exciton energy standard deviation stays almost constant, showing that no more net exciton dynamics happen from this time. In detail, there is still a very slow increase of the standard deviation, because the excitons will try to reach even lower energy chromophores. However, these chromophores are not numerous and therefore very widely spread across the sample, making it difficult for the excitons to diffuse to them, especially as these low energy chromophores will already have a high exciton probability and therefore

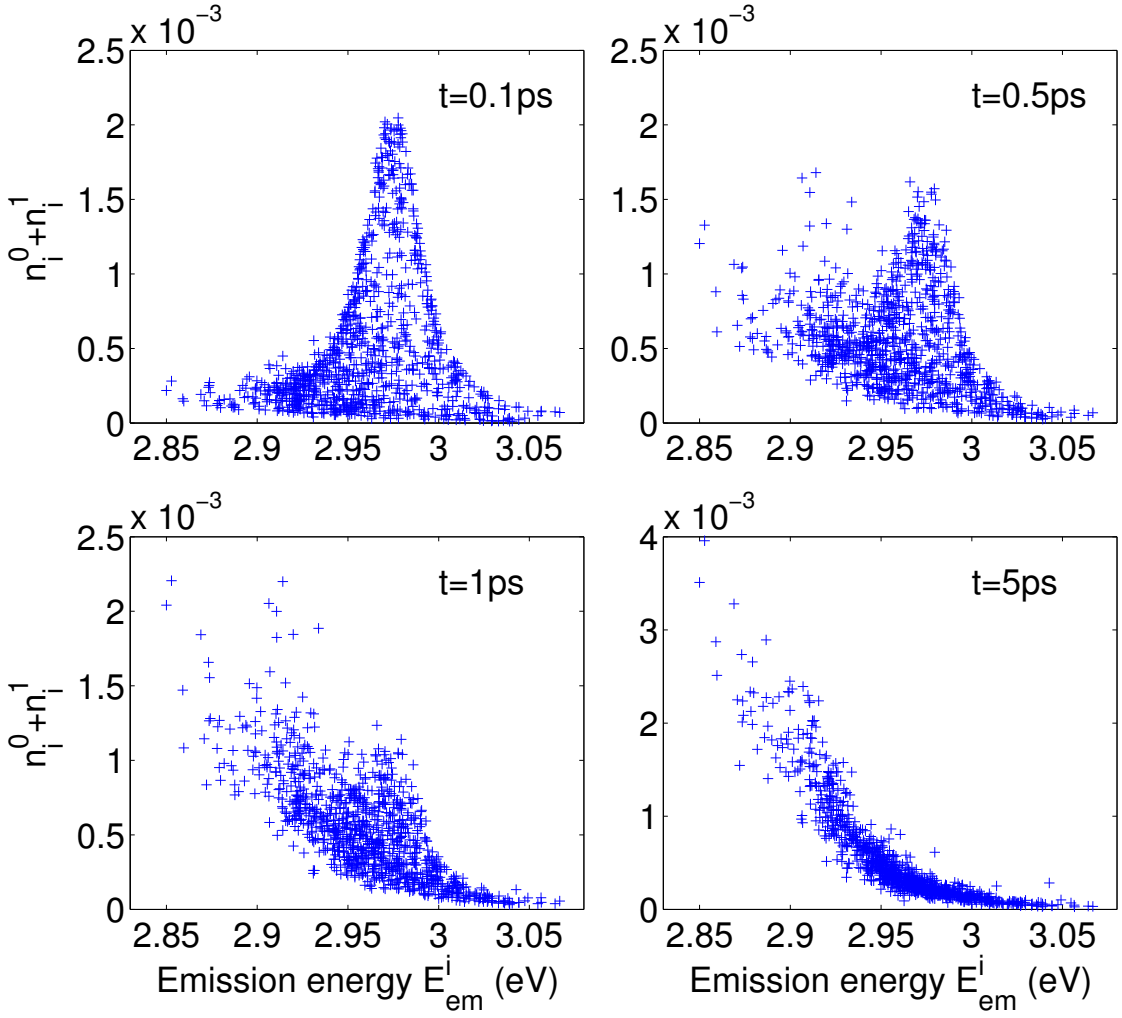

Figure 6.7: Plot of the total exciton occupation probability as a function of the chromophore emission energy. Note the change of scale of the t= 5 ps plot compared to the other plots.

experience Pauli blocking.

In the dynamic model, the lattice parameters, which are used to position randomly the close-packed chromophores, do not actually play a big role in the exciton dynamics, at constant density d. This has been verified by solving the rate-equations for grids of different lattice spacing, as displayed in figure 6.9(a). Indeed, we observe that for three different values of the lattice parameters (in the $(\boldsymbol{z})$ direction, the lattice spacing taken are 0.7, 0.9 and 1.1 nm, corresponding respectively to lattice spacings in the $(\boldsymbol{x})$ and $(\boldsymbol{y})$ directions of 3.70, 3.25 and 2.95 nm, to keep the film mass density constant), the calculated anisotropy decays remains extremely similar.

We have also simulated the exciton dynamics of ensembles of rods having the dipole properties, molecular length and masses of fluorene oligomers made of six fluorene units (O6) or 10 fluorene monomers (O10) - these parameters are summarized in table 6.2. As shown in figure 6.9(b), the resulting calculated fluorescence

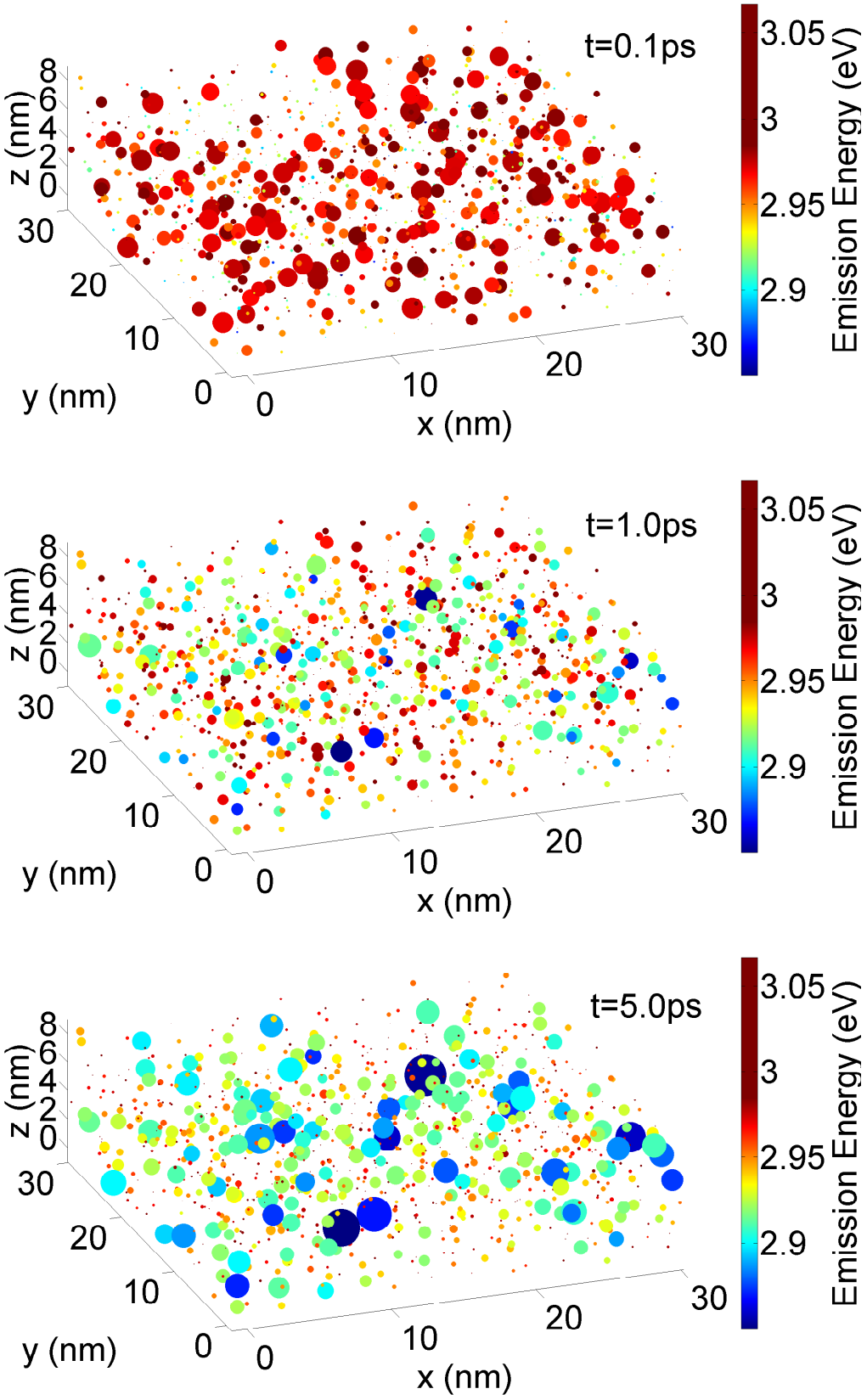

Figure 6.8: 3D plot of a small portion of the simulated film. The molecules are represented by a sphere situated at the centre of the chromophore, its colour being linked with the chromophore emission energy. Its surface area is proportional to the chromophore excitation probability. The plots represent the system shortly after the peak of the pump intensity 0.1 ps, 1 ps and 5 ps after (from top to bottom).

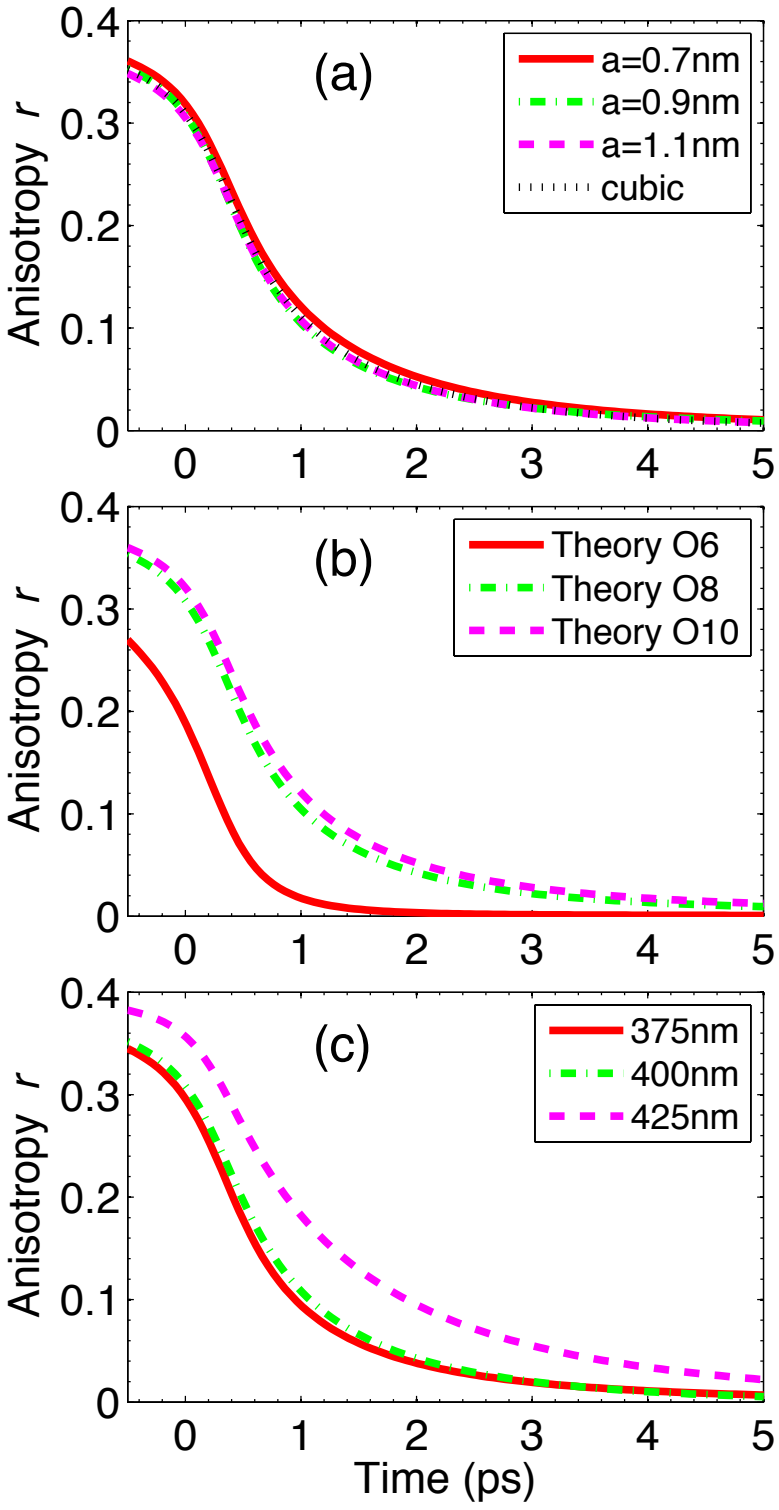

Figure 6.9: Predicted fluorescence anisotropy results for: (a) various configuration of the tetragonal lattice. The values displayed are the lattice spacing for the direction perpendicular to the sample, (z). The film density is kept constant. (b) various length of model chromophores, (c) different excitation wavelengths.

anisotropy for O6 chromophores is faster than for O8, because the molecular interactions are stronger for smaller length oligomers (at fixed transition dipole moment), which are also more closely packed. However, the results are identical for O8 and O10, giving further support that these lengths are typical conjugation lengths for polyfluorene molecules.

Having a successful microscopic model for exciton diffusion enables us to gain deeper knowledge of these diffusion mechanisms. It is possible to analyse the Förster-type interaction rates involved in the model to deduce the number and the strength of these interactions, and which chromophores are primarily involved. For instance, the middle plot of figure 6.10 shows, for the same parameters as above, a histogram of the time-constants associated with the out-scattering ($R_{ji}^{out,0p}$) rates, where the term $(1 - n_i^1 - n_i^0)$ is assumed to be unity at these low probabilities. We observe that about 6% of chromophores possess an interaction term $R_{ji}^{out,01}$ with another chromophore faster than 1 ps, and 16% between 1 and 2 ps, so that more than a fifth of the molecules have at least one neighbour for which the interaction is faster than 2 ps, explaining the fast anisotropy decay observed. In addition, the average absorption energies and the centre-to-centre separations of the chromophores as a function of their Förster interaction time is also displayed in figure 6.10. The fastest interactions correspond to chromophores with the largest energy difference, consistent with the spectral overlap argument given above. This shows that we should indeed expect the fast exciton diffusion processes to be over after a few picoseconds, and that most excitons directly go to the low energy sites, without going through molecules of intermediate energies. Additionally, with our excitation energy at 3.10 eV, we initially excite the interacting pairs with the fastest Förster hopping rates, explaining the fast depolarisation we observe. As expected, the centre-to-centre separation of the chromophore pairs increases with their Förster transfer times. It is important to note that the centre-to-centre chromophore separations of the fastest Förster rates are relatively large, above 3 nm, significantly larger than the average chromophore separation in the plane (0.9 nm). Therefore, the fastest Förster exciton transfers do not necessarily happen between an excited chromophore and its nearest neighbour, but between an excited chromophore and a spectrally matched lower energy chromophore. This explains the insensitivity of the exciton dynamics of the geometric parameters used for the generation of the ensemble of model chromophores. Indeed, rather than the distance of the closest neighbours, the spatial parameter of importance is the film density, as the chromophores interact with a range of chromophores situated further than the closest neighbour, and therefore a lot more chromophores (as the number of chromophores situated at a certain radius increases with the radius squared). This is further illustrated by the top and bottom plots of figure 6.10, where the homogeneous broadening has been changed to either $\sigma = 30$ meV (top)

or $\sigma = 110\,\text{meV}$ (bottom). In the case of $\sigma = 30\,\text{meV}$, the chromophore energies are almost all the same for interactions slower than 5 ps. What makes the interactions slower is then the increase of the centre-to-centre separation. In the case of $\sigma = 110\,\text{meV}$, there are many more pairs of very different energies, resulting in a much greater number of interacting pairs faster than 5 ps. We can also remark that the $R_{ji}^{out,00}$ hops are slower than the $R_{ji}^{out,01}$ hops. This is perhaps counter-intuitive, as the spectral overlap will be larger for the case where the donor emits at the absorption energy, but can be explained by the weaker absorption dipole moment, compared to the emission dipole.

Additionally, the microscopic rate-equation model enables the choice of different excitation wavelengths and effectively simulates the effect on the system. We would expect the exciton dynamics to be modified if the pump has an energy above or below the main absorption peak. Indeed, if the pump has a lower energy than the absorption peak, then the chromophores excited by the pump will already be the low energy ones, and thus no spectral diffusion will take place, whereas the opposite is expected if the pump excites the sample at much higher energy than the absorption peak. This is successfully predicted by our microscopic "rate-equation" model, as displayed in figure 6.9(c). The wavelengths we have chosen are 375 nm (3.30 eV), 400 nm (3.10 eV), and 425 nm (2.92 eV), compared to the absorption peak at 3.07 eV.

6.5.3 Exciton diffusion length

At low exciton density, when exciton-exciton annihilation effects are negligible, we are able to obtain diffusion properties from our model. Indeed, excitation of the ensemble of chromophores by a spatially Gaussian-shaped (rather than uniform) pump and recording its standard deviation over time will provide knowledge of the diffusion coefficient and of the diffusion length. When specified, we use such a technique to obtain the diffusion properties of the sample. An example of the excitation of the system by a Gaussian-shaped pump is provided in figure 6.11. The Gaussian is one dimensional, along the $\boldsymbol{x}$-axis (arbitrarily situated in the plane of the thin-film), and the plot of figure 6.11 shows the total exciton probability for all the chromophores situated in the vicinity of one of the 50 grid points along the $\boldsymbol{x}$-axis.

The standard one dimensional diffusion equation is [257]:

$$\frac{\partial n}{\partial t} = D\frac{\partial^2 n}{\partial x} \ . \tag{6.19}$$

By recording the standard deviation of the one dimensional exciton probability, σ_D, we obtain the diffusion coefficient D from the solution of this standard one-

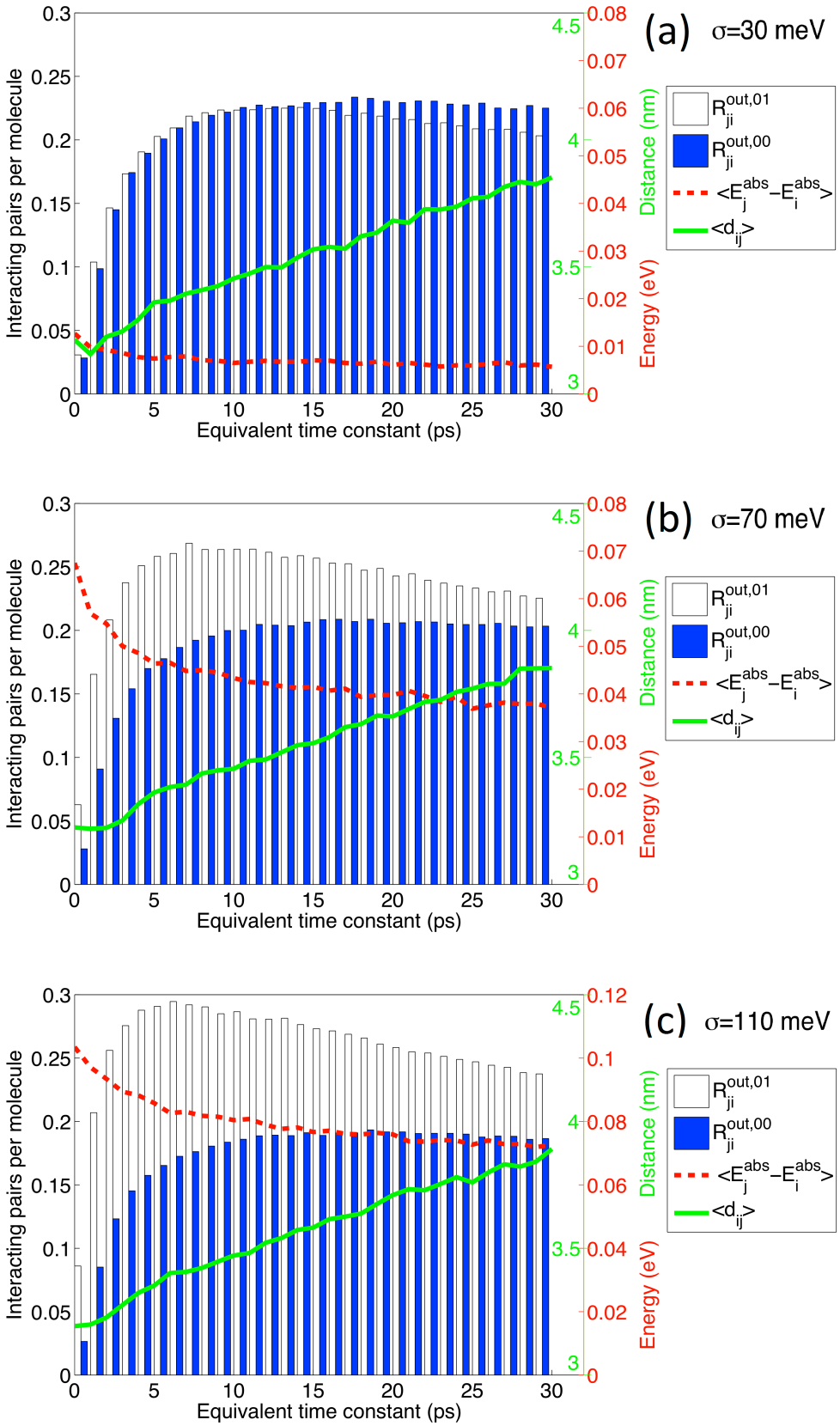

Figure 6.10: Histogram of the average numbers of neighbouring molecules interacting at the given timescale with one specific molecule, for the inhomogeneous broadenings (a) $\sigma = 30$ meV, (b) $\sigma = 70$ meV and (c) $\sigma = 110$ meV.

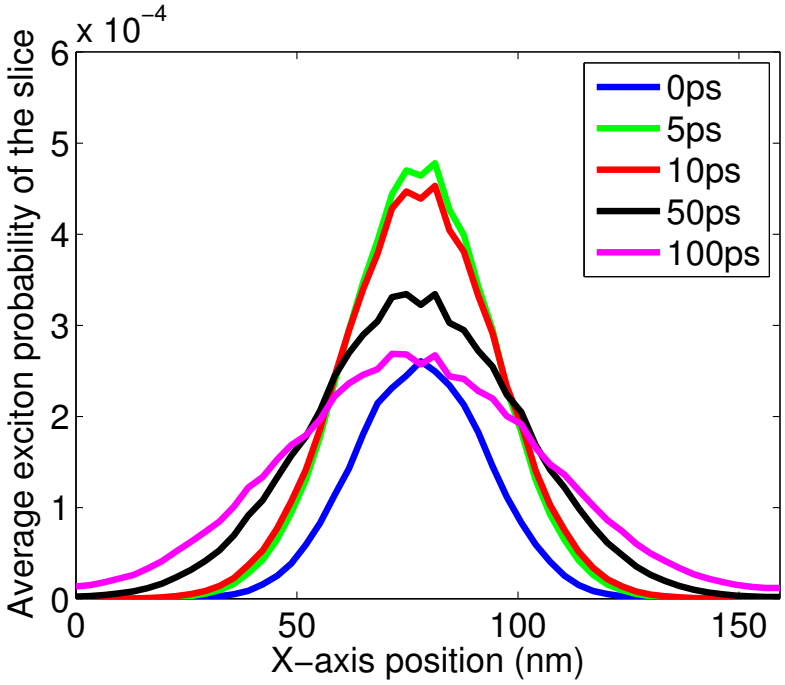

Figure 6.11: Plot of the total exciton probability as a function of the $\boldsymbol{x}$ coordinate, when the sample is excited by a one dimensional Gaussian-shaped pump along the $\boldsymbol{x}$-axis, at different times following excitation.

dimensional diffusion equation [257]:

$$D(t) = \frac{\sigma_D(t)^2 - \sigma_D(0)^2}{2t} \ . \tag{6.20}$$

From there, we calculate the exciton diffusion length L^D, given by [258, 259]:

$$L_D{}^2 = \int_0^{\tau^r} D(t)dt \ . \tag{6.21}$$

The exciton diffusion coefficient D and the quantity $L(t) = \sqrt{\int_0^t D(t')dt'}$ are plotted in figure 6.12. The usual exciton diffusion length is obtained from $L_D = L(\tau^r)$. As $\tau^r = 110\,\text{ps}$, we obtained an exciton diffusion length in polyfluorene film of approximately $L_D \approx 20\,\text{nm}$. This is very close to the exciton diffusion length measured experimentally by Monkman et al. [259] in polyfluorene films, their experiments leading to $L_D = 22\,\text{nm}$. This very good agreement with previously published results reassures us in the fact that our model enables us to describe ultra-fast exciton dynamics in polyfluorene films, at least at low pump intensities.

6.6 High pump intensity: exciton-exciton annihilation

In this Section we conduct a study of exciton-exciton annihilation, which plays an important role in the exciton dynamics of polyfluorene films at high pump inten-

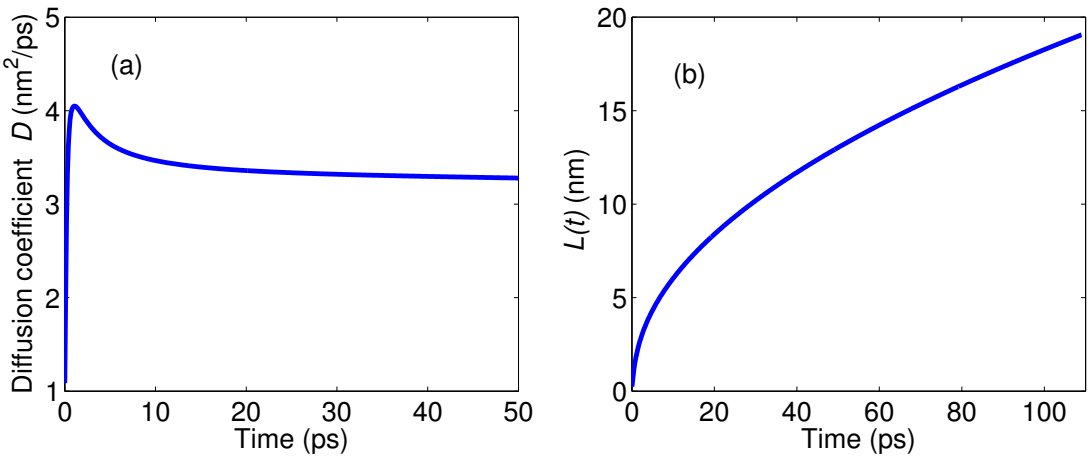

Figure 6.12: Plot of (a) the exciton diffusion coefficient D and (b) the quantity $L(t) = \sqrt{\int_0^t D(t')dt'}$ obtained by excitation of the sample by a one dimensional Gaussian pump.

sities [234]. In particular, as we have seen in Chapter 1, exciton-exciton annihilation can seriously impact the performance of organic lasers, because the amplifier materials can be subject to high photo-excitation densities.

6.6.1 Excited-state absorption parameter selection

The chromophores excited-state absorption properties are necessary for the computation of the exciton-exciton annihilation rates between two pairs of chromophores. However, with the current standard experimental techniques, it is not possible to accurately obtain the excited-absorption characteristics of molecular materials around the emission or absorption energies [123] - the energy range relevant for the calculation of the exciton-exciton annihilation rates. Computational methods for the calculations of such properties are not reliable yet either [123]. We therefore cannot fully predict exciton-exciton annihilation rates, but we will need to fit some parameters to experimental results.

We decided to arbitrarily fix the excited-state absorption peak of any chromophore at twice its emission peak (from the ground state). Therefore an excitation will have its emission resonant with excited-state absorption. This is supported by the strong exciton-exciton annihilation rates observed experimentally in PF8 films [234]. We do not include any vibrational peaks, because we do not want to add additional unknown parameters to the model. The homogeneous broadening γ_{XX} of the excited-state absorption peak is taken such as $\gamma_{XX} = 2\gamma$, to account for relaxation to the excited state before relaxation to the ground-state.

The parameters we still need to compute are the exciton-exciton annihilation rates between pairs are the excited-state absorption dipole length, l_{XX}, and mo-

ments, d_{XX}. We fixed l_{XX} to $l_{XX} = 5\,\text{nm}$, as this value is between the absorption and emission lengths. We now just need to find a realistic value for the excited-state absorption dipole moment. The exciton-exciton annihilation rate, η^{XX}, defined as the time-dependent quantity in the equation:

$$\frac{\mathrm{d}n}{\mathrm{d}t} = -\frac{n(t)}{\tau^r} - \eta^{XX} n(t)^2 \,, \tag{6.22}$$

where $n(t)$ is the exciton density of the sample, has been measured in PF8 films [234]. In these measurements, η^{XX} varies within the first 15 ps and then becomes constant, at $\eta^{XX} \approx 1.5 \times 10^{-8}\,\text{cm}^3/\text{s}$.

We calculated η^{XX} using equation (6.22), where the total density $n(t)$ is given in our calculations by $n(t) = \sum_i (n_i^1(t) + n_i^0(t))$. We observed that η^{XX} does not depend on the pump intensity (see figure 6.13). We can use the excited-state absorp-

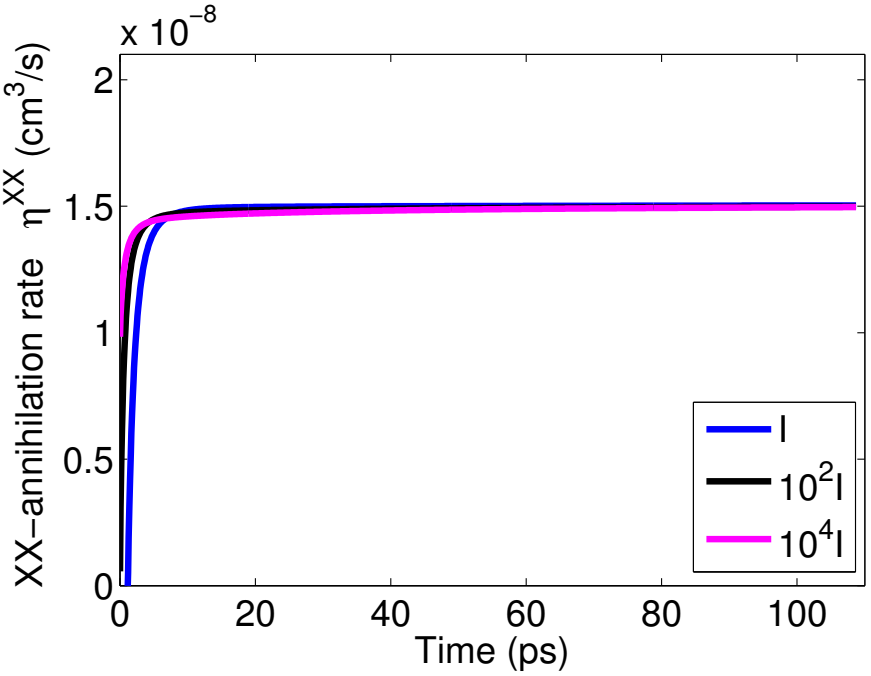

Figure 6.13: Exciton-exciton annihilation rates η^{XX} as a function of time, for three different pump intensities - the strongest pump leads to significant exciton-exciton annihilation, whereas the weakest pump barely affects the decay of the total exciton density.

tion dipole moment, d_{XX}, as the fitting parameter to obtain $\eta^{XX} \approx 1.5 \times 10^{-8}\,\text{cm}^3/\text{s}$ out of our calculations. With our set of fixed parameters, the dipole moment we obtain is $d_{XX} = 3.15\ e\text{Å}$, which is a value which is consistent with the absorption and emission dipole moments we calculated. The exciton-exciton annihilation rates η^{XX} we obtained with this set of parameters, for three different pump intensities, are plotted in figure 6.13.

6.6.2 Results and discussion

We wished to compare the results we obtained with our model to the experimental results published by Shaw et al. [234], where photoluminescence decays are recorded for a variety of pump intensities. For this purpose we need to relate the experimental pump intensities to the pump intensities of our model. We therefore fit the pump intensity of the model to one pump intensity used in the experiments. We chose the experimental pump intensity corresponding to an exciton density of 1.8×10^{17} cm^{-3}, as this is the lowest pump intensity where the recorded exciton photoluminescence exhibits exciton-exciton annihilation features. We can obtain a good fit of the experimental data for a theoretical pump intensity we call I. From there, we can calculate the exciton density decays for the multiples of I corresponding to the experimental observations. The results are represented in figure 6.14.

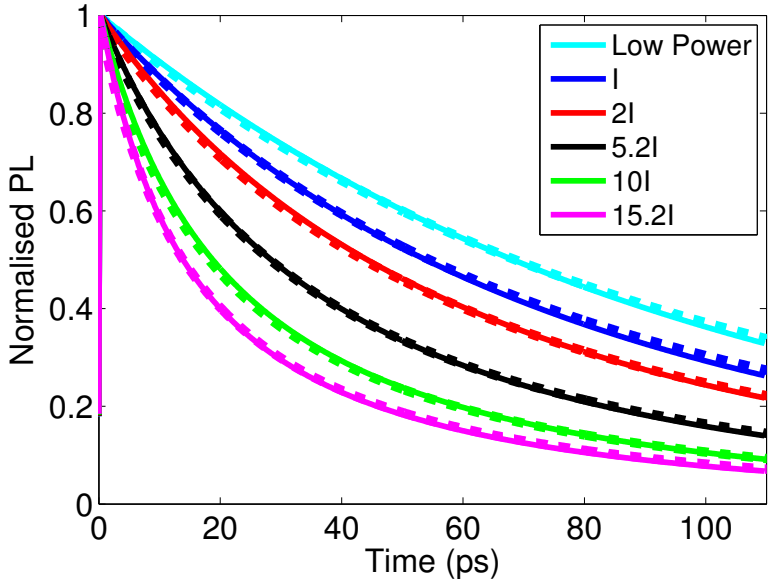

Figure 6.14: Variation of the photoluminescence for a series of different pump intensities. Theoretical data are represented by solid lines, fits to experimental data (from reference [234]) by dashed lines.

We observe very good agreement between the theoretical data and the fit to the experimental photoluminescence measurements (this fit is a three-exponential fit of the measured data-points, detailed in reference [234]). The photoluminescence decays are well reproduced by the calculations over the progression of the pump intensities. These results validate our model even further. This is also illustrated by figure 6.15. In this plot, we have compared the theoretical effective exciton lifetimes τ^r_{eff} with the experiments. The effective exciton lifetimes are taken as the times it takes to reach 1/e of the expected peak total exciton density. Very good agreement between the experiment and theory is obtained. In addition, we have plotted in figure 6.15 the effective exciton diffusion lengths L^D_{eff} associated with these effective

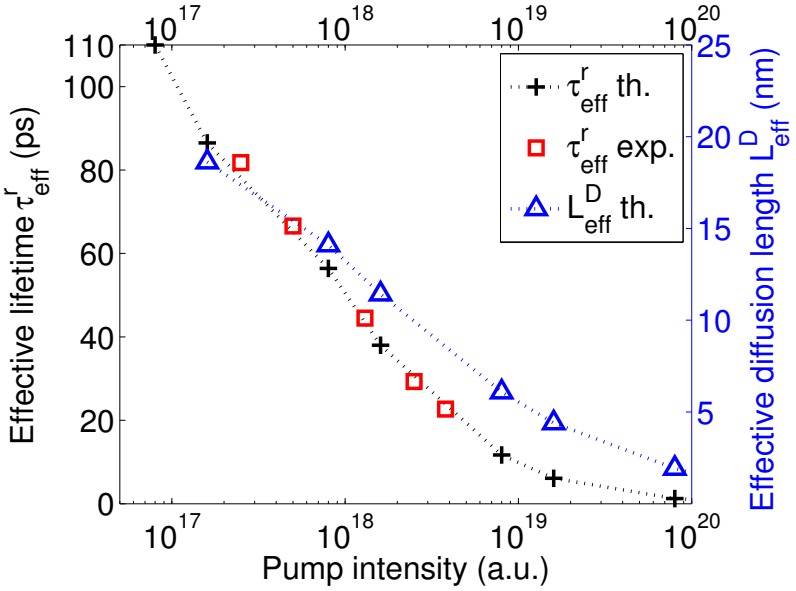

Figure 6.15: Variation of the effective exciton lifetime with pump intensity. The theoretical results are represented by the black line and the experimental results (from reference [234]) by the red squares. The associated effective exciton diffusion lengths are drawn in blue.

lifetimes. These effective diffusion lengths are obtained from figure 6.12: they are read from the diffusion length corresponding to the effective exciton lifetime (τ^r is replaced by τ^r_{eff} in equation (6.21)). It is clearly visible that for increasing pump intensities, the annihilation is the factor limiting the diffusion length.

Even if we had to fit one parameter to obtain some of these results, the overall quantitative agreement of all these results between experiments and theory suggest that our model captures very well all the physical processes involved in the ultrafast exciton dynamics of polyfluorene films. This is further supported by a series of calculations where Förster hopping is disabled in the calculations, so that the excitons cannot diffuse to other chromophores once they are created by the pump. However, exciton-exciton annihilation processes still take place. We have calculated the exciton-exciton rates and photoluminescence decays for such a situation. The results are displayed in figure 6.16. We observe that the calculated photoluminescence decays are not in as good agreement with the experiments as before, and that the exciton-exciton annihilation rates η^{XX} now depend on the pump intensities and vary much more strongly with time than when Förster energy transfer is allowed. This means that it is not possible to find a value to fit the parameter d_{XX} that enables us to reproduce the experimental results well. Indeed, we might be able to fit the photoluminescence decay for one pump intensity, but the other photoluminescence decays will not be in good agreement with the experiments. This again supports the fact that exciton diffusion processes are well captured in our model.

When Förster energy transfer is forbidden, we observe a decrease of the exciton-

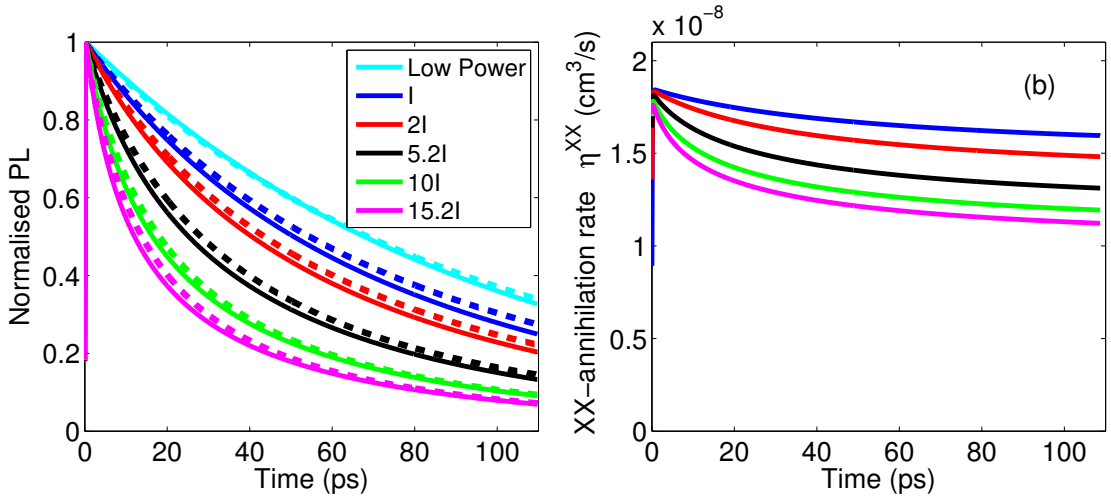

Figure 6.16: Calculated (a) photoluminescence decays and (b) exciton-exciton annihilation rates η^{XX} for different pump intensities, when Förster energy transfer is forbidden in the calculations. Theoretical data are represented by solid lines, experimental data (from reference [234]) by dashed lines.

exciton annihilation rates η^{XX}. This decrease comes from the fact that once highly populated neighbouring sites have been depleted by exciton-exciton annihilation, no more annihilations occur in the system. In contrast, when Förster energy transfer is allowed, the low energy, highly populated sites will receive excitons from other sites as exciton-exciton annihilation occurs on these low energy sites, so that exciton-exciton annihilation takes place at the same rate at any time. In agreement with [234], this indicates that exciton-exciton annihilation is diffusion-controlled in polyfluorene films. In such a case, the exciton-exciton annihilation rate η^{XX} can be expressed as [234]:

$$\eta^{XX} = 4\pi R_a D \left(1 + \frac{R_a}{\sqrt{\pi D t}}\right) , \tag{6.23}$$

where R_a is a constant (the "annihilation radius"). We notice that when $Dt \gg R_a$, then η^{XX} is constant, but when $Dt \ll R_a$, η^{XX} decreases with time. The first case corresponds to Förster hopping being enabled in our calculations, the second case to Förster hopping being disabled.

Despite the lack of available methods to obtain the parameters involved in exciton-exciton annihilation processes without fitting experimental results, we obtained meaningful results and predictions of exciton-exciton annihilation processes in polyfluorene films. In addition, these results further support the exciton diffusion results we presented in Section 6.5, where exciton-exciton annihilation was negligible, showing further evidence that exciton diffusion is well captured by our model.

6.7 Conclusions

We have developed a flexible model to understand and simulate exciton dynamics in films of linear chromophores. We have shown, by comparing the predictions with anisotropy experiments, that sufficient parameters can be obtained from simple spectra and quantum chemistry to allow good agreement without requiring any tuning parameters. Our model enables us to gain additional knowledge of exciton transfer processes that are not accessible experimentally; for instance, that excitons migrate directly to low energy chromophores and that, in consequence, energy-matching plays a more important role than chromophore proximity in determining the chromophore pairs where exciton transfer takes place. We have also extracted the exciton diffusion length of such a film, the value being in very good agreement with previously published experimental data. In addition, our model includes exciton-exciton annihilation. Despite the lack of available methods to obtain the parameters involved in exciton-exciton annihilation processes without fitting experimental results, we obtained meaningful results and predictions of exciton-exciton annihilation processes in polyfluorene films. These results show further evidence that exciton diffusion is well captured by our model, and provides us with insight on how Förster transfer plays a role in exciton-exciton annihilation processes.

Chapter 7

Conclusions and future work

We will conclude this thesis by summarising the most prominent results presented throughout these Chapters. We will then suggest some directions for future research and some important questions that remain to be addressed to further increase the understanding of the ultra-fast photo-dynamics of organic semiconductors, on the basis of the knowledge we have gained through the work presented here.

7.1 Conclusions

We have given an introduction to organic semiconductors, and in particular to their basic photo-physics, in Chapter 1. The importance of organic semiconductors for the fabrication of a new generation of electronic devices has been presented, in addition to the basic principles of the operation of these devices, with an emphasis on how the fundamental photo-physics properties of organic semiconductor materials govern characteristics and performances of the device. This enabled us to highlight the current challenges associated with molecular semiconducting materials. A theoretical description of exciton dynamics in real systems, that we could compare to experimental data measured by our collaborators at the University of St-Andrews, appeared to be a relevant way to address the fundamental challenges of exciton dynamics in these materials. This description thus constitutes the focus of the work presented in this thesis.

To develop successful models of exciton transfer in organic semiconductors, we have utilised the methods we have presented in Chapter 2. We believe that the combination of quantum chemistry methods, used at a level of theory which provides good predictions of measurable quantities, with a model using a density-matrix approach for large systems (such as the optical Bloch equations (OBE)), can provide good theoretical predictions of the exciton dynamics in molecular systems. Indeed, we have demonstrated that quantum chemistry calculations can describe very accurately single molecules properties, such as transition energies and dipoles, in fluorenes. Once these single-molecule properties are known, they can be used for the time-dependent simulations of the exciton density of realistic ensembles of fluorenes, the equations governing the system being derived from the OBE. However, we have shown that calculations of a system of slightly more than a couple of molecules in the framework of the OBE are not computationally tractable, and approximations

to the OBE will be needed to conduct large-scale simulations.

We have chosen to start our work with the study of a class of molecules with known conformation in solution, where intra-molecular exciton transfer is likely to happen: star-shaped molecules. More precisely, we investigated benzene- and truxene-cored molecules, with three branched arms made of fluorene chains - the length of these chains varying from zero to four fluorene units. Our theoretical results were supported by experimental measurements of the transition dipoles and energies. We found very good qualitative and quantitative agreement between our calculations and the experiments, indicating that the theoretical results could be relied upon. We gained valuable knowledge about the optical and electronic properties of these molecules: we demonstrated that the C_3-symmetry of the star-shaped molecules was responsible for degenerate absorption states, resulting in uniform photo-excitation all over the molecules (if excited by an isotropic light source). However, the excited-state geometry cannot be symmetric, due to the shape of the excited state energy potential, and as a consequence the excitation will necessarily relax to one of the three arms of the molecule - the actual arm where excitation relaxes depending on slight initial molecular conformal perturbations. This work was presented in Chapter 3

It was nevertheless not clear from this study which arm the excitation will choose to relax onto in the real star-shaped molecules. The time-scale of this relaxation process was also not known, as it is impossible to calculate such a quantity by density functional theory (DFT). In addition, incoherent exciton transfer between arms was a possibility which could not be investigated by DFT either. This is why we conducted a combined experimental and theoretical study of fluorescence anisotropy in solutions of these star-shaped molecules, described in Chapter 4. We demonstrated that the experimentally recorded fluorescence anisotropy could not correspond to fluorescence anisotropy detected in C_3-symmetric molecules, with degenerate absorption levels. We then proposed a theory to explain the measured fluorescence anisotropy on the basis of quantum chemistry calculations. Indeed, the recorded fluorescence anisotropy was what we would expect for non-degenerate "rod-like" molecules; we demonstrated that symmetry-breaking defects exist at room temperature, creating a splitting of the originally degenerate levels. This splitting is large enough that the experimental pump pulse would excite only one of the two absorption levels. By conducting a series of quantum chemistry calculations for a variety of defects, we reached the conclusion that molecules with one absorption energy lower than the original absorption levels would exhibit less depolarisation due to molecular relaxation than molecules with higher absorption energies. This was confirmed experimentally. In addition to the fast (hundreds of fs) anisotropy decay due to molecular relaxation, we have assigned the slower (few ps) anisotropy

decay to excitation transfer between arms. This was supported by calculations of the associated Förster rates.

Our work so far enabled us to gain more detailed knowledge of intra-molecular excitation transfer in these fluorene-based molecules. However, inter-molecular processes are also significant in organic films. In Chapter 5, we discussed the validity of the point- and line- dipole models by comparing the interaction energies calculated from these models for a series of configurations of pairs of oligofluorene molecules to the interaction energy extracted from quantum chemistry calculations. We demonstrated that even the line-dipole model could not accurately describe interactions at separations and conformations typical of films. We proposed an improved version of the line-dipole model which performs much better than the conventional line-dipole model, and enables very accurate calculation of interactions for any configuration, at the same low computational cost as the line-dipole model. Rather than using a sinusoidal sub-dipole moment distribution of the length of half a period, our improved model uses a sinusoidal distribution with a number of nodes and anti-nodes to mimic more accurately the charge distribution of the excited molecules.

In Chapter 6, we used this improved line-dipole model to calculate the interaction energies in a randomly generated large ensemble of 125 000 chromophores. These chromophores represent an ensemble of polyfluorene molecules, and are approximated as octamer oligofluorene molecules. The chromophores are randomly positioned and oriented and their density is the same as the experimental mass density of a PF8 fluorene film. These chromophores also each possess their own absorption and emission energies, to mimic inhomogeneous broadening. This enables the calculation of spectral overlaps between two chromophores, and therefore accurate estimation of incoherent Förster hopping rates between any pairs of chromophores. The parameters of this model are all fixed by quantum calculations or by experimental measurements of the emission and absorption spectra. We can calculate the fluorescence anisotropy of such a theoretical system. Comparison with experimental measurements of fluorescence anisotropy recorded out of a PF8 polyfluorene film shows very good agreement. In both cases, the observed anisotropy decay is very fast, on the order of 680 fs, indicating ultra-fast excitation migration in the ensemble of chromophores. We demonstrate that for this material, no mechanisms other than incoherent Förster hopping need to be invoked to explain the observed anisotropy decay, and that it is therefore the main mechanism governing measurable exciton transfer at this time-scale. We also demonstrate that the excitation transfers directly to the low-energy molecules, and that consequently the sample morphology plays a minor role in the exciton dynamics, with energy-matching (spectral overlap) having a much more significant role. In addition, we obtained exciton diffusion length in very good agreement with previously published experimental data, and

we also account for exciton-exciton annihilation at high pump intensity - we can reproduce the exciton lifetime variation with pump intensity very well. For all these reasons, we believe the model we have developed is a new powerful tool to simulate and understand further exciton dynamics mechanisms. The agreement of the experimental results with our theoretical predictions, showing sub-picosecond exciton transfer in polyfluorene films, which had, to the best of our knowledge, never been obtained prior to this research, strongly supports this.

7.2 Future work

With the validity of this exciton dynamics model having been demonstrated in polyfluorene films, it would be extremely interesting to use this model to investigate additional questions, such as how films of mixed different species behave, or what the influence of more complex morphologies is on the exciton dynamics, and to extend the model further. The research possibilities are numerous and would require an extensive amount of work, and will hopefully be the subject of further investigation in our group. As we have seen in the introductory Chapter, solar cells are made of blends of materials, and the energy transfer dynamics in such systems is therefore very complex. However it is crucial to know the diffusion properties of these devices to ensure the most efficient collection of charges at the electrodes. It could therefore be very helpful to be able to model diffusion in films of common blend of materials. A way to achieve this would be, for instance, to start by simulating systems of mixed-phase polyfluorenes (α- and β-phases). Indeed, this would be a simple extension to the model (and is actually already almost implemented). The resulting predictions would be easy to compare with already existing data for such a system, such as measurements of exciton-exciton annihilation rates - because the β-phase molecules are at much lower energy than the α-phase chromophores, they play the role of traps and quench the excitation.

Once mixed film systems are successfully simulated, the study of the influence of various possible morphologies on exciton dynamics will be of particular interest. This could indeed help us understand, for instance, how molecular species are mixed in such films, or how to improve the mixing to make the devices more efficient.

The model could also be extended to use more realistic sample morphologies. In the work we have presented, we have used an ensemble of randomly oriented and positioned chromophores to mimic an ensemble of polyfluorene molecules. A better ensemble of chromophores could be generated using molecular dynamics simulations. This would be more accurate as the chromophore sizes would be more realistic and better positioned to mimic polyfluorene chains or the mixing of two different species, for example. Comparison of exciton dynamics results from our model with other

experiments would also enable us to either confirm or refute the molecular dynamics results.

Using quantum chemistry with quadratic response theory would also provide us with theoretical excited-state absorption properties, and therefore exciton-exciton annihilation would be simulated without fitting any parameters. This would greatly enhance the model for high pump intensity cases. Similarly, having methods to calculate homogeneous broadening would be useful and allow one to avoid the need for experimental spectral data. Inhomogeneous broadening could possibly be obtained by molecular dynamics. In this case, a model relying totally on theory would be achieved, and no experiments would be necessary at all!

Additional physics mechanisms could also be included, for instance, coherent energy transfer. However, in polyfluorenes, it seems that coherent effects would not add much to the exciton dynamics at the 100 fs time-scale, and including coherences in the equations would not be an easy task. We believe the reasons for including such a mechanism are limited; however it would be useful to include other effects such as the creation of polarons to model processes taking place in solar cells better and free charges transport phenomena. Dexter transfer could be accounted for for the studies of relevant materials, by the calculation of molecular orbitals by quantum chemistry, and by the calculation of the subsequent molecular orbital overlaps - there is currently no computationally tractable way of doing this to the best of our knowledge.

It is clear that there are still lots of possibilities for further work to better understand energy transfer in organic semiconductors, building from the basis of the work we have presented in this thesis. In this context, the good results we obtained from our model, compared to the experiments, is a very encouraging sign that this research was focused in the right direction.

Appendix A

A.1 Spectral overlaps between two chromophores

Here we give the results needed for the evaluation of spectral overlaps between Lorentzian lineshapes. If $L(x,a)$ is a normalised Lorentzian:

$$L(x,a) = \frac{1}{\pi}\frac{\gamma}{\gamma^2 + (x-a)^2}, \tag{A.1}$$

centered at $x = a$, and of linewidth γ, then

$$\int_{-\infty}^{\infty} L(x,a)\ L(x,b)\ dx = \frac{2}{\pi}\frac{\gamma}{4\gamma^2 + (a-b)^2}. \tag{A.2}$$

If now the second lorentzian has the linewidth 2γ, the integral of the products is

$$\frac{3}{\pi}\frac{\gamma}{9\gamma^2 + (a-b)^2}. \tag{A.3}$$

These formulae are used to calculate the appropriate spectral overlaps.

A.2 Derivation of the source term

The Optical Bloch Equations (OBE) for a two-level system are [173]:

$$i\hbar\frac{\mathrm{d}p}{\mathrm{d}t} = (-\varepsilon - i\gamma)\,p - (1-n)\,\boldsymbol{d}\cdot\boldsymbol{E}(t), \tag{A.4}$$

$$\hbar\frac{\mathrm{d}n}{\mathrm{d}t} = 2\ \mathrm{Im}\left[p\ \boldsymbol{d}\cdot\boldsymbol{E}^*(t)\right], \tag{A.5}$$

where p is the polarisation between the two levels, n is the excitation probability (population of the higher level), γ the pure-dephasing, ε the energy difference between the two levels, d the transition dipole and E the pumping optical field.

Defining $\tilde{E}(t) = E(t)\mathrm{e}^{i\omega_0 t}$ and $\tilde{p}(t) = p(t)\mathrm{e}^{i\omega_0 t}$, with $\hbar\omega_0 = \varepsilon$ and using the Rotating Wave Approximation (RWA) for a monochromatic source of angular frequency ω_0 (on resonance with the two-level system), then

$$\tilde{E}(t) = \frac{E_0}{2}, \tag{A.6}$$

and similarly for $\tilde{p}$. The OBE can therefore be rewritten as:

$$i\hbar\frac{\mathrm{d}\tilde{p}}{\mathrm{d}t} = -i\gamma\tilde{p} - (1-2n)\boldsymbol{d}\cdot\tilde{\boldsymbol{E}}(t), \tag{A.7}$$

$$\hbar\frac{\mathrm{d}n}{\mathrm{d}t} = 2\mathrm{Im}\left[\tilde{p}\boldsymbol{d}\cdot\tilde{\boldsymbol{E}}^{*}(t)\right]. \tag{A.8}$$

With a monochromatic source of angular frequency ω_0, $\frac{\mathrm{d}\tilde{p}}{\mathrm{d}t} = 0$ and therefore $\tilde{p} = i(1-2n)\boldsymbol{d}\cdot\tilde{\boldsymbol{E}}(t)/\gamma$. The source term $\rho = \mathrm{Im}\left[\tilde{p}\boldsymbol{d}\cdot\tilde{\boldsymbol{E}}^{*}(t)\right]$ from the pump in the equation for n is then such that

$$\rho \propto (1-2n)\left|\boldsymbol{d}\cdot\tilde{\boldsymbol{E}}(t)\right|^{2}. \tag{A.9}$$

This is for a monochromatic source at angular frequency ω_0. From the OBE we can deduce the linear susceptibility $\chi(\hbar\omega)$:

$$\chi(\hbar\omega) = \frac{P(\hbar\omega)}{E(\hbar\omega)} = \frac{(1-2n)\ d}{\hbar\omega - \epsilon - i\gamma}. \tag{A.10}$$

Therefore, a monochromatic source at the angular frequency ω, close to ω_0, will produce the following polarisation in the frequency domain:

$$P(\hbar\omega) = \frac{(1-2n)\ d\ E(\hbar\omega)}{\hbar\omega - \epsilon - i\gamma}. \tag{A.11}$$

In such case:

$$\rho \propto \frac{(1-2n)\ \left|\boldsymbol{d}\cdot\tilde{\boldsymbol{E}}(t)\right|^{2}\gamma E(\hbar\omega)}{(\hbar\omega-\epsilon)^{2}+\gamma^{2}}, \tag{A.12}$$

$$\rho \propto (1-2n)\ \left|\boldsymbol{d}\cdot\tilde{\boldsymbol{E}}(t)\right|^{2}\mathcal{A}(\hbar\omega)E(\hbar\omega), \tag{A.13}$$

For a non-monochromatic pump pulse of frequencies ω around ω_0, the source term can therefore be expressed as:

$$\rho \propto (1-2n)\ \left|\boldsymbol{d}\cdot\tilde{\boldsymbol{E}}(t)\right|^{2}\int\mathcal{A}(\hbar\omega)E(\hbar\omega)d(\hbar\omega). \tag{A.14}$$

This, at low probability, is the expression we used in equation (6.7) of our model.

References

[1] B. Yacobi. *Semiconductor Materials: An Introduction to Basic Principles*, pp. 1–3. Springer, 2003.

[2] B. Bolto, R. McNeill, and D. Weiss. Electronic Conduction in Polymers. III. Electronic Properties of Polypyrrole. *Australian Journal of Chemistry* **16**(6), 1090–1103 (1963).

[3] T. H. Maiman. Stimulated Optical Radiation in Ruby. *Nature* **187**(4736), 493–494 (1960).

[4] N. J. Holonyak and S. F. Bevacqua. Coherent (visible) light emission from $Ga(As_{1-x}P_x)$ junctions. *Applied Physics Letters* **1**(4), 82–83 (1962).

[5] C. W. Tang and S. A. VanSlyke. Organic electroluminescent diodes. *Applied Physics Letters* **51**(12), 913–915 (1987).

[6] A. Tsumura, H. Koezuka, and T. Ando. Macromolecular electronic device: Field-effect transistor with a polythiophene thin film. *Applied Physics Letters* **49**(18), 1210–1212 (1986).

[7] M. Riordan, L. Hoddeson, and C. Herring. The invention of the transistor. *Reviews of Modern Physics* **71**, S336–S345 (1999).

[8] D. M. Chapin, C. S. Fuller, and G. L. Pearson. A New Silicon p-n Junction Photocell for Converting Solar Radiation into Electrical Power. *Journal of Applied Physics* **25**(5), 676–677 (1954).

[9] C. W. Tang. Two-layer organic photovoltaic cell. *Applied Physics Letters* **48**(2), 183–185 (1986).

[10] B. H. Soffer and B. B. McFarland. Continuously tunable, narrow-band organic dye lasers. *Applied Physics Letters* **10**(10), 266–267 (1967).

[11] N. Karl. Laser emission from an organic molecular crystal. *Physica Status Solidi A* **13**(2), 651–655 (1972).

[12] I. D. W. Samuel and G. A. Turnbull. Organic Semiconductor Lasers. *Chemical Reviews* **107**, 1272 (2007).

[13] D. Moses. High quantum efficiency luminescence from a conducting polymer in solution: A novel polymer laser dye. *Applied Physics Letters* **60**(26), 3215–3216 (1992).

[14] W. Brütting. *Physics of Organic Semiconductors.* Wiley-VCH Verlag, 1st edition, 2006.

[15] A. J. Heeger, S. Kivelson, J. R. Schrieffer, and W. P. Su. Solitons in conducting polymers. *Reviews of Modern Physics* **60**, 781–850 (1988).

[16] A. J. Heeger. Nobel Lecture: Semiconducting and metallic polymers: The fourth generation of polymeric materials. *Reviews of Modern Physics* **73**(14), 681–700 (2001).

[17] Wikimedia Commons. Data base of images in the public domain, http://commons.wikimedia.org.

[18] S. Brazovskii and N. Kirova. Physical theory of excitons in conducting polymers. *Chemical Society Reviews* **39**, 2453–2465 (2010).

[19] A. Moliton and R. C. Hiorns. Review of electronic and optical properties of semiconducting -conjugated polymers: applications in optoelectronics. *Polymer International* **53**(10), 1397–1412 (2004).

[20] N. Kirova, S. Brazovskii, and A. Bishop. A systematic theory for optical properties of phenylene-based polymers. *Synthetic Metals* **100**(1), 29–53 (1999).

[21] M. Wohlgenannt, X. M. Jiang, Z. V. Vardeny, and R. A. J. Janssen. Conjugation-Length Dependence of Spin-Dependent Exciton Formation Rates in Π-Conjugated Oligomers and Polymers. *Physical Review Letters* **88**, 197401 (2002).

[22] C. Kittel. *Introduction to Solid State Physics.* Willey, 1996.

[23] A. J. Heeger. Semiconducting polymers: the Third Generation. *Chemical Society Reviews* **39**, 2354–2371 (2010).

[24] J. D. Myers and J. Xue. Organic Semiconductors and their Applications in Photovoltaic Devices. *Polymer Reviews* **52**(1), 1–37 (2012).

[25] R. Knox. *Theory of excitons.* Academic Press, US, 1963.

[26] R. Smith. *Semiconductors.* University Press, Cambridge, 1978.

[27] S. F. Alvarado, P. F. Seidler, D. G. Lidzey, and D. D. C. Bradley. Direct Determination of the Exciton Binding Energy of Conjugated Polymers Using a Scanning Tunneling Microscope. *Physical Review Letters* **81**, 1082–1085 (1998).

[28] M. Chandross, S. Mazumdar, M. Liess, P. A. Lane, Z. V. Vardeny, M. Hamaguchi, and K. Yoshino. Optical absorption in the substituted phenylene-based conjugated polymers: Theory and experiment. *Physical Review B* **55**, 1486–1496 (1997).

[29] I. H. Campbell, T. W. Hagler, D. L. Smith, and J. P. Ferraris. Direct Measurement of Conjugated Polymer Electronic Excitation Energies Using Metal/Polymer/Metal Structures. *Physical Review Letters* **76**, 1900–1903 (1996).

[30] V. May and O. Kühn. *Charge and Energy Transfer Dynamics in Molecular Systems*. Wiley-VCH, 2d, revised and enlarged edition, 2008.

[31] T. Nelson, S. Fernandez-Alberti, A. E. Roitberg, and S. Tretiak. Nonadiabatic excited-state molecular dynamics: Treatment of electronic decoherence. *The Journal of Chemical Physics* **138**(22), 224111 (2013).

[32] I. Hwang and G. D. Scholes. Electronic Energy Transfer and Quantum-Coherence in -Conjugated Polymers. *Chemistry of Materials* **23**(3), 610–620 (2011).

[33] B. Kraabel, D. Moses, and A. J. Heeger. Direct observation of the intersystem crossing in poly(3-octylthiophene). *The Journal of Chemical Physics* **103**(12), 5102–5108 (1995).

[34] N. I. Nijegorodov and W. S. Downey. The Influence of Planarity and Rigidity on the Absorption and Fluorescence Parameters and Intersystem Crossing Rate Constant in Aromatic Molecules. *The Journal of Physical Chemistry* **98**(22), 5639–5643 (1994).

[35] D. Beljonne, Z. Shuai, G. Pourtois, and J. L. Bredas. SpinOrbit Coupling and Intersystem Crossing in Conjugated Polymers: A Configuration Interaction Description. *The Journal of Physical Chemistry A* **105**(15), 3899–3907 (2001).

[36] M. Yan, L. J. Rothberg, E. W. Kwock, and T. M. Miller. Interchain Excitations in Conjugated Polymers. *Physical Review Letters* **75**, 1992–1995 (1995).

[37] N. A. Montgomery, J.-C. Denis, S. Schumacher, A. Ruseckas, P. J. Skabara, A. Kanibolotsky, M. J. Paterson, I. Galbraith, G. A. Turnbull, and I. D. W. Samuel. Optical Excitations in Star-Shaped Fluorene Molecules. *The Journal of Physical Chemistry A* **115**(14), 2913–2919 (2011).

[38] D. Beljonne, G. Pourtois, C. Silva, E. Hennebicq, L. M. Herz, R. H. Friend, G. D. Scholes, S. Setayesh, K. Mu, and J. L. Bre. Interchain vs . intrachain

energy transfer in acceptor-. *Proceedings of the National Academy of Sciences* **99**(17), 10982 (2002).

[39] J. Franck and R. Livingston. Remarks on Intra- and Inter-Molecular Migration of Excitation Energy. *Reviews of Modern Physics* **21**, 505–509 (1949).

[40] T. Forster. 10th Spiers Memorial Lecture. Transfer mechanisms of electronic excitation. *Discussions of the Faraday Society* **27**, 7–17 (1959).

[41] R. M. Clegg. Förster resonance energy transfer—FRET what is it, why do it, and how it's done. In T. Gadella, editor, *Fret and Flim Techniques*, volume 33 of *Laboratory Techniques in Biochemistry and Molecular Biology*, pp. 1–57. Elsevier, 2009.

[42] A. Olaya-Castro and G. D. Scholes. Energy transfer from Förster–Dexter theory to quantum coherent light-harvesting. *International Reviews in Physical Chemistry* **30**(1), 49–77 (2011).

[43] G. D. Scholes. Long-range resonance energy transfer in molecular systems. *Annual Review of Physical Chemistry* **54**(1), 57–87 (2003).

[44] T. Förster. Zwischenmolekulare Energiewanderung und Fluoreszenz. *Annalen der Physik* **437**(1-2), 55–75 (1948).

[45] G. D. Scholes, X. J. Jordanides, and G. R. Fleming. Adapting the Förster Theory of Energy Transfer for Modeling Dynamics in Aggregated Molecular Assemblies. *The Journal of Physical Chemistry B* **105**(8), 1640–1651 (2001).

[46] D. L. Dexter. A Theory of Sensitized Luminescence in Solids. *The Journal of Chemical Physics* **21**(5), 836–850 (1953).

[47] R. D. Jenkins, G. J. Daniels, and D. L. Andrews. Quantum pathways for resonance energy transfer. *The Journal of Chemical Physics* **120**(24), 11442–11448 (2004).

[48] G. D. Scholes and D. L. Andrews. Damping and higher multipole effects in the quantum electrodynamical model for electronic energy transfer in the condensed phase. *The Journal of Chemical Physics* **107**(14), 5374–5384 (1997).

[49] D. Andrews. A unified theory of radiative and radiationless molecular energy transfer. *Chemical Physics* **135**(2), 195–201 (1989).

[50] A. Czader and E. R. Bittner. Calculations of the exciton coupling elements between the DNA bases using the transition density cube method. *The Journal of Chemical Physics* **128**(3), 035101 (2008).

[51] B. P. Krueger, G. D. Scholes, and G. R. Fleming. Calculation of Couplings and Energy-Transfer Pathways between the Pigments of LH2 by the ab Initio Transition Density Cube Method. *The Journal Physical Chemistry B* **5647**(98), 5378–5386 (1998).

[52] G. D. Scholes and G. R. Fleming. *Energy Transfer and Photosynthetic Light Harvesting*, pp. 57–129. John Wiley & Sons, Inc., 2005.

[53] G. D. Scholes and K. P. Ghiggino. Electronic Interactions and Interchromophore Excitation Transfer. *The Journal of Physical Chemistry* **98**(17), 4580–4590 (1994).

[54] V. May. Beyond the Forster theory of excitation energy transfer: importance of higher-order processes in supramolecular antenna systems. *Dalton Transactions* , 10086–10105 (2009).

[55] G. J. Daniels, R. D. Jenkins, D. S. Bradshaw, and D. L. Andrews. Resonance energy transfer: The unified theory revisited. *The Journal of Chemical Physics* **119**(4), 2264–2274 (2003).

[56] D. Onidas, T. Gustavsson, E. Lazzarotto, and D. Markovitsi. Fluorescence of the DNA Double Helix (dA)20(dT)20 Studied by Femtosecond Spectroscopy-Effect of the Duplex Size on the Properties of the Excited States. *The Journal of Physical Chemistry B* **111**(32), 9644–9650 (2007).

[57] B. Fückel, A. Köhn, M. E. Harding, G. Diezemann, G. Hinze, T. Basché, and J. Gauss. Theoretical investigation of electronic excitation energy transfer in bichromophoric assemblies. *The Journal of Chemical Physics* **128**(7), 074505 (2008).

[58] C.-P. Hsu, G. R. Fleming, M. Head-Gordon, and T. Head-Gordon. Excitation energy transfer in condensed media. *The Journal of Chemical Physics* **114**(7), 3065–3072 (2001).

[59] A. Nazir. Correlation-Dependent Coherent to Incoherent Transitions in Resonant Energy Transfer Dynamics. *Physical Review Letters* **103**, 146404 (2009).

[60] M. Grover and R. Silbey. Exciton Migration in Molecular Crystals. *The Journal of Chemical Physics* **54**(11), 4843–4851 (1971).

[61] B. Jackson and R. Silbey. On the calculation of transfer rates between impurity states in solids. *The Journal of Chemical Physics* **78**(6), 4193–4196 (1983).

[62] I. Franco, M. Shapiro, and P. Brumer. Femtosecond dynamics and laser control of charge transport in trans-polyacetylene. *The Journal of Chemical Physics* **128**(24), 244905 (2008).

[63] O. V. Prezhdo and P. J. Rossky. Relationship between Quantum Decoherence Times and Solvation Dynamics in Condensed Phase Chemical Systems. *Physical Review Letters* **81**, 5294–5297 (1998).

[64] H. Hwang and P. J. Rossky. Electronic Decoherence Induced by Intramolecular Vibrational Motions in a Betaine Dye Molecule. *The Journal of Physical Chemistry B* **108**(21), 6723–6732 (2004).

[65] O. Varnavski, I. D. W. Samuel, L.-O. Pålsson, R. Beavington, P. L. Burn, and T. G. III. Investigations of excitation energy transfer and intramolecular interactions in a nitrogen corded distrylbenzene dendrimer system. *The Journal of Chemical Physics* **116**(20), 8893–8903 (2002).

[66] D. C. Arnett, C. C. Moser, P. L. Dutton, and N. F. Scherer. The First Events in Photosynthesis: Electronic Coupling and Energy Transfer Dynamics in the Photosynthetic Reaction Center from Rhodobacter sphaeroides. *The Journal of Physical Chemistry B* **103**(11), 2014–2032 (1999).

[67] S. Savikhin, D. R. Buck, and W. S. Struve. Oscillating anisotropies in a bacteriochlorophyll protein: Evidence for quantum beating between exciton levels. *Chemical Physics* **223**(2–3), 303–312 (1997).

[68] T. Goodson. Time-resolved spectroscopy of organic dendrimers and branched chromophores. *Annual Review of Physical Chemistry* **56**(1), 581–603 (2005).

[69] T. Kakitani, A. Kimura, and H. Sumi. Theory of Excitation Transfer in the Intermediate Coupling Case. *The Journal of Physical Chemistry B* **103**(18), 3720–3726 (1999).

[70] K. M. Gaab and C. J. Bardeen. The effects of connectivity, coherence, and trapping on energy transfer in simple light-harvesting systems studied using the Haken-Strobl model with diagonal disorder. *The Journal of Chemical Physics* **121**(16), 7813–7820 (2004).

[71] J. Cao and R. J. Silbey. Optimization of Exciton Trapping in Energy Transfer Processes. *The Journal of Physical Chemistry A* **113**(50), 13825–13838 (2009).

[72] J. S. Swensen, C. Soci, and A. J. Heeger. Light emission from an ambipolar semiconducting polymer field-effect transistor. *Applied Physics Letters* **87**(25), 253511–253513 (2005).

[73] X. Gong, M. Tong, Y. Xia, W. Cai, J. S. Moon, Y. Cao, G. Yu, C.-L. Shieh, B. Nilsson, and A. J. Heeger. High-Detectivity Polymer Photodetectors with Spectral Response from 300 nm to 1450 nm. *Science* **325**(5948), 1665–1667 (2009).

[74] N. S. Sariciftci, L. Smilowitz, A. J. Heeger, and F. Wudl. Photoinduced Electron Transfer from a Conducting Polymer to Buckminsterfullerene. *Science* **258**(5087), 1474–1476 (1992).

[75] A. E. Siegman. *Lasers*. University Science Books, 1986.

[76] O. S. Avanesjan, V. A. Benderskii, V. K. Brikenstein, V. L. Broude, L. I. Korshunov, A. G. Lavrushko, and I. I. Tartakovskii. Anthracene Crystals Under Intensive Optical Pumping. *Molecular Crystals and Liquid Crystals* **29**(1), 165–174 (1974).

[77] M. A. Díaz-García, F. Hide, B. J. Schwartz, M. D. McGehee, M. R. Andersson, and A. J. Heeger. "Plastic" lasers: Comparison of gain narrowing with a soluble semiconducting polymer in waveguides and microcavities. *Applied Physics Letters* **70**(24), 3191–3193 (1997).

[78] R. H. Friend, G. J. Denton, N. Tessler, and M. A. Stevens. Spectral narrowing in optically pumped poly (p-phenylenevinylene) Films. *Advanced Materials* **9**(7), 547–551 (1997).

[79] G. Heliotis, R. Xia, D. D. C. Bradley, G. A. Turnbull, I. D. W. Samuel, P. Andrew, and W. L. Barnes. Blue, surface-emitting, distributed feedback polyfluorene lasers. *Applied Physics Letters* **83**, 2118 (2003).

[80] J. R. Lawrence, G. A. Turnbull, I. D. W. Samuel, G. J. Richards, and P. L. Burn. Optical amplification in a first-generation dendriticorganic semiconductor. *Optics Letters* **29**(8), 869–871 (2004).

[81] G. Tsiminis, J.-C. Ribierre, A. Ruseckas, H. S. Barcena, G. J. Richards, G. A. Turnbull, P. L. Burn, and I. D. W. Samuel. Two-Photon Absorption and Lasing in First-Generation Bisfluorene Dendrimers. *Advanced Materials* **20**(10), 1940–1944 (2008).

[82] G. Tsiminis, Y. Wang, P. E. Shaw, A. L. Kanibolotsky, I. F. Perepichka, M. D. Dawson, P. J. Skabara, G. A. Turnbull, and I. D. W. Samuel. Low-threshold organic laser based on an oligofluorene truxene with low optical losses. *Applied Physics Letters* **94**(24), 243304 (2009).

[83] S. V. Frolov, W. Gellermann, M. Ozaki, K. Yoshino, and Z. V. Vardeny. Cooperative Emission in π-Conjugated Polymer Thin Films. *Physical Review Letters* **78**, 729–732 (1997).

[84] G. Cerullo, S. Stagira, M. Nisoli, S. De Silvestri, G. Lanzani, G. Kranzelbinder, W. Graupner, and G. Leising. Excited-state dynamics of poly(paraphenylene)-type ladder polymers at high photoexcitation density. *Physical Review B* **57**, 12806–12811 (1998).

[85] N. Tessler, G. J. Denton, and R. H. Friend. Lasing from conjugated-polymer microcavities. *Nature* **382**(6593), 695–697 (1996).

[86] V. D. Mihailetchi, J. Wildeman, and P. W. M. Blom. Space-Charge Limited Photocurrent. *Physical Review Letters* **94**, 126602 (2005).

[87] V. G. Kozlov, V. Bulović, and S. R. Forrest. Temperature independent performance of organic semiconductor lasers. *Applied Physics Letters* **71**(18), 2575–2577 (1997).

[88] G. Wegmann, H. Giessen, A. Greiner, and R. F. Mahrt. Laser emission from a solid conjugated polymer: Gain, tunability, and coherence. *Physical Review B* **57**, R4218–R4221 (1998).

[89] G. Turnbull, T. Krauss, W. Barnes, and I. Samuel. Tuneable distributed feedback lasing in MEH-PPV films. *Synthetic Metals* **121**(1–3), 1757–1758 (2001).

[90] R. R. King, D. C. Law, K. M. Edmondson, C. M. Fetzer, G. S. Kinsey, H. Yoon, R. A. Sherif, and N. H. Karam. 40% efficient metamorphic GaInP/GaInAs/Ge multijunction solar cells. *Applied Physics Letters* **90**(18), 183516 (2007).

[91] M. Scharber and N. Sariciftci. Efficiency of bulk-heterojunction organic solar cells. *Progress in Polymer Science* **38**(12), 1929–1940 (2013).

[92] M. A. Green, K. Emery, Y. Hishikawa, W. Warta, and E. D. Dunlop. Solar cell efficiency tables (version 39). *Progress in Photovoltaics: Research and Applications* **20**(1), 12–20 (2012).

[93] W. Cai, X. Gong, and Y. Cao. Polymer solar cells: Recent development and possible routes for improvement in the performance. *Solar Energy Materials and Solar Cells* **94**(2), 114–127 (2010).

[94] T. Singh, N. Marjanović, G. Matt, S. Günes, N. Sariciftci, A. M. Ramil, A. Andreev, H. Sitter, R. Schwödiauer, and S. Bauer. High-mobility n-channel

organic field-effect transistors based on epitaxially grown C_{60} films. *Organic Electronics* **6**(3), 105–110 (2005).

[95] P. W. M. Blom, V. D. Mihailetchi, L. J. A. Koster, and D. E. Markov. Device Physics of Polymer:Fullerene Bulk Heterojunction Solar Cells. *Advanced Materials* **19**(12), 1551–1566 (2007).

[96] H. Hoppe and N. S. Sariciftci. Organic solar cells: An overview. *Journal of Materials Research* **19**, 1924–1945 (2004).

[97] W. A. Luhman and R. J. Holmes. Investigation of Energy Transfer in Organic Photovoltaic Cells and Impact on Exciton Diffusion Length Measurements. *Advanced Functional Materials* **21**(4), 764–771 (2011).

[98] P. Peumans, S. Uchida, and S. R. Forrest. Efficient bulk heterojunction photovoltaic cells using small-molecular-weight organic thin films. *Nature* **425**(6954), 158–162 (2003).

[99] O. A. Abdulrazzaq, V. Saini, S. Bourdo, E. Dervishi, and A. S. Biris. Organic Solar Cells: A Review of Materials, Limitations, and Possibilities for Improvement. *Particulate Science and Technology* **31**(5), 427–442 (2013).

[100] W. Helfrich and W. G. Schneider. Recombination Radiation in Anthracene Crystals. *Physical Review Letters* **14**, 229–231 (1965).

[101] J. H. Burroughes, D. D. C. Bradley, A. R. Brown, R. N. Marks, K. Mackay, R. H. Friend, P. L. Burns, and A. B. Holmes. Light-emitting diodes based on conjugated polymers. *Nature* **347**(6293), 539–541 (1990).

[102] B. W. D'Andrade and S. R. Forrest. White Organic Light-Emitting Devices for Solid-State Lighting. *Advanced Materials* **16**(18), 1585–1595 (2004).

[103] Y.-S. Tyan. Organic light-emitting-diode lighting overview. *Journal of Photonics for Energy* **1**(1), 011009–011009–15 (2011).

[104] G. Schwartz, S. Reineke, T. C. Rosenow, K. Walzer, and K. Leo. Triplet Harvesting in Hybrid White Organic Light-Emitting Diodes. *Advanced Functional Materials* **19**(9), 1319–1333 (2009).

[105] M. C. Gather, A. Köhnen, and K. Meerholz. White Organic Light-Emitting Diodes. *Advanced Materials* **23**(2), 233–248 (2011).

[106] W. Brütting, J. Frischeisen, T. D. Schmidt, B. J. Scholz, and C. Mayr. Device efficiency of organic light-emitting diodes: Progress by improved light outcoupling. *Physica Status Solidi A* **210**(1), 44–65 (2013).

[107] S. Reineke, M. Thomschke, B. Lüssem, and K. Leo. White organic light-emitting diodes: Status and perspective. *Reviews of Modern Physics* **85**, 1245–1293 (2013).

[108] M. A. Baldo, D. F. O'Brien, M. E. Thompson, and S. R. Forrest. Excitonic singlet-triplet ratio in a semiconducting organic thin film. *Physical Review B* **60**, 14422–14428 (1999).

[109] M. A. Baldo, O. D. F., Y. You, A. Shoustikov, S. Sibley, M. E. Thompson, and S. R. Forrest. Highly efficient phosphorescent emission from organic electroluminescent devices. *Nature* **395**(6698), 151–154 (1998).

[110] B. Wang, G. Helander, J. Qiu, P. Puzzo, T. Greiner, M. Hudson, S. Wang, W. Liu, and H. Lu. Unlocking the full potential of organic light-emitting diodes on flexible plastic. *Nature Photonics* **5**(12), 753–757 (2011).

[111] S. Reineke, F. Lindner, G. Schwartz, N. Seidler, K. Walzer, B. Lussem, and K. Leo. White organic light-emitting diodes with fluorescent tube efficiency. *Nature* **459**(7244), 234–238 (2009).

[112] L. Xiao, Z. Chen, B. Qu, J. Luo, S. Kong, Q. Gong, and J. Kido. Recent Progresses on Materials for Electrophosphorescent Organic Light-Emitting Devices. *Advanced Materials* **23**(8), 926–952 (2011).

[113] J. Kido, H. Hayase, K. Hongawa, K. Nagai, and K. Okuyama. Bright red light-emitting organic electroluminescent devices having a europium complex as an emitter. *Applied Physics Letters* **65**(17), 2124–2126 (1994).

[114] F. So and D. Kondakov. Degradation Mechanisms in Small-Molecule and Polymer Organic Light-Emitting Diodes. *Advanced Materials* **22**(34), 3762–3777 (2010).

[115] Royal Society of Chemistry. Organic Electronics for a Better Tomorrow: Innovation, Accessibility, Sustainability. Technical report, Royal Society of Chemistry, 2012.

[116] N. C. Miller, E. Cho, R. Gysel, C. Risko, V. Coropceanu, C. E. Miller, S. Sweetnam, A. Sellinger, M. Heeney, I. McCulloch, J.-L. Brédas, M. F. Toney, and M. D. McGehee. Factors Governing Intercalation of Fullerenes and Other Small Molecules Between the Side Chains of Semiconducting Polymers Used in Solar Cells. *Advanced Energy Materials* **2**(10), 1208–1217 (2012).

[117] V. N. Gorshkov, S. Tretiak, and D. Mozyrsky. Semiclassical Monte-Carlo approach for modelling non-adiabatic dynamics in extended molecules. *Nature Communications* **4** (2013).

[118] J. Cabanillas-Gonzalez, G. Grancini, and G. Lanzani. Pump-Probe Spectroscopy in Organic Semiconductors: Monitoring Fundamental Processes of Relevance in Optoelectronics. *Advanced Materials* **23**(46), 5468–5485 (2011).

[119] J. Clark, T. Nelson, S. Tretiak, G. Cirmi, and G. Lanzani. Femtosecond torsional relaxation. *Nature Physics* **8**(3), 225–231 (2012).

[120] D. A. Vithanage, A. Devižis, V. Abramavičius, Y. Infahsaeng, D. Abramavičius, R. C. I. MacKenzie, P. E. Keivanidis, A. Yartsev, D. Hertel, J. Nelson, V. Sundström, and V. Gulbinas. Visualizing charge separation in bulk heterojunction organic solar cells. *Nature Communications* **4** (2013).

[121] K. Ishii, S. Nakanishi, and N. Tsurumachi. Ultrafast transition between polariton doublet and alternating current Stark triplet in organic one-dimensional photonic crystal microcavity. *Applied Physics Letters* **103**(1), 13301–13303 (2013).

[122] N. Banerji. Sub-picosecond delocalization in the excited state of conjugated homopolymers and donor-acceptor copolymers. *J. Mater. Chem. C* **1**, 3052–3066 (2013).

[123] S. Ling, S. Schumacher, I. Galbraith, and M. J. Paterson. Excited-State Absorption of Conjugated Polymers in the Near-Infrared and Visible: A Computational Study of Oligofluorenes. *The Journal of Physical Chemistry C* **117**(13), 6889–6895 (2013).

[124] F. Jensen. *Introduction to Computational Chemistry*. Wiley-VCH Verlag, 1999.

[125] S. Schumacher, I. Galbraith, A. Ruseckas, G. A. Turnbull, and I. D. W. Samuel. Dynamics of photoexcitation and stimulated optical emission in conjugated polymers: A multiscale quantum-chemistry and Maxwell-Bloch-equations approach. *Physical Review B* **81**, 245407 (2010).

[126] H. Bässler. Charge Transport in Disordered Organic Photoconductors a Monte Carlo Simulation Study. *physica status solidi (b)* **175**(1), 15–56 (1993).

[127] S. C. J. Meskers, J. Hübner, M. Oestreich, and H. Bässler. Dispersive Relaxation Dynamics of Photoexcitations in a Polyfluorene Film Involving Energy

Transfer: Experiment and Monte Carlo Simulations. *The Journal of Physical Chemistry B* **105**(38), 9139–9149 (2001).

[128] P. K. Watkins, A. B. Walker, and G. L. B. Verschoor. Dynamical Monte Carlo Modelling of Organic Solar Cells: The Dependence of Internal Quantum Efficiency on Morphology. *Nano Letters* **5**(9), 1814–1818 (2005).

[129] C. Groves and N. Greenham. Monte Carlo Simulations of Organic Photovoltaics. In *Topics in Current Chemistry 2013*, Topics in Current Chemistry, pp. 1–22. Springer Berlin Heidelberg, 2013.

[130] D. Mendels and N. Tessler. Drift and Diffusion in Disordered Organic Semiconductors: The Role of Charge Density and Charge Energy Transport. *The Journal of Physical Chemistry C* **117**(7), 3287–3293 (2013).

[131] M. Mesta, M. Carvelli, J. de Vries Rein, H. van Eersel, M. van der Holst, J. Jeroen, M. Schober, M. Furno, B. Lüssem, K. Leo, P. Loebl, R. Coehoorn, and P. A. Bobbert. Molecular-scale simulation of electroluminescence in a multilayer white organic light-emitting diode. *Nat Mater* **12**(7), 652–658 (2013).

[132] L. Meng, Y. Shang, Q. Li, Y. Li, X. Zhan, Z. Shuai, R. G. E. Kimber, and A. B. Walker. Dynamic Monte Carlo simulation for highly efficient polymer blend photovoltaics. *The Journal Physical Chemistry B* **114**(1), 36–41 (2010).

[133] S. Athanasopoulos, E. V. Emelianova, A. B. Walker, and D. Beljonne. Exciton diffusion in energetically disordered organic materials. *Physical Review B* **80**(19), 1–7 (2009).

[134] C. Daniel, S. Westenhoff, F. Makereel, R. H. Friend, D. Beljonne, L. M. Herz, and C. Silva. Monte Carlo Simulation of Exciton Bimolecular Annihilation Dynamics in Supramolecular Semiconductor Architectures. *The Journal Physical Chemistry C* **111**(51), 19111–19119 (2007).

[135] M. Grage, Y. Zaushitsyn, A. Yartsev, M. Chachisvilis, V. Sundström, and T. o. Pullerits. Ultrafast excitation transfer and trapping in a thin polymer film. *Physical Review B* **67**(20), 1–5 (2003).

[136] O. R. Tozer and W. Barford. Exciton Dynamics in Disordered Poly(p-phenylenevinylene). 1. Ultrafast Interconversion and Dynamical Localization. *The Journal of Physical Chemistry A* **116**(42), 10310–10318 (2012).

[137] V. M. Kenkre. *The master equation approach: Coherence, energy transfer, annihilation, and relaxation*. Springer Berlin Heidelberg, 1982.

[138] M. Yang and G. R. Fleming. Influence of phonons on exciton transfer dynamics: comparison of the Redfield, Förster, and modified Redfield equations. *Chemical Physics* **282**(1), 163–180 (2002).

[139] D. Marx and J. Hutter. *Ab Initio Molecular Dynamics: Basic Theory and Advanced Methods*. Cambridge University Press, 2009.

[140] M. Levitt. Protein folding by restrained energy minimization and molecular dynamics. *Journal of Molecular Biology* **170**(3), 723–764 (1983).

[141] M. Karplus and J. A. McCammon. Molecular dynamics simulations of biomolecules. *Nature Structural & Molecular Biology* **9**(9), 646–652 (2002).

[142] A. Jabbarzadeh and R. I. Tanner. Molecular dynamics simulation and its application to nano-rheology. *Rheology Reviews* , 165–216 (2006).

[143] J. Kohanoff. *Electronic Structure Calculations for Solids and Molecules*. Theory and Computational Methods. Cambridge University Press, 2006.

[144] J. B. Foresman and E. Frisch. *Exploring Chemistry with Electronic Structure Methods*. Gaussian Inc., 2nd edition, 1996.

[145] N. C. Handy and A. M. Lee. The adiabatic approximation. *Chemical Physics Letters* **252**(5–6), 425–430 (1996).

[146] M. Born and R. Oppenheimer. Zur Quantentheorie der Molekeln. *Annalen der Physik* **389**(20), 457–484 (1927).

[147] P. Hohenberg. Inhomogeneous Electron Gas. *Physical Review* **136**(3B), B864–B871 (1964).

[148] W. Kohn. Self-Consistent Equations Including Exchange and Correlation Effects. *Physical Review* **140**(4A), A1133–A1138 (1965).

[149] M. A. Marques, C. A. Ullrich, F. Nogueira, A. Rubio, K. Burke, and E. K. U. Gross. *Time-Dependent Density Functional Theory*. Springer Berlin Heidelberg, 2006.

[150] C. A. Ullrich and Z.-H. Yang. A Brief Compendium of Time-Dependent Density Functional Theory. *Brazilian Journal of Physics* , 1–35 (2013).

[151] R. Van Leeuwen. Key concepts in time-dependent density-functional theory. *International Journal of Modern Physics B* **15**(14), 1969–2023 (2001).

[152] E. Runge and E. K. U. Gross. Density-Functional Theory for Time-Dependent Systems. *Physical Review Letters* **52**, 997–1000 (1984).

[153] A. D. Becke. Density-functional exchange-energy approximation with correct asymptotic behavior. *Physical Review A* **38**, 3098–3100 (1988).

[154] C. Lee, W. Yang, and R. G. Parr. Development of the Colle-Salvetti correlation-energy formula into a functional of the electron density. *Physical Review B* **37**, 785–789 (1988).

[155] A. D. Becke. Densityfunctional thermochemistry. III. The role of exact exchange. *Journal of Chemical Physics* **98**(7), 5648–5652 (1992).

[156] T. Yanai, D. P. Tew, and N. C. Handy. A new hybrid exchange–correlation functional using the Coulomb-attenuating method (CAM-B3LYP). *Chemical Physics Letters* **393**(1–3), 51–57 (2004).

[157] Y. Zhao and D. Truhlar. The M06 suite of density functionals for main group thermochemistry, thermochemical kinetics, noncovalent interactions, excited states, and transition elements: two new functionals and systematic testing of four M06-class functionals and 12 other functionals. *Theoretical Chemistry Accounts* **120**(1-3), 215–241 (2008).

[158] W. J. Hehre, R. F. Stewart, and J. A. Pople. Self-Consistent Molecular-Orbital Methods. I. Use of Gaussian Expansions of Slater-Type Atomic Orbitals. *The Journal of Chemical Physics* **51**(6), 2657–2664 (1969).

[159] P. Hariharan and J. Pople. The influence of polarization functions on molecular orbital hydrogenation energies. *Theoretica chimica acta* **28**(3), 213–222 (1973).

[160] M. J. Frisch, J. A. Pople, and J. S. Binkley. Self-consistent molecular orbital methods 25. Supplementary functions for Gaussian basis sets. *The Journal of Chemical Physics* **80**(7), 3265–3269 (1984).

[161] T. Clark, J. Chandrasekhar, G. W. Spitznagel, and P. V. R. Schleyer. Efficient diffuse function-augmented basis sets for anion calculations. III. The 3-21+G basis set for first-row elements, Li–F. *Journal of Computational Chemistry* **4**(3), 294–301 (1983).

[162] *Gaussian09 User's Reference.*

[163] S. Schumacher, A. Ruseckas, N. A. Montgomery, P. J. Skabara, A. L. Kanibolotsky, M. J. Paterson, I. Galbraith, G. A. Turnbull, and I. D. W. Samuel. Effect of exciton self-trapping and molecular conformation on photophysical properties of oligofluorenes. *The Journal of Chemical Physics* **131**, 154906 (2009).

[164] M. J. Frisch, G. W. Trucks, H. B. Schlegel, G. E. Scuseria, M. A. Robb, J. R. Cheeseman, G. Scalmani, V. Barone, B. Mennucci, G. A. Petersson, H. Nakatsuji, M. Caricato, X. Li, H. P. Hratchian, A. F. Izmaylov, J. Bloino, G. Zheng, J. L. Sonnenberg, M. Hada, M. Ehara, K. Toyota, R. Fukuda, J. Hasegawa, M. Ishida, T. Nakajima, Y. Honda, O. Kitao, H. Nakai, T. Vreven, J. J. A. Montgomery, J. E. Peralta, F. Ogliaro, M. Bearpark, J. J. Heyd, E. Brothers, K. N. Kudin, V. N. Staroverov, R. Kobayashi, J. Normand, K. Raghavachari, A. Rendell, J. C. Burant, S. S. Iyengar, J. Tomasi, M. Cossi, N. Rega, J. M. Millam, M. Klene, J. E. Knox, J. B. Cross, V. Bakken, C. Adamo, J. Jaramillo, R. Gomperts, R. E. Stratmann, O. Yazyev, A. J. Austin, R. Cammi, C. Pomelli, J. W. Ochterski, R. L. Martin, K. Morokuma, V. G. Zakrzewski, G. A. Voth, P. Salvador, J. J. Dannenberg, S. Dapprich, A. D. Daniels, Ö. Farkas, J. B. Foresman, J. V. Ortiz, J. Cioslowski, and D. J. Fox. Gaussian 09 Revision A.1, 2009. Gaussian Inc. Wallingford CT 2009.

[165] W. J. Hehre, W. A. Lathan, R. Ditchfield, M. D. Newton, and J. A. Pople. Gaussian 70, 1970. Quantum Chemistry Program Exchange, Program No. 237.

[166] R. Dennington, T. Keith, and J. Millam. GaussView Version 5, 2009. Semichem Inc. Shawnee Mission KS 2009.

[167] K. Sriwichitkamol, S. Suramitr, P. Poolmee, and S. Hannongbua. Structures, absorption spectra, and electronic properties of polyfluorene and its derivatives: a theoretical study. *Journal of Theoretical and Computational Chemistry* **05**(03), 595–608 (2006).

[168] E. Jansson, P. C. Jha, and H. Ågren. Chain length dependence of singlet and triplet excited states of oligofluorenes: A density functional study. *Chemical Physics* **336**(2–3), 91–98 (2007).

[169] K. I. Igumenshchev, S. Tretiak, and V. Y. Chernyak. Excitonic effects in a time-dependent density functional theory. *The Journal of Chemical Physics* **127**(11), 114902 (2007).

[170] V. Marcon, N. van der Vegt, G. Wegner, and G. Raos. Modeling of Molecular Packing and Conformation in Oligofluorenes. *The Journal of Physical Chemistry B* **110**(11), 5253–5261 (2006).

[171] U. Scherf and D. Neher, editors. *Polyfluorenes*, volume 212 of *Advances in polymer science*. Springer, Berlin, 2008.

[172] C. Cohen-Tannoudji, J. Dupont-Roc, and G. Grynberg. *Optical Bloch Equations*, pp. 353–405. Wiley-VCH Verlag GmbH, 2008.

[173] L. Allen and J. H. Eberly. *Optical Resonance and Two-Level Atoms*. Dover Publications, soft cover edition, 1987.

[174] M. Lindberg and S. W. Koch. Effective Bloch equations for semiconductors. *Physical Review B* **38**, 3342–3350 (1988).

[175] S. Mukamel. *Principles of Nonlinear Optical Spectroscopy (Oxford Series on Optical and Imaging Sciences)*. Oxford University Press, USA, new edition, 1999.

[176] M. Richter, T. Renger, and A. Knorr. A Bloch equation approach to intensity dependent optical spectra of light harvesting complex II : Excitation dependence of light harvesting complex II pump-probe spectra. *Photosynthesis Research* **95**, 119–127 (2007).

[177] H. Haug and S. W. Koch. *Quantum theory of the optical and electronic properties of semiconductors*. World Scientific Publishers, New Jersey, 4th edition, 2004.

[178] K. E. Atkinson. *An introduction to numerical analysis*. Wiley-VCH Verlag GmbH, 2nd edition, 1989.

[179] S. Banerjee and G. Gangopadhyay. Spectra of displaced distorted oscillator molecular system. *Chemical Physics Letters* **359**(3–4), 295–302 (2002).

[180] J.-C. Denis, S. Schumacher, and I. Galbraith. Quantitative description of interactions between linear organic chromophores. *The Journal of Chemical Physics* **137**(22), 224102 (2012).

[181] F. C. Spano. The Spectral Signatures of Frenkel Polarons in H- and J-Aggregates. *Accounts of Chemical Research* **43**(3), 429–439 (2010).

[182] M. Kasha, H. R. Rawls, and M. Ashraf El-Bayoumi. The exciton model in molecular spectroscopy. *Pure and Applied Chemistry* **11**, 371 (1965).

[183] P. L. Burn, S.-C. Lo, and I. D. W. Samuel. The Development of Light-Emitting Dendrimers for Displays. *Advanced Materials* **19**(13), 1675–1688 (2007).

[184] T. P. I. Saragi, T. Spehr, A. Siebert, T. Fuhrmann-Lieker, and J. Salbeck. Spiro Compounds for Organic Optoelectronics. *Chemical Reviews* **107**(4), 1011–1065 (2007).

[185] A. L. Kanibolotsky, I. F. Perepichka, and P. J. Skabara. Star-shaped [small pi]-conjugated oligomers and their applications in organic electronics and photonics. *Chemical Society Reviews* **39**, 2695–2728 (2010).

[186] M. Joffre, D. Yaron, R. J. Silbey, and J. Zyss. Second order optical nonlinearity in octupolar aromatic systems. *The Journal of Chemical Physics* **97**(8), 5607–5615 (1992).

[187] S. Brasselet, F. Cherioux, P. Audebert, and J. Zyss. New Octupolar Star-Shaped Strucures for Quadratic Nonlinear Optics. *Chemistry of Materials* **11**(7), 1915–1920 (1999).

[188] M. H. Hoang, M. J. Cho, D. C. Kim, K. H. Kim, J. W. Shin, M. Y. Cho, J.-s. Joo, and D. H. Choi. Photoreactive -conjugated star-shaped molecules for the organic field-effect transistor. *Organic Electronics* **10**(4), 607–617 (2009).

[189] K. Kreger, M. Bäte, C. Neuber, H.-W. Schmidt, and P. Strohriegl. Combinatorial Development of Blue OLEDs Based on Star Shaped Molecules. *Advanced Functional Materials* **17**(17), 3456–3461 (2007).

[190] M. Y. Cho, S. J. Kim, Y. D. Han, D. H. Park, K. H. Kim, D. H. Choi, and J. Joo. Highly Sensitive, Photocontrolled, Organic Thin-Film Transistors Using Soluble Star-shaped Conjugated Molecules. *Advanced Functional Materials* **18**(19), 2905–2912 (2008).

[191] A. L. Kanibolotsky, R. Berridge, P. J. Skabara, I. F. Perepichka, D. D. C. Bradley, and M. Koeberg. Synthesis and Properties of Monodisperse Oligofluorene-Functionalized Truxenes: Highly Fluorescent Star-Shaped Architectures. *Journal of the American Chemical Society* **126**(42), 13695–13702 (2004).

[192] X.-H. Zhou, J.-C. Yan, and J. Pei. Synthesis and Relationships between the Structures and Properties of Monodisperse Star-Shaped Oligofluorenes. *Organic Letters* **5**(19), 3543–3546 (2003).

[193] M. Moreno Oliva, J. Casado, J. T. López Navarrete, R. Berridge, P. J. Skabara, A. L. Kanibolotsky, and I. F. Perepichka. Electronic and Molecular Structures of Trigonal Truxene-Core Systems Conjugated to Peripheral Fluorene Branches. Spectroscopic and Theoretical Study. *The Journal of Physical Chemistry B* **111**(16), 4026–4035 (2007).

[194] W.-Y. Lai, R. Xia, Q.-Y. He, P. A. Levermore, W. Huang, and D. D. C. Bradley. Enhanced Solid-State Luminescence and Low-Threshold Lasing from

Starburst Macromolecular Materials. *Advanced Materials* **21**(3), 355–360 (2009).

[195] Y. M. Sun, K. Xiao, Y. Q. Liu, J. L. Wang, J. Pei, G. Yu, and D. B. Zhu. Oligothiophene-Functionalized Truxene: Star-Shaped Compounds for Organic Field-Effect Transistors. *Advanced Functional Materials* **15**(5), 818–822 (2005).

[196] M. Wu, Z. Gong, A. J. Kuehne, A. L. Kanibolotsky, Y. J. Chen, I. F. Perepichka, A. R. Mackintosh, E. Gu, P. J. Skabara, R. A. Pethrick, and M. D. Dawson. Hybrid GaN/organic microstructured light-emitting devices via ink-jet printing. *Opt. Express* **17**(19), 16436–16443 (2009).

[197] M.-S. Yuan, Z.-Q. Liu, and Q. Fang. Donor-and-Acceptor Substituted Truxenes as Multifunctional Fluorescent Probes. *The Journal of Organic Chemistry* **72**(21), 7915–7922 (2007).

[198] H. A. Jahn and E. Teller. Stability of Polyatomic Molecules in Degenerate Electronic States. I. Orbital Degeneracy. *Proceedings of the Royal Society of London. Series A - Mathematical and Physical Sciences* **161**(905), 220–235 (1937).

[199] J. Gierschner, J. Cornil, and H.-J. Egelhaaf. Optical Bandgaps of -Conjugated Organic Materials at the Polymer Limit: Experiment and Theory. *Advanced Materials* **19**(2), 173–191 (2007).

[200] R. S. Knox and H. van Amerongen. Refractive Index Dependence of the Förster Resonance Excitation Transfer Rate. *The Journal of Physical Chemistry B* **106**(20), 5289–5293 (2002).

[201] S. J. Strickler and R. A. Berg. Relationship between Absorption Intensity and Fluorescence Lifetime of Molecules. *The Journal of Chemical Physics* **37**(4), 814–822 (1962).

[202] M. J. Paterson, M. J. Bearpark, M. A. Robb, L. Blancafort, and G. A. Worth. Conical intersections: A perspective on the computation of spectroscopic Jahn-Teller parameters and the degenerate 'intersection space'. *Physical Chemistry Chemical Physics* **7**, 2100–2115 (2005).

[203] A. Bar-Haim, J. Klafter, and R. Kopelman. Dendrimers as Controlled Artificial Energy Antennae. *Journal of the American Chemical Society* **119**(26), 6197–6198 (1997).

[204] M. Drobizhev, A. Karotki, A. Rebane, and C. W. Spangler. Dendrimer molecules with record large two-photon absorption cross section. *Optics Letters* **26**(14), 1081–1083 (2001).

[205] S.-J. Chung, K.-S. Kim, T.-C. Lin, G. S. He, J. Swiatkiewicz, and P. N. Prasad. Cooperative Enhancement of Two-Photon Absorption in Multibranched Structures. *The Journal of Physical Chemistry B* **103**(49), 10741–10745 (1999).

[206] F. Terenziani, C. Katan, E. Badaeva, S. Tretiak, and M. Blanchard-Desce. Enhanced Two-Photon Absorption of Organic Chromophores: Theoretical and Experimental Assessments. *Advanced Materials* **20**(24), 4641–4678 (2008).

[207] Y. Wang, G. Tsiminis, Y. Yang, A. Ruseckas, A. L. Kanibolotsky, I. F. Perepichka, P. J. Skabara, G. A. Turnbull, and I. D. Samuel. Broadly tunable deep blue laser based on a star-shaped oligofluorene truxene. *Synthetic Metals* **160**(13–14), 1397–1400 (2010).

[208] R. Kopelman, M. Shortreed, Z.-Y. Shi, W. Tan, Z. Xu, J. S. Moore, A. Bar-Haim, and J. Klafter. Spectroscopic Evidence for Excitonic Localization in Fractal Antenna Supermolecules. *Physical Review Letters* **78**, 1239–1242 (1997).

[209] M. R. Wasielewski. Self-Assembly Strategies for Integrating Light Harvesting and Charge Separation in Artificial Photosynthetic Systems. *Accounts of Chemical Research* **42**(12), 1910–1921 (2009).

[210] M. Guo, O. Varnavski, A. Narayanan, O. Mongin, J.-P. Majoral, M. Blanchard-Desce, and T. Goodson. Investigations of Energy Migration in an Organic Dendrimer Macromolecule for Sensory Signal Amplification. *The Journal of Physical Chemistry A* **113**(16), 4763–4771 (2009).

[211] A. Narayanan, O. Varnavski, O. Mongin, J.-P. Majoral, M. Blanchard-Desce, and T. G. III. Detection of TNT using a sensitive two-photon organic dendrimer for remote sensing. *Nanotechnology* **19**(11), 115502 (2008).

[212] S.-C. Lo and P. L. Burn. Development of Dendrimers: Macromolecules for Use in Organic Light-Emitting Diodes and Solar Cells. *Chemical Reviews* **107**(4), 1097–1116 (2007).

[213] O. Varnavski, G. Menkir, T. G. III, P. L. Burn, I. D. W. Samuel, J. M. Lupton, and R. Beavington. Erratum: "Ultrafast polarized fluorescence dynamics in an organic dendrimer" [*Appl. Phys. Lett.* **77**, 1120 (2000)]. *Applied Physics Letters* **78**(23), 3749–3749 (2001).

[214] O. P. Varnavski, J. C. Ostrowski, L. Sukhomlinova, R. J. Twieg, G. C. Bazan, and T. Goodson. Coherent Effects in Energy Transport in Model Dendritic Structures Investigated by Ultrafast Fluorescence Anisotropy Spectroscopy. *Journal of the American Chemical Society* **124**(8), 1736–1743 (2002).

[215] O. Varnavski, T. Goodson, L. Sukhomlinova, and R. Twieg. Ultrafast Exciton Dynamics in a Branched Molecule Investigated by Time-Resolved Fluorescence, Transient Absorption, and Three-Pulse Photon Echo Peak Shift Measurements. *The Journal of Physical Chemistry B* **108**(29), 10484–10492 (2004).

[216] T. G. Goodson. Optical Excitations in Organic Dendrimers Investigated by Time-Resolved and Nonlinear Optical Spectroscopy. *Accounts of Chemical Research* **38**(2), 99–107 (2005).

[217] E. Y. Poliakov, V. Chernyak, S. Tretiak, and S. Mukamel. Exciton-scaling and optical excitations of self-similar phenylacetylene dendrimers. *The Journal of Chemical Physics* **110**(16), 8161–8175 (1999).

[218] W. Verbouwe, M. Van der Auweraer, F. C. De Schryver, J. J. Piet, and J. M. Warman. Excited State Localization or Delocalization in C3-symmetric Amino-substituted Triphenylbenzene Derivatives. *Journal of the American Chemical Society* **120**(6), 1319–1324 (1998).

[219] L. Latterini, G. D. Belder, G. Schweitzer, M. V. der Auweraer, and F. D. Schryver. Femtosecond polarized transient absorption spectroscopy of a C3-symmetric amino-substituted phenylbenzene derivative. *Chemical Physics Letters* **295**(1–2), 11–16 (1998).

[220] M. Fujitsuka, D. W. Cho, H.-H. Huang, J.-S. Yang, and T. Majima. Structural Relaxation in the Singlet Excited State of Star-Shaped Oligofluorenes Having a Truxene or Isotruxene as a Core. *The Journal of Physical Chemistry B* **115**(46), 13502–13507 (2011).

[221] J. Lackowicz. *Principles of Fluorescence Spectroscopy.* Kluwer Academic/Plenum Publishers, 3rd edition, 2006.

[222] R. S. Knox and D. Gülen. Theory of polarized fluorescence from molecular pairs: Förster transfer at large electronic coupling. *Photochemistry and Photobiology* **57**(1), 40–43 (1993).

[223] K. Wynne and R. Hochstrasser. Coherence effects in the anisotropy of optical experiments. *Chemical Physics* **171**(1–2), 179–188 (1993).

[224] G. G. Gurzadyan, T.-H. Tran-Thi, and T. Gustavsson. Time-resolved fluorescence spectroscopy of high-lying electronic states of Zn-tetraphenylporphyrin. *The Journal of Chemical Physics* **108**(2), 385–388 (1998).

[225] N. A. Montgomery, G. Hedley, A. Ruseckas, J.-C. Denis, S. Schumacher, A. L. Kanibolotsky, P. J. Skabara, I. Galbraith, G. A. Turnbull, and I. D. W. Samuel. Dynamics of fluorescence depolarization in branched oligofluorene-truxene molecules. *Physical Chemistry Chemical Physics* **14**, 9176 (2012).

[226] I. Soutar, L. Swanson, R. E. Imhof, and G. Rumbles. Synchrotron-generated time-resolved fluorescence anisotropy studies of the segmental relaxation of poly(acrylic acid) and poly(methacrylic acid) in dilute methanolic solutions. *Macromolecules* **25**(17), 4399–4405 (1992).

[227] C. Sissa, A. Painelli, M. Blanchard-Desce, and F. Terenziani. Fluorescence Anisotropy Spectra Disclose the Role of Disorder in Optical Spectra of Branched Intramolecular-Charge-Transfer Molecules. *The Journal of Physical Chemistry B* **115**(21), 7009–7020 (2011).

[228] F. Terenziani, C. Sissa, and A. Painelli. Symmetry Breaking in Octupolar Chromophores: Solvatochromism and Electroabsorption. *The Journal of Physical Chemistry B* **112**(16), 5079–5087 (2008).

[229] S. Günes, H. Neugebauer, and N. S. Sariciftci. Conjugated Polymer-Based Organic Solar Cells. *Chemical Reviews* **107**, 1324 (2007).

[230] D. L. Andrews, C. Curuchet, and G. D. Scholes. Resonance energy tranfer: beyond the limits. *Laser Photonics Review* **5**, 114 (2011).

[231] R. Q. Albuquerque, C. C. Hofmann, J. Köhler, and A. Köhler. Diffusion-limited energy tranfer in blends of oligofluorenes with an anthracene derivative. *The Journal Physical Chemistry B* **115**, 8063 (2011).

[232] L. Cerdan, E. Enciso, V. Martin, J. Banuelos, I. Lopez-Arbeloa, A. Costela, and I. Garcia-Moreno. FRET-assisted laser emission in colloidal suspensions of dye-doped latex nanoparticles. *Nature Photonics* **6**, 623 (2012).

[233] A. L. Stevens, A. Kaeser, A. P. H. J. Schenning, and L. M. Herz. Morphology-Dependent Energy Transfer Dynamics in Fluorene-Based Amphiphile Nanoparticles. *ACS Nano* **6**, 4777 (2012).

[234] P. E. Shaw, A. Ruseckas, J. Peet, G. C. Bazan, and I. D. W. Samuel. Exciton–Exciton Annihilation in Mixed-Phase Polyfluorene Films. *Advanced Functional Materials* **20**(1), 155–161 (2010).

[235] M. E. Madjet, A. Abdurahman, and T. Renger. Intermolecular {C}oulomb couplings from ab initio electrostatic potentials: application to optical transitions of strongly coupled pigments in photosynthetic antennae and reaction centers. *The Journal Physical Chemistry B* **110**, 17268 (2006).

[236] V. Czikklely, H. Forsterling, and H. Kuhn. Extended dipole model for aggregates of dye molecules. *Chemical Physics Letters* **6**(3), 207–210 (1970).

[237] S. Siddiqui and F. Spano. H- and J-aggregates of conjugated polymers and oligomers: A theoretical investigation. *Chemical Physics Letters* **308**(1–2), 99–105 (1999).

[238] W. J. D. Beenken and T. O. Pullerits. Excitonic coupling in polythiophenes: Comparison of different calculation methods. *The Journal of Chemical Physics* **120**(5), 2490–2495 (2004).

[239] J. Cornil, D. Beljonne, D. A. Dos Santos, J. P. Calbert, and J. L. Bredas. Intermoleculr interactions in electroluminescent conjugated polymers. *Thin Solid Films* **363**, 72 (2000).

[240] S. Marguet, D. Markovitsi, and P. Millie. Influence of Disorder on Electronic Excited States : An Experimental and Numerical Study. *The Journal Physical Chemistry B* **5647**(98), 4697–4710 (1998).

[241] D. Beljonne, J. Cornil, R. Silbey, P. Millie, and J. L. Bredas. Interchain interactions in conjugated materials: The exciton model versus the supermolecular approach. *The Journal of Chemical Physics* **112**(10), 4749–4758 (2000).

[242] S. Westenhoff, C. Daniel, R. H. Friend, C. Silva, V. Sundström, and A. Yartsev. Exciton migration in a polythiophene: probing the spatial and energy domain by line-dipole Forster-type energy transfer. *The Journal of Chemical Physics* **122**(9), 094903 (2005).

[243] C. Groves, O. G. Reid, and D. S. Ginger. Heterogeneity in Polymer Solar Cells: Local Morphology and Performance in Organic Photovoltaics Studied with Scanning Probe Microscopy. *Accounts of Chemical Research* **43**(5), 612–620 (2010).

[244] A. A. Virkar, S. Mannsfeld, Z. Bao, and N. Stingelin. Organic Semiconductor Growth and Morphology Considerations for Organic Thin-Film Transistors. *Advanced Materials* **22**(34), 3857–3875 (2010).

[245] J. Rivnay, S. C. B. Mannsfeld, C. E. Miller, A. Salleo, and M. F. Toney. Quantitative Determination of Organic Semiconductor Microstructure from the Molecular to Device Scale. *Chemical Reviews* **112**(10), 5488–5519 (2012).

[246] F. P. V. Koch, J. Rivnay, S. Foster, C. Müller, J. M. Downing, E. Buchaca-Domingo, P. Westacott, L. Yu, M. Yuan, M. Baklar, Z. Fei, C. Luscombe, M. A. McLachlan, M. Heeney, G. Rumbles, C. Silva, A. Salleo, J. Nelson, P. Smith, and N. Stingelin. The impact of molecular weight on microstructure and charge transport in semicrystalline polymer semiconductors–poly(3-hexylthiophene), a model study. *Progress in Polymer Science* **38**(12), 1978–1989 (2013).

[247] S. Tretiak, A. Saxena, R. L. Martin, and A. R. Bishop. Conformational Dynamics of Photoexcited Conjugated Molecules. *Physical Review Letters* **89**, 097402 (2002).

[248] B. Bouvier, J.-P. Dognon, R. Lavery, D. Markovitsi, P. Millié, D. Onidas, and K. Zakrzewska. Influence of Conformational Dynamics on the Exciton States of DNA Oligomers. *The Journal of Physical Chemistry B* **107**(48), 13512–13522 (2003).

[249] H. Lin, S. R. Tabaei, D. Thomsson, O. Mirzov, P.-O. Larsson, and I. G. Scheblykin. Fluorescence Blinking, Exciton Dynamics, and Energy Transfer Domains in Single Conjugated Polymer Chains. *Journal of the American Chemical Society* **130**(22), 7042–7051 (2008).

[250] M. Bednarz, V. A. Malyshev, and J. Knoester. Intraband relaxation and temperature dependence of the fluorescence decay time of one-dimensional Frenkel excitons: The Pauli master equation approach. *The Journal of Chemical Physics* **117**(13), 6200–6213 (2002).

[251] M. Takahata, M. Nakano, H. Fujita, and K. Yamaguchi. Mechanism of exciton migration of dendritic molecular aggregate: a master equation approach including weak exciton–phonon coupling. *Chemical Physics Letters* **363**(5–6), 422–428 (2002).

[252] M. Nakano, M. Takahata, S. Yamada, K. Yamaguchi, R. Kishi, and T. Nitta. Exciton migration dynamics in a dendritic molecule: Quantum master equation approach using ab initio molecular orbital configuration interaction method. *The Journal of Chemical Physics* **120**(5), 2359–2367 (2004).

[253] R. Hidayat, A. Fujii, M. Ozaki, M. Teraguchi, T. Masuda, and K. Yoshino.

Exciton dynamics in disubstituted polyacetylenes. *Synthetic Metals* **119**(1), 597–598 (2001).

[254] W. M. Zhang, T. Meier, V. Chernyak, and S. Mukamel. Exciton-migration and three-pulse femtosecond optical spectroscopies of photosynthetic antenna complexes. *The Journal of Chemical Physics* **108**(18), 7763–7774 (1998).

[255] R. G. E. Kimber, E. N. Wright, S. E. J. O'Kane, A. B. Walker, and J. C. Blakesley. Mesoscopic kinetic Monte Carlo modeling of organic photovoltaic device characteristics. *Physical Review B* **86**, 235206 (2012).

[256] A. Ruseckas, P. Wood, I. D. W. Samuel, G. R. Webster, W. J. Mitchell, P. L. Burn, and V. Sundström. Ultrafast depolarization of the fluorescence in a conjugated polymer. *Physical Review B* **72**, 115214 (2005).

[257] J. Crank. *The mathematics of diffusion*. Oxford: Clarendon Press, 2nd edition, 1975.

[258] A. Bruno, L. X. Reynolds, C. Dyer-Smith, J. Nelson, and S. A. Haque. Determining the Exciton Diffusion Length in a Polyfluorene from Ultrafast Fluorescence Measurements of Polymer/Fullerene Blend Films. *The Journal of Physical Chemistry C* **117**(39), 19832–19838 (2013).

[259] A. Monkman, C. Rothe, S. King, and F. Dias. Polyfluorene Photophysics. In U. Scherf and D. Neher, editors, *Polyfluorenes*, volume 212 of *Advances in Polymer Science*, pp. 187–225. Springer Berlin Heidelberg, 2008.